SURFACE MODIFICATION OF β-PHASE TI ALLOY BY PLASMA SPRAY DEPOSITION TECHNIQUE FOR ORTHOPEDIC APPLICATIONS

A Thesis

Submitted in partial fulfillment of the requirements for the

award of the degree of

DOCTOR OF PHILOSOPHY

in

Mechanical Engineering

By

Harjit Singh

41700234

Supervised By

Dr. Chander Prakash

Co-supervised By

Dr. Sunpreet Singh

LOVELY PROFESSIONAL UNIVERSITY

PUNJAB

2021

DECLERATION

I declare that the thesis entitled "**Surface modification of β-phase Ti alloy by Plasma spray deposition technique for Orthopedic Applications**" has been prepared by me under the guidance of Dr. Chander Prakash, Professor, School of Mechanical Engineering, Lovely Professional University, Phagwara, Punjab and Dr.Sunpreet Singh, Research fellow, National University of Singapore, Singapore. No part of this thesis has formed the basis for the award of any degree or fellowship previously.

HARJIT SINGH

Registration No.41700234

School of Mechanical Engineering

Lovely Professional University

Phagwara, Punjab.

Date:-

Lovely Professional University,

Punjab, India

Certificate

This is to certify that the thesis titled "**Surface modification of β-phase Ti alloy by Plasma spray deposition technique for Orthopedic Applications**" being submitted by **Mr. Harjit Singh** to the Lovely Professional University, Punjab, India for the award of the degree of **DOCTOR OF PHILOSOPHY** is a record of bonafide research carried out by him under our guidance and supervision. Mr. Singh has worked for about three years on the above problem and the work has reached the standard fulfilling the requirements and the regulations relating to the degree. To the best of our knowledge the work incorporated in this thesis has not been submitted to any other University or Institute for the award of any other degree or diploma.

Dr. Chander Prakash
Professor
Mechanical Engineering Department,
Lovely Professional University,
Phagwara, Punjab (India)

Dr. Sunpreet Singh
Research Fellow
Mechanical Engineering Department,
National University of Singapore,
Singapore.

ABSTRACT

This research work presents the development of low elastic high strength β-phase Ti-35Nb-7Ta-5Zr alloy for orthopedic application especially HIP-stem. The β -phase Ti-35Nb-7Ta-5Zr alloy was subjected to heat treatment to enhance the mechanical properties and wear resistance. After that, deposition of hydroxyapatite (*HA*) and titanium oxide (TiO_2) reinforced hydroxyapatite (*HA*) on Ti-35Nb-7Ta-5Zr alloy by plasma spray deposition technique has been carried out for required application. The effect of TiO_2 reinforcement (15 and 30 wt. %) in HA has been studied on coatings morphology, microstructure, mechanical properties, corrosion resistance, and i*n-vitro* bioactivity was investigated. Effect of plasma spray process parameters such as reinforcement of TiO_2 in HA, gas flow rate, and powder feed rate on the coating characteristics such as micro-hardness and adhesion strength has been studied. The microstructure, elemental composition, and phase composition were characterized by FE-SEM, EDS, and XRD. The biomechanical behavior of the deposited coatings was investigated in terms of surface hardness, elastic modulus, and adhesion strength. The surface characteristic such as roughness, porosity, micro-cracks, coating thickness has been studied. The *In-vitro* corrosion resistance of coatings was assessed using electrochemical potentiodynamic polarization test using Potentiostat/Galvanostat (Series PGSTAT-12, GAMERY) in simulated body fluid (SBF). The bioactivity of the coated surface was accessed by determining the hydrophilic/hydrophobic nature of surfaces, using a wettability test. The hydrophilic/hydrophobic performance of coatings depends upon the water contact angle (º). The *in-vitro* bioactivity has also been studied using osteoblastic Mg-63 cell lines. The wear resistance of HA and HA-TiO_2 coatings was evaluated by pin-on-disc wear test rig (DUCOM, Instruments Pvt. Ltd, Banglore, India).

A low elastic (55 GPa) β-phase type Ti-Nb-Ta-Zr alloy has been developed using vacuum arc melting process. The tensile strength and micro-hardness of the β-TNTZ sample after heat treatment have been increased from 590 to 1195MPa and 245 to 515HV, respectively. The elastic modulus of the β-$TNTZ_{th}$ alloy is 89 GPa, which is lower than the Ti-4Al-4V alloy (110 GPa) and Co-Cr alloy (220 GPa).

The optimized process parametric levels for obtaining maximum surface micro-hardness and adhesion strength are: powder ratio – 30% wt. of TiO_2, gas flow rate – 40 l/min, and powder feed rate – 32 g/min. At, optimized setting, the *HA/*TiO_2 coating exhibited cracks free and dense

surface in comparison with *HA*-coating. The reinforcement of TiO_2 improved the microstructure and mechanical bonding of coating with substrate. The thickness of HA, HA-15TiO_2, and HA-30TiO_2 coatings were measured approximately ~185-200 μm. The *HA-30TiO₂* (*HA-*T_y) coating exhibit high surface hardness (1.35 GPa) and adhesion strength (28.75MPa). The surface roughness of *HA*, HA-15TiO_2, and HA-30TiO_2 coatings were measured 7.65, 5.45, and 4.85 μm, respectively. The obtained surface roughness was in good agreement with the values reported in literature and also sufficient to promote bone-ingrowth around the implant. The reinforcement of TiO_2 in HA formed lamellar structure and rich layer of TiO_2 acted as a reservoir to hold the protein in the host body and improved the osseointegration and corrosion resistance. The *HA*-coated samples have better corrosion resistance as compared to uncoated samples. When TiO_2 was alloyed, the Tafel extrapolation curve again more shifted toward the left side that indicates samples hold low current density as compared to *HA* and uncoated samples. The I_{corr} and E_{corr} values of HA-15TiO_2 coating were measured as 8.15 μA/cm^2 and -370mV, respectively. Similarly, for HA-30TiO_2 coating, the values were 9.17 μA/cm^2 and -420 mV, respectively. The HA-30TiO_2 coating exhibit best and highest corrosion resistance. The HA-15%TiO_2 and HA-30%TiO_2 coatings possessed a higher cellular proliferation rate as compared to *HA*-coated and un-coated specimens. The findings thus indicate that the surface chemistry of the HA/TiO_2 coating helped to increase the bone ingrowth and osseointegration process.

At, gas flow rate 32 l/min and feed rate 40 g/min, the reinforcement of TiO_2 improved the microstructure of coating by prevented the formation of micro-cracks in the layer and improved the mechanical bonding of coating with the substrate. The HA/TiO_2 coating exhibited a dense surface in comparison with HA-coating. The coating thickness was measured for HA and HA-TiO_2 coated surface was 125 μm and 120 μm, respectively. Moreover, the reinforcement of TiO_2 formed lamellar structure in the HA-matrix and formed various non-apatite phases like α/β-TCP phases, Ca3(PO4)2, CaO, TTCP along with TiO_2, which enhanced the mechanical properties and bioactivity of the coating. The adhesion strength of HA-TiO_2 coating (32.95 MPa) was higher than the HA-coating (25.79 MPa). The hardness and elastic modulus of HA-TiO_2 coating were measured around 2.95 GPa and 41.5 MPa, which was beneficial to enhance the wear resistance properties. The HA-TiO_2 coating exhibited more crystalline content (89.6%) as compared to HA coatings (74.8%). The surface roughness for the as-coated HA and HA-TiO_2 coatings was found to be 4.65 μm and 3.5 μm, respectively. The skewness and kurtosis are the important parameters of surface roughness that affect the corrosion and wear

performance of biomedical implants. The skewness in the surface roughness of both surfaces was negative. The HA-coated surface has very deep valleys in the layer as a result roughness is a high Kurtosis of more than 9.5, this may affect the corrosion and wear performance. The hardness of as-sprayed HA and HA-30wt. % coatings were measured 1.65 GPa and 2.95 GPa, respectively. The elastic modulus of as-sprayed HA and HA-30wt. % coatings were measured 15.7 GPA, and 41.75 GPa, respectively. The adhesion strength of the coating is increased with the addition of TiO_2 in HA. The adhesion strength of HA and HA-TiO_2 coating was measured around 25.79 MPa and 32.95 MPa, respectively. The water contact angle after 3 minutes on un-coated, HA-coated, and HA-TiO_2 coated samples was measured 97.8º, 49.5 º, and 32.5º, respectively. It has been found that HA-TiO_2 has the lowest water contact angle, which revealed that the coating has the highest wettability and excellent bioactivity. The delamination of HA-TiO_2 coating can be seen, but very less as compared to HA-coating. The TiO_2 prevents the delamination of HA particles from the coating. Moreover, with the reinforcement of TiO_2, the brittleness of the coating is reduced, as a result, less friction developed. Moreover, TiO_2 is a ceramic element that helped in reducing the friction of the coating layer and as a result, less wear occurred. At optimized setting, a biomimetic layer of HA-TiO_2 was deposited on the β-TNTZ alloy, which can be further used as HIP-stem for the Indian population.

Acknowledgements

I express my deep sense of gratitude and indebtedness to my thesis supervisors, Dr. Chander Prakash, Dr. Sunpreet Singh for providing precious guidance, inspiring discussions and constant supervision throughout the course of this work. Their timely help, constructive criticism, and conscientious efforts made it possible to present the work contained in this thesis.

I would like to thank Dr. Loviraj Gupta, Dean LTFS, Lovely Professional University, Phagwara, for creating a healthy working environment at campus and for timely help I received from his. I thank Vijay Kumar Singh, School of Mechanical Engineering for facilitating various equipments for completion of this work. I am grateful to all staff members of the department for their useful suggestions and for the help rendered to me in carrying out this work.

I am grateful to Dr Sunpreet Singh research associate National University of Singapore for providing help during experimentation, testing, and analysis.

I would also express my gratitude to Prof. B.S. Pabla, Professor, National Institute of Technical Teachers Training & Research, Chandigarh for his cooperation during the micro-hardness testing and wear resistance experiments.

I am also thankful to my fellow research scholar for their support and cooperation during my experimentation. I offer my regards and blessings to all of those who supported me in any respect during the completion of my Ph. D work.

Deep sense of gratitude is expressed to authorities of Lovely Professional University, Phagwara, for permitting the author to pursue his research work and extending necessary facilities during the experimental and analysis work. I also express my sincere thanks to **Dr. Vijay Kumar Singh**, Head School of Mechanical Engineering lovely Professional University, Phagwara, for their cooperation and support.

I would like to thank my panel members who provided valuable suggestions during the course and all the staff members of School of Mechanical engineering who have been very patient and co- operative with us.

I would like to thank Lovely Professional University for giving me opportunity to use their resource and work in such a challenging environment. I am grateful to the individuals whom contributed their valuable time towards my thesis.

I humbly dedicate this work to my mother **Smt. Santosh** and my wife **Mrs.Amarjeet Kaur**, my daughter **Damanpreet Kaur**, and my sisters **Mrs. Saroj Bala, Mrs. Parveen and Mrs.Ashu** who are the source of inspiration and encouragement behind this research work. The author sincerely acknowledge the help extended by them during the tenure of this work by sacrificing their comforts and always supported me throughout all my studies at university and encouraged me with their best wishes.

About all author is highly indebted to Great and Gracious almighty God who blessed me with spiritual support and courage at each and every stage of this work.

HARJIT SINGH

TABLE OF CONTENTS

List of Figures

List of Tables

CHAPTER-I

INTRODUCTION

This chapter presents the current trends on the synthesis/ development of biomaterials and surface modification/processing/treatment of biomaterials for biomedical application. In the first phase, the significance of biomaterial is presented. The technique for the development of porous and solid biomedical implants is discussed in details for their successful applications. Powder metallurgical, additive manufacturing and 3-D printing technologies are found good potential techniques for the development of porous mechanically tuned of metallic and ceramic-based implants for medical applications. In the second phase, an innovative engineering technique for surface modification, processing, and treatment of implants is discussed to enhance the bioactivity, mechanical properties, and corrosion and wear resistance properties. Electric discharge machining, electrochemical deposition, and plasma spar deposition are the best and potential innovative engineering technique to improve the mechanical properties and bioactivity. The book chapter also presents the future scope for the development and surface modification of biomedical implants.

1.1. Introduction and requirement of Biomaterials

From recent studies, it is confirmed that the demand for joint and bone replacement increases rapidly. It is estimated that maximum human beings having the age of more than 45 years are fighting with the problem of weakening the bone, inflammation of the human's bone joints and weakening of the cartilages resulted in the bone degradation under continuous cyclic loading conditions [1-2]. This is the main cause of the degradation of the mechanical and physical behavior of natural human's bone and bone joint loss in friction. Total joint replacement (TJR) is the best way to solve these problems, where load-bearing joints are replaced with artificial implants [3-4]. Artificial implants comprise whole or part of a living structure which replaces a natural function to improve the quality of the human body and made-up of biomaterials. Fig. 1.1 presents the possible implants used in the human body such as lintraocular lenses,

bone plates, dentistry joint replacements to more complex material like pacemakers, blood vessels, artificial heart, histopathology, and prosthetic arterial grafts etc.

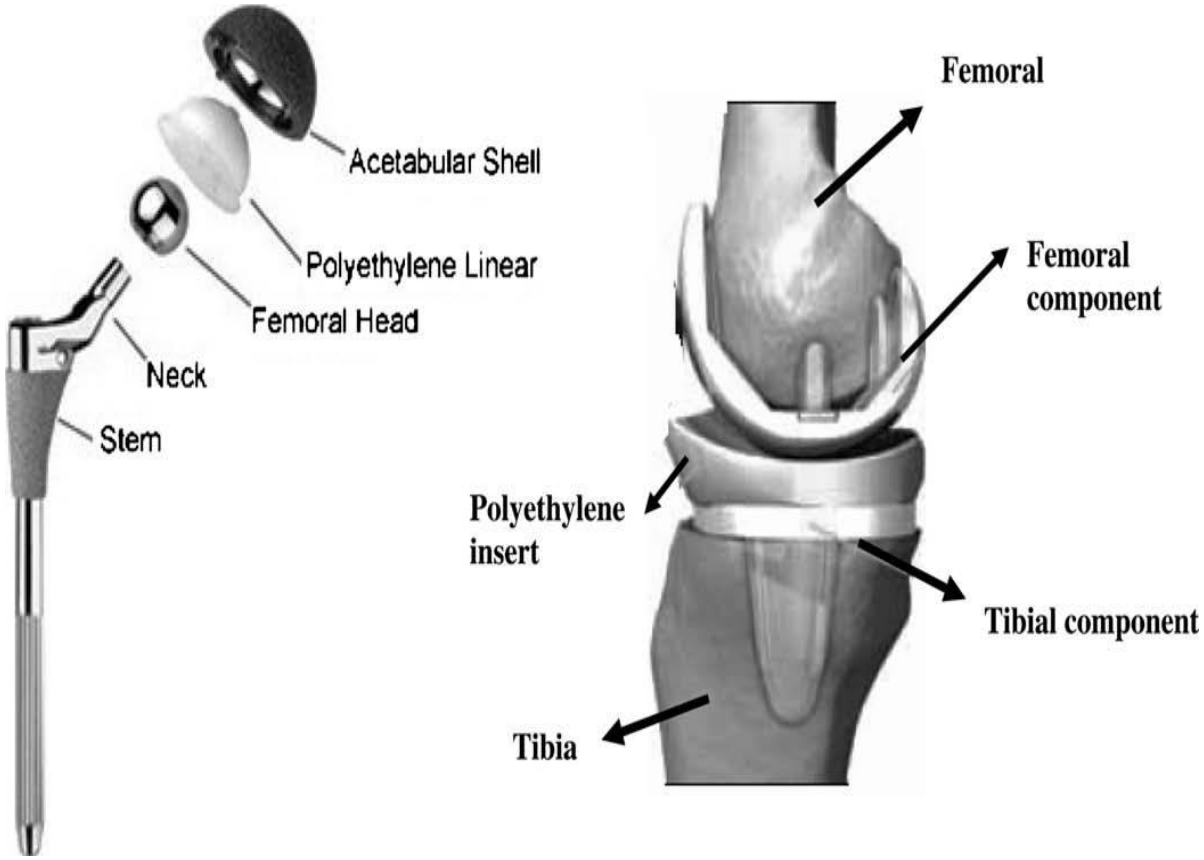

Figure 1.1. Artificial implants used in the human body to restore the functionality of dysfunctional joints or parts [2]

All biomaterials when implanted in a human body, their achievement mainly depend on three factors: (i) properties of biomaterials such as mechanical, chemical and morphology; (ii) biocompatibility/nontoxic of biomaterials; and acceptable by the body of patients and the capability of surgeon [5-6]. According to the responses of implanted biomaterials, the major dominant metallic biomaterials, such as cobalt-based (Co) alloys, stainless steel (SS), magnesium-based alloys, and titanium (Ti). These biomaterials are superior metallic materials due to their ability to carry significant stress and go through the plastic deformation prior unit to the fail, as this show their specific ultimate tensile strength (UTS) and fracture toughness. (Table 1.1)

Table 1.1. Characteristic of biomaterials and bone

Materials	Young's modulus (GPa)	Ultimate tensile strength (MPa)	Fracture toughness (MPa √m)
Co	240	900-1540	~100
SS	200	540-1000	~100
Ti	105-125	900	~80
Cortical bone	10-30	130-150	2-12

It is essential to cite that SS, Co alloys, and Ti alloys have a much larger value of stiffness than to cortical bone [1]. They ought to be decent mechanical properties as well as chemical also. Generally, host reaction occurs after the implantation of biomaterial such as blood-material interaction, acute inflammation, chronic inflammation, foreign body reaction etc. There are various types of reaction to a broad spectrum of implant biomaterials nearby implant site. Although these alloys are pleasant mechanical and chemical properties yet they have a lifespan of 10–15 years only.

In order to deal with such problems, researchers have taken so many initiatives to make implantation successful. These innovations are the development of new fabrication route for the synthesis of porous implants and surface engineering (Coating/deposition and finishing of implants) [7-8].

1.2. Fabrication technique to synthesize porous implants

In spite of the incredible advancement that has been accomplished in biomaterials, the fixation of the implant with the bone is still an issue because of the elastic modulus's mismatch [1]. The elastic modulus of the metallic implant is much greater than bones which lead to creating stress shielding and results is immolation failed [9]. One thought to accomplish this has been the advancement of materials that exhibit porous structure [10]. The structural porosity reduces the stiffness of Ti-alloy and therefore results in the low elastic modulus [11-12]. Moreover, the porous structure not only solves the

problem of stress shielding but also provides suitable conditions to promote tissue growth around the implant and improved the implant stability [13].

The use of porous coated and fully or partially porous orthopedic implants is increasing day by day due to better implant - bone in growth performance. Major parameters influencing the formation of new bone near the implant material is bone resorption, the viability of the surrounding bone and the stability of the porous implant-bone interface. Percentage of porosity, pore size, and the implant material has significant effects on the porous implant performance [14]. In order to achieve bone ingrowth (osseointegration) into porous implant surface and inner pores, the implant must have adequate porosity, which ranges between 35 to 70%. Cook et al. showed the bone in-growth of 35 to 40% with porous implants implanted to mongrel dogs [15]. Cameron et al. investigated the rate of bone growth in 65 % dense cobalt based implants [16]. Hofmann showed human cancellous bone ingrowth into 55% Ti6Al4V14 core and Ti coated implants [17]. Research has also been performed to determine optimum parameters for bone formation in porous implant surfaces. Experimental results based on the animal implantation using porous materials have shown that the pore sizes affected bone ingrowth. In an investigation performed by Bobyn et al., bone growth was observed into porous surface down to 50 μm pore size and porous cobalt based porous implant with pore size ranging between 50 μm and 400 reached the maximum fixation strength after 8 weeks of implantation [18]. Hulbert et al reported that the minimum pore size between 75 and 100 μm to regenerate a significant level of mineralized natural bone [19]. Barth et al. reported an optimum pore size of 400 μm for bone ingrowth in porous fiber titanium implant. Melikyan and Itin implanted sintered porous titanium specimens of 100-300 μm pore size in rabbits and reported successful growth of bone tissue into the implant [20]. The optimum pore size for the growth of osteblasts and vascularization was reported in the range of 300-400 μm by Tsuruga, et al. This result was obtained by implanting 106-212, 212-300, 300-400, 400-500 and 500-600 μm pore size hydoxyapatite implants in rats [21]. Similar results for optimum size of pores i.e. 200-500 μm in a porous surface coated Ti6Al4V specimens, implanted into the femoral modularly canal of dogs for six months were reported by Clemow et al [22]. Studies also showed that higher bone and implant interlocking strength occurred when porous tantalum implants with an average pore size of 430 μm are used [23]. The *in-vivo*

studies were performed in rabbit to evaluate bone ingrowth into titanium scaffolds with variable pore sizes i.e. 60 μm, 100 μm, 200 μm and 600 μm [24]. However, when the size of the pore is increased to 1.0 mm, the formation of fibrous tissue was more than the growth of bone [25]. There are a number of techniques which have been used to synthesize porous structure in bulk material. The potential techniques are powder metallurgical process using temporary space holder techniques and foaming agent, and additive manufacturing/3-D printing [26].

1.2.1 Powder metallurgy route using temporary space alloying and foaming agent

The powder metallurgy (PM) route has been most widely used for the development of porous scaffolds, because in this process pore characteristics are easy to control and capability to generate very close to the final shape of the product [27-28]. The fabrication of porous structure in PM route consist first alloying of removable temporary space holders with powder particles then pressure-less sintering [29]. The most commonly used removable temporary space holders (RTSH) are sugar pallet, sodium chloride (NaCl), carbamide, magnesium, tapioca, saccharose, dextrin, and woven wire mesh, which removed by evaporation or by dissolution followed by the sintering process [7,10,30]. Figure 1.2 presents the schematic representation of fabrication method to developed porous structure through RTSH technique.

High porosity (90%) NiTi alloys were synthesized by powder metallurgical route using NaCl as a RTSH. The finding presented that the shape and size of structural porosity depend upon the NaCl particles [31]. Zhang et al. used carbonate (NH_4HCO_3) as a temporary space holder to fabricate Ti-HA composite by using spark plasma sintering technique. The developed composite not only possessed near to human bone's elastic modulus (~ 8.2–15.8 GPa) but also high compressive strength (~ 86–388 MPa) [32]. Exhaustive research efforts have been made for the fabrication of Ti-based porous scaffold. But, the drawback of Ti-based porous scaffold is non-degradable nature, which was removed from the body after another surgical process [33-34]. In concern of the metallic biomaterials issues, magnesium (Mg) based alloys/composites have gained attentions as an alternative material for the developing scaffolds, because of their superior biodegradability, biocompatibility, and low elastic modulus [35].

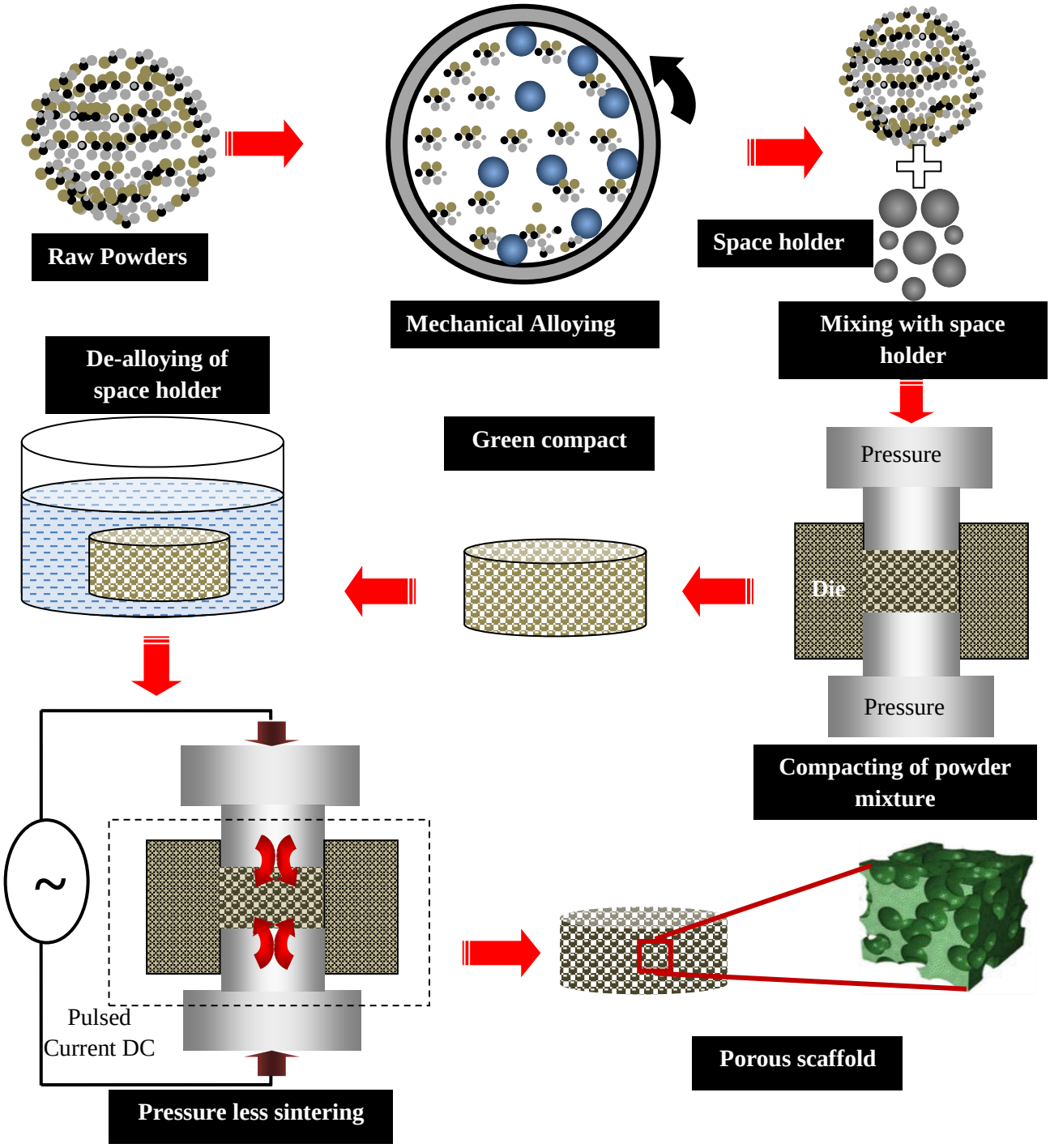

Figure 1.2. Fabrication route of the porous scaffold by powder metallurgy process

Yazdimamaghani et al. critically reviewed and presented the studies carried out in the development of porous magnesium-based scaffolds for tissue engineering (TE) applications using temporary space holder technique and other methodologies [36]. It

has been reported that temporary space holder technique was a potential methodology for the development of 3D open porous structure [10]. The major techniques to control the pore shape and size of Mg-scaffolds were 3D printed negative salt pattern, woven mesh wire, and removable space holders. Kirkland et al. (2011) used 3D printed negative salt pattern to fabricate porous Mg-based scaffold with controlled architecture. The findings indicate that the technique can successfully produce an ordered open cell porous Mg scaffold [37]. Further, a highly porous (72-76 %) biodegradable AZ91D alloy was developed using negative NaCl salt pattern technique with a controlled pore size of 10-1000 μm. The in-vivo results indicate that the Mg-scaffold was degraded after three months of implantation and has consistent biocompatibility with a required inflammatory host reaction [38].

Moreover, the major drawback of Mg is high degradation rate in the human body, which results in various inflammatory diseases after post-implantation [39-40]. In this context, Hedayati et al. (2008) fabricated AZ-61 bio-degradable porous alloys using NaCl as temporary space alloying technique and, studied the degradation behavior and fatigue resistance. The element Zinc controls the degradation rate of Mg and improved the corrosion properties [41]. Furthermore, porous Mg-Zn scaffold was developed using carbamide ($CO(NH_2)_2$) of the size of 200–400 μm as temporary space holder technique. The effect of structural porosity on the mechanical properties was studied and found that mechanical properties degraded with the increase in structural porosity. Bakhsheshi-Rad et. al. (2018) fabricated doxycycline loaded porous hybrid Mg-Ca-TiO_2 scaffold using spherical carbamide as a temporary space holder. The elements Ca and TiO_2 were used to enhance the corrosion properties and bioactivity. The developed scaffold possesses a interconnected porosity in the range of 65-67 % of size 600–800 μm with upright compressive strength (5±0.1 MPa). The antibacterial property was improved by the doxycycline and used as alternative applicants for infection avoidance for bone TE applications [42]. Ghomi et al. (2018) fabricated bioactive porous bredigite ($Ca_7MgSi_4O_{16}$) scaffold via space holder method using NaCl as temporary space holders. Highly interconnected porous scaffold with a porosity of 86% was developed with pore size 400-600 μm. The developed scaffold has compressive strength 1.1 MPa

and proposed as a potential candidate for the bone repair and regeneration in bone TE application [43].

Singh and Batanagr (2017) critically reviewed and presented the studies carried out on the development of porous titanium and magnesium-based scaffolds for TE applications using various fabrication techniques [44]. The powder metallurgy (PM) technique has been best quoted due to being an economical method and more convenient to control the pore size, pore density, and morphology of the scaffolds. Further, they fabricated 3D open Ti-woven wire mesh based cellular structure of Mg10Zn alloy by using as a space holding. The developed scaffold has 60% porosity and ultimate tensile strength is found to be around 76 MPa [45]. The developed scaffold is proposed as a bone scaffolding material for TE. Dutta et al. (2017) developed porous bio-degradable Mg-based scaffolds spherical naphthalene particle as temporary space holder (porogen). The developed scaffolds have a porosity ranging from 8-40% with pore size 30-60μm. The compressive strength of the developed scaffold decreased with increase in the porogen content from 184 MPa to 24 MPa [46].

1.2.2 Additive manufacturing and 3-D Printing

These days, additive manufacturing technique in the form of 3-Dimension printing has been widely used to develop 3-D porous biomedical implants with controlled pore characteristics such as size, shape, and distribution [47]. In 3-D printing technique, metal-implant parts were fabricated by a layer-by-layer printing process in which parts are designed using CAD. In metal 3-D printing process metallic parts are fabricated by layer-by-layer printing of metallic-powders and together fusion/sintering of powder carried out by laser technique. Here, two types of most widely laser sintering technique were used such as Selective Laser Melting (SLM) and Direct Metal Laser Sintering (DMLS) [48]. Figure 1.3 presents the SLM/DMLS proves.

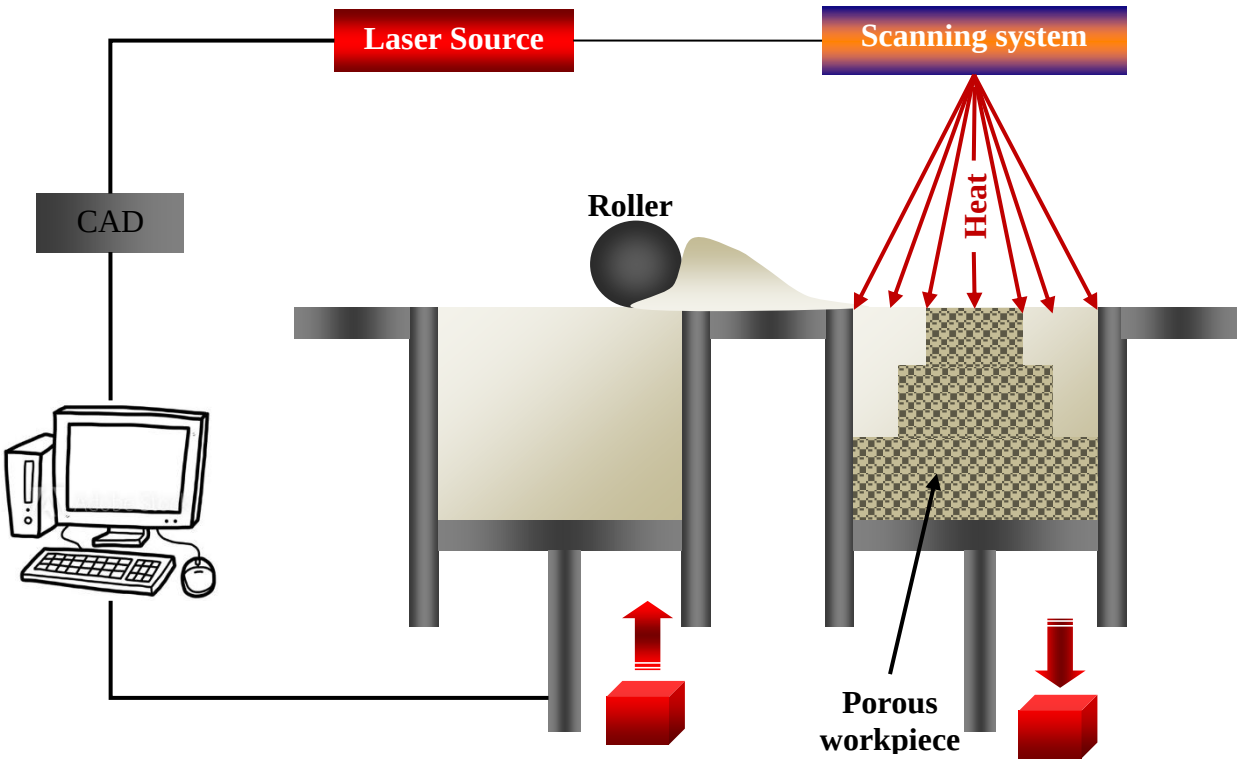

Figure 1.3. Schematic representation of the SLM/DMLS process

In the early ages, the SLM technology was used to developed fully-dense components [49]. The utilization of SLM to develop porous component was reported by Wang et al. [50]. Highly porous patient-specific Ti-based implant was developed with 70% porous structure exhibiting pore size from 200-500 μm. Pattanayak et al. investigated the effect of SLM process parameters on the pore characteristics and optimized the process parameters to synthesize porous Ti-implant [51].

Further, the attainability of manufacturing grid structures in Ti-6Al-4V with high geometrical exactness utilizing SLM was explored by Weißmann et al. [52]. Moreover, it has been reported that SLM has potential to fabricate customize complicated structure. Recently, Shipley et al. critically reviewed the application of SLM to develop Ti-6Al-4V based porous implant [53]. They presented and addressed the various challenges during optimization of SLM process parameters and their influence on the porous structure. Khorasani et al. studied the effect of SLM process parameters (laser power, scan speed, hatch space, laser pattern angle coupling, along with heat treatment as a post-process) on the mechanical properties (density, hardness, tensile strength) and pore characteristics (Surface quality) has been studied [54].

Zao et. al. fabricated the Ti-6Al-4V alloy by electron beam melting (EBM) and SLM technique and compared their in-vitro corrosion and bioactivity performance. The SLM-synthesized implant possessed excellent bioactivity and EBM-synthesized exhibits good corrosion resistance [55]. Ran et. al. studied the osteogenesis of 3-D printed Ti-6Al-4V implant at different pore size by SLM process and it has been found that implant with 600 μm pore size promotes excellent bone-ingrowths [56].

Figure 1.4 presents the 3-D printed Ti-6Al-4V implant and Fig.1.5 presents the bioactivity analysis of synthesized implants. From Fig. 1.4(a), it can be seen that different shape and size samples were developed using different architecture using 3D printing technique. Figure 1.4(b) shows the EDS spectrum of as-developed Ti-alloy based samples. Highly pure materials were printed without any impurity or foreign material inclusion. Figure 1.4 (c) to (e) shows the different porosity size in different implants. The structural porosities varied in the range of 400 to 800 μm in size. These structural porosities helped the bone ingrowth process. The tissue grow and entrapped in these porous structure and made the implantation successful. The bioactivity has been accessed using cell culture technique. Figure 1.5 represents fluorescence images of osteoblasts adhered to porous Ti6Al4V implants after culture for 14 days. Cells were stained with actin filament (red), cell nuclei (blue). Three regions of each sample were randomly captured and all experiments were performed in triplicate.

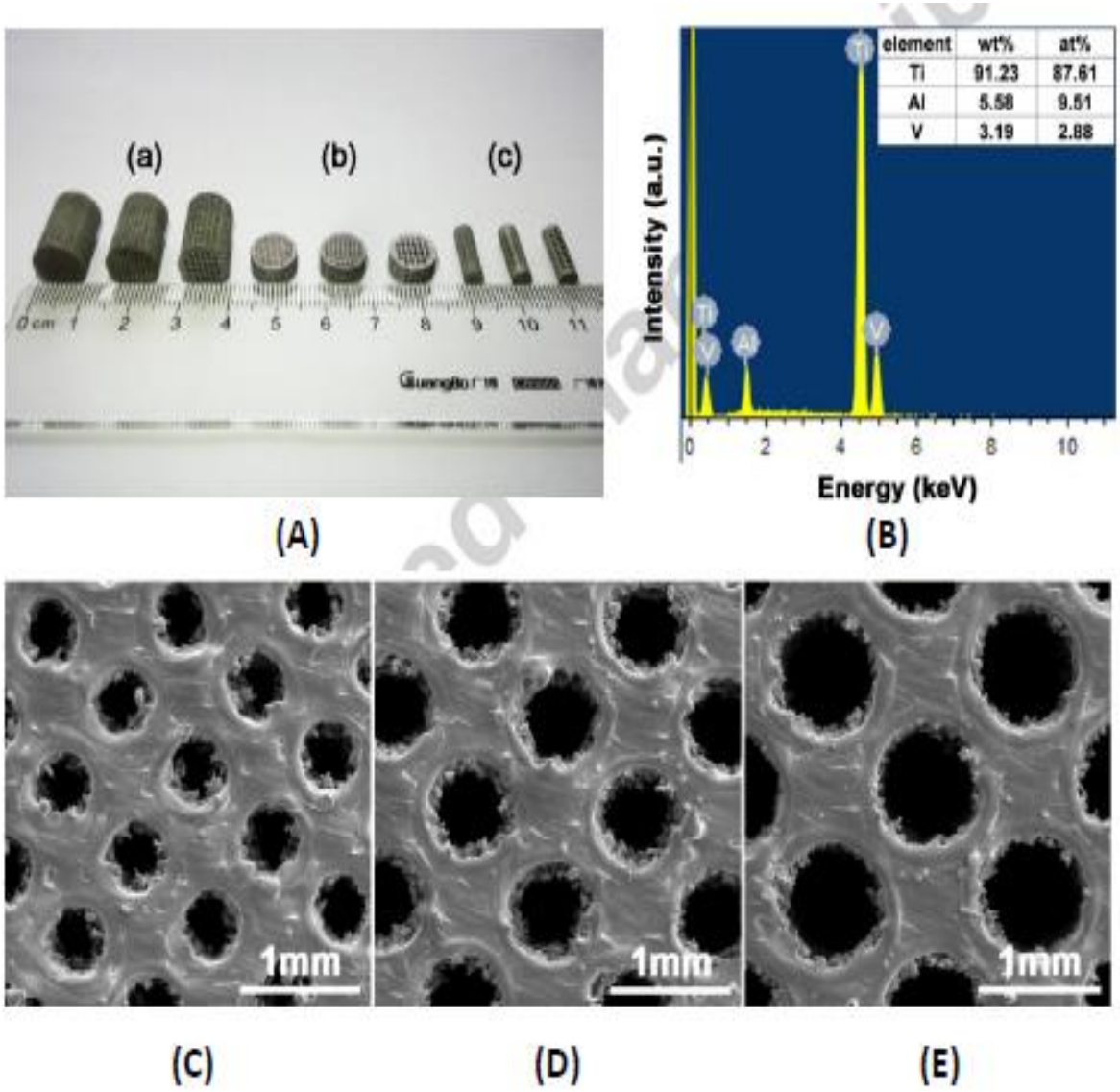

Figure 1.4. (A) Macrographs of 3D-printed porous Ti6Al4V specimens for mechanical test (a), *in vitro* (b) and *in vivo* (c) studies; (B) Chemical compositions of the fabricated samples detected by EDS; and SEM images of (C) 401µm, (D) 607 µm, and (E) 801 µm.

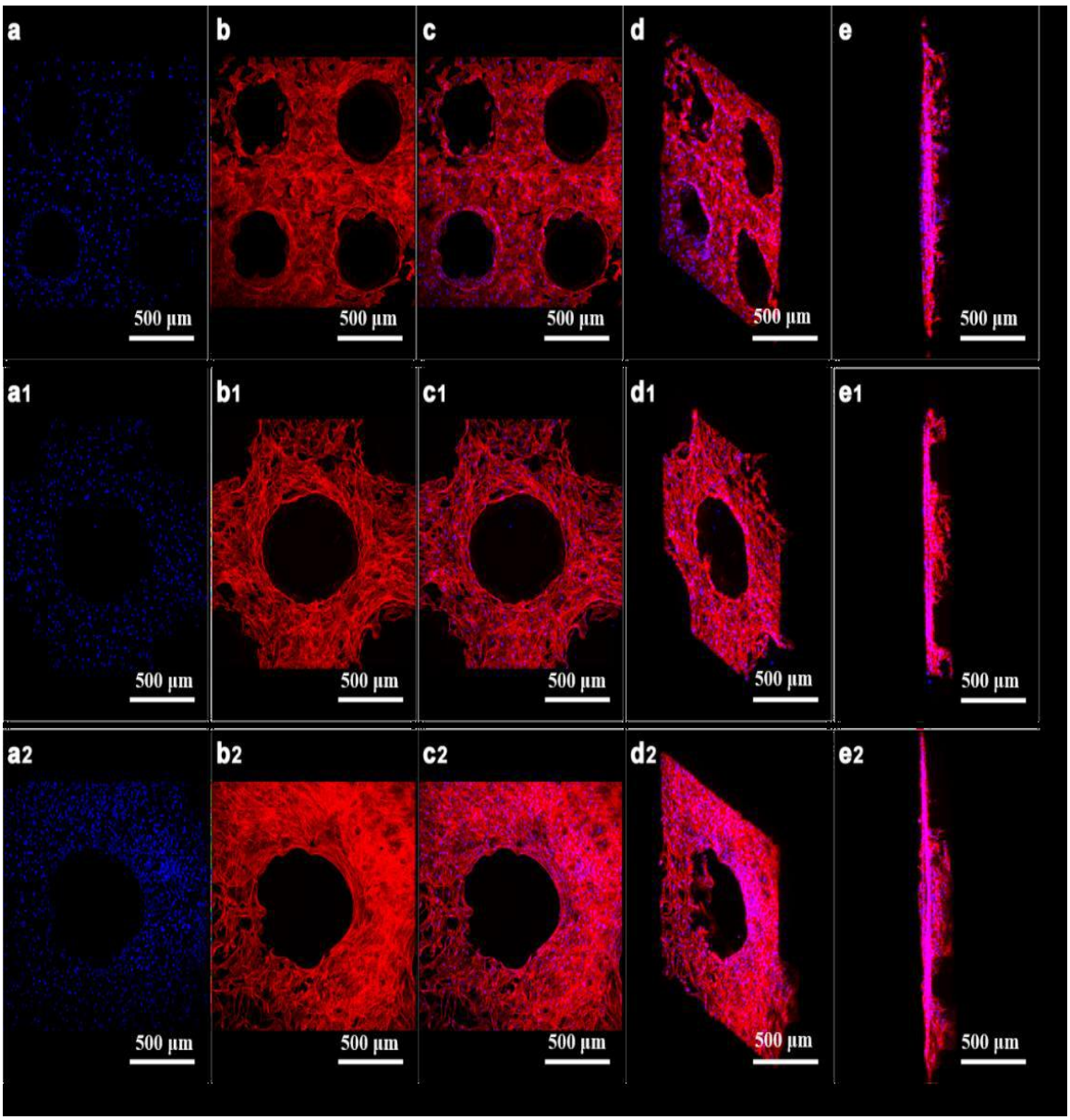

Figure 1.5. Representative fluorescence images of osteoblasts adhered to porous Ti6Al4V implants after culture for 14 days.

Yan et. al. fabricated Gyroid triply periodic minimal surface (TPMS) lattices based Ti-6Al-4V alloy using SLM. Figure 1.6 presented the CAD model of pore morphology. The effect of heat treatment on mechanical properties and effect of HA coating of bioactivity of implant was studied. The compressive strength of Ti-6Al-4V implant is decrease with heat treatment. On the other hand, the HA coating enhances the bioactivity of implant. Figure 7 presented the porous Ti-implant coated with HA layer in simulated body fluid [57].

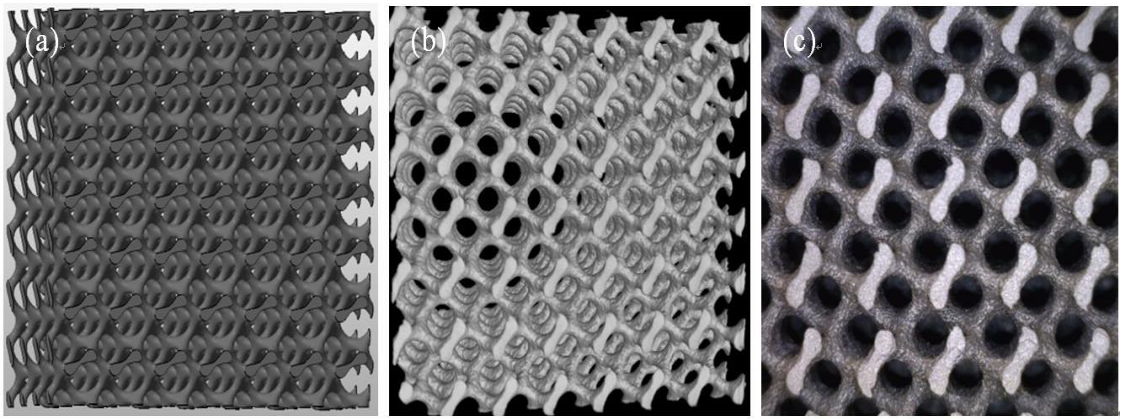

Figure 1.6. (a) CAD model, (b) micro-CT reconstruction model and (c) optical

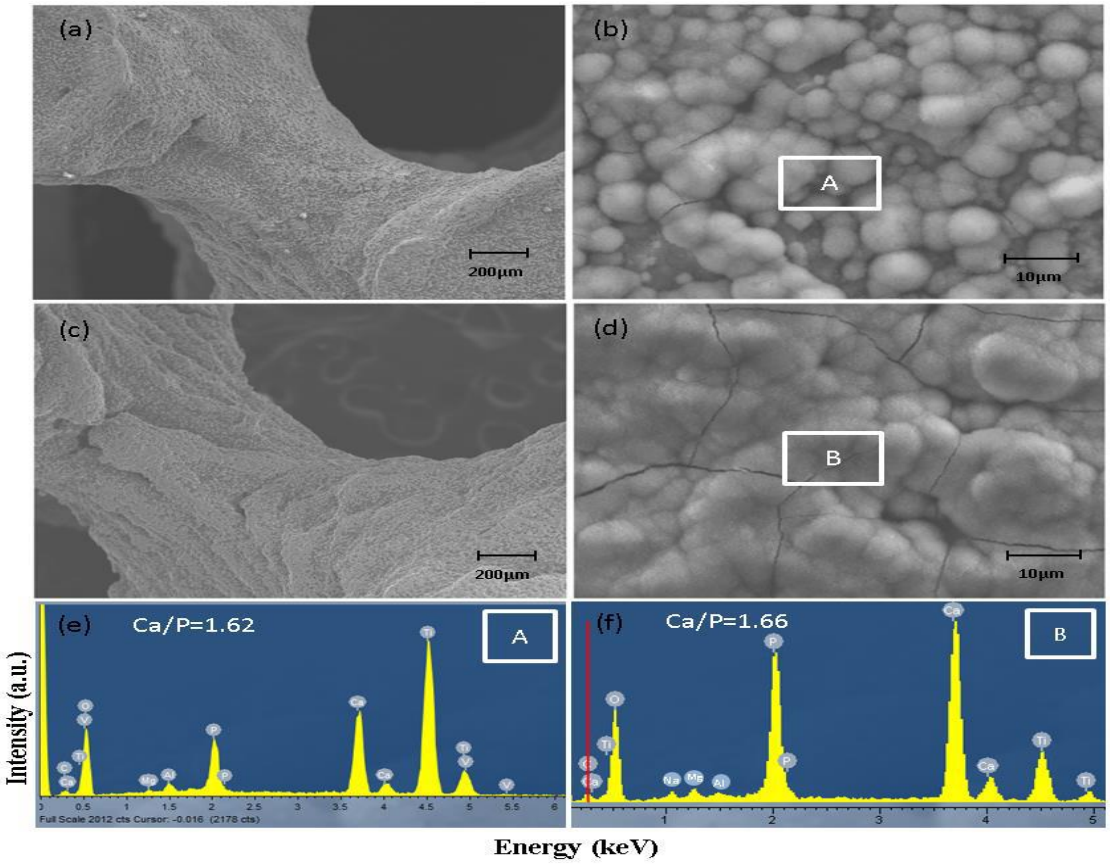

Figure 1.7. Surface morphologies of the Ti-6Al-4V TPMS lattices after soaked in SBF for: (a) and (b) 2 weeks, and (c) and (d) 3 weeks. EDX analysis on the Ti-6Al-4V TPMS lattices

soaked in SBF for (e) 7 days and (f) 14 days, corresponding to area A and B in (b) and (d), respectively

1.2.3 Electrospinning

From the last decade, the electrospinning process gained great attention because of being a highly versatile method for spinning a wide range of polymeric fibers of nano-size [58-59]. Electrospun nanofibers have been widely used biomedical scaffolds for TE application. In the electrospinning process, an electrostatic force was used to the spine polymer solution or melts to produce fine-fibers from nanometer to micrometer to enhance surface area which is beneficial for cell interaction and growth [60-61]. Figure 1.8 presents the standard vertical and horizontal electrospinning processes. A high voltage power supply, a spinner, and a collecting plate are the three main components of electrospinning process. A polymeric solution is transferred to a syringe and pumped through capillaries or tubes to the spinneret, which forms a suspended droplet at the tip. A DC voltage source of several tens of KVs is used to generate an electric field between syringe tip and a collector [62-63]. Due to an electric field, electrostatic charge controls surface tension and a charged jet is produced and accumulates on the collector plate. The polymer fiber produced is called electrospun or nanofibers. A large number of natural and synthetic polymers including polylactic acid, polyurethanes, silk fibroin, collagen, hyaluronic, polycaprolactone, acid, cellulose, and chitosan collagen were used for the development of scaffolds for TE application [65]. Ruckh et al. reported that polycaprolactone (PCL) was the potential and ultimate polymer for the scaffold TE application owing to its superior biocompatibility and processability [66]. The developed nanofibrous scaffold improved the osseointegration activities and excellent cell adhesion and growth was observed.

Doustgani et al. fabricated a fibrous nanocomposite-scaffold of PCL along with PVA (average diameter ~ 123 ± 32 nm) and HA (average diameter ~ 123 ± 32 nm) nanoparticles for aligned and random nanofibers, respectively. The bioactivity of the fibrous nanocomposite was estimated by *in-vitro* cell culture test using mesenchymal stem cells (MSCs) cell lines and it was reported that the developed nanocomposite supported cell adhesion, growth, proliferation, and differentiation [67]. A critical downside of electrospinning process is the low-efficiency level (low production) due to a single needle. An innovative advancement has been accomplished to enhance the productivity of current electrospinning process by multiplication of the jets using multi-

nozzle construction [68]. The production was increased but causes several problems such as low reliability, quality, and high maintenance cost.

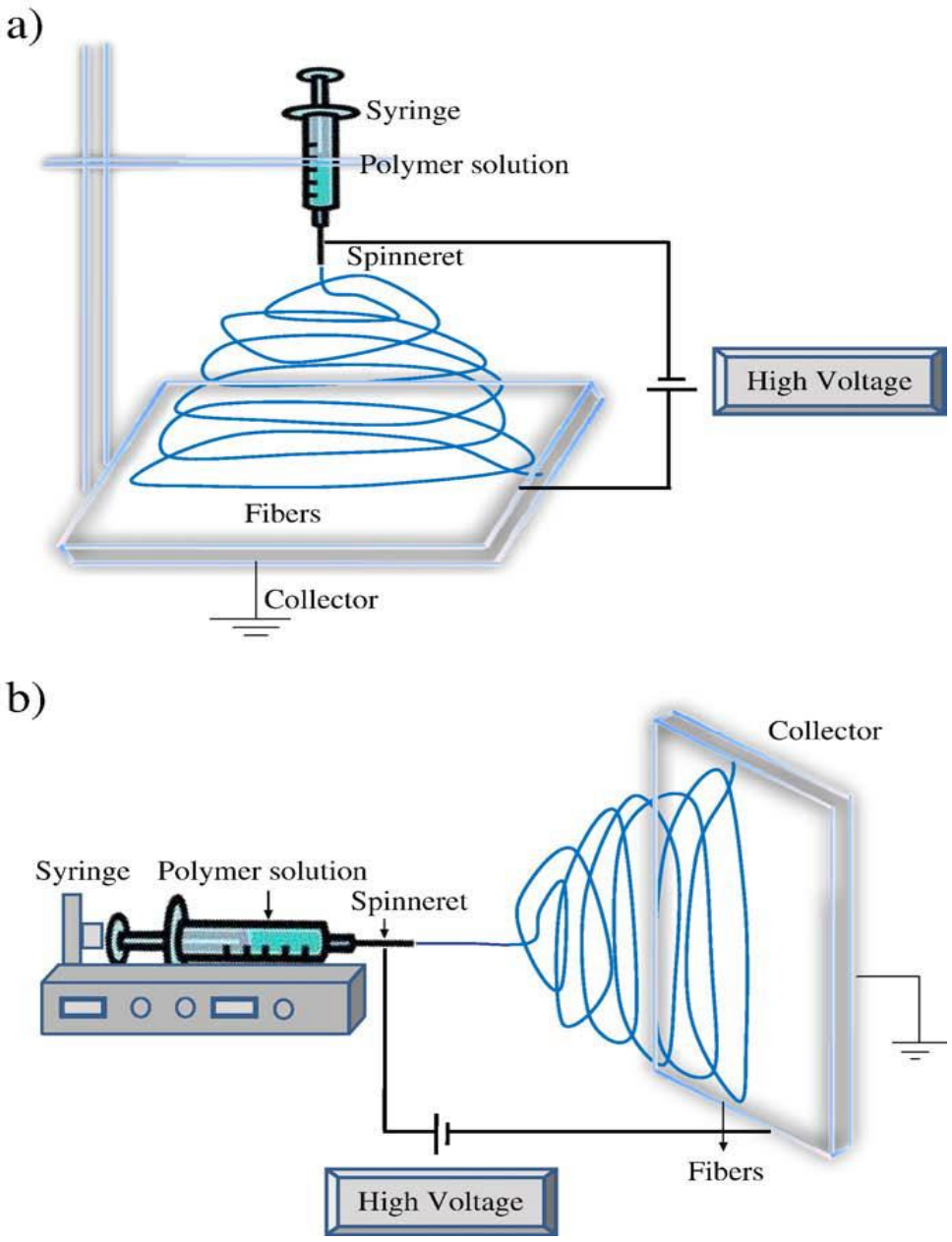

Figure 1.8. Schematic diagram of setting up of electrospinning apparatus (a) typical vertical set up and (b) horizontal set up of electrospinning apparatus.

Petrík et. al. developed an innovative nozzle-free electrospinning technology, which overcome the associated problem with conventional electrospinning and multi-nozzle electrospinning process [69]. In this process, a polymer wrapped over a rotating drum and nanofiber mats were formed when subjected to the high-voltage electric field.

Esmaeilzadeh et. al. synthesized cellulose-based nanofibers for TE applications using the nozzle free electrospinning process [70]. Despite several advantages of these solution electrospinning processes, still facing few challenges in cell infiltration due to its too small pore characteristics and tightly-packed nonwoven networks. Recently developed melt electrospinning was an innovative technique, which fabricates highly porous (with porosities of 98%) scaffold by direct writing technique [71]. In this procedure, the ideal polymer is dissolved and afterward pushed to a spinneret, at which high voltage is connected between spinneret and collector, bringing about the electrostatic shock and stacking filaments over one another [72]. Because of the viscosity of the liquid polymer, this procedure can create micro and sub-micron scale fibers. Moreover, dissolve electrospinning presents exact authority over the spatial plan of these strands in three measurements contrasted with arrangement electrospinning, which suffers from fly hazards as a result of dissolvable vanishing [73]. Additionally, it needn't bother with the utilization of dangerous solvents and is able to do creating structures with adjustable pore sizes, which are appropriate for cell entrance. Melt electrospinning has been used to process a variety of biodegradable polymers such as PCL [74-75], PLA [76], PLGA [77].

1.3. Innovative Surface Engineering/ Surface modification techniques

Surface engineering is processing/alteration of the surface characteristics of the object obtained through removing or adding the material. The surface engineering processes are majorly classified into two categories surface modification (treatment, cladding, and machining) and surface finishing (polishing and grinding). To enhance the service life of biomaterials these surface modification and surface finishing technique are used on the surface of biomaterial to increase the productivity in the harsh environment of the human body. By this life expectancy has been increasing because of the improvements in the biomaterial surface by the surface alteration. Table 1.2 presents the various surface modification techniques and everyone have their own advantages and drawbacks.

Table 1.2. Surface Modification techniques for metallic alloy as a biomedical implant [4]

Surface Modification Methods	Modified Layer	Objective
Mechanical Methods ▪ Machining ▪ Grinding ▪ Polishing ▪ Blasting	The rough or smooth surface formed by the subtraction process	Produce specific surface topographies; clean and roughen surface; improve adhesion in bonding
Chemical Methods • Acidic treatment • Alkaline treatment	<10 nm of the surface oxide layer ~1 μm of sodium titanate gel ~5 nm of dense inner oxide and porous outer layer	Remove oxide scales and contamination Improve biocompatibility, bioactivity or bone conductivity
Sol-gel	~10 μm of the thin films, such as CaP, TiO_2, and silica	Improve biocompatibility, bioactivity or bone conductivity
Anodic oxidation	~10 nm to 40 μm of TiO_2 layer, adsorption, and incorporation of electrolyte anions	Produce specific surface topographies; improve corrosion resistance and biocompatibility
Chemical Vapour Deposition	~1 μm of TiN, TiC, TiCN, diamond, and diamond-like carbon thin film	Improve wear resistance, corrosion resistance, and blood compatibility
Glow Discharge Plasma	~1 nm to ~100 nm of surface modified layer	Clean, sterilize, nitride surface; remove the native oxide layer
Biochemical Methods	Modification through silanized titania, self-assembled monolayers, photochemistry, protein resistance, etc	Induce specific cell and tissue response by means of surface immobilized peptides, proteins, or growth factors
Physical Methods ▪ Thermal Spray ▪ Flame spray	~30 to 200 μm of coatings, such as titanium, HA, calcium silicate, Al_2O_3, ZrO_2, TiO_2	Improve wear resistance, corrosion resistance, and biological properties

▪ HVOF ▪ DGON		
PVD ▪ Evaporation ▪ Ion plating ▪ Sputtering	~1 µm of TiN, TiC, TiCN, diamond, and diamond-like carbon thin film	Improve wear resistance, corrosion resistance, and blood compatibility
Ion Implantation and Deposition Beam-line ion Implantation and P-III	~10 nm of the surface modified layer and/or ~µm of thin film	Modify surface composition; improve wear, corrosion resistance, and biocompatibility

Among all the coating methods, thermal spray coating is potential good techniques to deposit a hard, corrosion and wear resistance layer on implant surface [4].

1.3.1 Electro-deposition Technique

Electro-deposition is an electrochemical process to deposit a protective micro-, sub-micron, and nano-scale layer on a substrate of conducting materials [78]. The electro-deposition process is based on Faraday's law of electrolysis that expresses the delivery amount of the chemical charge by an electrical current is corresponding to the amount of electricity that passes [79]. Figure 1.9 presents the schematic illustration of Electro-deposition setup which consists electrochemical cell for electrolyte handling, a working electrode, a counter electrode, a reference electrode, and an external electrical circuit. The working electrode is connected to cathode terminal where electro-deposition takes place and counter-electrode is connected to the anode to complete the electrical circuit. Various metal salts are dissolved to make an aqueous solution of electrolytes containing positive and negative ions. The electric-current streaming between the electrodes in the presence of an external-voltage as a consequence of the moving charged species, by means of migration and diffusion, towards the surfaces of the polarized anodes. At the surface of the anodes, the conduction system must change from ionic to electronic, an interface procedure intervened by the event of electrochemical responses that advance the decrease or the oxidation (redox responses) of the ionic species. In addition to the above components, thermometer is used to measure temperature during the process and

a magnetic/ultrasonic stirrer is used to shake the electrolyte in order to bring new supply of metallic salts/ions to the cathode, therefore, facilitates replacement of metal ions at the cathode allowing the use of advanced current density and better current scattering. It sweeps away the foams which may cause pitting at deposit surface [80].

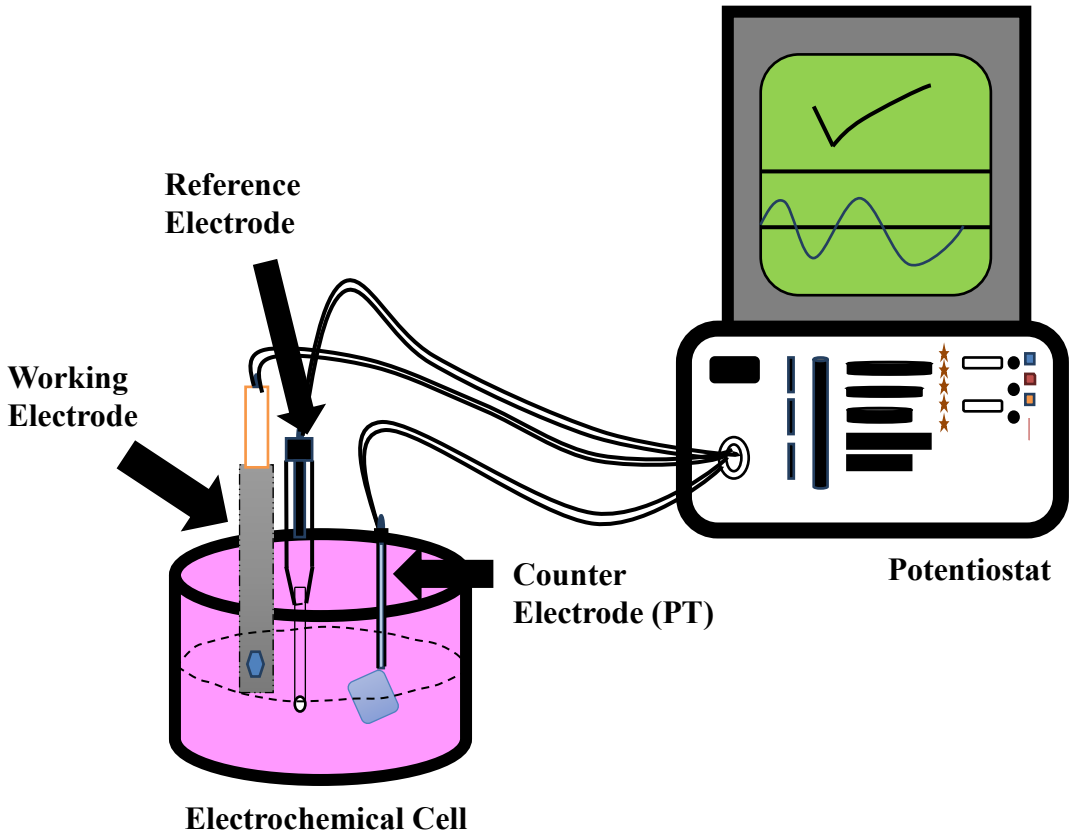

Figure 1.9. Three electrode cell with Potentiostat/Galvanostat

There are two types of electrodeposition system, Galvanostatic, and Potentiostatic. The current between the electrodes in the Galvanostatic plating system is kept constant. In pontentiostatic plating system, the potential of the working electrode is kept constant. Reactions that occur at cathode and anode are called half-cell reactions.

Cathode Reaction: $M^{n+} + ne^- \rightarrow M^0$

Anode Reaction: $M(s) \rightarrow Mz^{+}(aq) + ze^{-}$

The various parameters affecting the process are current density, electrolyte concentration, potential, temperature of the electrolyte, pH of electrolyte, duty cycle and RPM of the stirrer. Increase in current density increases precursor thickness, its porosity, the grains become fine. Low current density produces gross grain structures due to little scope for creation of new nuclei. High concentrations of electrolytes are used to increase the conductivity of solution and cathode efficiency. Firm and adherent deposits can be obtained with higher electrolyte concentration and intermediate current density.

A number of research studies have been reported by various researchers about the electrodeposition of biomimetic layer to enhance the wear and corrosion resistance of implant. Qiu *et al.* [81] electrodeposited HAP-TiO_2 composite coatings on the surface of Ni-Ti alloy by the process. Addition of TiO_2 to the electrolyte results in needle-flower-like crystals of HAP. The adhesive strength of HAP-TiO_2 coating and HAP coating were measured to be 23.7MPa and 13.4MPa respectively. Thicknesses of coatings were 7µm in both cases. Qiu *et al.* [82] also produced HAP-ZrO_2 composite coatings on Ni-Ti alloy by the same process. The needle-flower-like crystals of HAP were obtained due to the addition of ZrO_2 to the electrolyte solution. The HAP-ZrO_2 coated surface exhibited higher corrosion resistance and potential as compared to uncoated surface. The thickness of the HAP and HAP-ZrO_2 coatings were about 7µm and 8µm, respectively. The adhesive strength of HAP-ZrO_2 coating and HAP coating were measured to be 24.2 MPa and 13.4 MPa respectively. Peng *et al.* [83] deposited optical semitransparent and adherent thin CaP coatings on CP-Ti alloy surface in modified SBF using periodic pulsed potentials. The average thickness of coatings was measured around 200 nm with surface nanoporoisities with a pore size in the range of a few nanometers to 1µm. The deposited CaP coatings layer possessed Ca/P ratio of 1.65. The root-mean-square (RMS) roughness values on Ti-CaP surfaces and untreated Ti substrates were about 300 nm and 110 nm respectively. Adhesion strength, wear resistance and corrosion resistance of coatings enhanced due to pulsed voltage supply. Kar *et al.* [84] fabricated the surfaces of CP-Ti with HAP in order to make these materials bioactive and to enhance osseointegration with pulsed electrodeposition

process. The effect of alkali treatment (annealing) at different temperature without treatment, 450 °C and 600 °C on the bond strength of coating and it has been observed that the adhesion strength of the coating was 16-21MPa, 32-37MPa and 38-44MPa respectively. Saremi and Golshan [85] produced nano-HAP coatings by cathodic electrodeposition on Ti-6Al-4V substrate. The effects of the variation of the electrochemical process variable which include voltage, current density and pulse conditions were analysed to determine the change in the microstructure of the deposit. Nano-size particles of three phases of calcium phosphates were obtained at t_{on} and t_{off} 60s and 90s respectively. The amorphous phase with spherical particles with Ca/P ratio of 1.38 and a diameter of 100 nm was obtained. Santos *et al.* [86] used cathodic electrodeposition to deposit Ti-6Al-4V surface with HAP nano/micro single crystals. Large HAP single crystals oriented along the c-axis appeared to grow up in an amorphous HAP base material. Park *et al.* [87] used pulse electrodeposition method to produce calcium phosphate/chitosan coatings with variation of the deposition cycle and contents of chitosan solution. The electrodeposition was performed by pulsing the voltage during 5 to 20 cycles. The composite coatings have shown a high corrosion resistance than bare Ti-6Al-4V substrate. Gopi *et al.* [88] electrodeposited CNTs reinforced HAP coatings on CP-Ti substrate at a potential of -1.4 V. Adhesion strength, hardness and elastic modulus values were measured to be 15.8-22MPa, 6.1-7.5 GPa, and 115-130 MPa respectively. Yan *et al.* [89] fabricated a wear resistive antibacterial coating on pure titanium through deposition of hydroxyapatite and nano-Ag effectuated by hybridization of chitosan (CS) with Ag+ and Ca^{2+} . Pulsed electrodeposition mode was used. Uniformly dispersed spherical nanoparticles of composite coating were obtained at optimized deposition potential and Ag-apatite concentration with excellent bio inductive activity.

Lee [90] studied the effect of electroplated HAP-TiO_2 composite coatings on the wear and corrosion resistance in Hanks' solution on Ti-6Al-4V alloy. The anodizing treatment was conducted at 10 V at different durations of time (i.e. 40, 50, 60, 120 and 180 min). After the anodizing process, HAP-TiO_2 composite coatings were fabricated at constant current densities of 10mA/cm^2 in the electrolyte at 80 ^{0}C for 60 min. The electrolyte was magnetically agitated at a speed of 200 rpm to produce HAP-TiO_2

coating. Microhardness of the coatings was ranging from 380.62 to 890.92 Hv and the maximum hardness of 890.92Hv was obtained with 180-minute anodized sample. R_a and RMS values varied from 500-650 nm and 750-900 nm respectively and higher values correspond to the higher duration of anodizing. An increase in corrosion resistance and a decrease in coefficient of friction of the coatings with increasing anodizing duration of alloy substrate were observed. Huang *et al.* [91] presented the antibacterial efficacy and cytocompatibility of electroplated Cu and Zn co-substituted HAP (Zn-Cu-HAP) coating on CP-Ti. Cu^{2+} was substituted into hydroxyapatite structure to improve the antibacterial property. Cu ions released from Zn-Cu-HAP and produced strong antibacterial effect due to the high antimicrobial ratio (K> 95%). Zn^{2+} acts as secondary material into Cu-HAP to reduce Cu concentration. A dense coating of thickness approximately 10μm was obtained. The adhesion strength of Zn-Cu-HAP and HAP coating was approximately 12MPa and 10MPa respectively. Zn-Cu-HAP coating exhibit superior corrosion protection for Ti substrates. Saremi and Golshan [92] used pulsed cathodic electrodeposition to produce a film of osteoconductive and biocompatible HAP on Ti-6Al-4V biomedical implants. The process was done at different potentials of 3, 4.5 & 6 volts and different duty cycles of 0.4, 0.5 and 0.05. Nucleation process enhanced at higher potentials resulting in an increase in a number of fine grain particles. Smaller particles were produced at higher duty cycles. Grain growth has effected when the number of cycles increased, owing to the fact that more base material was generated at optimum values of pH and concentration of the electrolyte. The low temperature of electrolyte reduced the grain growth and diffusion process was stopped. Fine particles were obtained on the polished surface due to the conversion of the nucleation process from heterogeneous to homogeneous mode. When current density increased from 1mA/cm^2 to 4mA/cm^2, thicker coatings were obtained.

1.3.2 Electric Discharge Machining

Electrical discharge machining (EDM) process is the only non-conventional machining process, which can machine effectively hard to cut materials [4]. EDM is generally a thermal and electric machining process that produces a large number of electrical sparks

in a fraction of seconds. These intense sparks produce a large amount of heat to remove material from the workpiece surface [93]. Figure 1.10 shows the experimental and material removal mechanics during EDM machining process.

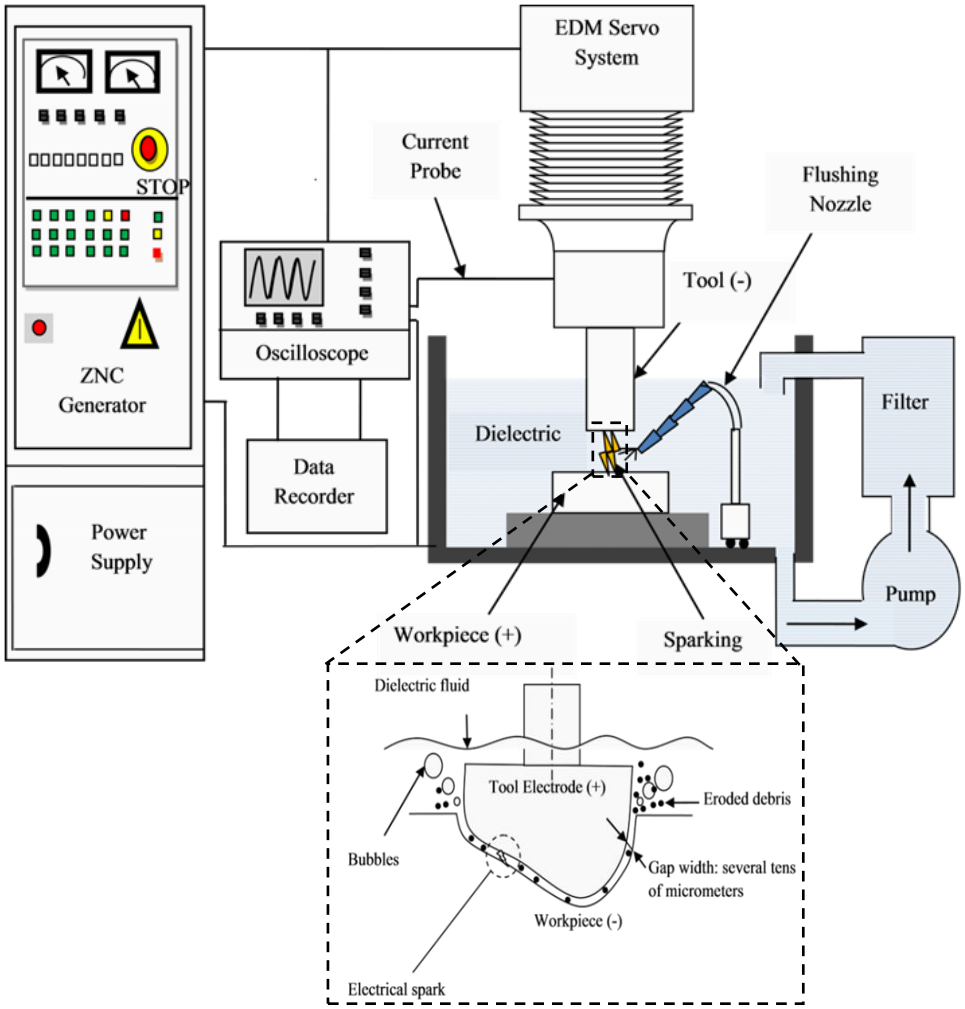

Figure 1.10. Schematic illustrated the mechanism of material removal in EDM process

Moreover, EDM can produce a biocompatible layer on the surface, which also enhanced the surface hardness and corrosion resistance of Ti-64 alloy [94]. Peng et. al. used EDM to machine the Ti-64 alloy and tuned the surface characteristics as required for the osseointegration process [95]. The nanoporous layer has been synthesized by EDM, which promising to promote cell adhesion and growth. Ben at al. investigated the effect of EDM to improve the surface, chemical, and metallurgical properties of the Ti-64 alloy [96-97]. Recently, Prakash et al. critically reviewed the utility of EDM

process for machining Ti and its alloy for biomedical applications [4]. Owing to electro-thermal process, the material gets thermally influenced and various surface imperfections like high surface roughness and micro-cracks were developed on the machined surface. These developed surface irregularities reduced the quality and performance of machined-medical implants such as despoiled corrosion performance, and fatigue performance of implant and as a result bone-implant interface failure. In order to avoid the formation of surface defects, numerous progressions/hybridization in EDM process has been carried out such as Wire-EDM, Ultrasonic Vibration Assisted EDM (UVAEDM), Rotary Assisted EDM (RAEDM), HyFlex EDM, Electro Discharge Coating/surface modification by composite or green tool electrode, Near Dry EDM and Powder Mixed EDM (PMEDM) [98].

Most of the researchers used powder mixed dielectric to deposit workpiece surface [99-100]. Prakash et al. investigated the effect of Si-mixed EDM to alter the surface characteristics to improve the biocompatibility, mechano-corrosion, and wear resistance properties of a specially designed Ti-35Nb-7Ta-5Zr (β-phase) for orthopedic applications [101]. Xie et. al. reported that the surface hardness of 45-C steel has been increased from 415 to 1420 Hv using graphite-mixed EDM [102]. Arun et. al. synthesized a hard-layer of Ni-W coating on tool-steel by Ni&W-mixed EDM to improve the tribological performance [103]. Ekmekci et al. reported that hydroxyapatite (HA) enriched bioceramic layer can be successfully deposited on Ti-64 surface using HA-mixed EDM process [104]. Ou and Wang used EDC to deposit HA-enriched layer on Ti alloy to enhance the biocompatibility of base material [105]. Recently, Prakash et al. uncovered the ability of powder-mixed EDM process to deposit nano-HA layer to enhance the mechanical, corrosion, bioactivity of Mg-based biodegradable implants [106]. Figure 1.11 shows the experimental and material removal mechanics during the PM-EDM machining process.

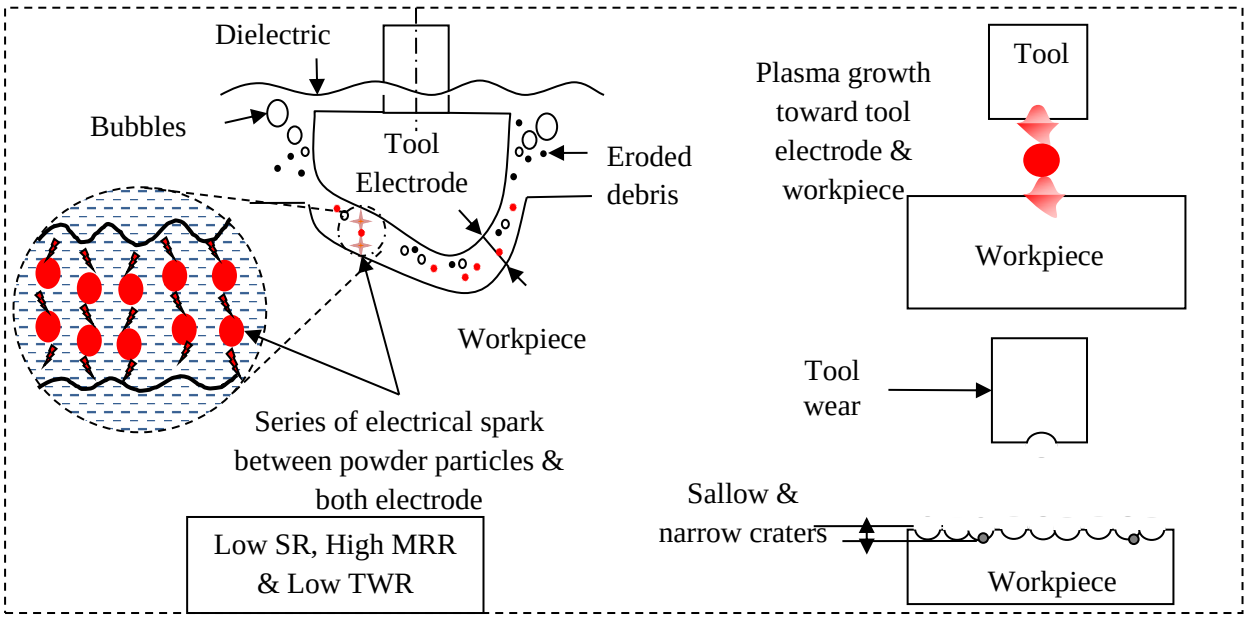

Figure 1.11. Mechanism of material removal from the workpiece in PMEDM process [98]

1.3.3 Thermal Spray Coating process

Thermal spraying a common way of coating the materials, for industrial benefits, bypassing the deposition material (powder or wire) through a heating zone where it is melted. Finally, the coatings are developed because of the propelling of the melted or semi-melted particles towards the substrates [107]. Since the mid-1980s, thermal spraying is considered the most promising technique to apply bioactive films on metallic implants for orthopedic application [108]. Thermal sprayed coating processes for biomedical applications include plasma spray deposition, HVOF spraying, detonation-gun (D-GUN) spaying), warm spraying, cold spraying/Cold Gas Dynamic Spraying (CGDS), flame spraying. In thermal spray process the deposition of feedstock on the surface of materials primarily used as a powder. The powder is proposed onto the plasma jet, diffuse from the plasma torch. In the jet stream, the temperature rises up to the 10,000°K, the material in the form of powder get melted and propelled towards the surface of the substrate. On the surface of substrate molten droplets strike the surface and flatten after that rapidly solidify and form a coat. The schematic of the thermal spray process is shown in Figure 1.12. This system is consisting of the torch, plasma jet, powder, injector, and the substrate. Plasma spray process is a high-

temperature process, in which the jet stream temperature varies in the range from 8000 to 15,000°C, allows to deposit of a large number of biomaterials [109-110].

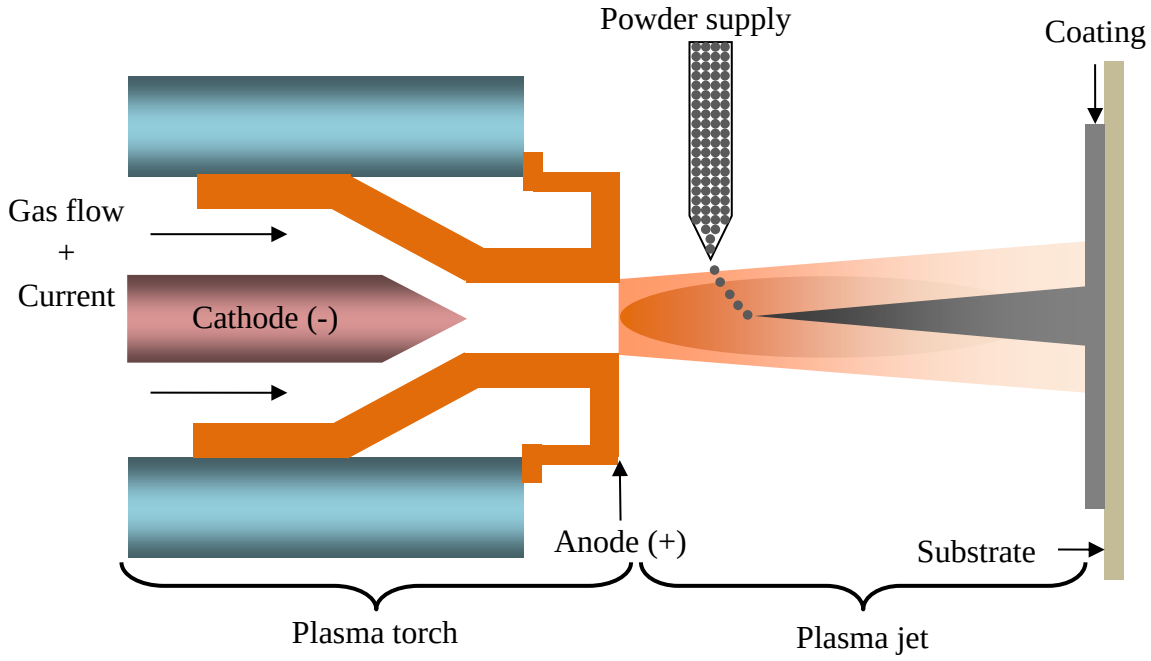

Figure 1.12. Schematic representation of Thermal Spray Deposition process

Li, *et al.*, (2004) deposited pure hydroxyapatite coating (HA) and 50%HA+50%TiO_2 coating (HT) on Ti substrate by plasma spraying deposition process. The effect of heat treatment followed by the coating on the mechanical properties has been studied. The heat treatment enhanced the coating bond strength and removed the residual stress developed during the coating process [111]. Sarao *et al*. (2012) deposited the composite coating of Hydroxyapatite (HA) along with titanium oxide (TiO_2) in the ratio of 50:50 in weight percentage by a thermal-spray deposition process. The cell culture investigation of the coated layer presents the conceivable applications in the biomedical field. The electrochemical examination demonstrated that HA-TiO_2 coatings enhanced the corrosion resistance of Ti-alloy after immersion in human body host conditions [112]. Sidhu *et al.*, (2018) enhance the mechanical properties and corrosion resistance of SS 304 L alloy by depositing HA+15% Al_2O_3 coating using plasma spraying deposition [113]. Galdino *et al.* (2018) deposited HA-TiO_2 (50-50% volume) coating on the surface of Ti-6Al-4V alloy by a plasma spray technique. Microstructure and morphology of coated surface at different HA-TiO_2 composition was investigated and

it has been found that best range for the HA-TiO_2 composition is somewhere in the range of 47% and 53%, respectively [114]. Hu, *et al.*, (2018) deposited HA/TiO_2 and HA/ZrO_2 coating on stainless steel substrates by high velocity suspension flame spray (HVSFS) deposition process for biomedical applications. The HA/TiO_2 coating possessed higher mechanical properties than HA/ZrO_2 [115]. Hameed et. al. (2019) successfully deposited hydroxyapatite using on Ti-6Al-4V alloy using axial suspension plasma spray technique. The mechanical, in-vitro corrosion and bioactivity analysis results of the coating that exhibit excellent cell adhesion, superior adhesion strength, and better corrosion resistance [116]. Hazoor Singh, *et al.*, (2018) studied the corrosion and bioactivity of HA/TiO_2 composite coating deposited by plasma spray deposition process. The 50%HA/50%TiO_2 composite coating exhibited excellent corrosion and bioactivity [117].

1.3.4 Surface Finishing of implants

Surface finishing processes are used to transform/alter the surface characteristics primarily occur because of preceding manufacturing process like casting or forming process [118]. Low surface roughness of a part is important to limit erosion powers and to upgrade wear resistance and mechanical properties, for example, fatigue life and durability. The goal of the present work is to survey distinguishing divisions of nano-finishing processes applicable to freeform/sculptured surfaces. Conventional techniques for accomplishing high surface complete incorporate lapping, grinding, turning, honing, polishing, furthermore, and burnishing. Figure 1.13 presents conventional and advanced finishing processes. Conventional finishing processes like lapping, honing, polishing, and ball burnishing are the oldest methods to get the fine surface finish of about 0.08 to 0.25μm [119-120]. In the lapping process, free rough particle in the form of the concentrated slurry is utilized to rub against the workpiece. The finishing process then deal between lapping plate, abrasive and workpiece. At the point when abrasive particle stream unreservedly makes splits along the surface of the workpiece. Further which are then evacuated to get at last a smoother surface [121-122].

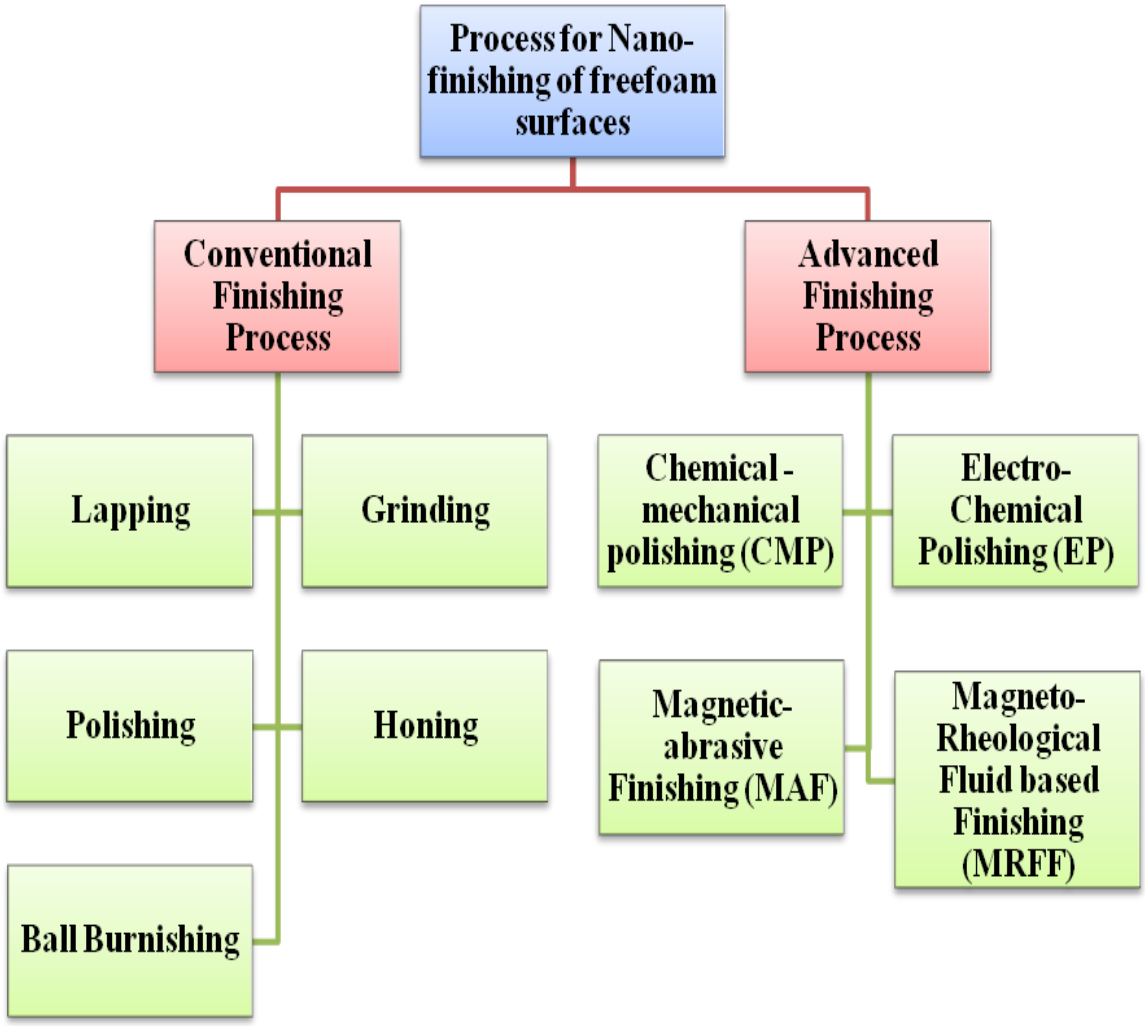

Figure 1.13. Various types of process to finish the freeform surfaces

In this process, there is no change to any dimensional accuracy because of very low material removal rate. Figure 1.14 shows the schematic representation of the lapping process. In the grinding process, abrasive particle are bounded on a plate or wheel. The rotating wheel or plate is press against the linear travelling workpiece for fast removal of stock. The surface finish of about 0.9 to 5 µm is achievable by grinding process. Low grinding ratio is seen with the prominent wearing of the wheel while grinding of hard-brittle materials. Besides, while grinding debris tried to block the wheel. This will now influenced the uniform distribution of abrasive grain in grinding wheel [123-124].

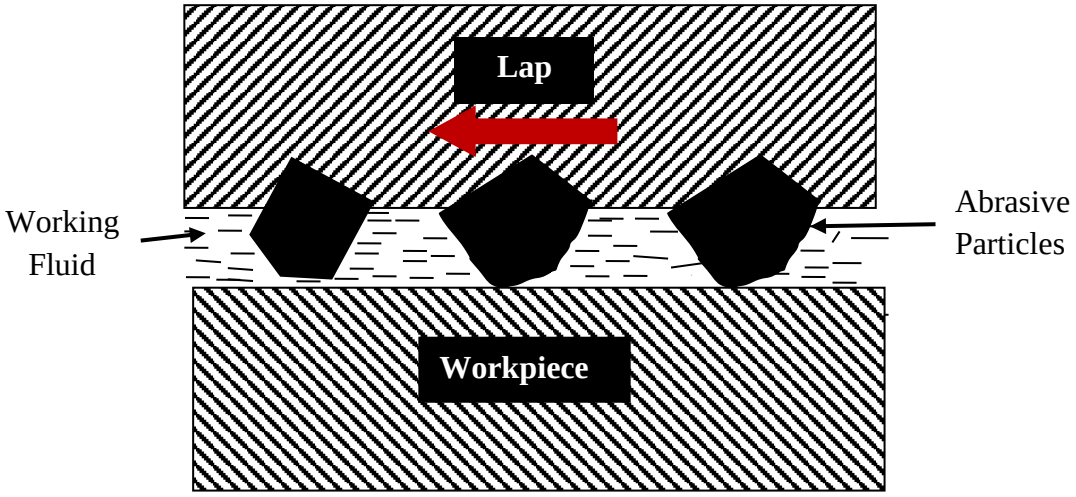

Figure 1.14. Scheme of the Lapping process

Today the polishing of bio-implant is usually joined with high precision CNC procedure till the operative proficiency to affirm the uniform evacuation of material over entire complex surfaces. The smoothness of polished spherical cups and balls has obtained up to nanoscale, with the progress of refined polishing machines [123]. Cheung et al. examined the factor that influences the nano surface generation in ultra-precision polishing. The investigation offered reasonable techniques for upgrading the surface finish of freeform components. Better surface finish was procured including/plus less cost and operative time. An arrangement of ideal polishing conditions for machining Ti-based knee implants was then presented and uncertainly confirmed. Super finished orthopedic implants alongside surface smoothness of beneath 10 nm were accomplished [125]. Honing is also a finishing process used for internal finishing of work piece. In this process, a honing stone is used which is composed of abrasive grains of very fine powder. It is basically utilized for betterment of the geometric form of a surface, but side by side it may improve the surface texture too [121]. This process is also used in automobile sector to finish the internal cylinder walls of the engine. Burnishing process also used for internal finishing of holes or tubes. It provides better results if compared with the honing process. In this process, a hardened steel balls or rolls are pressed on to the surface of workpiece and imparting a feed motion to the same surface [126]. Even though vast applications of these conventional finishing processes, but still their have some limitations such as low surface finish and dimensional accuracy

seen in these processes. That's why these processes are not suitable on newly developed harder and tougher materials. There are following disadvantages of the conventional finishing processes:

a) Very expensive when machining harder materials up to higher precision.
b) More energy utilization.
c) Normal force applied on workpiece surface is more, which further can harm the finished surface.
d) Unfit to finish complicated 3-D shapes and time-consuming.

To deal with above-stated issues in conventional grinding and polishing process, modern and advanced finishing processes such as electrolytic in-process dressing (ELID) grinding, chemical-mechanical polishing (CMP), and magnetic abrasive finishing (MAF) processes were developed [126-128]. ELID is a hybrid process which includes electrolytic process for dressing the grinding wheel and grinding process for metal removal [129]. The hard and fine abrasive particles are bounded in grinding wheel which perform material removal process. Figure 1.15 shows the schematic representation of ELID grinding process. Ohmori et al. [130] studies stated that a smooth surface with nano-scale roughness on hard-brittle materials impressively produces by ELID grinding. Accordingly, on-going researchers have demonstrated the interesting suitability of ELID grinding on manufacturing metallic and ceramic-based bioimplants. Kotani et al. [131] employed present same technology to finish Co-Cr-Mo alloys. Mirror-like surface finish that compare positively with polished ones was accomplished. An oxide layer formed on the surface of the product's which is considered in prevention the corrosion was found to be improving by rising the electrolytic current used in machining. But then also the danger of peeling of inducing abrasive grain on decline the surface finish will be there.

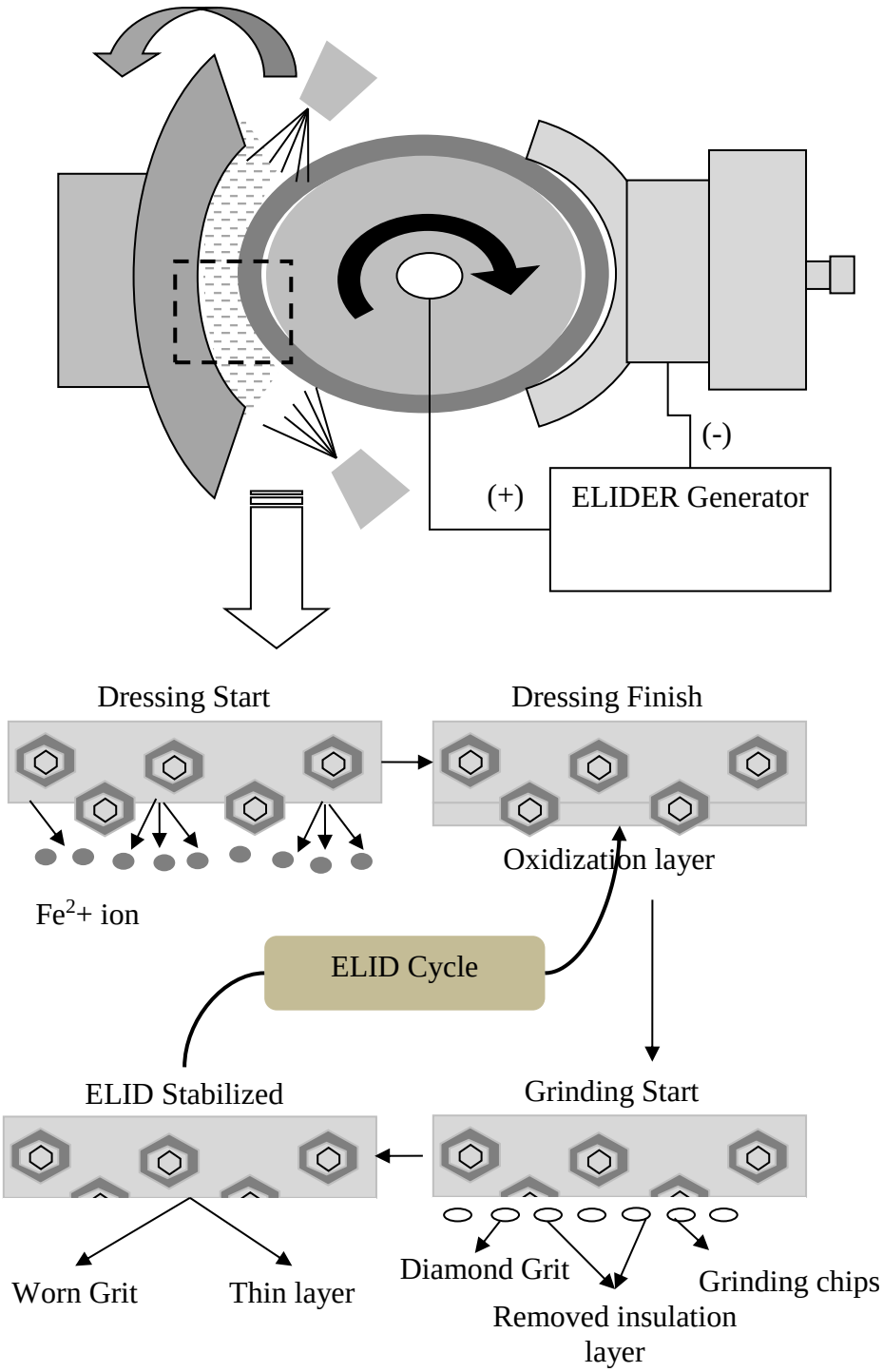

Figure 1.15. Schematic representation of ELID set-up and finishing process

Kotani et al. [23] proposing another ELID grinding system to machine inside the surface of a hemispherical cup. The hybrid process unite ELID grinding to be presented as appropriate for surface finishing process for sliding parts. The magnetic abrasive finishing (MAF) process has been widely adopted for the finishing of engineering

components [133-134]. MAF is a modern precision machining procedure in which the finishing is carried out with the help of magnetic force and abrasive particle [135]. Recently, magnetorheological fluid-based finishing (MRFF) process developed by Jain and co-authors were reported a very potential technique for biomedical applications [136]. The MRFF process has several advantages upon conventional finishing processes. MRFF is an unconventional finishing process, in which finishing action was carried out by utilizing magnetic field and magnetic abrasives particles in the working gap. Figure 1.16 presents the schematic representation of the magnetorheological fluid-based finishing process. A homogeneous mechanical blend of rough and iron particles is set-up for the magnetic abrasive finishing process. This blend is called Magnetic Abrasive Powder and the particles are, therefore, called Magnetic Abrasive particles (MAPs). The MAPs are used in magnetic abrasive finishing of flat and cylindrical (external and internal) surfaces. Many times the abrasive particles are bonded by a sintering process, to the magnetic particles. The particles are then called bounded magnetic abrasive particles (BMAPs). Lubricating oil is sometimes added to the blend to acquire holding strength, and then it is called as loosely bounded magnetic abrasive particles (LMAPs) or it might be a basic mechanical blend of the two, called as unbounded magnetic abrasive particles (UMAPs). A magnet is brought close to the surface of the workpiece maintaining some gap between the two. The shape of the magnet depends upon the shape of the work surface which is to be finished. The magnetic field generator can be either electromagnetic coils or permanent magnets. The gap between the magnet and workpiece is known as finishing gap or machining gap or working gap. When a magnetic field is produced by the magnet, the iron particles in the mixture get magnetized and get aligned along the lines of magnetic force. The abrasive particles in the mixture get trapped in the iron particles matrix or, get sandwiched between the iron particles and thereby, the abrasive particles are held by the magnetic force too. Overall, this alignment of the magnetic abrasive particles forms a brush-like structure known as Flexible Magnetic Abrasive Brush (FMAB). The brush is termed “Flexible” due to its capacity to take the shape of any of surface profile irregularities, if present on the work surface. The normal magnetic force acting on the abrasive particles that are in contact with the workpiece produces indentation into the workpiece. The relative movement between the induced rough particles of the FMAB

and workpiece produces the essential shearing action at the abrasive–workpiece interface to expel material from the work-piece as smaller than expected chips. MRFF tool was developed for processing complex freeform surfaces, in order to attain nano-scale level surface roughness.

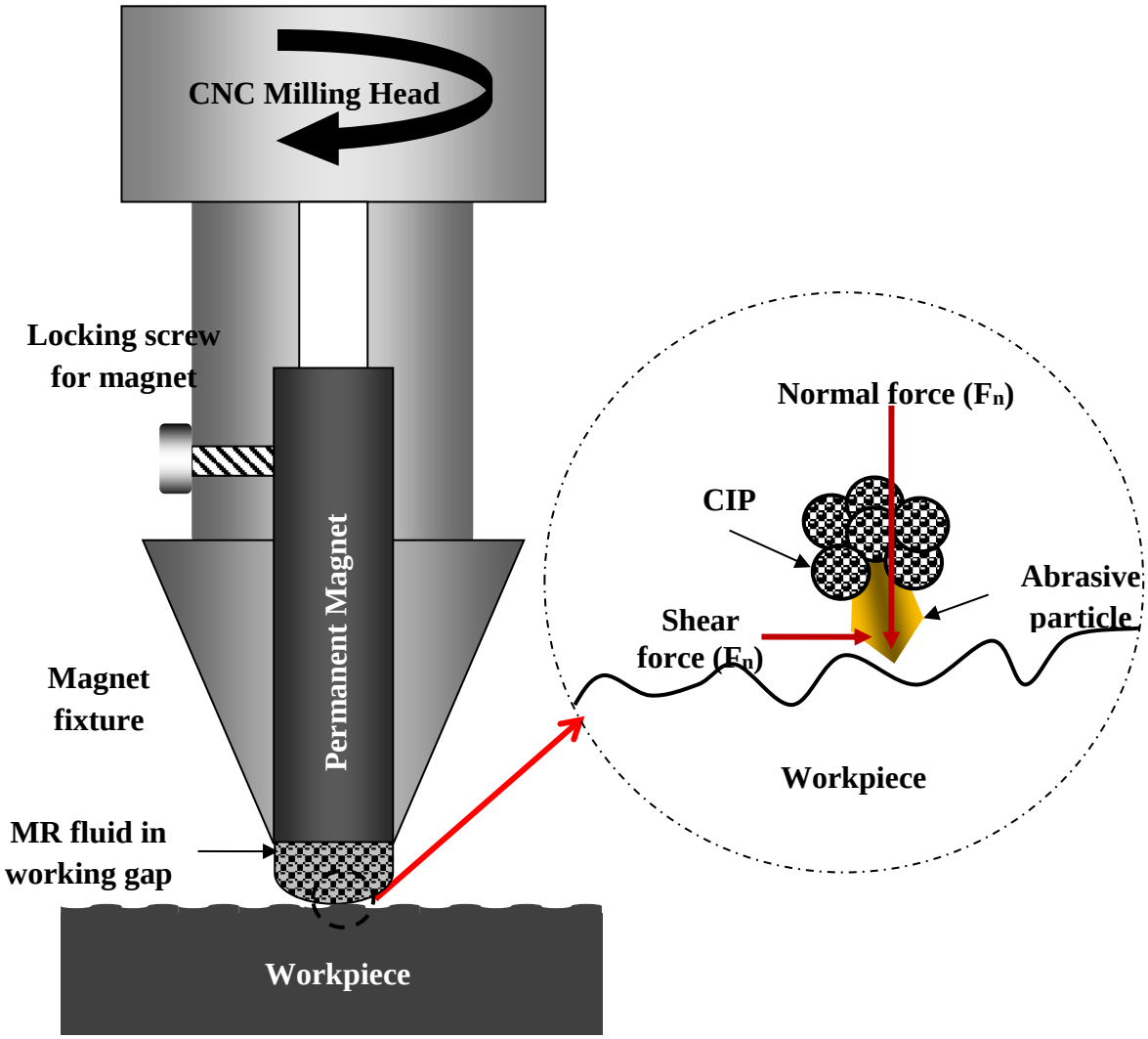

Figure 1.16. Schematic representation of magnetorheological fluid-based finishing (MRFF) process

According to literature, MRFF for finishing of knee implants and nano-level finish has been achieved [137]. Nagdeve et al. further modified MRFF and developed a new rotational-magnetorheological abrasive flow finishing process (R-MRFF) for the knee implant applications. In this Inverse replica of the workpiece as a finishing fixture is recommended for finishing of freeform surfaces up to nano-level roughness [138].

Kumar et al. also used R-MRFF for finishing of knee implants [139]. Barman et. al. reported that not only abrasive particles were sufficient for the finishing process, but MRFF fluid composition also affect the surface integrity. To finish the titanium alloy at the nanometer level, two types of acidic base medium are prepared and specific composition of the various acidic base medium is very important to generate required surface morphology on the implant [140].

CHAPTER-II

LITERATURE REVIEW

This section presents background information on various coating materials and several coating techniques used till date. The information here is a summary of important information found in a comprehensive literature review, journal articles, thesis and books related to Plasma spray technique and alloying of coating materials to enhance bioactivity performance of implant. Each result of the research is examined for the relevance to the subject of thesis.

From the last decade, hydroxyapatite (*HA*) has been used as vital biological coating-materials for load-bearing implant applications especially hip implants [141-143]. HA, a bio-ceramic element, is one of the most extensively used coating material that can enhance the surface energy and bioactivity of metallic biomaterials such as SS-316L, Ti-6Al-4V, and Co-Cr alloy. Further, several coating techniques have been exhaustively used for the deposition of HA on metallic implants which includes: micro-arc oxidation [144], sol-gel [145], electro-chemical deposition [146], electrochemical anodic oxidation [147], sputtering ion coating [148-149], physical vapor deposition [150], electric discharge machining [151], plasma spray [152-153], etc. Among these, plasma sprays a well-established deposition technique has been widely used for the deposition of HA on Ti-based implants [152-154]. Nevertheless, as per the guidelines of the Food and Drug Administration (FDA), USA [155], the plasma spray technique is the only clinically approved due to its excellent deposition rate and compact coating formation in contrast to other methods [156].

Further, the coating of HA, via plasma spray technique, has been found to enhance the corrosion resistance and bioactivity of Ti-based and other metallic alloys [157]. On the contrary, it is reported that HA is brittle, fragile, and possesses lacking physical properties (such as less fracture resistance and bond strength) with the substrate material, which often degrades in a long-term performance [158-160]. Further, various attempts have been made to enhance the physical characteristics and reduce the brittleness and fragile nature of HA through reinforcing or alloying with

other biomimetic ceramics: such as Al2O3 [161], TiO2 [162-163], ZrO2 [164], CNTs [165-166], Graphene [167-168], yttria-stabilized zirconia (YSZ) [169], and SiO2 [170].

Singh et al. developed the HA-Nb coating on magnesium-alloy using plasma spray coating technique for biomedical applications. The coating has been developed to enhance bio-activity performance and degradation of Mg-alloy. The alloying/reinforcement of Nb (10%, 20%, and 30%) in HA-matrix on mechanical properties, and corrosion resistance, and bioactivity have been studied. Figure 2.1 shows the coating cross-section morphology of various coatings developed on Mg-alloy. The high content of Nb-element reduced the brittleness of HA and improved the adhesion of coating. The HA-Nb coating exhibit excellent mechanical, corrosion resistance and bioactivity [171].

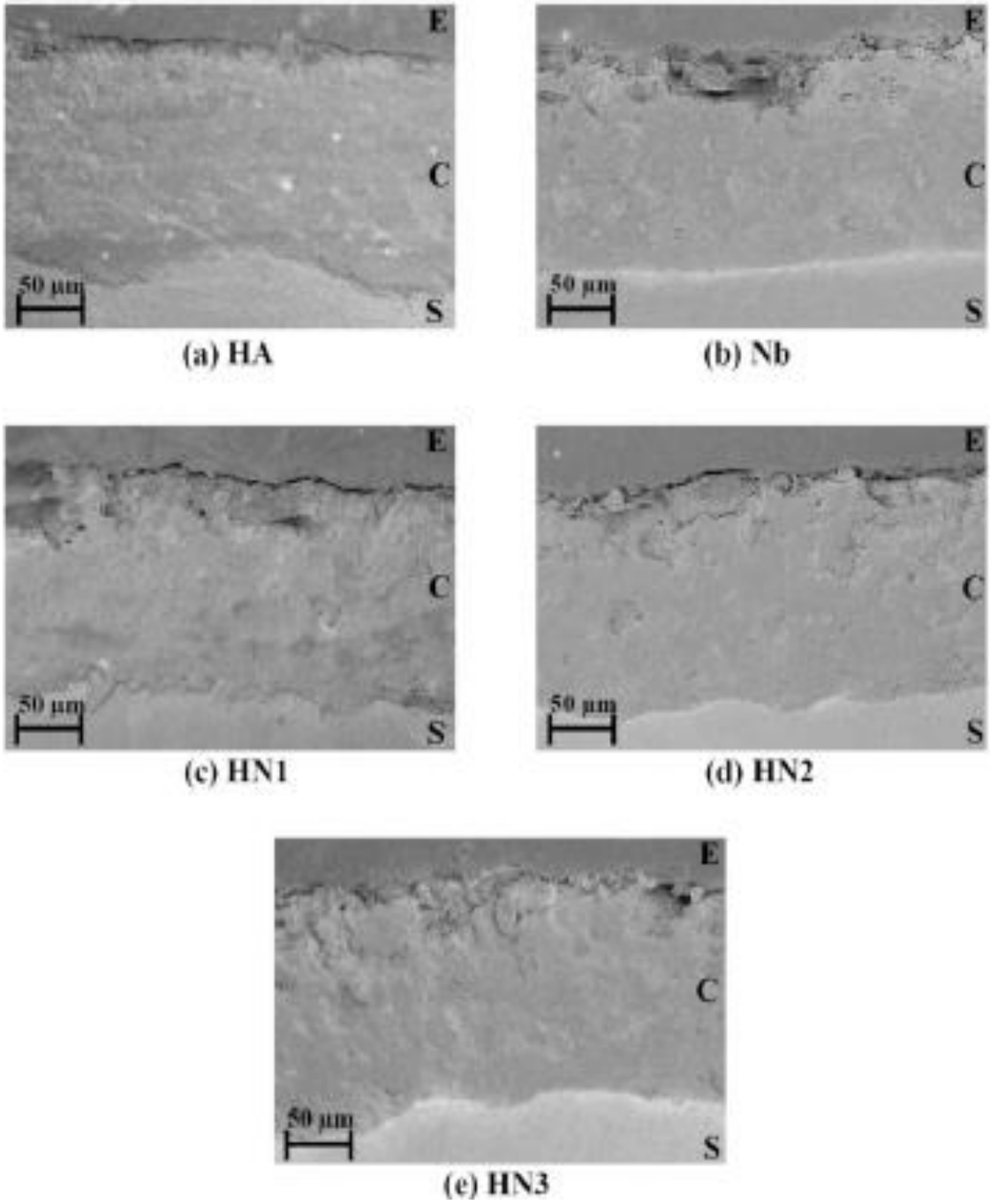

Figure 2.1. HA-Nb coating on Mg-alloy: (a) HA, (b) Nb, (c) HA-10Nb, (d) HA-20Nb, and (e) HA-30Nb

Pillai et al. synthesized bio-inspired HA/β-TCP coating on titanium based alloy for biomedical application. The effect of heat treatment on the coating morphology, corrosion resistance has been evaluated. Figure 2.2 and 2.3 shows the cross-section and top surface morphology of β-TCP and HA/β-TCP coatings before and after heat

treatment. The coating thickness was observed in the range of 75-100 μm. The coating has excellent bonding with the substrate [172].

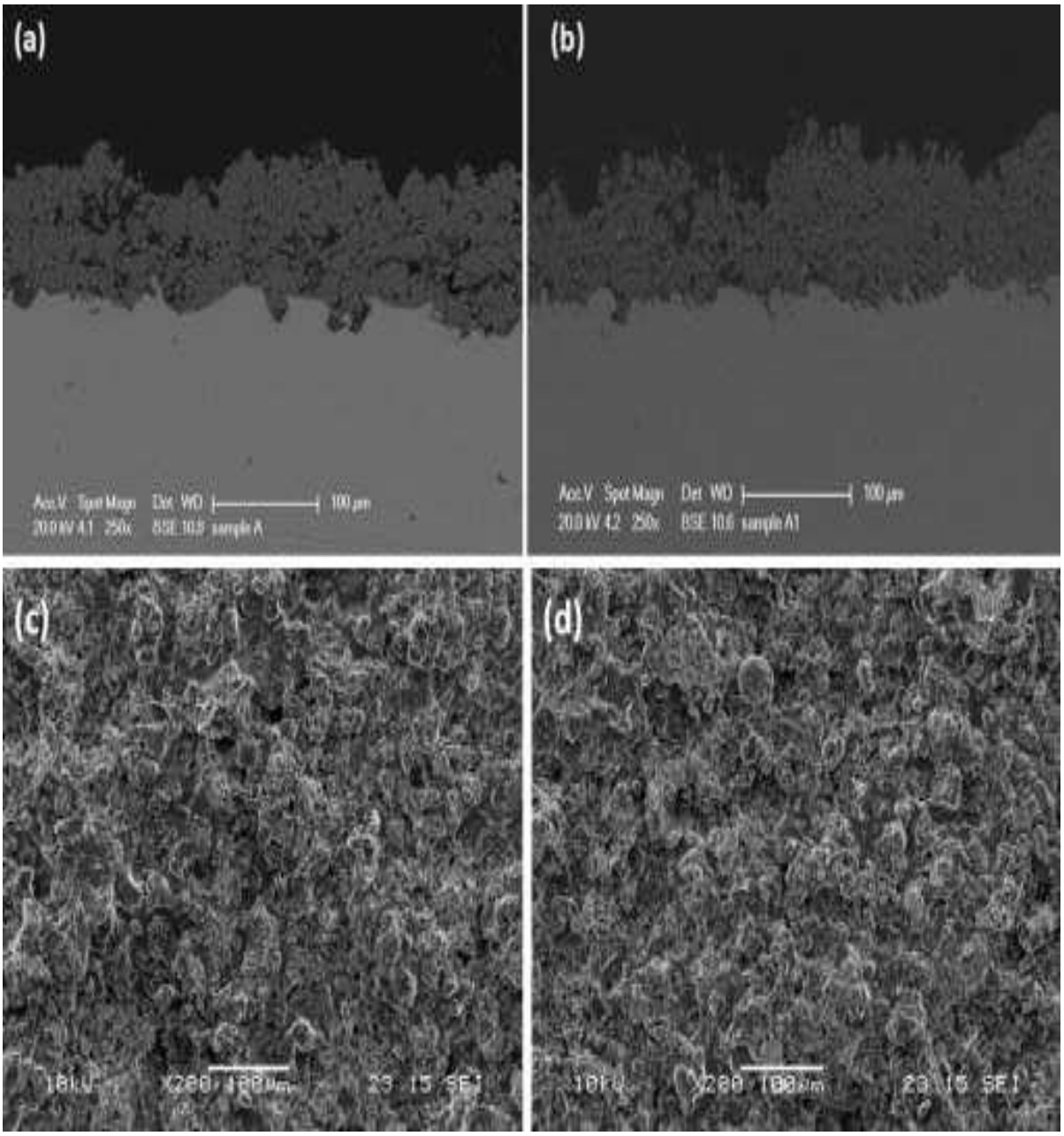

Figure 2.2. Cross-section and top surface morphology of (a-c) β-TCP and (b-d) HA/β-TCP coatings before heat treatment

Both coating specimens display a heterogenous partly and completely melted surface fusion of particles consisting of high ribs of embedded, dispersed molten metal, micro-cracks, micro-globules and surface porosity, all of which are the expected surface characteristics obtained from the plasma scraper.

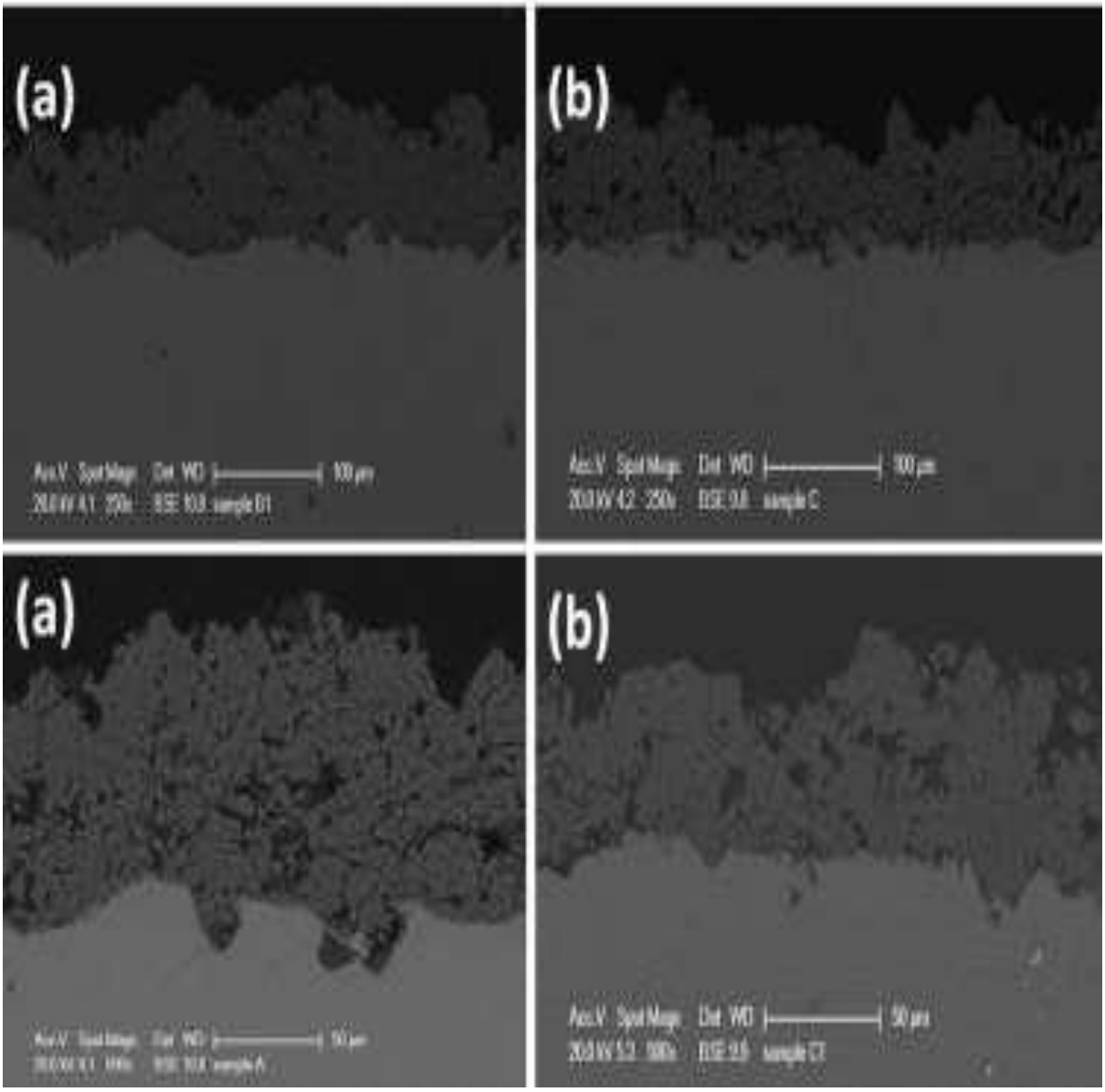

Figure 2.3. Cross-section (a-c) β-TCP and (b-d) HA/β-TCP coatings before and after heat treatment

Ebrahimi et al. deposited a double-layer composite coating of HA-Al_2O_3-SiO_2 on pure-titanium alloy using plasma spray coating technique for biomedical application. The effect of SiO_2 alloying composition (wt. % of 10, 20 and 30) in the coating on the surface morphology and biocompatibility has been studied. The coating morphology has been improved with the alloying of SiO_2 in HA/Al_2O_3. The SiO_2 reduced the brittleness of the coating and improved the adhesion strength of coatings. The surface roughness has been increased with the addition of SiO_2 in HA/Al_2O_3 matrix. The HA-

coating has highest surface hardness and better wettability. The HA-Al_2O_3-20SiO_2 coating exhibit excellent bioactivity and mechanical properties [173].

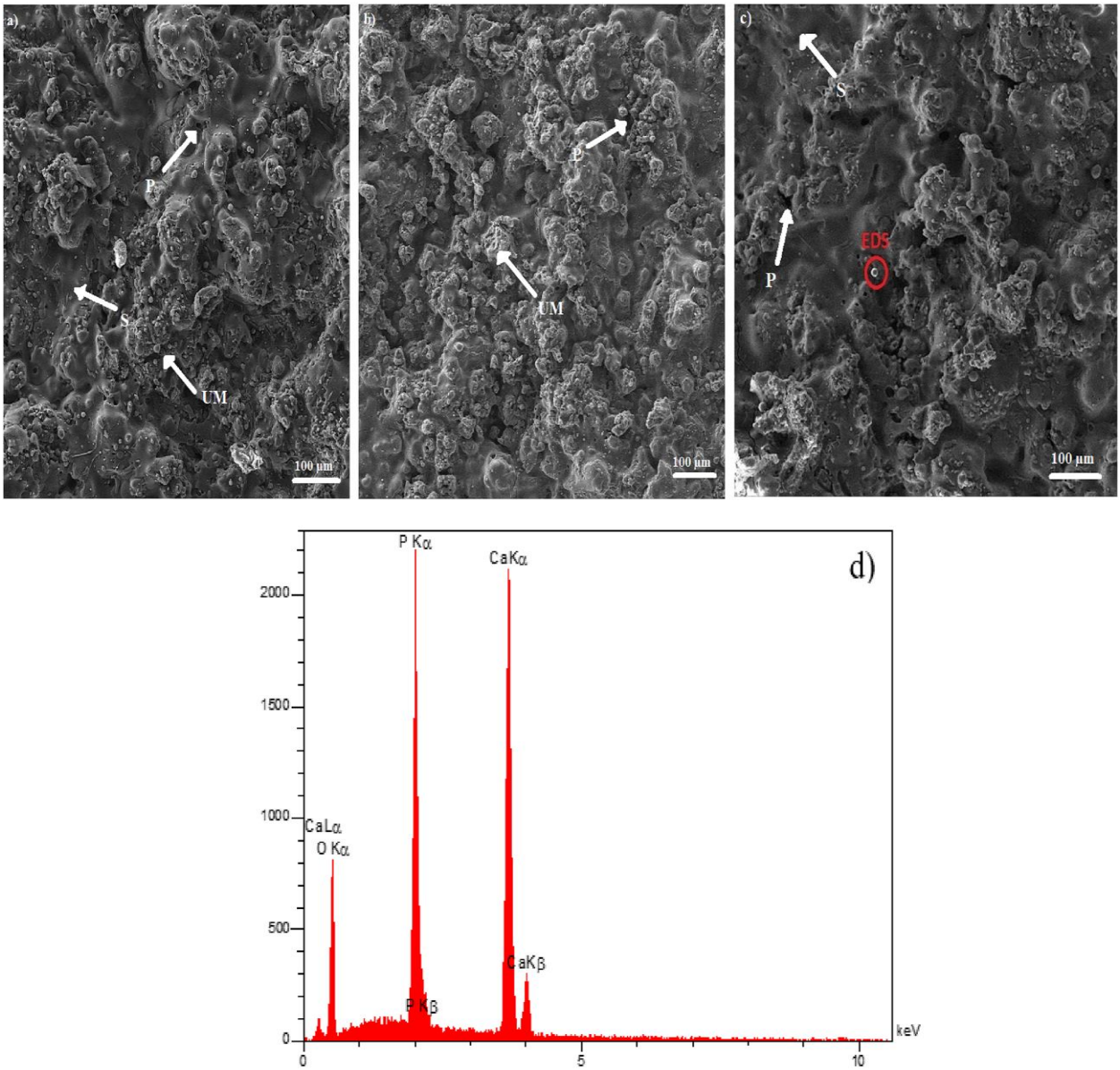

Figure 2.4. Top surface morphology of coating: (a) HA-Al_2O_3-10SiO_2, (b) HA-Al_2O_3-20SiO_2, (c) HA-Al_2O_3-30SiO_2, and (d) EDS-spectrum of coating

Unabia et al. synthesized the biomimetic Cu-doped HA coating on Ti-alloy using plasma spray deposition technique. Surface morphology and crystallinity examination has been carried out in details. Figure 2.5 shows the top surface and cross-section morphology of HA and Cu-HA coating [174]. Both coating specimens display a heterogeneous partly and completely melted surface fusion of particles consisting of

high ribs of embedded, dispersed molten metal, micro-cracks, micro-globules and surface porosity, all of which are the expected surface characteristics obtained from the plasma scraper. The crystallinity analysis revealed that 61 to 81% purity of TCP phases were present in the Cu-doped HA coating. The coating possessed excellent biocompatibility and can be used for orthopedic applications.

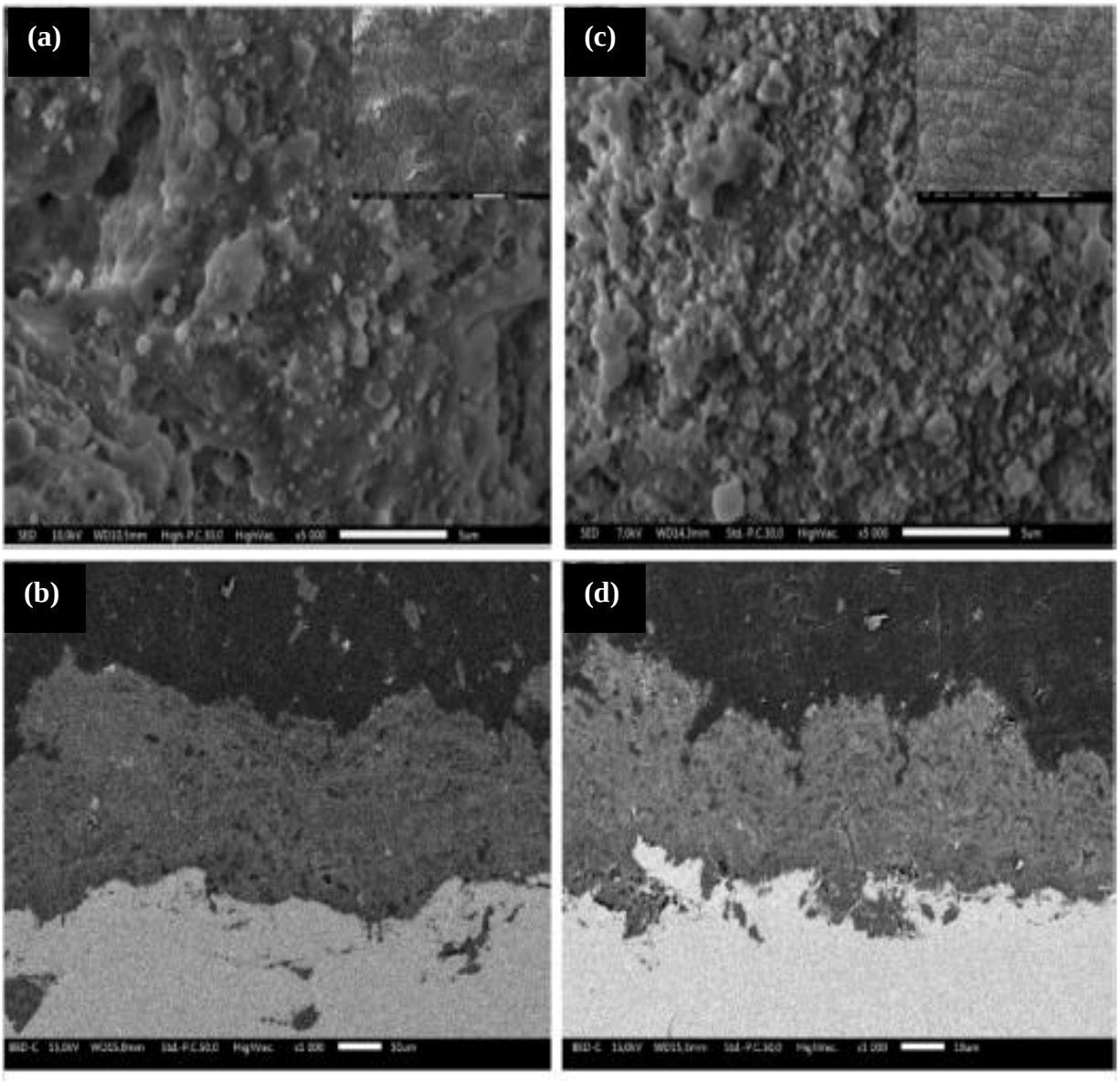

Figure 2.5. Top surface and cross-section morphology of (a-b) HA and (c-d) Cu-HA coating

Zhang et al. developed HA-TiO_2 coating on Ti-6Al-4V alloy using plasma spray coating technique for orthopedic applications. The effect of spray-distance on the

coating morphology and tribological properties has been investigated. The exhibit porous structure and as the spray-distance increased the structural porosity increased, which deceased the mechanical performance of coating. The wear resistance and tribological performance analysis revealed that HA-TiO_2 coating have better wear performance when coating deposited at 80 mm spray-distance [175].

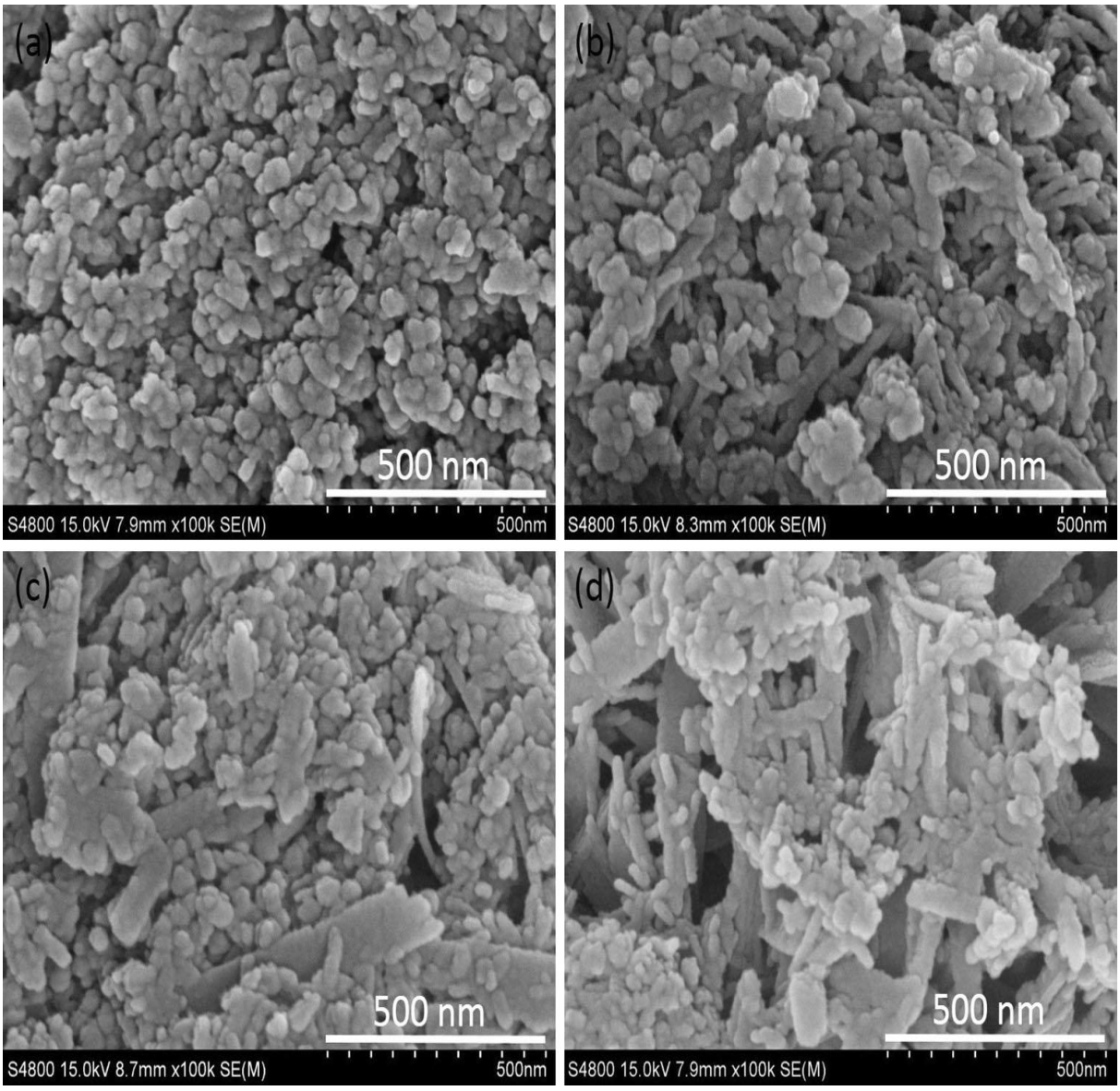

Figure 2.6. Top surface morphology of HA-TiO_2 coating at spray distance (a) 80 mm, (b) 90mm, (c) 100 mm, and (d) 110 mm

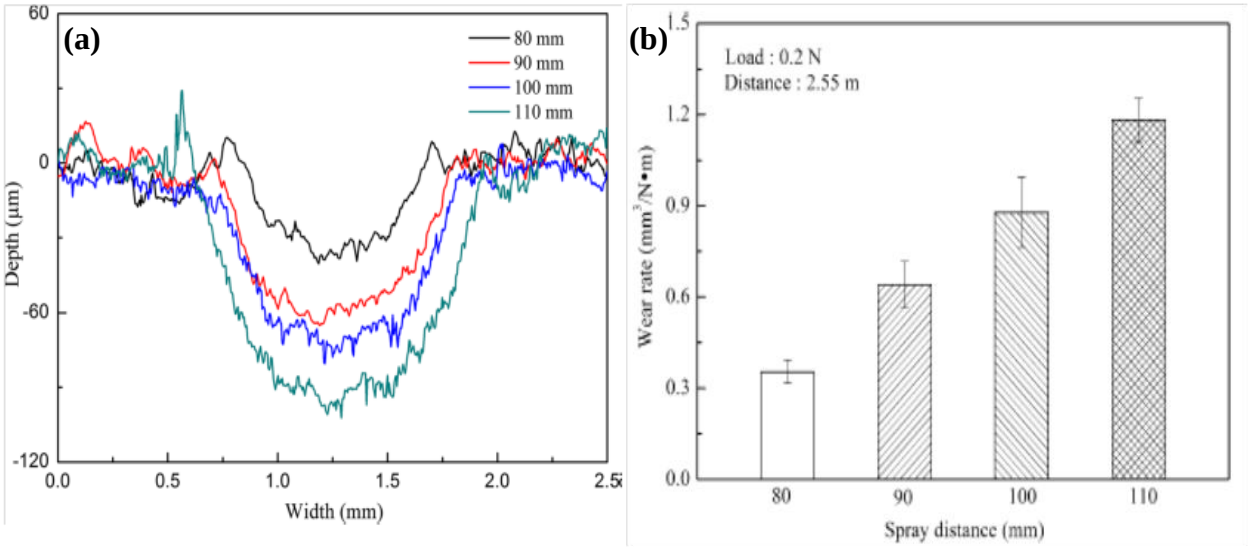

Figure 2.7. (a) Wear track behavior and (b) wear rate of coating at different spray-distance

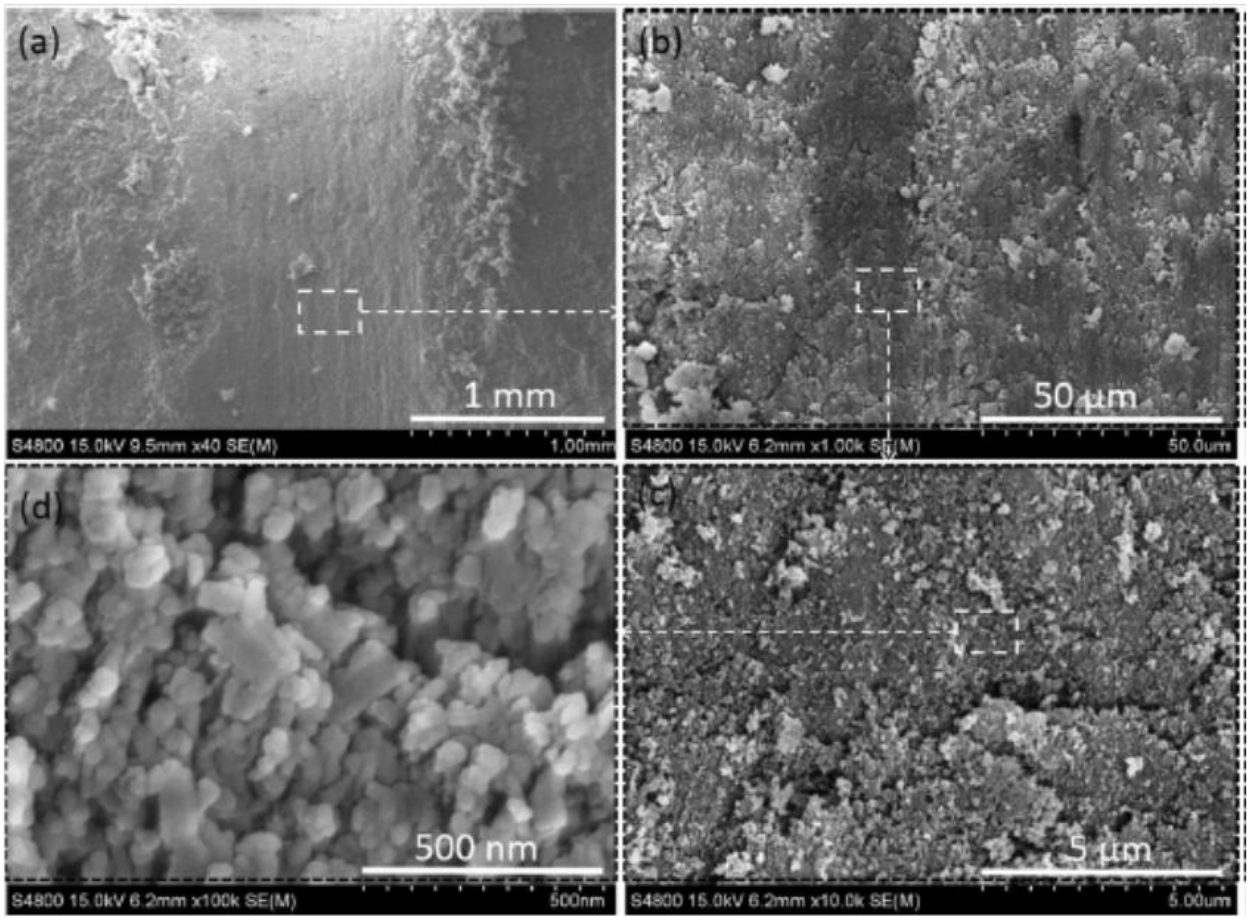

Figure 2.8. Wear morphology of coating at 100 mm distance at different magnification view

Clavijo-Mejía et al. developed Bovine-derived biomimetic HA-coating (BHA) on 304SS steel for biomedical application. The performance of BHA-coating developed through HVOF has been compared with the BHN-coating obtained through atmospheric plasma spray (APS) process. Figure 2.9 shows the cross-section and top surface morphology of BHA-coating developed through HVOF and APS technique. From the cross-section micrograph, it can be seen that a dense coating of thickness in the range of 100-125 μm has been obtained. The HVOF coated surface have flat and smooth morphology as compared with APS-coating [176].

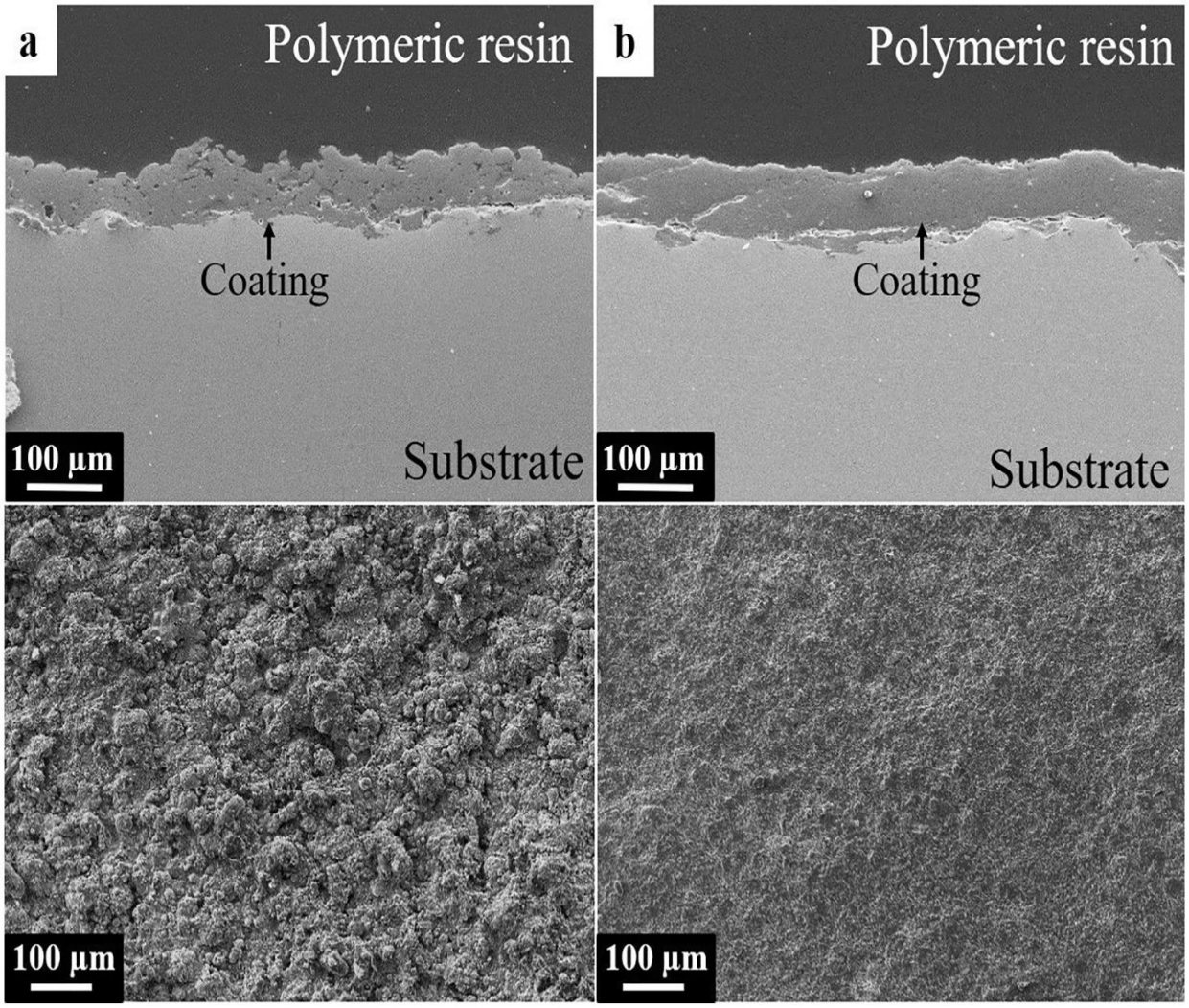

Figure 2.9. Cross-section and top surface morphology of BHA-coating developed through APS (a-c) and HVOF (b-d) technique

Degradation performance of coating has been evaluated by immersion test. The immersion test has been performed in SBF solution for 3, 5, and 7 day. Figure 2.10 and

2.11 shows the degraded morphology of BHA-coating obtained through APS and HVOF process. From the immersion morphology, it can be seen that APS-derived coating promotes higher growth of apatite-layer. Patel like crystal structure can be clearly seen on coating surface after 10 days of immersion, which confirmed that structure is bioactive. Form the all results, it can be concluded that BHAP-coating developed by APS possessed dense layer, defect free morphology, thickness, proper roughness and purity which is beneficial for osseointegration process.

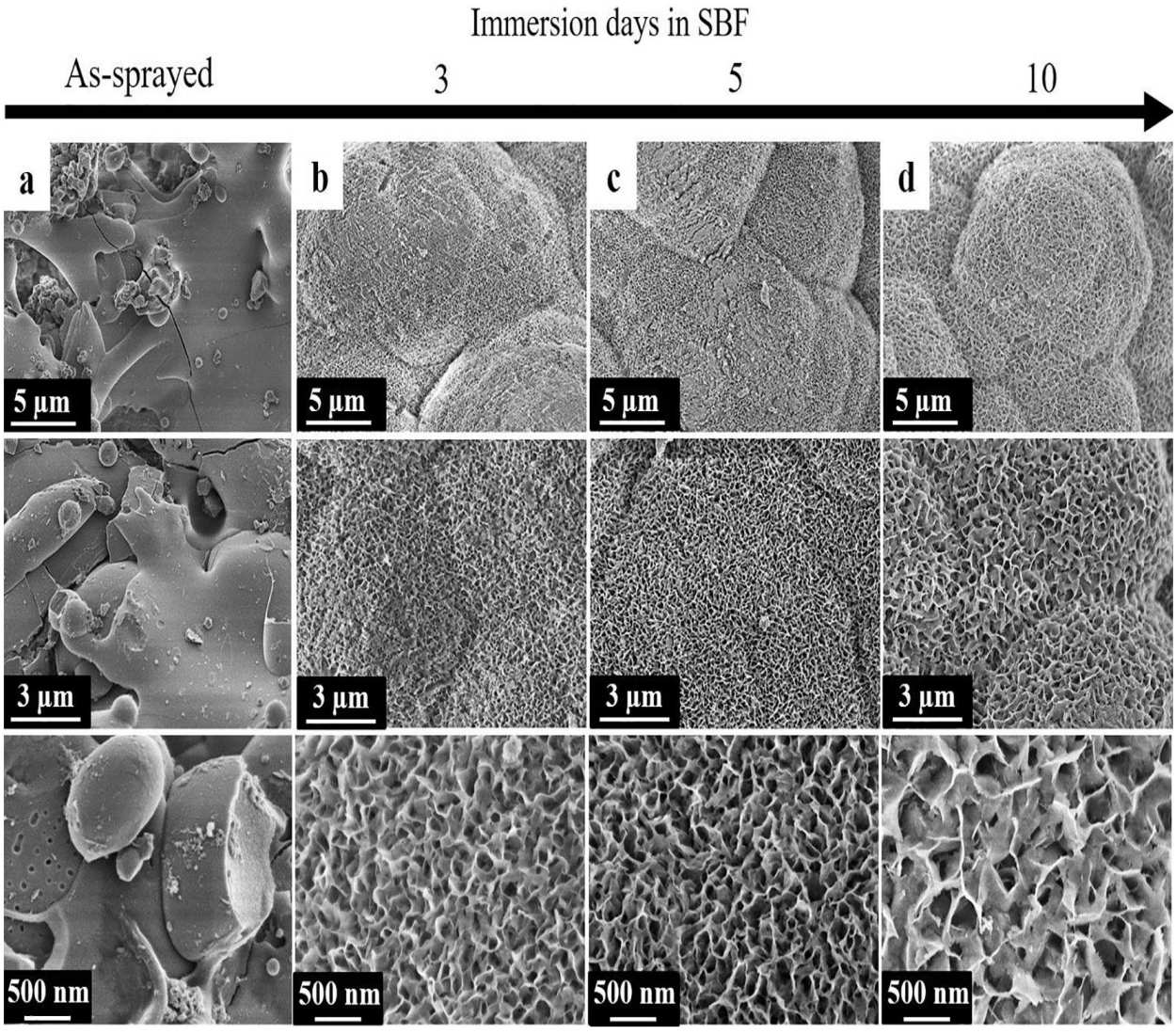

Figure 2.10. Morphology of BHA-coating obtained through APS process after immersion test for (a) 3 days, (b) 5 days, and (c) 7 days at different magnifications

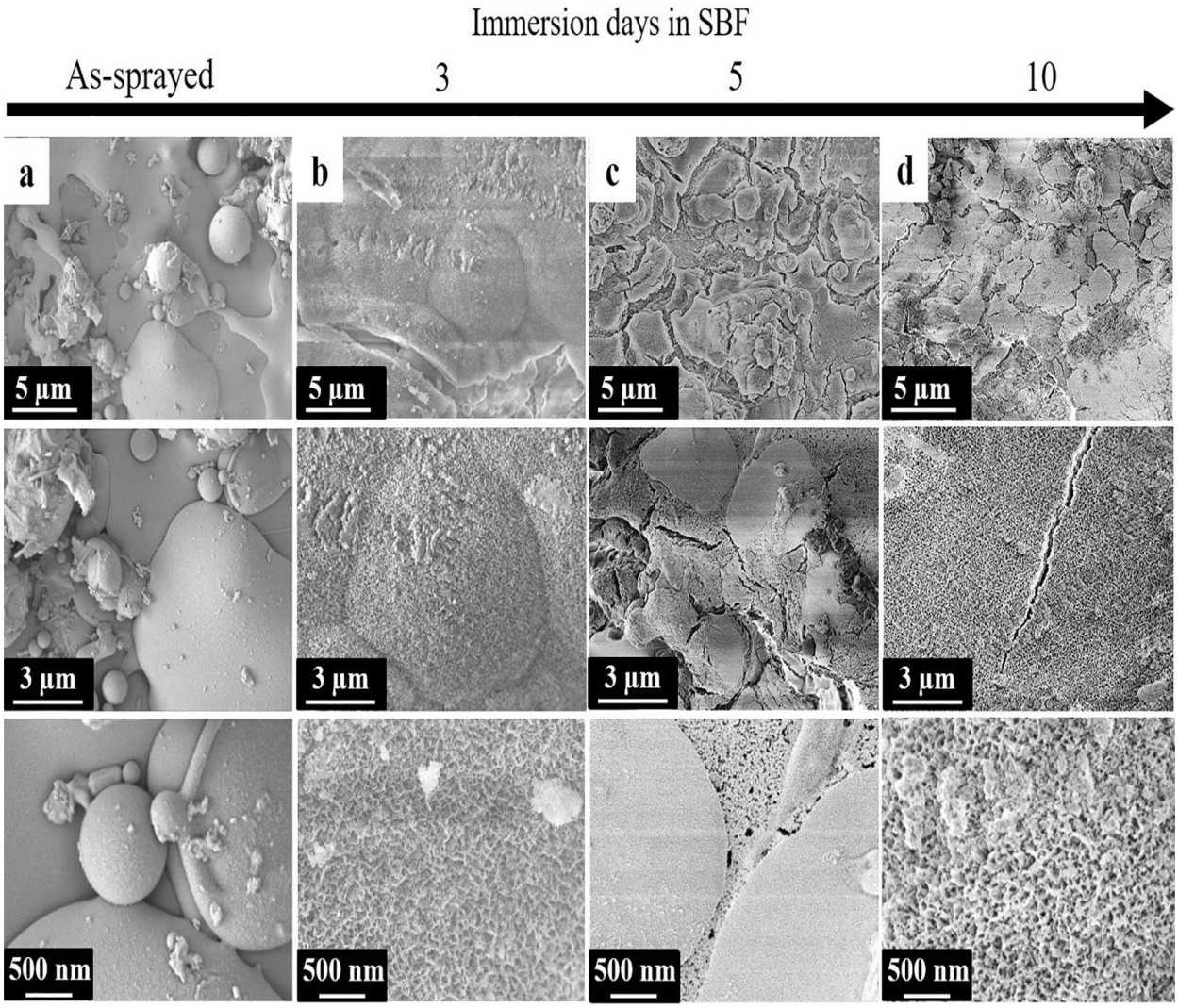

Figure 2.11. Morphology of BHA-coating obtained through HVOF process after immersion test for (a) 3 days, (b) 5 days, and (c) 7 days at different magnifications

Kuo et al. synthesized porous Ta-coating on Ti-alloy using vacuum plasma spray process for orthopedic applications. Mechanical properties such as micro-hardness, elastic modulus, and adhesion strength has been studied. The surface morphology, coating thickness, surface roughness, and porosity have been studied. Immersion test in SBF-solution and cell culture analysis using Mg-63 cell line has been performed to access the bioactivity of coatings. The effect of alkali treatment (AT), AT and heat treatment (AHT), and AHT with ultrasonic cleaning (AHT-UC) on the coating performance has been studied [177].

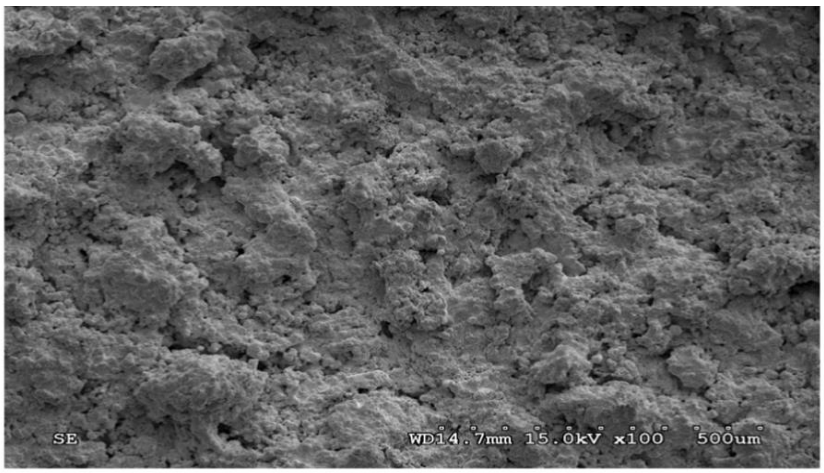

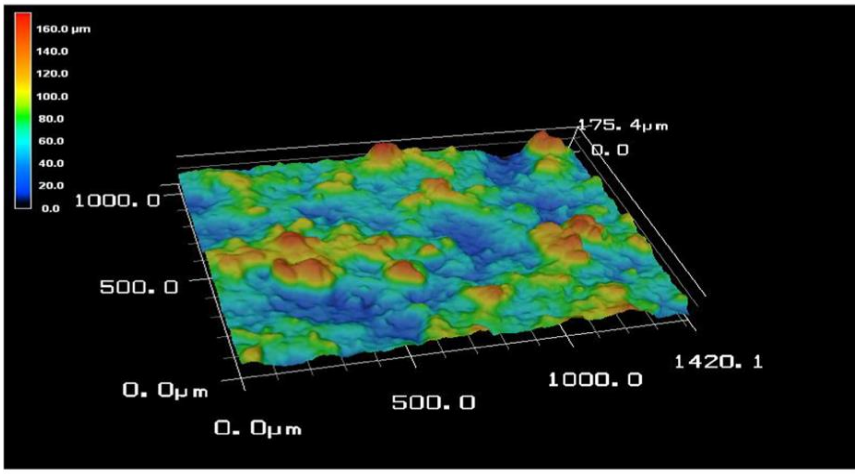

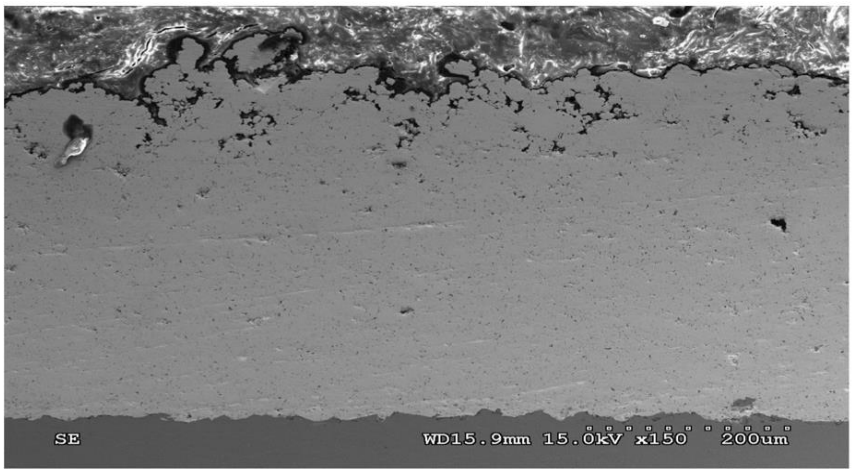

Figure 2.12. Porous-Ta coating: (a) Top morphology, (b) 3D surface, (c) cross-section

The coating possessed 55 MPa adhesion strength, the average structural porosity was around 13%, and surface rightness was obtained 23 μm. The AHT-UC possessed excellent mechanical bioactivity because the microstructure become amorphous, which stipulates the apatite growth and favorable for bone in-growth process. **Hameed et al.** studied and compared the performance of Ha-coating developed though atmospheric plasma spray (APS) and axial suspension plasma spray (SPS). The microstructure, coating purity, thickness, surface defects, mechanical properties, corrosion resistance, and bioactivity have been extensively studied [178].

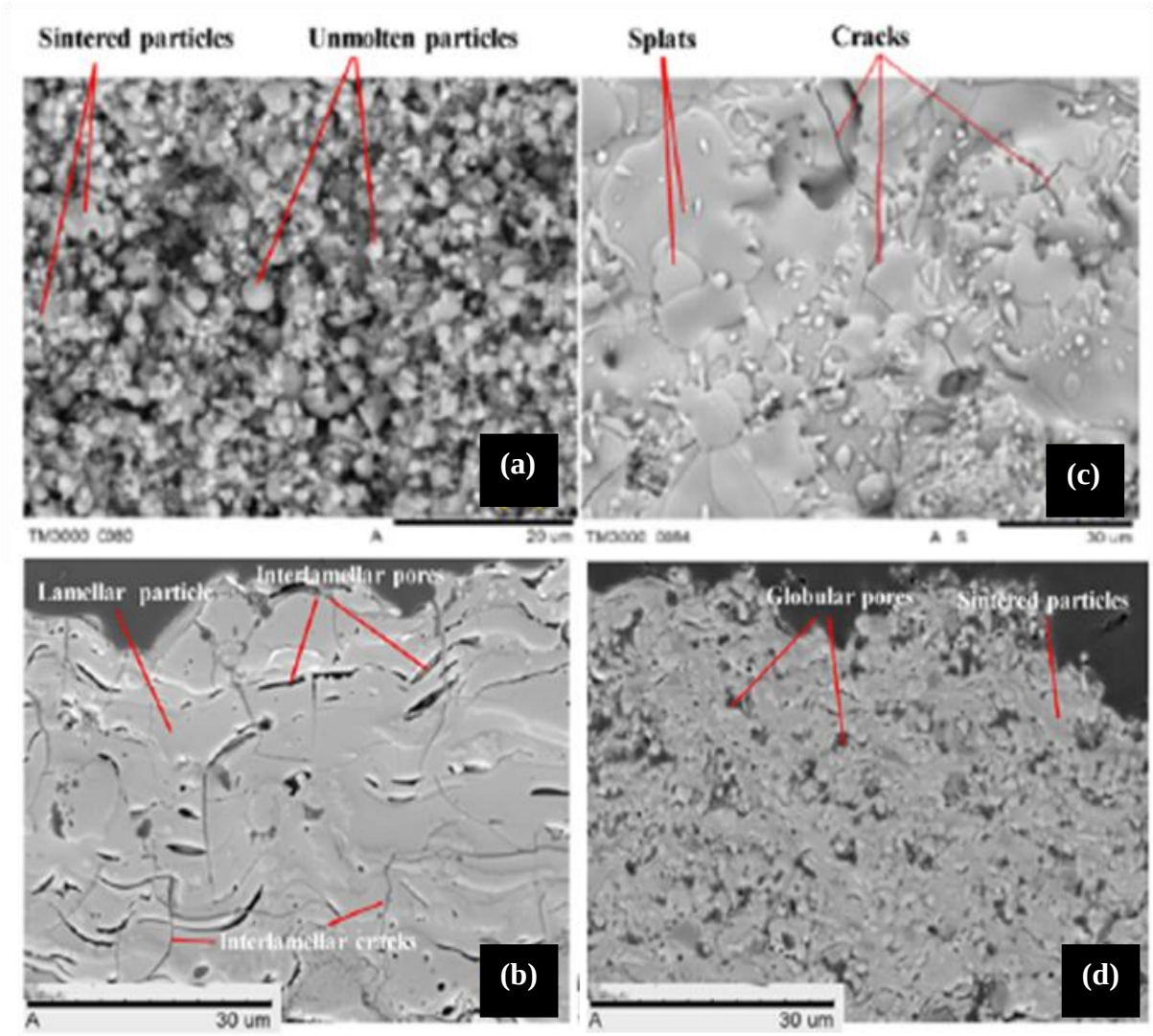

Figure 2.13. Top and cross-section morphology of HA-coating obtained through APS (a-b) and SPS (c-d) technique

The effect of gas flow rate and type-of-powder suspension on the coating performance has been studied. The maximum surface roughness and porosity was obtained 4.18 μm and 17.82%, respectively. The maximum surface hardness and adhesion strength of coating was obtained 334 Hv and 38.84 MPa, respectively. The SPS-based coating possessed better corrosion resistance and purity. The SPS-coating exhibit better bioactivity as compared to APS.

Ke et al. developed functional graded MgO/Ag_2O alloyed HA-coating on the Ti-surface using plasma spray deposition process. To improve the adhesion strength of coating a bond coat of HA was deposited prior to coating using laser deposition technique. After that, biocompatible coating of MgO/Ag_2O/HA was deposited using plasma spray technique. Figure 2.13 shows the coating procedure on the Ti-alloy [179].

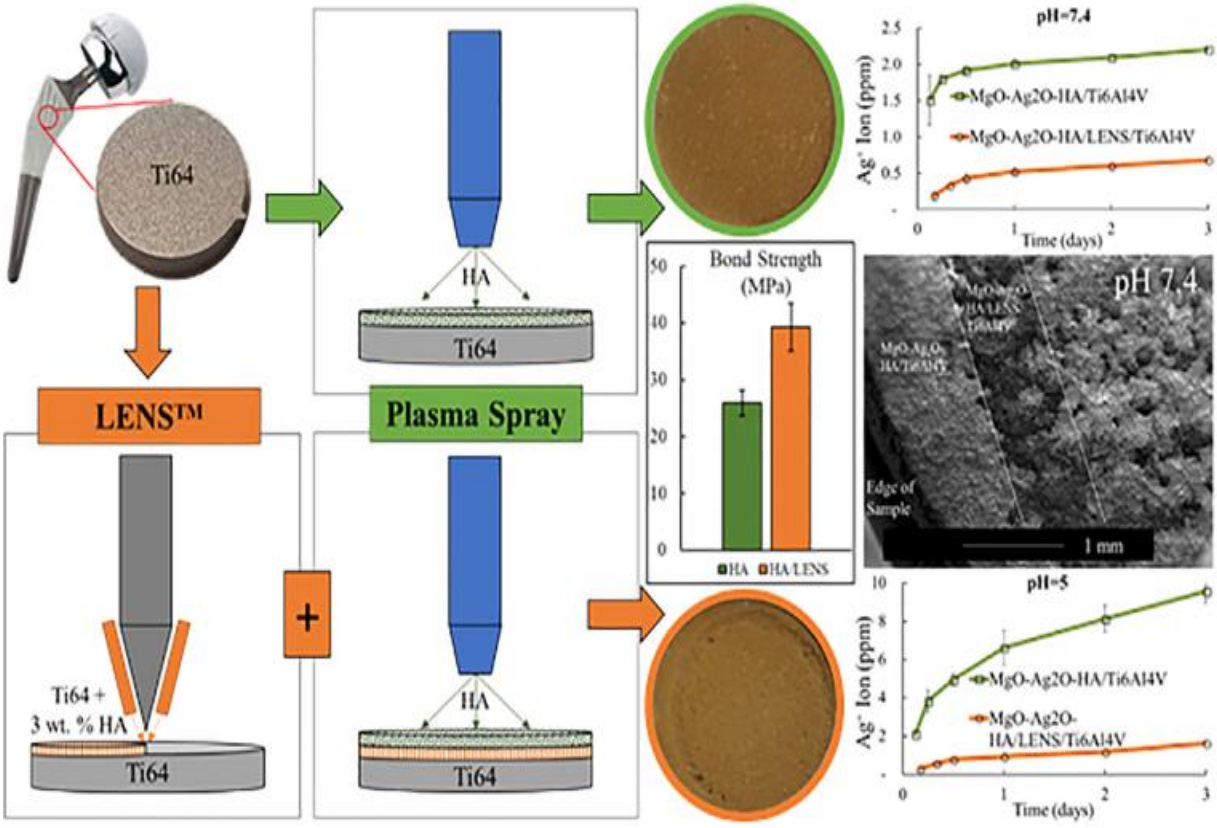

Figure 2.14. Deposition of functional graded MgO/Ag_2O alloyed HA-coating on the Ti-surface using laser and plasma spray process

Figure 2.14 shows the cross-section and top morphology of HA-bond coat using laser deposition and functional graded MgO/Ag_2O alloyed HA-coating using plasma spray process. From the micrographs, it can be seen that the HA-coating is tightly bound

with the substrate and possessed surface hardness of 735 HV. On the other hand, the functional graded MgO/Ag_2O alloyed HA-coating also exhibit good adhesion and coating possessed surface hardness of 685 HV. The adhesion strength has been improved by 52%.

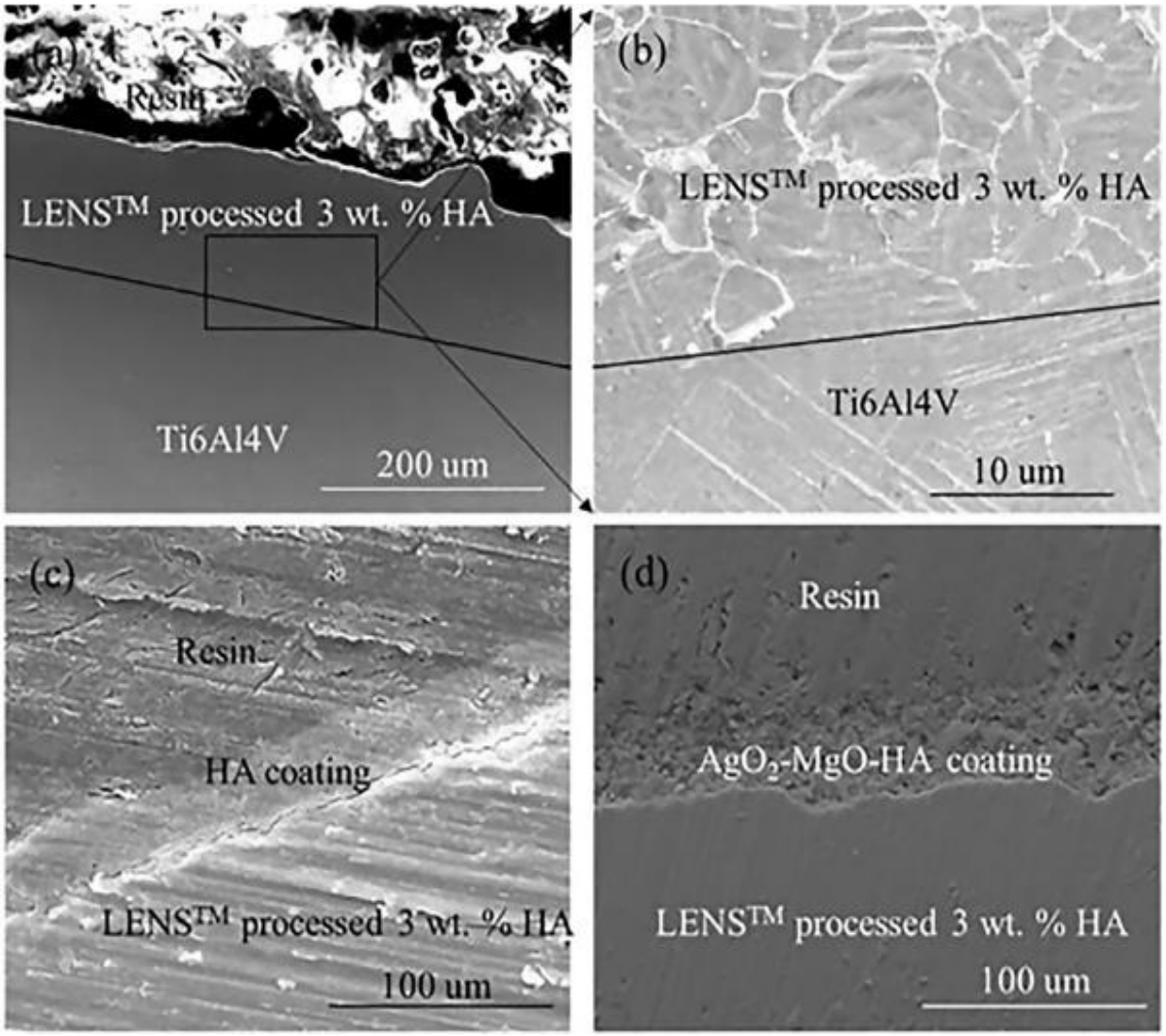

Figure 2.15. (a-b) cross-section and top morphology of HA-bond coat using laser deposition, (c-d) functional graded MgO/Ag_2O alloyed HA-coating using plasma spray process

Figure 2.15 shows the attached cell morphology of Mg-63 cells of HA-bond coat using laser deposition and functional graded MgO/Ag_2O alloyed HA-coating using plasma spray process. Form the micrographs, it can be seen that, the cell growth and adhesion

increased with the incubation time. Clear picture of nuclei formation and filopodias can be seen. The cells were speared over the entire surface of coating.

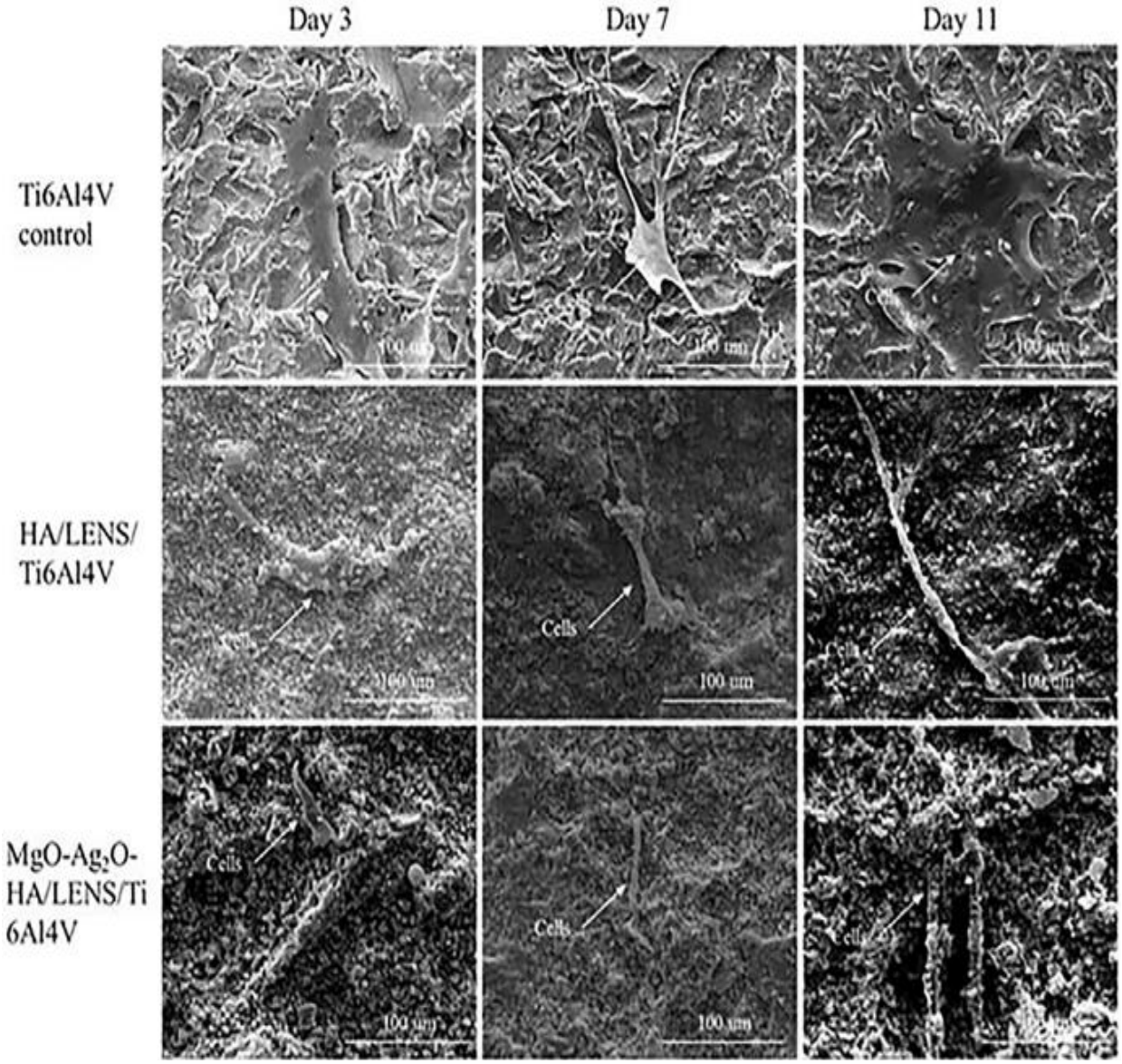

Figure 2.16. Bioactivity and cell adhesion analysis after 3, 7, and 11 day on un-treated, HA-deposited by laser, and functional graded MgO/Ag_2O alloyed HA-coating

Singh et al. developed the HA-based coating on SS-316L using vacuum plasma spray technique for biomedical applications. The effect of 10%Al_2O_3 and 10%ZrO_2 reinforcement in the HA-matrix on the coating morphology, adhesion strength, micro-hardness, corrosion resistance, and corrosion resistance and bioactivity has been analyzed. Moreover, the effect of heat treatment on the coating morphology, adhesion

strength, micro-hardness, corrosion resistance, and corrosion resistance and bioactivity has been analyzed. Figure 2.16 shows the top surface morphology of HA-10%Al_2O_3 and HA-10%ZrO_2 coatings before and after heat treatment [180].

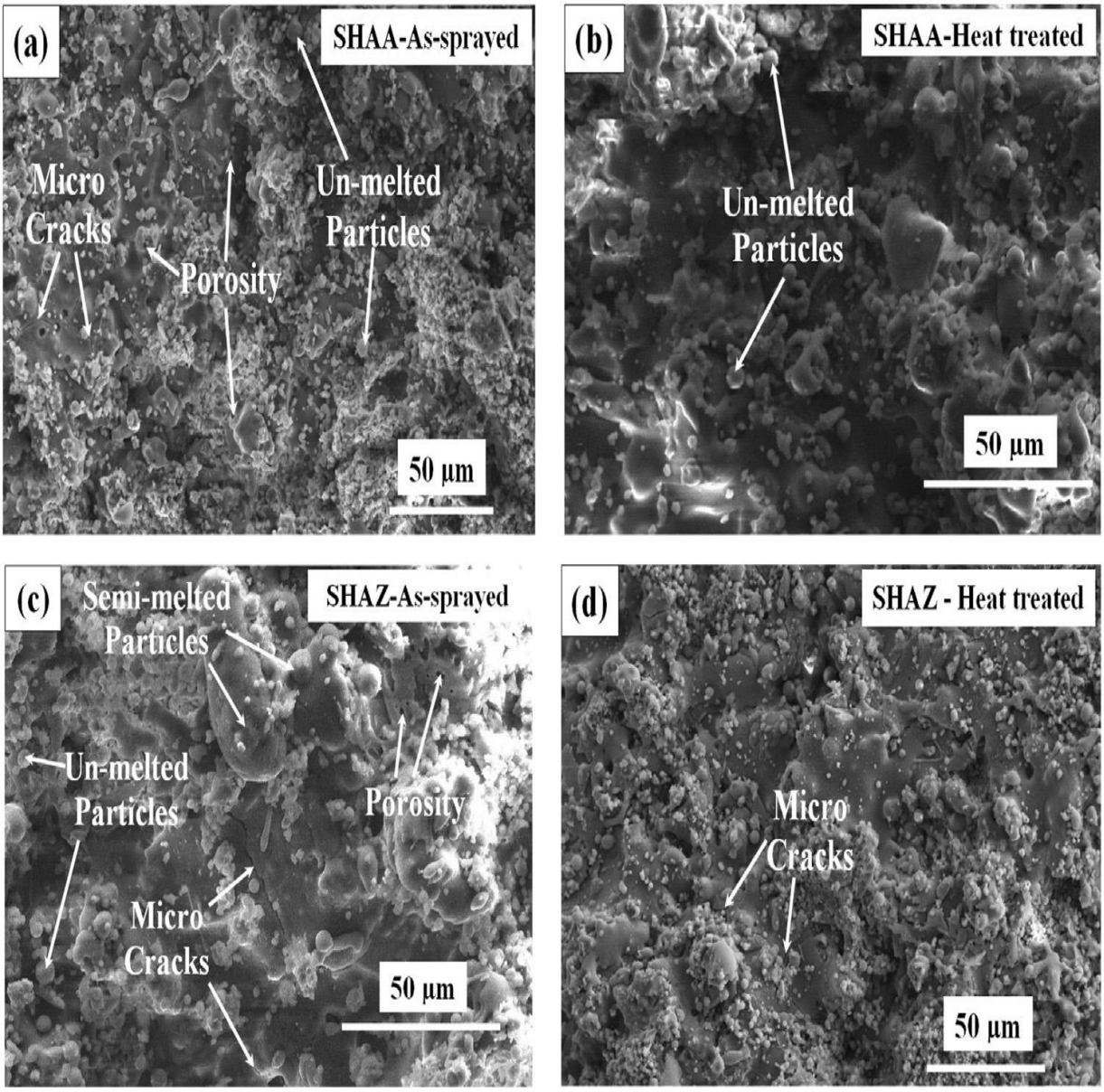

Figure 2.17. Top surface morphology of HA-10%Al_2O_3 and HA-10%ZrO_2 coatings before (a,c) and after heat treatment (b,d).

From the SEM-micrograph, it can be seen that before coating possessed micro-cracks, unmelted, and semi-melted particles. After heat treatment, the microstructure has been improved and surface defects have been removed. Figure 2.16 shows the micro-hardness of HA-10%Al_2O_3 and HA-10%ZrO_2 coatings before and after heat treatment.

The micro-hardness of HA-10%Al_2O_3 after heat treatment has been improved after heat treatment.

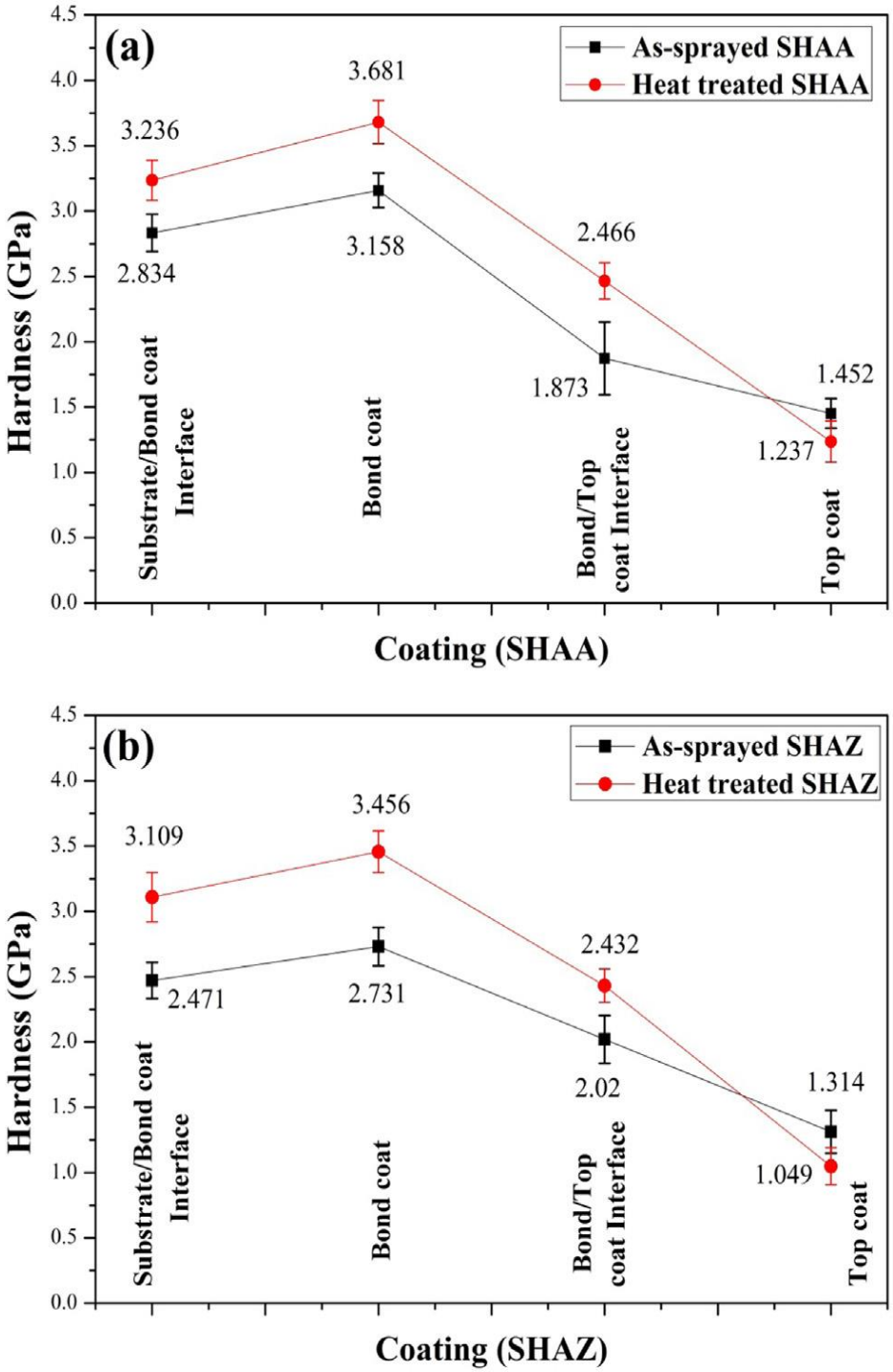

Figure 2.18. Coating micro-hardness of HA-10%Al_2O_3 and HA-10%ZrO_2 coatings before and after heat treatment

Figure 2.17 shows the corrosion performance of un-treated, HA-10%Al_2O_3 coating, and heat-treated HA-10%Al_2O_3 coating. Form the Tafel plot, it can be seen that the heat-treated HA-10%Al_2O_3 coating has low current density as compared to un-treated and HA-10%Al_2O_3 coating.

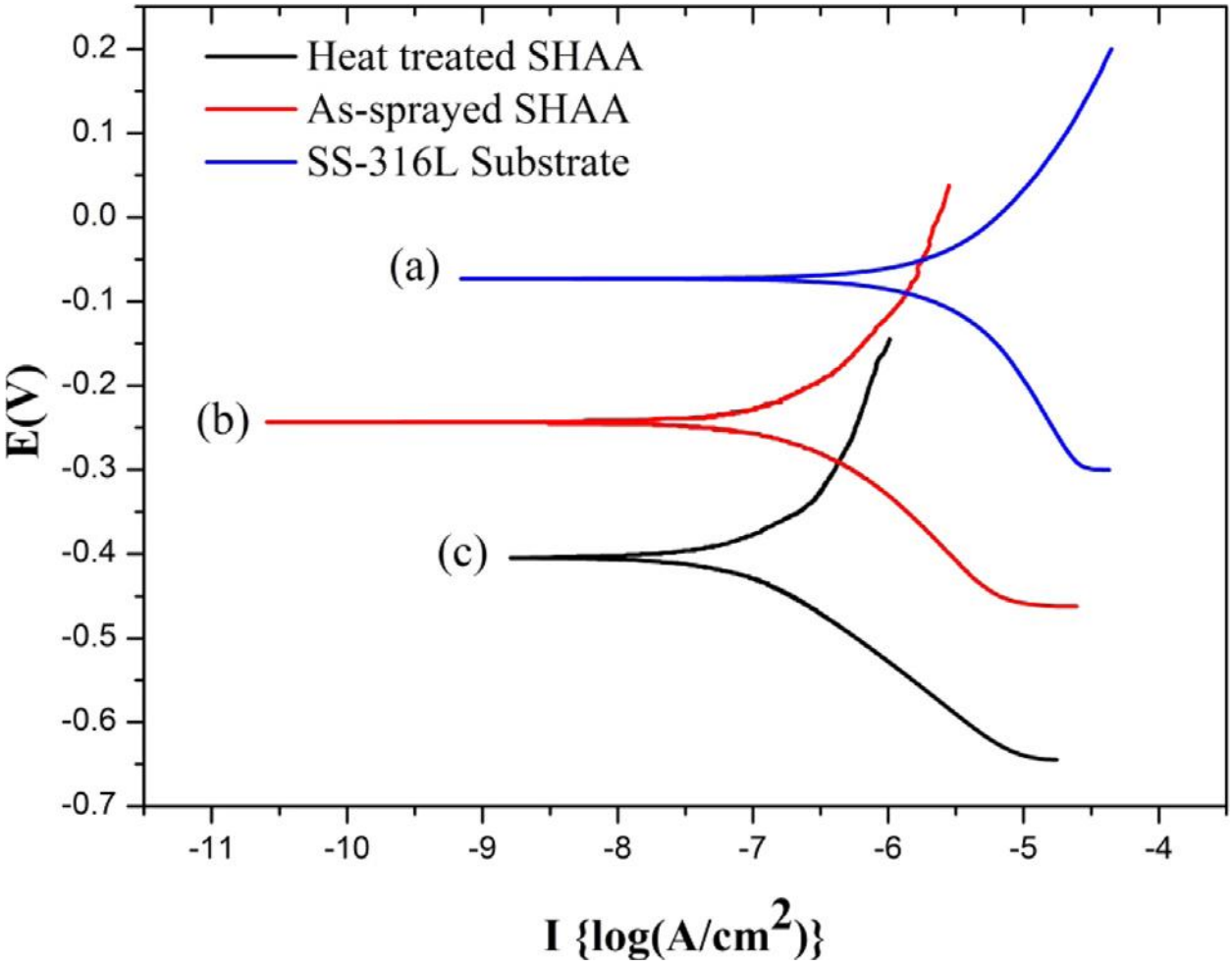

Figure 2.19. Corrosion resistance of un-treated, HA-10%Al_2O_3 coating, and heat-treated HA-10%Al_2O_3 coating

Kaur et al. developed the HA and HA-TiO_2 coating on the Ti-alloy using HVOF process for biomedical application. The effect of 25%TiO_2 reinforcement in HA-matrix on the coating micro-structure, mechanical properties, and corrosion resistance has been studied [181]. The reinforcement of TiO_2 reduced the brittleness of HA and improved the bio-mechanical performance of coating. The structural porosities reduced by the alloying of TiO_2 reinforcement in HA-matrix. The microhardness of coating has been increased to 560 MPa form 350 MPa.

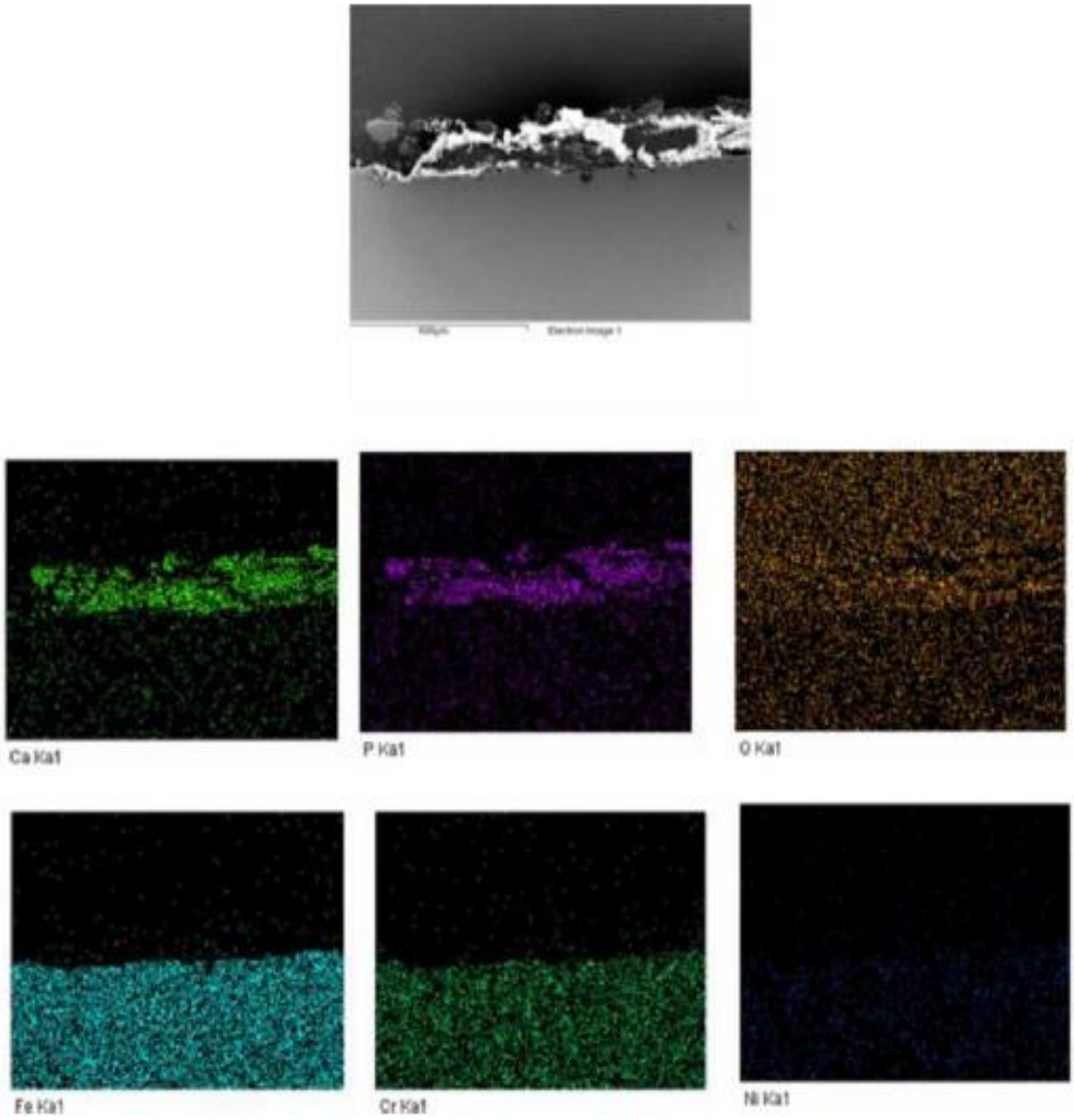

Figure 2.20. Cross-section morphology of HA-TiO_2 coating and EDS mapping

CHAPTER-III

PROBLEM FORMULATION

This chapter presents a brief introduction to the research and outline of the report. On the basis of introduction and literature review, research gaps have been identified and in order to fulfill these gaps, research objectives have been finalized.

3.1. Gaps in Literature

From the study of exhaustive literature survey, following research gaps have been identified:-

1. The earlier studies on surface modification of Ti-6Al-4V and SS-316L biomaterials by plasma spraying technique have been reported in this area.
2. Surface modification of biomaterial β-Phase Titanium alloy by plasma sprayings has been not reported yet. From the available literature, it can be seen that a comprehensive knowledge of plasma spraying of β-Phase Titanium alloy with a wide parametric range is lacking.
3. Analysis of the machining parameters that contribute to the biocompatibility of Ti alloy such as Coating Layer Thickness (CLT), Surface hardness (HV), Adhesion Strength, Wear resistance, Corrosion resistance, Surface Crack density (SCD) and Surface roughness (Ra) needs to reinvestigate & re-establish the facts.
4. The role of nano-scale surface roughness on biological response in terms of bone in-growth (Osseointegration) on the treated surface of β-Phase Ti alloy by plasma spraying technique have not been attempted yet.
5. There is a lack of information in the existing literature regarding optimization of plasma spraying process parameters for machining of titanium alloys.

3.2. Proposed Research and Problem formulation

β-Phase Ti-Nb-Ta-Zr titanium alloys started to gain much popularity due to their excellent specific strength, lower modulus (55 GPa), superior tissue compatibility, and

higher corrosion resistance. Titanium (Ti) osseointegration is critical for the success of orthopaedic implants. The surface modification of implant material is required to improve the biocompatibility and to make surface active so that bone in-growth or osseointegration takes place. Further, several coating techniques have been exhaustively used for the deposition of HA on metallic implants which includes: micro-arc oxidation, sol-gel, electrolytic deposition, electrochemical anodic oxidation, sputtering ion coating, physical vapour deposition, electric discharge machining, plasma spray, etc. Among these, plasma sprays a well-established deposition technique has been widely used for the deposition of HA on Ti-based implants. Nevertheless, as per the guidelines of the Food and Drug Administration (FDA), USA, the plasma spray technique is the only clinically approved due to its excellent deposition rate and compact coating formation in contrast to other methods [155].

As per the literature and best of the author's knowledge, there is no study available that reported the modification of Ti-Nb-Ta-Zr alloy using plasma spray deposition PSD, which is the novelty of research work. This research gap attracts the interest of authors to investigate the modification of β-phase alloy Ti-35Nb-7Ta-5Zr (*β-TNTZ)*, by depositing a composite coating of *HA/TiO_2* through PSD process to improve anti-corrosion and biological performances. Therefore, the potential of the plasma spray process to deposit a composite coating of *HA/TiO_2* on *β-TNTZ* for the *hip-stem* has been analyzed. The current research also presents the insight into the effect of *TiO_2* reinforcement (15 and 30wt. %) in *HA* on the microstructure, morphology, mechanical properties, corrosion resistance, and bioactivity of *HA/TiO_2* coated *β-TNTZ* alloy.

3.3. Research Objectives

After an exhaustive literature survey, following objectives have been selected to fill the research gaps for the present research work:

1. Fabrication and characterization of β-Phase Ti alloy by vacuum arc melting process for orthopaedic application. To determine the mechanical properties yield strength and elastic modulus of β-Phase Ti alloy and compare them with those of commercially available material like Ti and AISI 316-L medical steel.

2. Surface Modification of β-Phase Ti alloy by plasma spraying technique. Experimental investigation on the deposition of biomimetic composite layer of HA-TiO_2 on β-Phase Ti alloy. The experimentation should enable the variation of the composition of biomimetic composite layer e.g. ration of HA and TiO_2.
3. To study the surface characteristics of modified surface by plasma spraying technique. The surface integrity will be evaluated by examining the Surface roughness (SR), coating layer thickness (CLT), elemental and phase composition by scanning electron microscope (SEM), TEM, and X- ray diffraction (XRD).
4. To study the surface properties such as adhesion strength, Surface hardness (HV), Corrosion and Wear resistance of modified surface by plasma spraying technique.
5. To determine the effect of plasma spray deposition on the corrosion-fatigue performance of β-Phase Ti alloy and compare them with those of commercially available material like Ti and AISI 316-L medical steel.
6. To evaluate the biological response of plasma spray treated β-Phase Ti Implant by Cell Culture test (In-Vitro). The biological response will be determined in terms of osteoblasts response. Osteoblasts response will be measured by cytotoxic effect, cell adhesion, cell proliferation and differentiation by seeding human osteoblasts (HOS) cells on the modified surface.

3.4. Research Design and Methodology

1. The β-Phase titanium alloy (Ti-Nb-Ta-Zr) will be fabricated by vacuum arc melting process. The β-Phase titanium alloy (Ti-Nb-Ta-Zr) will be characterized in terms of mechanical properties and microstructure point of view.
2. Surface Modification of β-Phase Ti alloy by plasma spraying technique. The plasma spraying technique is available at Metallizing Equipment Co. Pvt. Ltd., Jodhpur. Experimental investigation on the deposition of biomimetic composite layer of HA-TiO_2 on β-Phase Ti alloy. The effect percentage composition of HA and TiO_2 on the surface properties will be studied.

3. Process performance will be measured in terms of Surface roughness (SR) at different scale, recast layer thickness, surface hardness, corrosion and wear resistant surface.
4. The relationship will be established between the various input and output process parameters using design of experiment technique and output parameter will be optimized by Taguchi's methodology.
5. The coating surface will be analyzed in order to understand the surface topography using various techniques like SEM, TEM, XRD, Surface hardness tester and Surface roughness tester.
6. The *In-vitro* corrosion resistance of coatings was assessed using electrochemical potentiodynamic polarization test using Potentiostat/Galvanostat (Series PGSTAT-12, GAMERY) in simulated body fluid (SBF).
7. The bioactivity of the coated surface was accessed by determining the hydrophilic/hydrophobic nature of surfaces, using a wettability test.
8. Then the biological evaluation of plasma spray surface of β-Phase Ti implant in terms of bone in-growth (osseointegration) will be studied by Cell Culture test (In-Vitro). The biological response will be determined to measure the obsteoblasts response in terms of cytotoxic effect, cell adhesion, cell proliferation and differentiation by seeding human osteoblasts (HOS) cells on plasma spray surface.

Figure 3.1. shows the flow chart of methodology adopted for the experimentation, testing, and analysis.

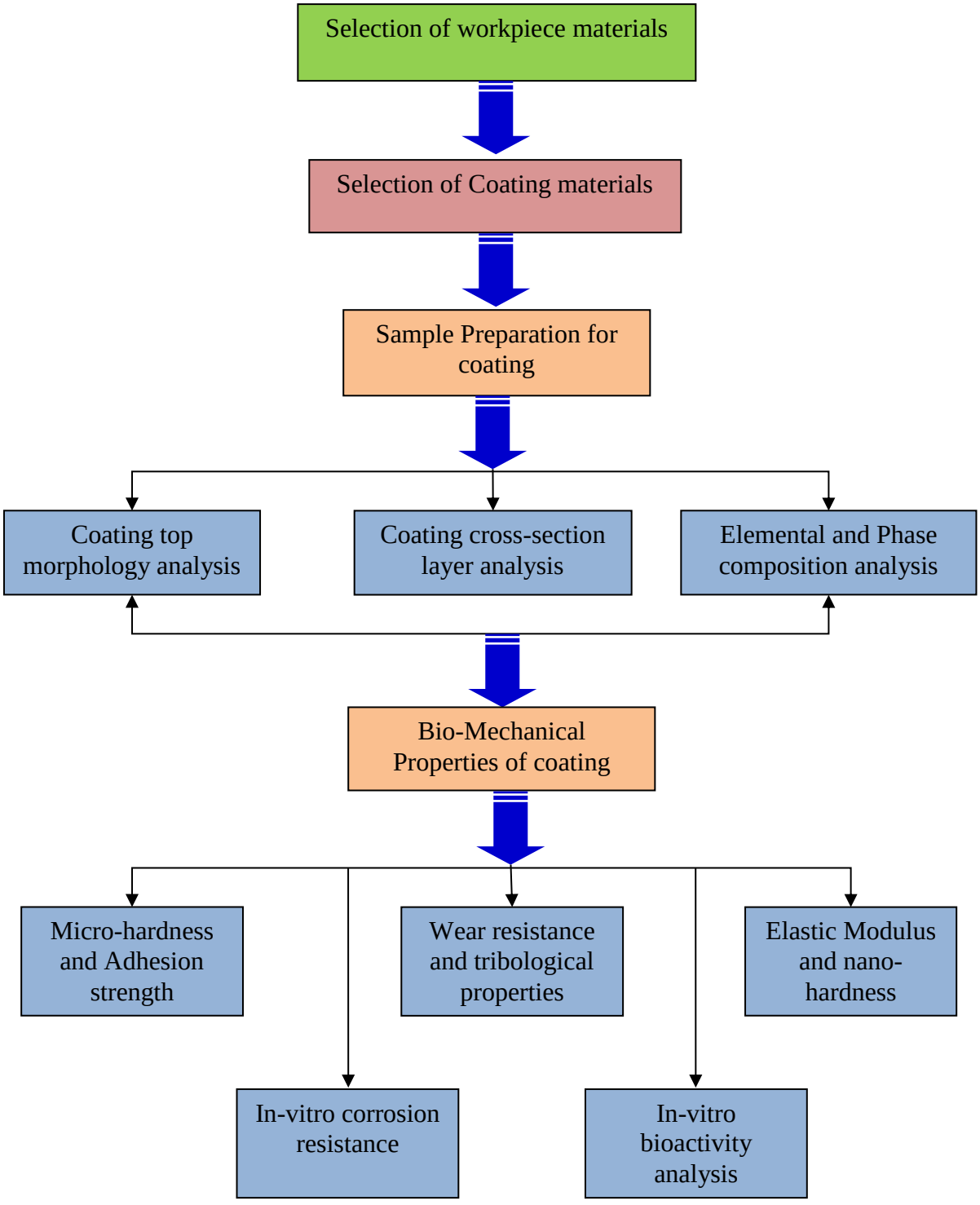

Fig. 3.1. Flowchart of methodology adopted for coating and analysis

CHAPTER-IV

EXPERIMENTATION AND CHARACTERIZATION

This chapter covers the details of the materials, methods, experimentation and characterization.

4.1. Selection and Development of Workpiece/implant Materials

For this study, a new class of β-phase Ti-35Nb-7Ta-5Zr has been used as a substrate material for coating. The β-phase Ti-Nb-Ta-Zr alloy has been developed using vacuum-arc melting process. The *β*-phase Ti alloy is the best biomaterial used for fabrication of implants in comparison to other metallic biomaterialss like SS-316L and Ti-6Al-4V alloy, because of its low elastic modulus (~ near the bone), excellent mechanical properties and biocompatibility. Table 4.1 shows the properties of β-phase Ti-35Nb-7Ta-5Zr in comparison to other metallic biomaterials.

Table 4.1. Properties of *β*-Ti alloy compared to human bone, Ti-6Al-4V, and SS-316L

Properties	***β*-Ti Alloy**	**Ti-6Al-4V Alloy**	**SS 316L Alloy**	**Bone Alloy**
Hardness	285 HV	349 HV	218 HV	-
Density (Kg/m^3)	5700	4430	8000	2000
Elasticity Module (GPa)	55	110	210	15-20
Strength (MPa)	560-950	960-970	485	150
Poisson's ratio	0.33	0.34	0.3	0.3
Melting Point (ºC)	1765	1660	1400	-
Specific Heat (J/Kg ºC)	450	526	500	-
Thermal Conductivity (W/m ºC) at 20 ºC)	9.8	6.7	21.5	-
Coefficient of expansion (10^{-6} ºC^{-1})	9.03	8.6	14.9	-

Vacuum arc melting is a secondary melting process for production of metal ingots with high chemical and mechanical homogeneity for great demanding applications like Biomaterial, aerospace industries. In this process, the heat source used is a standard tungsten Inert gas welding unit. Heating is done by an electric arc struck between a tungsten electrode and metals placed in the crucible in an inert atmosphere. Repeated melting is performed to improve the homogeneity of the alloy. The β-phase Ti-Nb-Ta-Zr alloy was re-melted 4-times using an electric arc to ensure the homogeneity. Figure 4.1 (a) and (b) shows the image of vacuum arc melting set-up and an as-cast ingot of β-Ti alloy, respectively. The β -phase Ti-35Nb-7Ta-5Zr alloy was subjected to heat treatment to enhance the mechanical properties and wear resistance. Figure 4.1 (c) shows the cycle for the heat treatment process.

For microstructure, elemental, and phase composition examination, the samples of size 10×5 mm were cut from the as-developed ingot through wire-cut electric discharge machining process (Model Ecocut, Electronica, India). To investigate the micro-structural properties, the workpiece samples were well polished using adequate polishing methods and then samples were etched with Kroll solution (2 ml HF, 5 ml HNO_3 and 93 ml H2O) for approximately 15s. The microstructure and elemental composition of the as-developed β-TNTZ (β-$TNTZ_{ht}$) alloy has been studied using FE-SEM coupled with EDS (7600F, JEOL, Japan).

The micro-hardness was determined by Vickers micro-hardness tester (HM-125, Mitutoyo, Japan) using a 200g load for holding time 15s. The specimen's blanks for tensile were fabricated from the sheet material of β-phase Ti alloy (Ti-Nb-Ta-Zr). Tensile testing was conducted on 100KN Universal Testing Machine (UTM, BIS), as can be seen in Figure 4.2. All specimens used in this study for tensile testing were conventional tensile ''dog-bones'', fabricated according to the dimensions consistent with ASTM Standard E8-04 (load bearing cross-section = 2 mm × 1.5 mm, total length 80 mm), as can be seen in Figure 4.3. Tensile tests were carried out with a strain rate of 10^{-4} s^{-1}. Stress v/s strain graph was plotted.

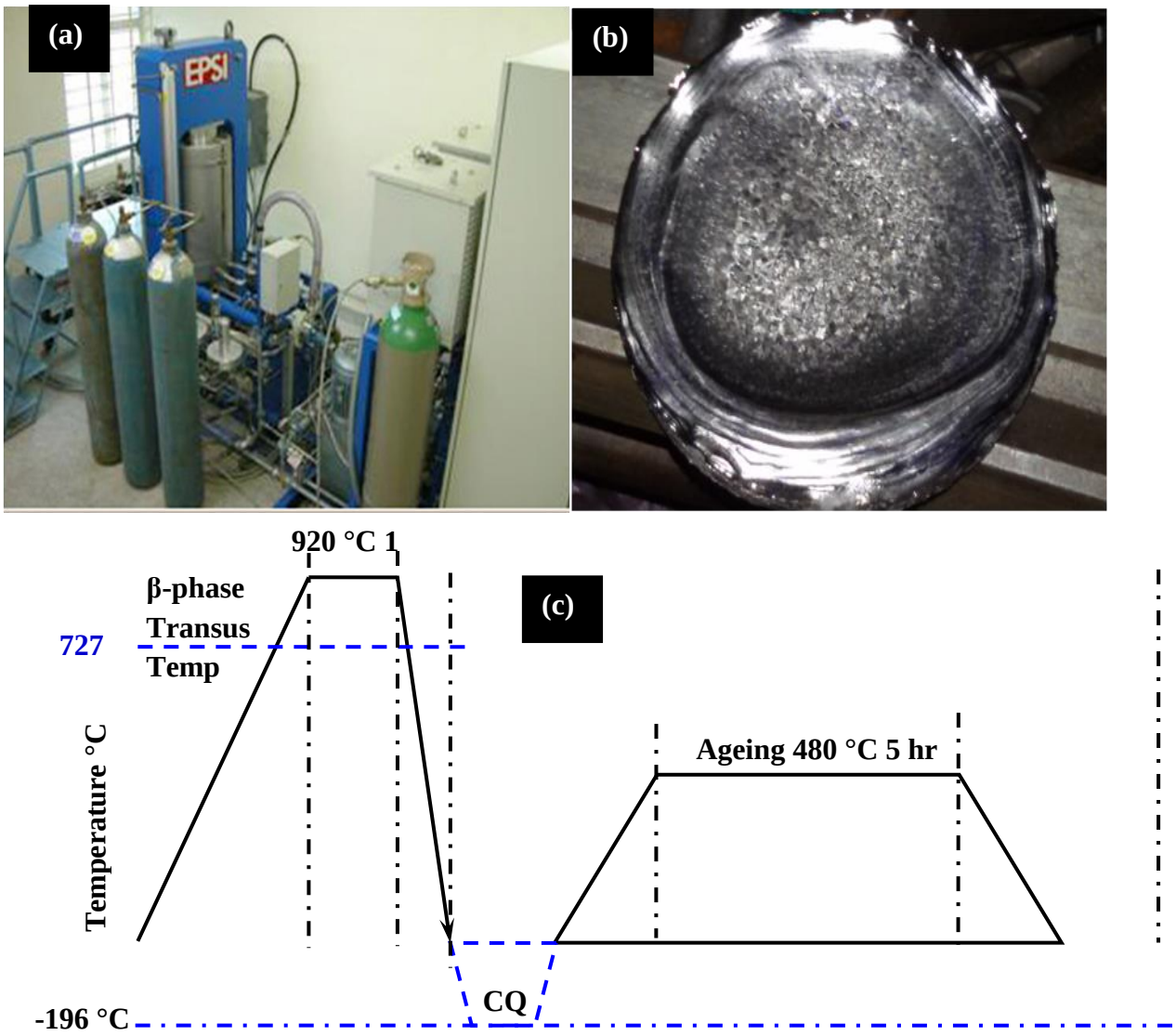

Figure 4.1. (a) Photograph of vacuum arc melting set-up and (b) as-casted workpiece material, (c) Heat treatment cycle

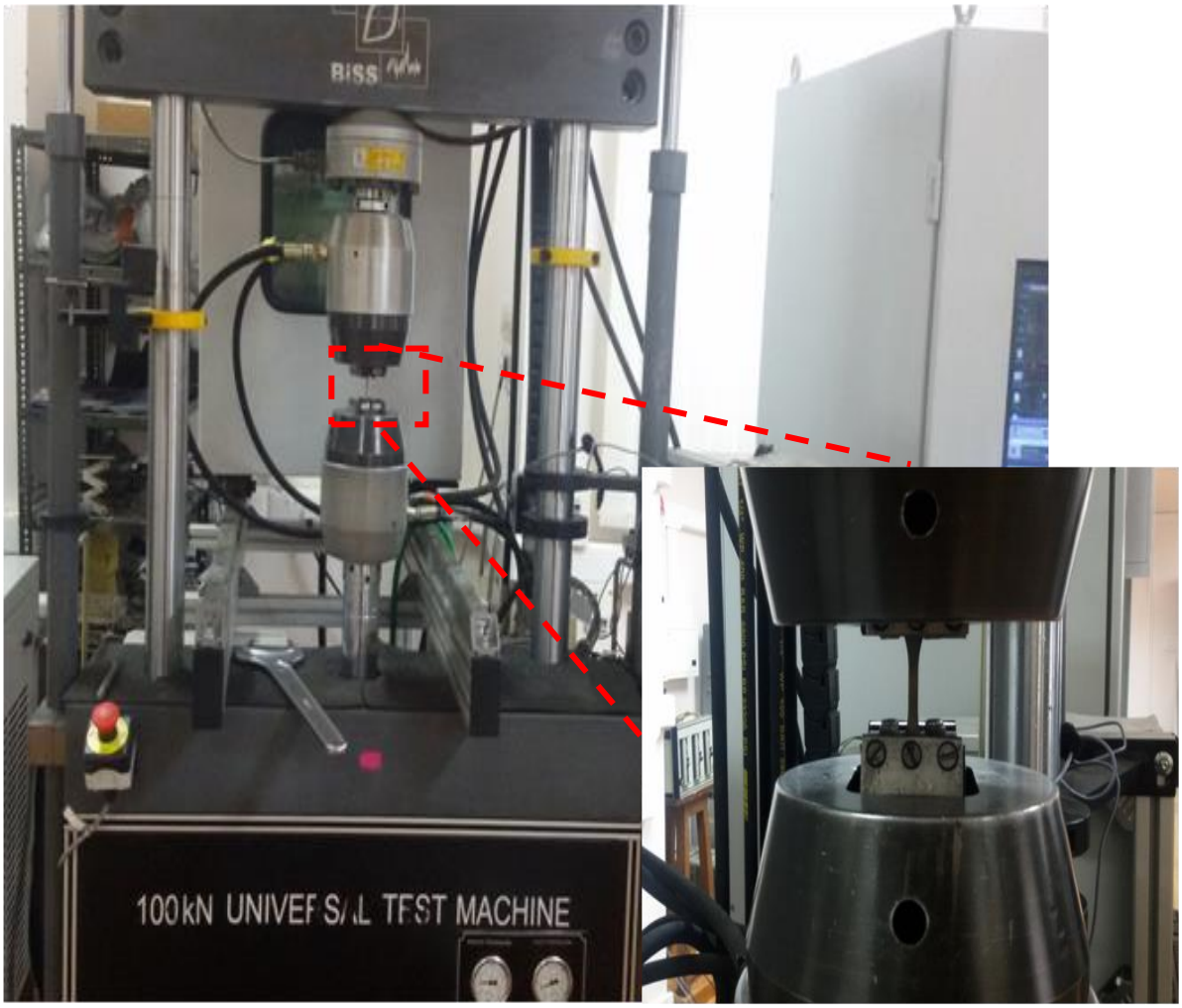

Figure 4.2. 100KN Universal Testing Machine (IIT, Kanpur)

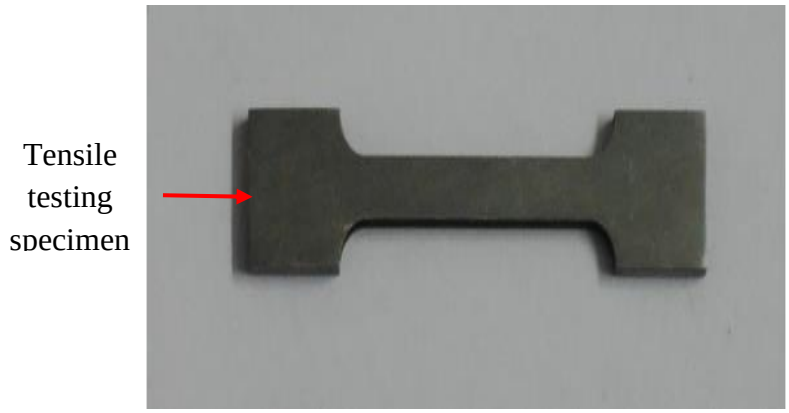

Figure 4.3. Dog-bone-shaped sample for tensile

4.2. Selection of feedstock and Coating Materials

High purity (> 98%) HA powder (10-25 µm) and TiO_2 powder (20-50 µm) were procured from Sigma Aldrich, US. Figure 4.4 presents the morphology and EDS spectrum of as procured powders.

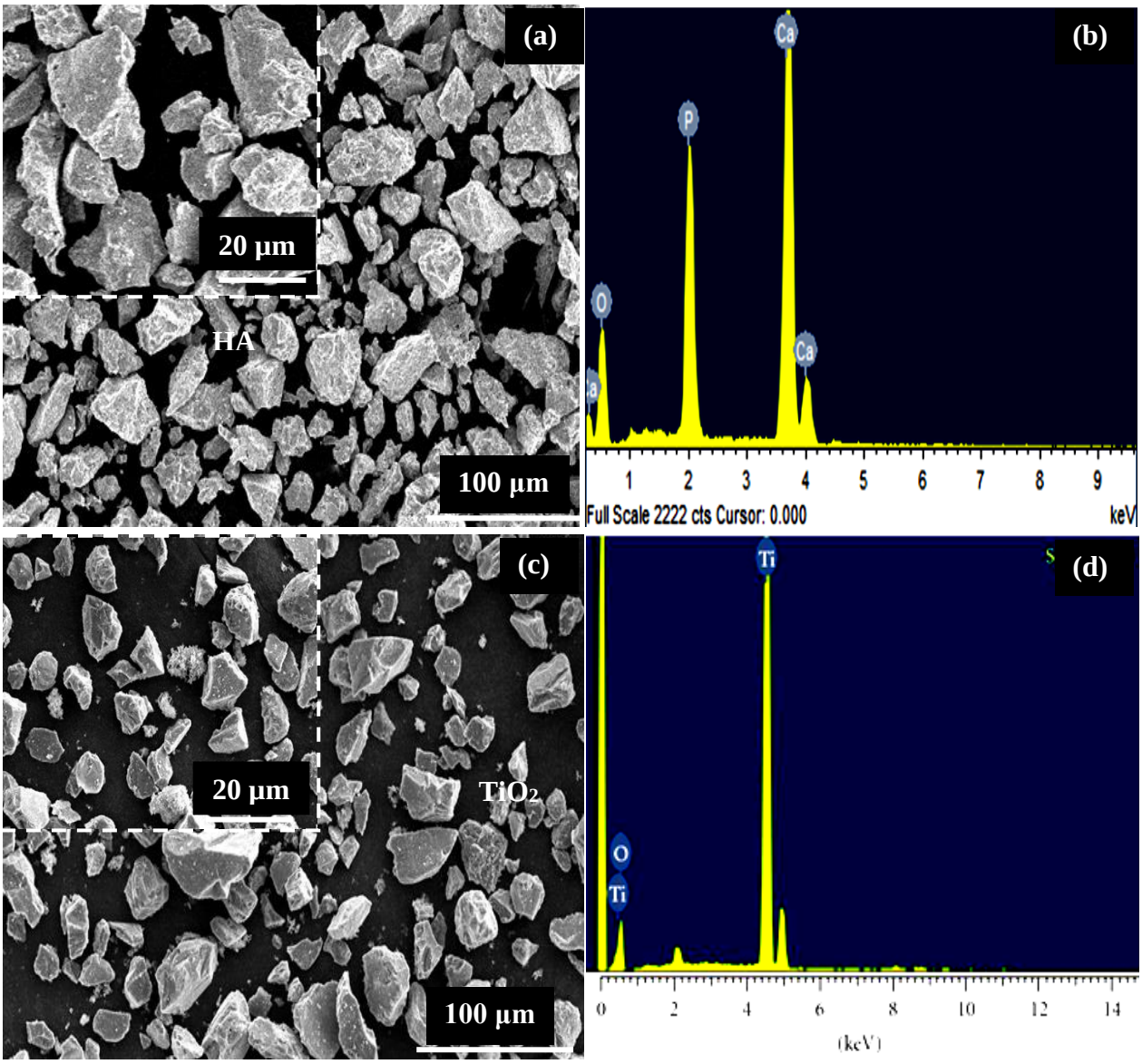

Figure 4.4. SEM image and EDS spectrum of raw powder before Mechanical Alloying (a) HA and (b) TiO_2

Before plasma spraying, HA and TiO_2 were mixed in the appropriate ratio. Figure 4.5 shows the SEM-morphological and EDS spectrum of alloyed powder mixture of HA-

TiO_2. After mixing, the powder of pure-HA and mixture of HA-TiO_2 were used as feedstock for coating on the β-Ti substrate specimens.

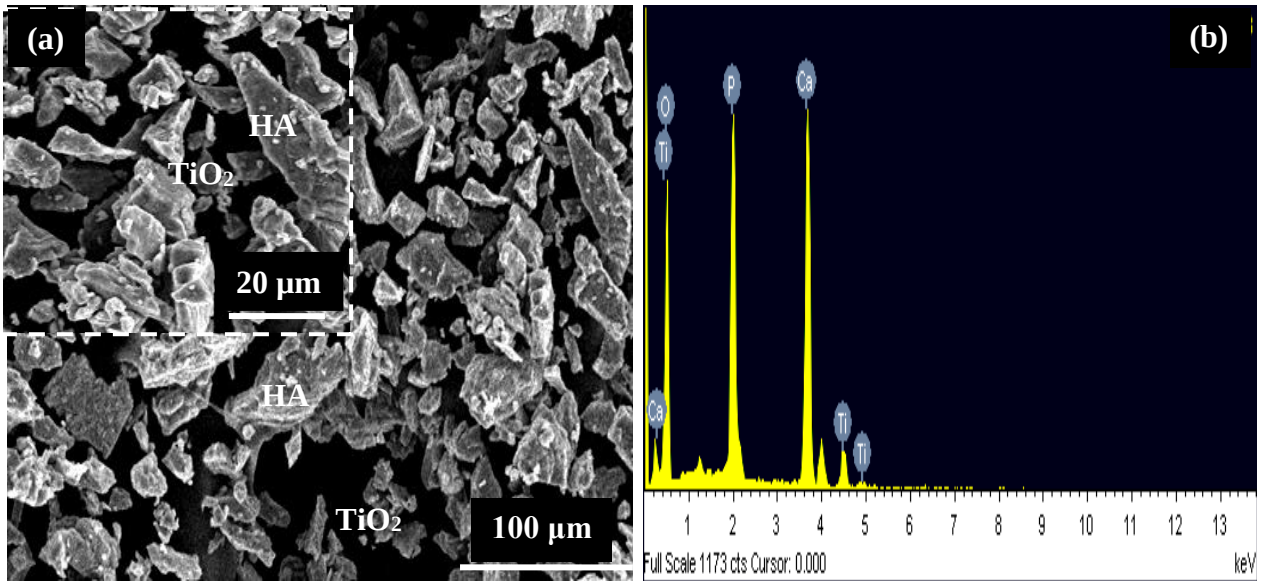

Figure 4.5. (a) SEM micrograph and (b) EDS spectrum of powder mixture of HA-TiO_2

4.3. Experimentation and set-up

The coating of HA and HA-TiO_2 powder mixture has been carried out using the plasma spray deposition technique. Cylindrical shape specimens (ø 25.4 × 38 mm in length) were prepared for coating process. Before coating, the substrate surface was grit blasted with alumina (Al_2O_3) to achieve the roughness (4.5 µm) on substrate surface. After that, the specimen's surface was cleaned to remove the loose alumina from the blasted-surface. The plasma was generated using a torch and powder was suspended in the plasma. The experimental set-up of plasma spray coating technique is shown in Figure 4.6. The HA and TiO_2 were mixed in the appropriate ratio as per table 4.2. The high velocity plasma at high temperature partially and fully melts the powder particles. The powder particles in semi-molten and molten form deposited on the workpiece surface and makes mechanical interlocking. The schematic representation of the depiction of coating via plasma spray deposition is shown in

Figure 4.7. Table 4.3 presents the TiO_2 ration in HA-matrix used for the deposition of HA/TiO_2 composite coating.

Figure 4.6. Experimental set-up of plasma Spray Deposition process

Table 4.2. Plasma Spray Parameters

Spraying Parameters	Value
Primary Gas Flow (Argon)	30, 35, 40 NLPM
Secondary Gas Flow (Hydrogen)	2.0 NLPM
Voltage	65 volt
Current	500Amp
Feed rate	32, 36, and 40 g/min
Spray Distance	100 mm

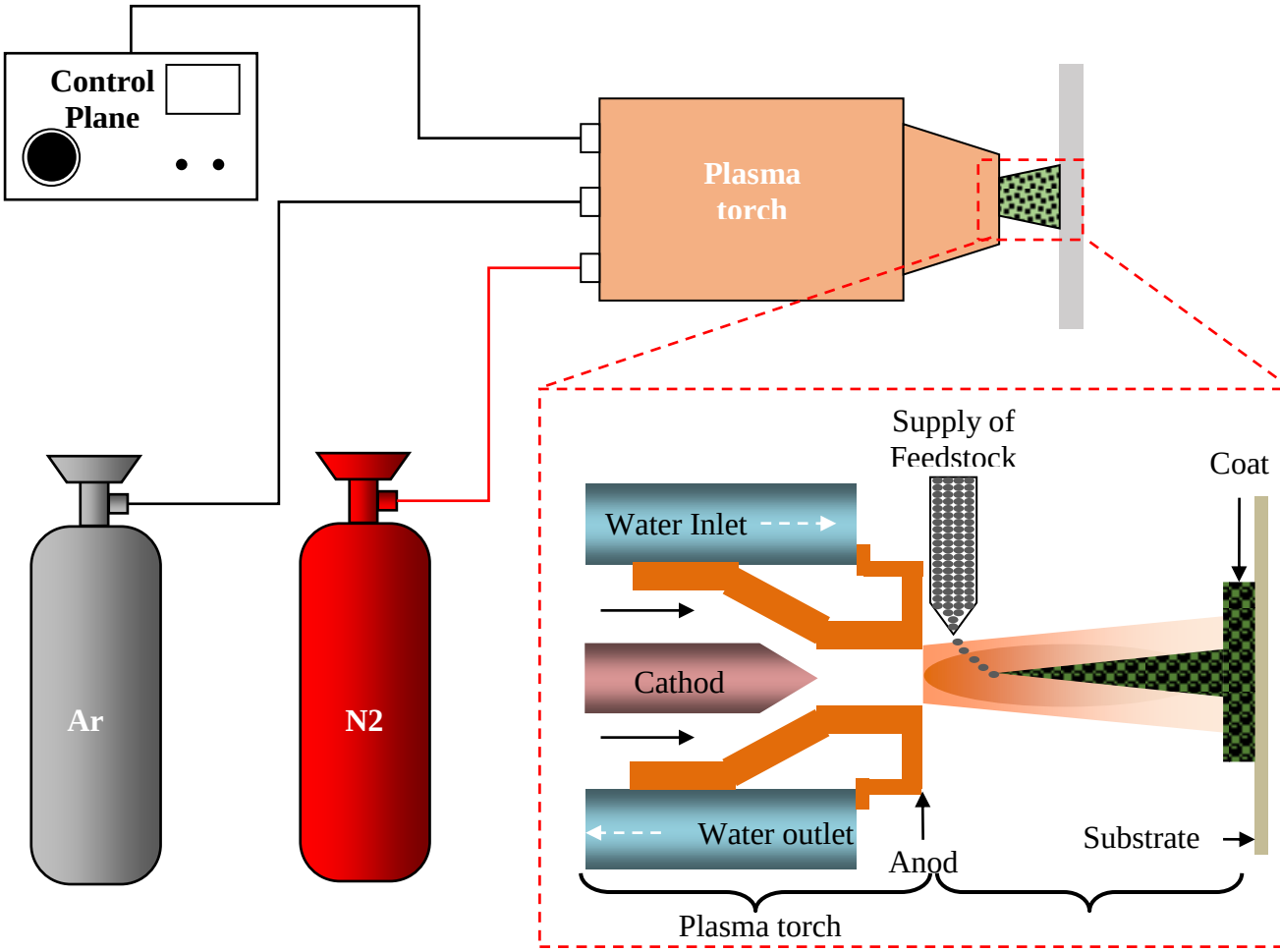

Figure 4.7. Schematic representation of Plasma Spray Deposition process

Table 4.3. Coating feedstock for PSD

Feedstock	Percentage weight (%wt.)	
	HA	TiO_2
HA	100	0
HA-T_x	85	15
HA-T_y	70	30

In order to examine the effect of process paramters such as feedstock compoistion, gas flow rate, and powder feed rate on the coating out put charetercticss such as coating surface hardness and adhesion strength was studied. In order to reliable results, the design of experiment (DOE) study was planned according to input process

paramters and their level. Table 4.5 shows the input process paramresr and their level to the experimentation.

Table 4.4. Input process parameters and their levels

Parameters	Levels		
	L-1	L-2	L-3
Reinforcement of TiO_2 in HA (A)	0	15	30
Gas flow rate (B)	30	35	40
Powder feed rate (C)	32	36	40

4.4. Characterization of surface morphology

The microstructure, elemental, and phase distributions of the PSD based coated substrates have been investigated through FE-SEM (make: JEOL-7600F) coupled with EDS and XRD. Further, the coating cross-section has been studied to find out the thickness of the deposited coating material, as per [182-183]. The thickness of the coating layer was measured by taking the cross-section of the coated samples. For this, the coated specimens were cut using a low-speed diamond cutter and subsequently grounded using 1/0, 2/0, 3/0, 4/0, and 5/0 graded emery paper. Finally, the polishing of grounded specimens was carried out using the diamond paste to the obtained mirror-like super finished surface. After that, the polished cross-section of the coated surface was investigated under FE-SEM to examine the coating thickness [184]. Figure 4.8 shows the image of FE-SEM coupled with EDS. The EDS mapping scan was carried out to analyze the dispersal of coated elements in the deposited layer and distribution of elements through the thickness. The analysis was carried out at 15 KeV. The phases composition of before and after coating were investigated by X-ray diffraction (XRD) with CuK radiation at an incident angle range of 20–80º. Figure 4.9 shows the image of XRD-machine.

Figure 4.8. Field Emission Scanning Electron Microscope (FE-SEM) with EDS (Brand: HITACHI, Model: SU8010)

Figure 4.9. XRD equipment for Phase Composition Analysis, Brand: X'pert-PRO, PANalytical, Almelo, The Netherlands

4.5. Structural Porosity of Coating

The coating porosity was determined through image analysis using computerized optical microscope (Zeiss Axiovert 200 MAT), fitted with imaging software (Zeiss Axiovision (Release 4.1)), which is well-matched with ASTM B276 standard. The porosity levels were measured by capturing an image of the coating cross-section and differentiating between porosity and bulk coating by grey level areas. The analysis of the grey areas between the pores and bulk coating gives percentage porosity. A total of 10 cross-section pictures were analyzed for each coating to avoid the overlap between two locations and determine the porosity levels.

4.6. Surface Micro-hardness (MH)

For the microhardness measurements, the test surfaces were prepared using adequate grinding and polishing methods according to the ASTM standard (ASTM-E384-11). The samples were sectioned with a low-speed precision saw, and the sectioned surfaces were polished with an emery paper of 220, 600, 800, 1200, or 2000 grade. Then, the samples were mirror-polished using a diamond paste on a napped cloth. The cross-sectional surface of the samples was examined for the microhardness measurements that were conducted on a Vickers hardness tester (Mitutoyo HM-125). An indentation load of 2.45 N was applied with a holding time of 10 s. Five hardness readings were recorded for each sample in a straight line from the recast layer to the base material. Figure 4.10 (a) and (b) shows the microhardness equipment and well-polished cross section surface of the sample for microhardness measurements, respectively. Figure 4.11 shows the Schematic representation of indentation mark of diamond indenter tip for micro-hardness measurement.

Microhardness is the hardness of a material gauged with instruments using small indenters. Therefore, a lower amount of force is applied relative to the standard measuring instruments, allowing measurements on thinner sheets or smaller test materials that may not respond accurately to measurements conducted with standard instruments.

F= Load in kgf

d = Arithmetic mean of the two diagonals, d1, and d2 in mm

HV = Vickers hardness

$$HV = \frac{2F\ Sin\ \frac{136°}{2}}{d^2}$$

$$HV = 1.854\frac{F}{d^2}$$

When the mean diagonal of the indentation has been determined the Vickers hardness may be calculated from the formula, but is more convenient to use conversion tables.

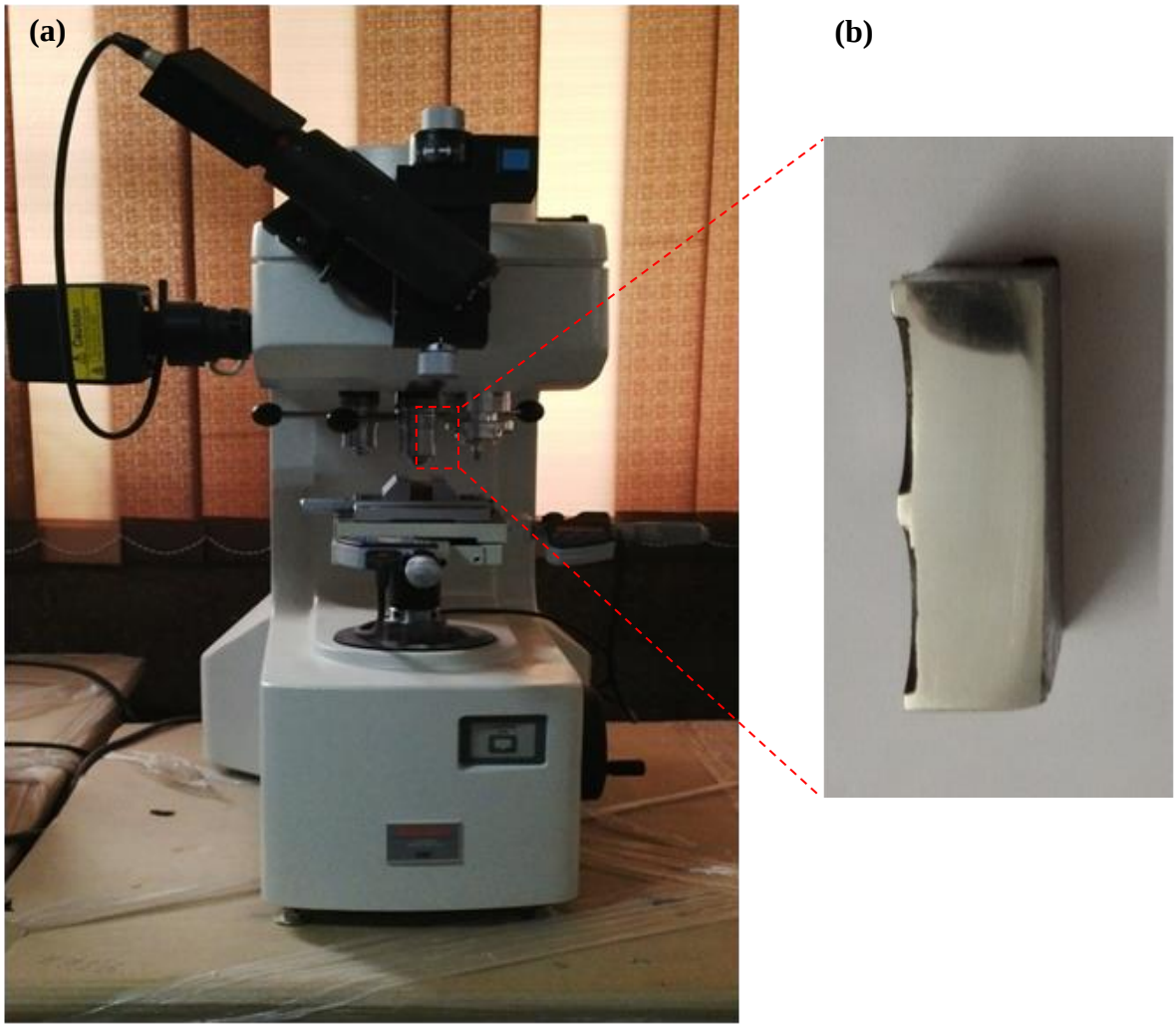

Figure 4.10. (a)Mitutoyo microhardness tester and (b) well-polished cross section surface of the sample for microhardness measurements

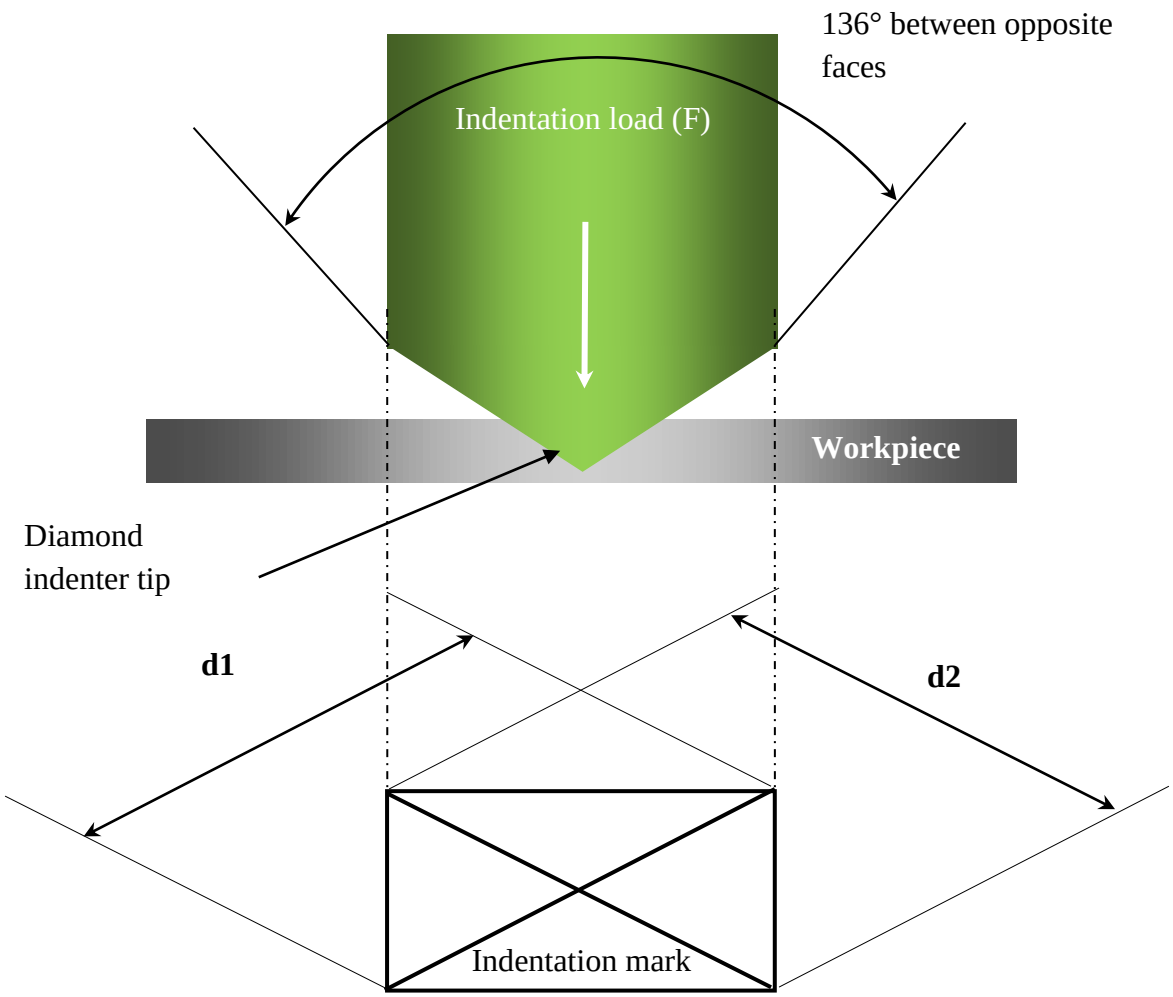

Figure 4.11. Schematic representation of indentation mark of diamond indenter

4.7. Elastic Modulus Analysis

The bio-mechanical properties, such as nano-hardness, elastic modulus, and adhesion strength, have been investigated. The hardness and elastic modulus of the coating was measured by nano-indentation technique. For this, well-grounded and polished cross-sections were used for making an indentation [184]. The samples were sectioned with a low-speed precision saw, and the sectioned surfaces were polished with an emery paper of 220, 600, 800, 1200, or 2000 grade. Then, the samples were mirror-polished using a diamond paste on a napped cloth. The indentations were conducted across the cross-section of coated surface. The tests were performed using the Hyistron TI-950 indentation system using Berkovich indenter using 1000 μN with dwell time 2s. Both characteristics were determined by the Oliver-Pharr method, as reported previous

study [185-186]. Figure 4.12 shows the Hyistron TI-950 indentation system available at IIT, Ropar.

Figure 4.12. Hyistron TI-950 indentation system available at IIT, Ropar

The hardness of the composite was calculated using eq. 4.1:

$$\text{Hardness (H)} = \frac{P_{max}}{A} \quad (4.1)$$

Where, P_{max} is the maximum applied load and A is the projected contact area of the indenter.

The elastic modulus (E) of the composite was calculated using eq. 4.2:

$$\frac{1}{E_r} = \frac{(1-\upsilon^2)}{E} + \frac{(1-\upsilon_i^2)}{E_i} \quad (4.2)$$

Where, E_r and υ are the reducing elastic modulus and possion's ratio of the tested material. v_i and E_i are the possion's ratio and elastic modulus of the indenter. E_r is calculated according to eq. 4.3:

$$E_r = \frac{1}{2\beta}\frac{\sqrt{\pi}}{\sqrt{A}}\frac{dP}{dh} \quad (4.3)$$

Where, β is the geometrical factor to correct non-symmetrical indenter shape (For Berkovich indenter β = 1.034). Slope (dP/dh) is calculated from eq. 4.4:

$$h_c = h_{max} - \varepsilon\frac{P_{max}}{dP/dh} \quad (4.4)$$

Where, h_c is contact depth, h_{max} is maximum deflection, and ε is constant (For Berkovich indenter ε = 0.75).

4.8. Adhesion Strength Analysis

Standard tensile adhesion test (ASTM C633), which was especially designed for thermal spray coatings, was used to evaluate the bond strength of as-sprayed and heat treated reinforced HA coatings. Each test specimen consists of two identical cylindrical Ti-6Al-4V stubs, one with coating on the surface and other without (Loading rod). Special adhesive glue (DP-460 Epoxy Adhesive, 3M USA) with a maximum adhesive strength of 40 MPa was used to attach the uncoated stubs with coated ones. The facings of the loading rods were grit blasted to enhance the adhesion strength. The two stubs were then placed into V groove gravity fixture for proper alignment and one solid steel cylinder (1 in. diameter and 2 in. long) was placed on the top of two assembled stubs to keep them in compression during the glue curing for 12 h at room temperature. The test was performed using tensile machine (Zwick Roell, Singapore) in which lower arm was fixed and load was applied with movable upper arm. A constant cross-head speed of 1 mm/min. was used to apply the tensile load. The samples having nearly uniform coating thickness of about 190 µm were tested for bond strength test. The bond strength was calculated by dividing the load at which the coating was separated from the substrate to the cross-sectional area. Three samples were tested for each condition and the average bond strength coupled with standard deviation was recorded.

4.9. Corrosion Testing

The electrochemical analysis was performed to assess the corrosion rate of the non-machined and machined implant surfaces via potentiodynamic polarization

measurements. The tests were performed using an electrochemical workstation (Potentiostat/Galvanostat Series PGSTAT-12, Autolab, Kanaalweg, The Netherlands), as can be seen in Figure 4.13. Ringer's solution was used as an electrolyte to simulate human body fluid conditions at pH 7.2. The chemical composition of the solution was shown in Table 4.6. Before performing the corrosion tests, the specimens were immersed in Ringer's solution for 24 h for stabilization. All experiments were performed at (37 ± 1)°C, which corresponds to the normal temperature of the human body. The exposed area of the samples in the Ringer's solution was 1 cm^2. The test material was used as the working electrode, graphite rod was used as the counter electrode, and Ag/AgCl electrode was used as the reference electrode. Potentiodynamic polarization curves were obtained at a scan rate of 1 mV/s from −0.1 V vs. the open-circuit potential to the breakdown of passive region.

Table 4.5. Chemical composition of SBF solution

Sr. No.	Reagents used	Grams in 1000ml
1	NaCl	8.03
2	$NaHCO_3$	0.35
3	KCl	0.22
4	$K2HPO_43H_2O$	0.23
5	$MgCl_26H_2O$	0.31
6	$CaCl_2$	0.29
7	Na_2SO_4	0.07
8	$((HOCH_2)_3CNH_2)$	6.11
9	1MHCL	1-4 ml

Data were collected and analyzed on a computer equipped with NOVA software. The corrosion rate was determined using the Tafel extrapolation method. In the Tafel method, tangents are drawn on a plot of *E* (potential) vs. log *I* (current). Upon extrapolation of the tangents, the latter intersects at a point corresponding to the corrosion potential (E_{Corr}), which can then be correlated to the corrosion current (I_{Corr}) on the *x*-axis.

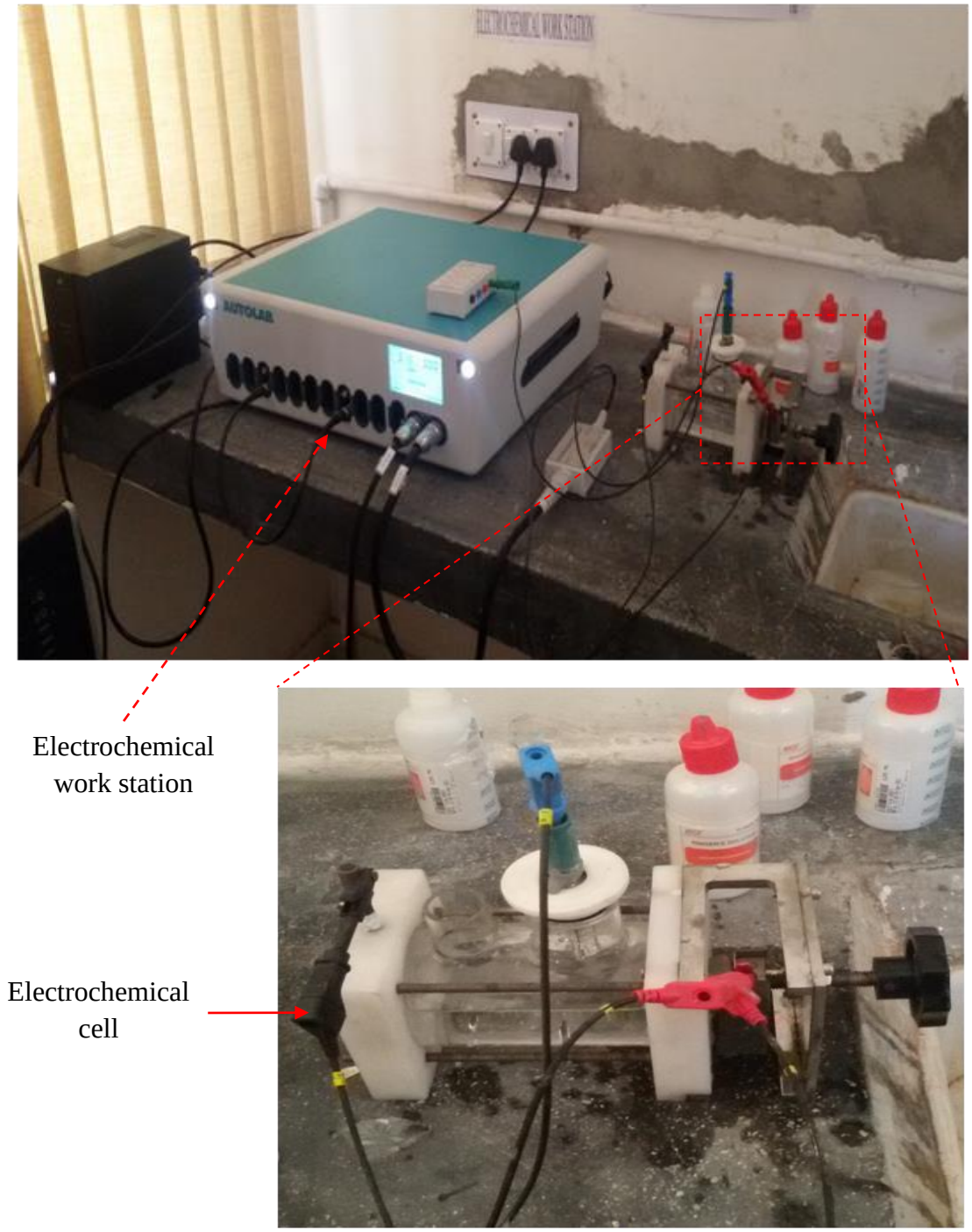

Figure 4.13. Photograph of electrochemical test rig for corrosion testing

4.10. Wettability test

The bioactivity of the coated surface was accessed by determining the hydrophilic/hydrophobic nature of surfaces, using a wettability test. The

hydrophilic/hydrophobic performance of coatings depends upon the water contact angle (º). Thin sheets of 10×10×2 mm^3 were fabricated at a different set of experiments. The drop shape analyser apparatus based on the sessile drop method was employed for the contact angle measurements with deionized waters as drops. A high-resolution CCD camera was used to capture the images during angle formation and tangent method to calculate the contact angle between the surface and drop. The measurements were repeated three times to calculate the average and to obtain the standard deviation.

4.11 In-Vitro Biocompatibility Analysis

In-vitro biocompatibility of the surfaces was evaluated using human osteoblastic cell line MG-63 [187-189]. The MG-63 human osteoblast-like cell line was procured from the National Centre for Cell Science (NCCS) (Pune, India), and used for biological evaluation of the non-coated and coated PSD surfaces. The cells were cultured in a T-25 flask containing Dulbecco's Modified Eagle Medium supplemented with 10% bovine serum and 1 vol.% penicillin (Invitrogen) in an incubator at 37°C and 5% CO_2 until confluent. Figure 4.14 shows the un-confluent cell (after 4 hours of cell incubation) and full confluent cells (after 4 days of cell incubation), respectively. The culture medium was replaced with fresh medium every third day. The β-Ti alloy samples were autoclaved and sterilized with ultraviolet radiation for 20 min in a biological hood before cell culture. After sterilization, the samples were inserted into a 12-well polystyrene multi dish. Confluent cells were seeded and cultured on plastic polystyrene (control) and β-Ti alloy plates at a cell density of 1×10^5 cells/cm^2. Initial attachment of the cells was evaluated after 8 and 24 h of culture. Cells were counted using a Countess Automated Cell Counter (Invitrogen) and a hemocytometer.

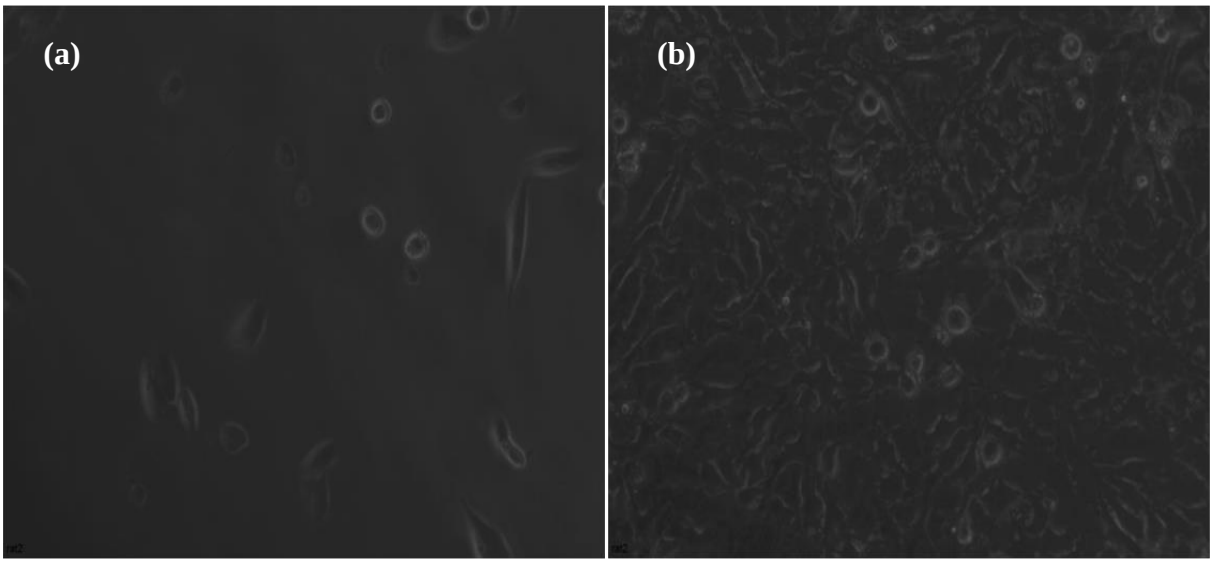

Figure 4.14. Optical micrographs of un-confluent and fully confluent cells

Cell proliferation was evaluated by MTT assay and measuring DNA content. The MTT assay was (3-[4,5-dimethylthiazol-2-yl]-2,5-diphenyltetrazolium bromide) assays were performed after the MG-63 cell was cultured on specimens for 1 day, 3 days, and 7 days. At the determined time point, the culture medium was removed, and the MTT reagent (50 mL/ well, M2128; Thiazolyl Blue Tetrazolium Bromide, Sigma-Aldrich) was added to the culture plate and incubated at 37ºC for 4 hours. Then, the MTT reagent was removed and dimethyl sulfoxide (50 mL) was added to each well to dissolve the formazan crystals. Results of the MTT assay were expressed as the optical density, which was measured at 570 nm using an enzyme-linked immunosorbent assay (ELISA) reader (ELx800; Biotek, Winooski, VT, USA). The DNA content was measured with a commercially available kit (Quant-iT^{TM} PicoGreen$^{®}$ dsDNA assay, Invitrogen, Carlsbad, CA). DNA assay is a method used to measure cell turnover and proliferation, hence an indicator of cell turnover in the presence or absence of a test material. DNA assay was carried out on the different surface treatment samples of β-phase titanium alloy as MG-63 cells were lysed at 3-time points (Days 1, 3, 7) using a freeze/thaw method which was described above in the previous section. Total DNA was assessed using a fluorometric assay incorporating bis benzimidazole (Hoechst 33258). A fluorescent effect is produced due to the interaction of the reagent with cell DNA. The fluorescence intensity is

proportional to the amount of DNA and thus the number of cells in the sample. The Mg-63 cells were trypsinized and placed into new wells. DNA was extracted at each time point using a freeze/thaw technique. Hoechst 33258 was allowed to react with the lysate and DNA standards (calf thymus DNA, Sigma) of concentrations 0, 0.31, 0.63, 1.25, 2.5, 5, 10, and 20 μg/ml in saline sodium citrate buffer (pH 7.0). Measurement of fluorescence was performed by using a plate Chameleon V (Hidex) and subsequently the DNA content was calculated from the standard curve. Cells were harvested as described above and 50 mL of lysed cell content were diluted with 50 mL of 0.05% Triton-X-100. Fluorescence measurements were obtained using a fluorescent multimode detector (DTX880, Beckman Coulter, Brea, CA) with reference to a standard.

Alkaline phosphatase is a membrane-bound enzyme and is used as a marker of osteoblast differentiation. In the current study, alkaline phosphatase (ALP) was performed on the different surface modification treatments to evaluate the differentiation of osteoblast cells on the surfaces. The assay was carried out with cell lysates collected at different time points (Days 1, 3 and 7) using the freeze/thaw cycle, in which MG-63 cells were trypsinized, counted and seeded at 1 x 10^6 per 50μl; the medium was replaced at 2-day intervals throughout the experiment. At each time point the plates were removed from the incubator and placed into a laminar flow cabinet, the media was discarded and the wells were gently washed with 1 ml PBS (Phosphate Buffered Saline, Serotec. UK) then 1 ml of distilled water was added to each well, then the plates were frozen for 15 minutes at –80°C and transferred to an incubator at 37°C for 20 minutes. Following each cycle, cells were thoroughly mixed. This freeze/thaw technique was repeated twice more. Subsequently, the cell lysate was frozen into small vials; such samples were used for the ALP activity measurements after 1, 3 and 7 days in culture, by adding 50 μl of each cell lysates from the test materials into appropriate 96 well plate and then the addition of 50 μl of substrate reagents solution. Glycine solution was prepared by dissolving 0.75 g of glycine powder into 90 ml of distilled water adjusted to pH of 10.3 and then the volume was made up to 100 ml. The substrate-agent was obtained with 20 mg p-nitrophenyl phosphate, 17 mg magnesium chloride hexahydrate, 40μl Triton-X 100

and made up to 5 ml with 0.1M glycine. A standard curve was prepared fresh by diluting of 200 mg p-nitrophenyl phosphate in 0.1M glycine solution (pH 10.3), to give a range of different concentration values of standards (50, 25, 12.5, 6.25, 3.125, 1.563, 0.782, and 0 μg/ml). 100 μl of each p-nitrophenol standards was then aliquoted into 96 well plate accordingly, and then the plates were placed on a shaker for 2 minutes and read at 0 and 20 minutes using Dynex plate reader at a wavelength of 410 nm. For cell differentiation alkaline phosphatase (ALP), osteocalcin and Osteoprotegerin activity assays were performed after 24 hrs of cell culture.

At given time points, the cultured samples were taken from the incubator, and the cells were fixed with 2.5% glutaraldehyde for 30 min, then washed three times with phosphate buffered saline solution, then dehydrated progressively in ethanol at varying concentrations of 30, 50, 70, 90, and 100% for 10 min. Then, the samples were dried for 24 h in a desiccator before gold sputtering for FE-SEM analysis of the samples. Figure 4.15 shows the photographs of cultured dried samples after fixation.

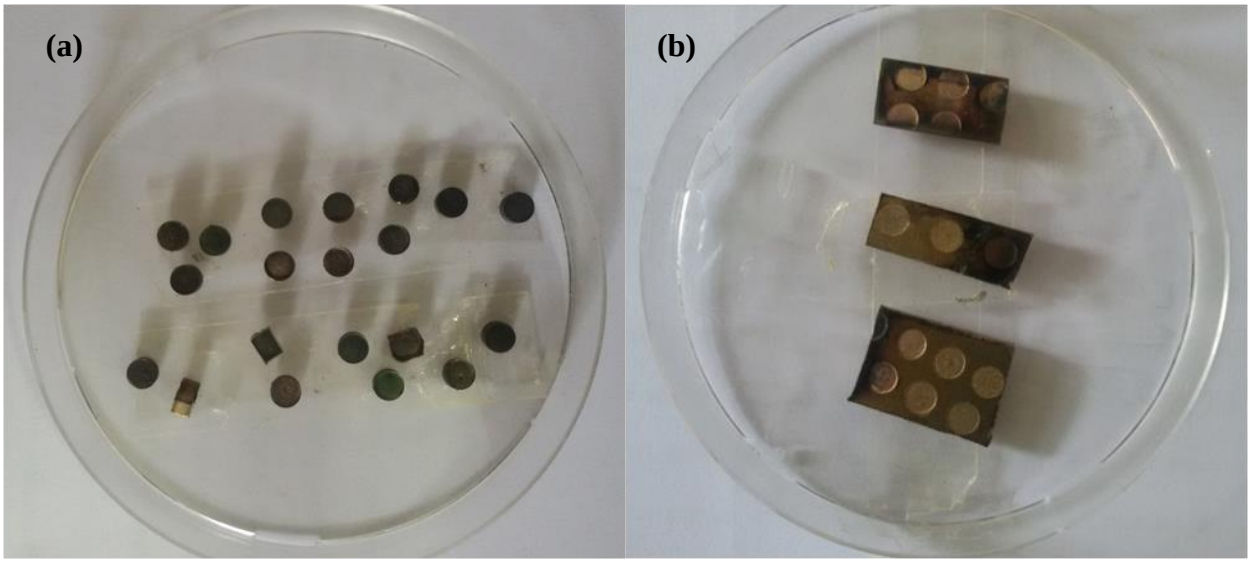

Figure 4.15. Photograph of cell cultured samples after fixation

4.11. Wear Testing

The wear resistance of HA and HA-TiO_2 coatings was evaluated by pin-on-disc wear test rig (DUCOM, Instruments Pvt. Ltd, Banglore, India). Figure 4.16 shows the experimental set-up of wear test rig. To perform wear test, a pin of ϕ 5 × 10 mm was

prepared from the coated samples. The pin was rubbed against Al_2O_3 abrasive based counter surface and sliding distance was taken 500 m. The sliding velocity for wear test was taken 0.1 m/s. The amount of specific wear rate K (mm3.N-1.m-1) and the coefficient of friction were determined. Worn surface morphology was evaluated by FE-SEM.

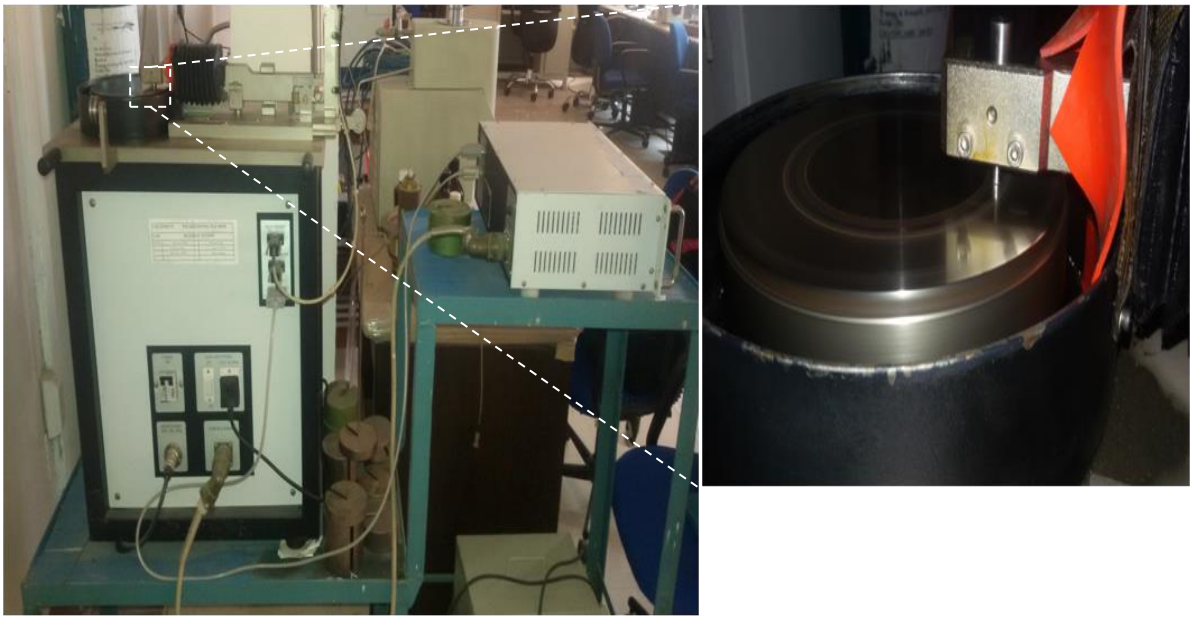

Figure 4.16. Photograph of wear test rig

4.12. Statistical Analysis

All data are presented as mean ± standard deviation (SD). All experiments were repeated three times to ensure the validity of the observations. The data were examined using analysis of variance (ANOVA) and the significant difference between groups was determined using the Student's *t*-test at a 95% confidence interval. A *p* value of less than 0.05 was considered as statistically significant.

CHAPTER-V

RESULTS AND DISCUSSIONS

This chapter covers the discussions of results and analysis in two phases. The first phase covers the discussion of the results and analysis of experimental work, in which the surface characteristics of β-phase Ti alloy after coating process has been investigated. A comprehensive and critical investigation of the microstructure, surface morphology, surface chemistry, surface roughness, coating layer thickness, surface crack density, and surface microhardness has been conducted to evaluate the efficacy of plasma spray deposition as a surface modification technique has been presented in this section. The second phase covers the effect of these surface characteristics on corrosion resistance, wear resistance, and bioactivity of the modified surface has been evaluated.

5.1. Microstructure and Mechanical Property Examination of β-Ti alloy

Figure 5.1 and 5.2 shows the microstructure, elemental-composition, phase-composition, and mechanical properties of β-TNTZ and β-$TNTZ_{ht}$ alloy, respectively. Figure 5.1 shows the microstructure, associated EDS-spectrum, and HR-TEM crystallography structure of as-developed β-TNTZ alloy. The micro-structural examination revealed that β-TNTZ alloy possessed metastable β-phase with coarse grain size ranging ~250µm, as reported elsewhere [190]. The crystallographic examination showed that β-TNTZ alloy consisted of metastable 'β' phase in the matrix, refer Fig. 5.1(a). The associated EDS spectrum of β-TNTZ alloy shows the significant peaks of Ti (52.94%), Nb (35%), Ta (7%), Zr (5%), and O (0.06%) elements confirm to the base elemental composition of the alloy, refer Fig. 5.1(b). From the crystallographic examination, it can be observed that as-developed alloy comprised β-phase.

Figure 5.2 shows the microstructure, associated EDS-spectrum, and HR-TEM crystallography structure of β-TNTZ alloy after heat treatment. The microstructure

was refined and grain size (100-150µm) was reduced significantly after heat treatment, refer Fig. 5.2(a). Furthermore, the heat-treatment process precipitated the 'α′ and nano-structured 'ω' phases, as observed elsewhere [191-192]. The associated EDS spectrum of β-TNTZ$_{ht}$ alloy indicated the peaks of Ti (52.79), Nb (35%), Ta (7%), Zr (5%), C (0.15%), and O (0.25%) elements, refer Fig. 3(d). The presence of the 'C' and 'O' elements was attributed owing to the cryogenic quenching, which further enhanced the mechanical properties.

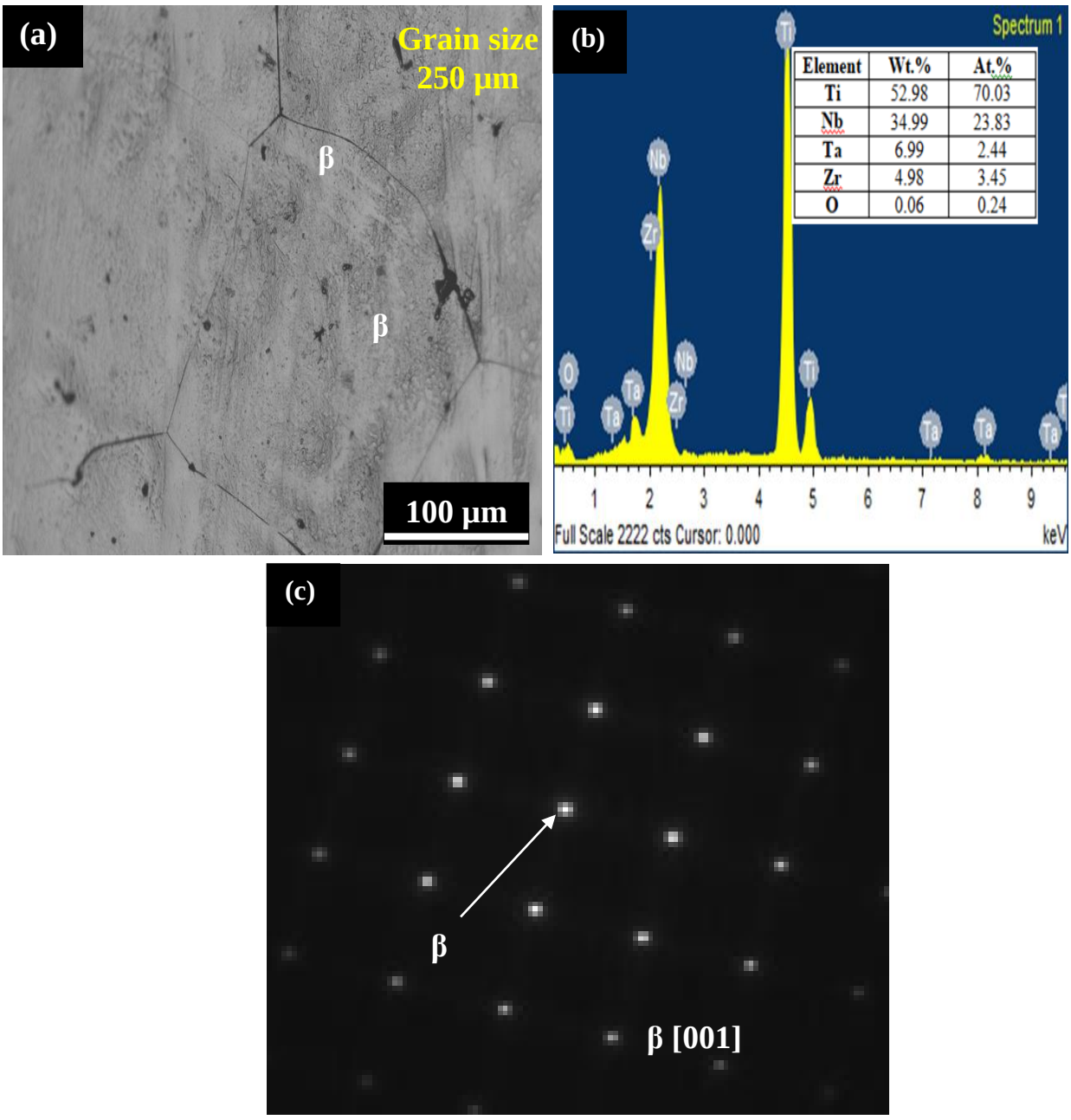

Figure 5.1. (a) Microstructure, (b) Elemental composition, and (c) Crystallography of un-treatment β-phase Ti-35Nb-7Ta-5Zr alloy

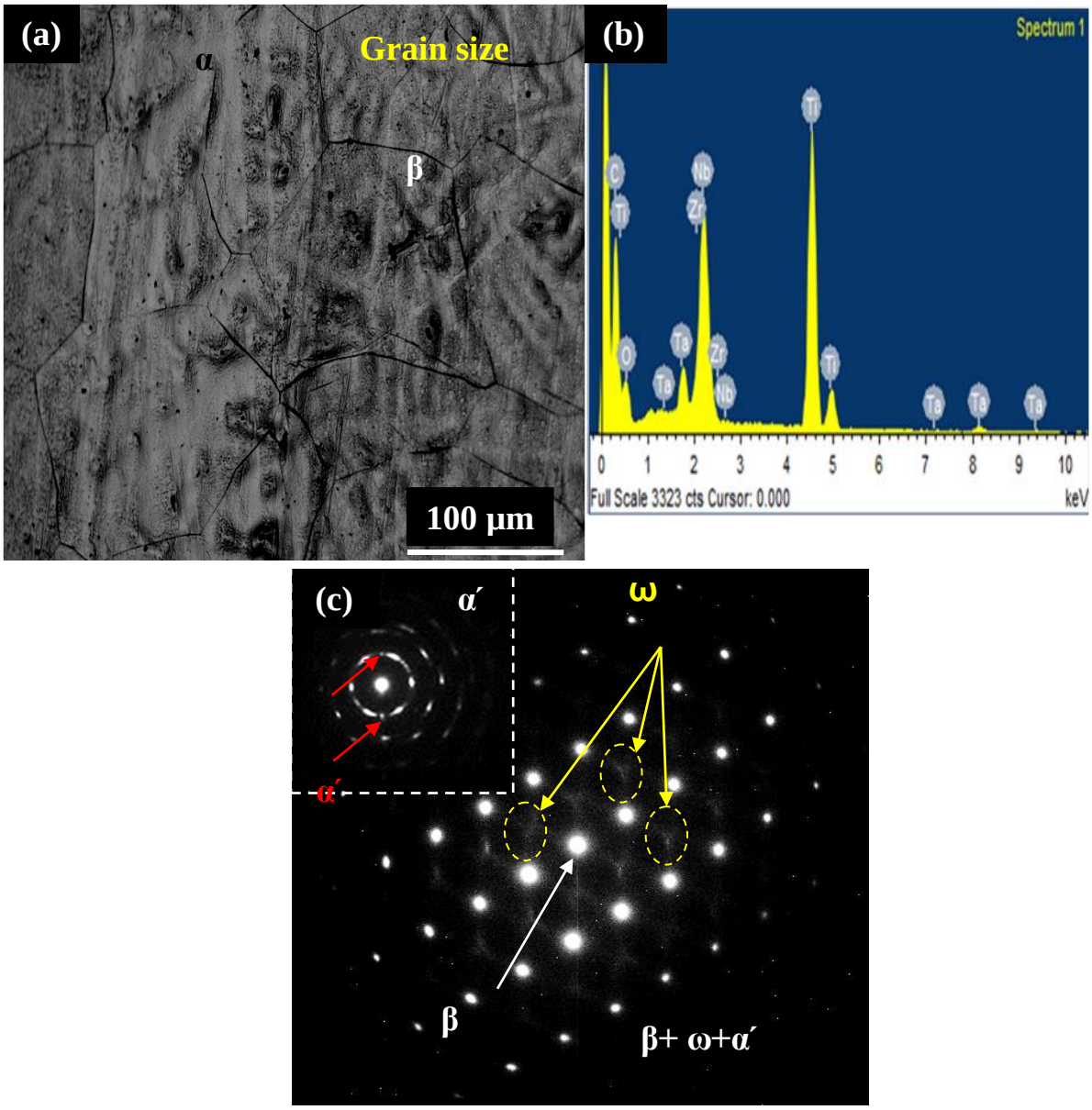

Figure 5.2. (a) Microstructure, (b) Elemental composition, and (c) Crystallography of β-phase Ti-35Nb-7Ta-5Zr alloy after heat treatment

Figure 5.3 shows the XRD pattern of β-phase Ti-alloy before and after heat treatment. From the XRD patterns it can be seen that β-TNTZ alloy exhibited β-phase peaks majorly. However, minute peaks of 'α'-phase' has formed due to aging, which is in good agreement with results published elsewhere [190-193]. The percentage area of grain boundaries in the β-TNTZ$_{ht}$ sample is smaller than the as-developed β-TNTZ sample, owing to the wetting phenomena among the grain boundaries. As a result of this, the brittle structure has been formed that improved mechanical properties.

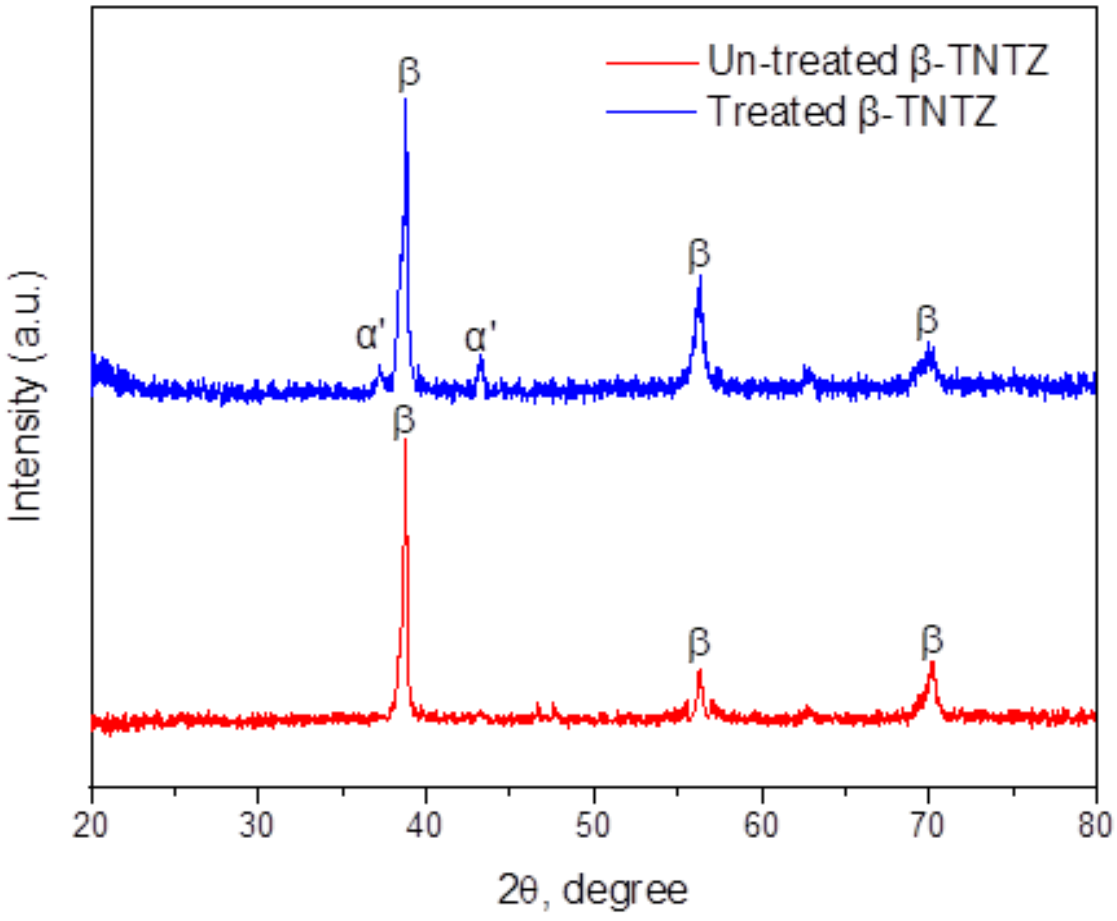

Figure 5.3. XRD pattern of *β*-phase Ti alloy (Ti-Nb-Ta-Zr) before and after heat treatment

The tensile test was performed on the *β*-Ti alloy as per the procedure explained in chapter 4. The tensile test specimen was prepared according to ASTM standard and well-polished surface. The stress versus strain curve obtained from tensile tests of the well-polished *β*-Ti alloy is presented in Figure 5.4. From the tensile test, it can be concluded that the *β*-phase Ti alloy exhibits excellent mechanical properties compatible for implant replacements. The Mechanical properties are such as tensile strength (UTS) 590 Mpa with percentage elongation of 13.47%, exhibit low young's modulus 55 Mpa near to the cortical bone (approximately10–30GPa) as compared to Ti-6Al-4V alloy and SS-316L. The mechanical properties of the *β*-Ti alloy in comparison to other titanium alloys used in biomedical applications. The *β*-Ti alloy has high elongation compared to Ti-6Al-4V, but still in the range adequate for biomedical applications, according to Niinomi [193].

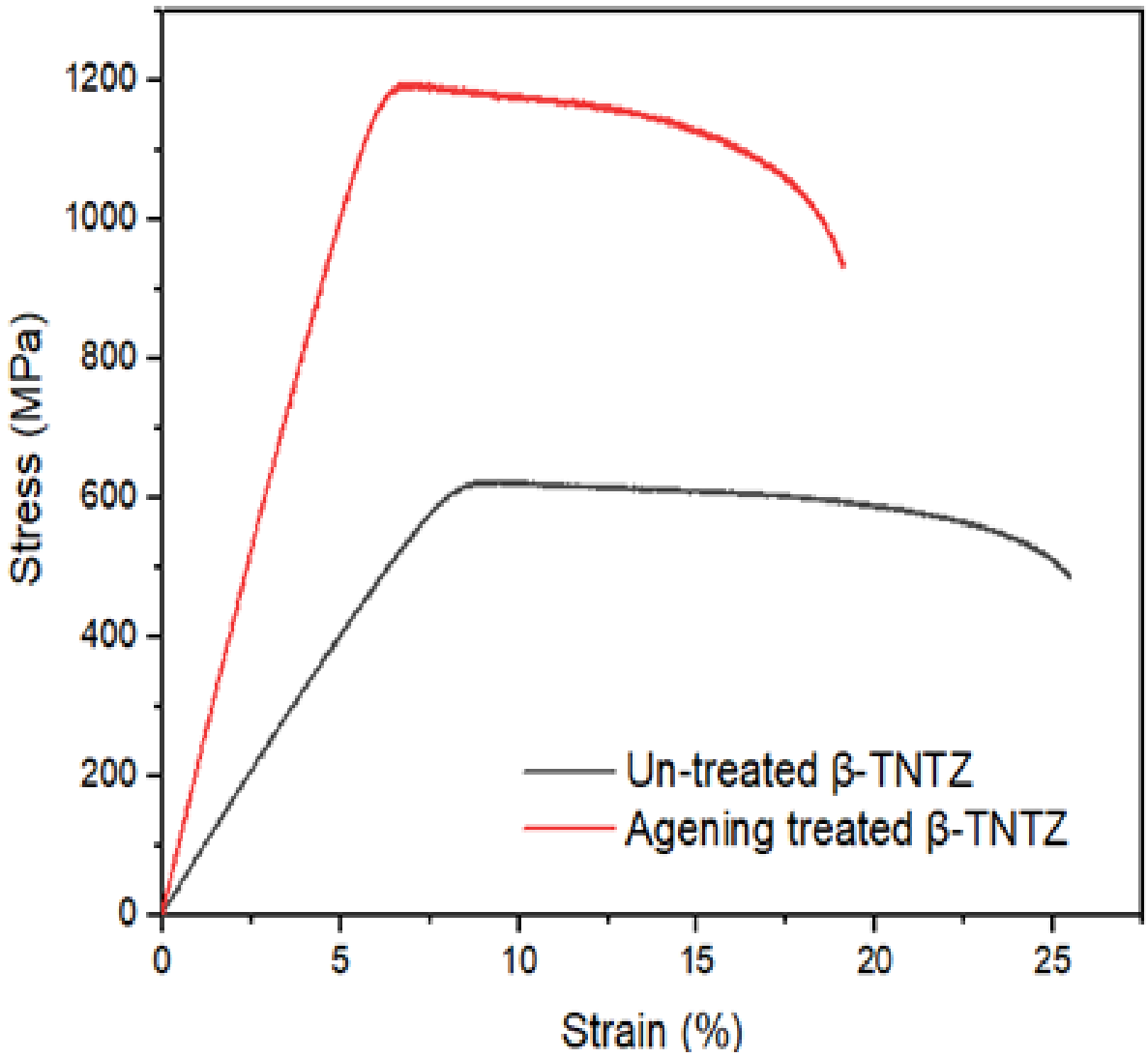

Figure 5.4. Stress-strain diagram of β-Ti alloy before and after heat treatment

The microhardness of the as-developed *β*-Ti alloy was obtained 245 HV, which is low and results in poor wear resistance in load bearing applications. In order to improve the wear resistance and strength, heat treatment was carried out, which improve the strength and hardness of alloy. The tensile strength and micro-hardness of the β-TNTZ sample after heat treatment have been increased from 590 to 1195MPa and 245 to 515HV, respectively. The elastic modulus of the β-TNTZ$_{ht}$ alloy is 89 GPa, which is lower than the Ti-4Al-4V alloy (110 GPa) and Co-Cr alloy (220 GPa). The mechanical properties obtained through the heat-treatment process suggest that the β-TNTZ is high strength alloy and can be used for the HIP, knee and acetabular component applications.

In the present research work, the heat-treated β-TNTZ alloy was proposed for the HIP-stem application. Despite the excellent mechanical properties, the β-TNTZ alloy surface required surface modification, because the HIP-stem is coated with bioactive materials, which provide the better osseointegration and better stability to the implantation. So, in the current research the β-TNTZ alloy was coated with HA and HA-TiO_2 based materials using plasma spray coating technique. The details examination in terms of surface morphology, costing thickness, surface-hardness, adhesion strength, corrosion resistance, wear resistance and bioactivity has been analyzed in the next sections.

5.2. Coating Experimentation and Parametric Analysis

The HA and HA-TiO_2 based coating materials has been deposited on the β-TNTZ alloy using plasma spray coating techniques. The preliminary or pilot experimentation has been performed in order to identify the influential input parameters which affect the coating characteristics in terms of micro-hardness and adhesion strength. As per literature and preliminary or pilot experimentation reinforcement of TiO_2 in HA, gas flow rate, and powder feed rate was selected as presented in Table 5.1.

Table 5.1. Input process parameters and their levels

Parameters	Levels		
	L-1	L-2	L-3
Reinforcement of TiO_2 in HA (A)	0	15	30
Gas flow rate (B)	30	35	40
Powder feed rate (C)	32	36	40

As per the selected process parameters and their level as presented in Table 5.1, the design of experiment (DOE) technique has been planned for the experimentation. Accordingly, L-9 orthogonal array (OA) has been chosen for experimentation. The micro-hardness and adhesion strength of coating surface was chosen for evaluation of coating performance. Table 5.2 shows the DOE plan and experimentation has been performed accordingly.

Table 5.2. Design of experiment plan

Sr. No	Reinforcement of TiO_2 in HA	Gas flow rate	Powder feed rate
1	0	30	32
2	0	35	36
3	0	40	40
4	15	30	36
5	15	35	40
6	15	40	32
7	30	30	40
8	30	35	32
9	30	40	36

The micro-hardness and adhesion strength of coatings as per DOE plan was recorded as shown in Table 5.3. The results obtained in Table 5.3 were used for the statistical analysis, for micro-hardness and adhesion strength, by using MINITAB-17 statistical software package.

Table 5.3. Design of experiment plan

Sr. No	Reinforcement of TiO_2 in HA	Gas flow rate	Powder feed rate	Surface Hardness (GPa)		Adhesion Strength (MPa)	
				Mean	S/N Ratio	Mean	S/N Ratio
1	0	30	32	125.55	41.98	18.15	25.18
2	0	35	36	125.42	41.97	17.50	24.86
3	0	40	40	137.66	42.78	17.05	24.63
4	15	30	36	120.32	41.61	16.35	24.27
5	15	35	40	110.13	40.84	17.65	24.93

6	15	40	32	303.86	49.65	29.50	29.40
7	30	30	40	145.81	43.28	18.65	25.41
8	30	35	32	300.81	49.57	30.19	29.60
9	30	40	36	302.84	49.62	30.13	29.58

Taguchi's methodology has been used to analyze the design of experiments (DOE). Taguchi method has been widely used in engineering problems to optimize performance characteristics by means of selecting process parameters and their levels. This method is a combined form of mathematical and statistical tools operated for the process improvement and development of products. This method can provide optimal combinations of parameters with minimum variability.

Taguchi's DOE technique proposed the design matrix of experimental trial runs based on the orthogonal array depending upon on the number of parameters and their levels. As per Taguchi, many OAs were suggested to suit the combination of parameters and their levels. On the basis of appropriate design matrix, experiments can be performed to get the inference about the quality. The standard two-level, three-level and five-level arrays as reported by Ross et al. [194] are:

a) Two-level arrays: L_4, L_8, L_{12}, L_{16}, L_{32}

b) Three-level arrays: L_9, L_{18}, L_{27}

c) Five-level array: L_{25}

The number as subscript in the array designation indicates the number of trials in that array. The degree of freedom (DOF) available in an OA is:

$$f_{L_N} = N - 1$$

Where f_{L_N} = total degrees of freedom of an OA

L_N =OA designation

N = number of trials

When a particular OA is selected for an experiment, the following inequality must be satisfied as reported by Ross et al. [194]:

$f_{L_N} \geq$ Total DOF required for parameters and interactions.

Depending on the number of levels in the parameters and total DOF required for the experiment, a suitable OA is selected.

Taguchi's methodology classified signal to noise (S/N) ratio as objective functions into to three categories, namely, lower-the-better, higher-the-better, or nominal the better. Accordingly, the loss functions are narrated below:

a) Higher-the-Better

$$\frac{S}{N}\text{ratio} = -10\log\left(\frac{1}{n}\sum_{i=1}^{n}\frac{1}{y_{ij}^2}\right)$$

b) Lower-the-Better

$$\frac{S}{N}\text{ratio} = -10\log\left(\frac{1}{n}\sum_{i=1}^{n}y_{ij}^2\right)$$

Where y_{ij} = i^{th} replicate of j^{th} response, n = number of replicates = 1, 2,….,n; j =1, 2,…,k.

c) Nominal-the- Better

$$\frac{S}{N}\text{ratio} = 10\log\left(\frac{\bar{y}^2}{s^2}\right)$$

Where,

$$\bar{y} = \frac{y_1 + y_2 + y_3 \ldots\ldots\ldots\ldots\ldots + y_n}{n}$$

and

$$s^2 = \frac{\sum(y_i - \bar{y})^2}{n-1}$$

A nominal-the-best type of problem is one where minimization of the mean squared error around a specific target value is desired. In the present study, surface microhardness and adhesion strength need to be maximized hence the “higher the better” type response is selected. The technique is applied to the study with following steps shown in Figure 5.5.

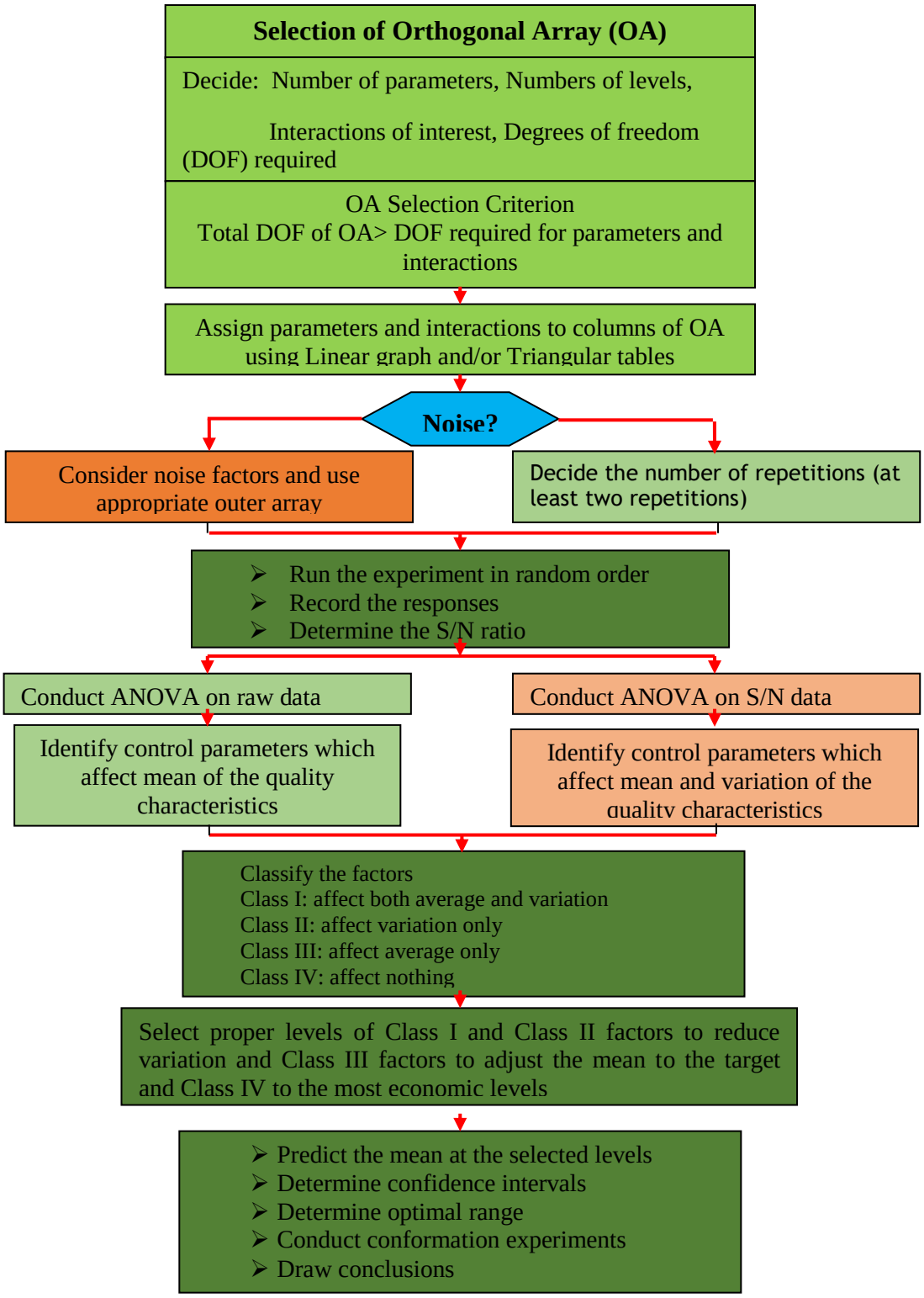

Figure 5.5. Taguchi experimental design and analysis flow diagram

A statistical analysis of variance (ANOVA) can be performed to determine the effect of process parameters on the performance measure. The optimum conditions can be found out by observing the minimum or maximum points for the performance

measures from S/N plots. The optimum conditions identified through the analysis are required to be confirmed by confirmation experiments. The response variable fitted using a polynomial quadratic equation to correlate each response variable to the independent input parameters. The mathematical model of each response is generated and described in the form of second-order non-linear Eq. 5.1:

$$Y = \beta_o + \sum_{i=1}^{n} \beta_i X_i + \sum_{i=1}^{n} \beta_i X_{ii}^2 + \sum_{i=1}^{n} \beta_i \, j \, X_i \sum_{i=1}^{n} \beta_i X_i \, X_j \qquad 5.1$$

Where Y is the corresponding response; X_i is the input parameter; X_{ii}^2 and X_iX_j are the squares and interaction terms of these input parameters; β_o, β_i, β_{ij}, and β_{ii} are the regression coefficients of parameters. The analyses were made using three-dimensional response surface plots constructed for each polynomial equation with Minitab-16 software (Minitab, Inc.). After achieving the optimum conditions for performance measures, the final step is to verify the performance at optimum conditions. After predicting the performance measures at optimum conditions, comparisons can be made with the experimental value of performance measures to check the percentage improvement in performance measure.

5.2.1. Effect of coating parameters on Micro-hardness

The observed average of means and S/N ratios for the obtained surface micro-hardness and adhesions strength after experimentation is shown in Table 5.2. The effect of reinforcement concentration of TiO_2, gas flow rate, and powder feed rate has been studied on diffusion surface micro-hardness and adhesions strength by observing the mean and S/N ratios plots. Higher-the-better type criterion was selected for analyzing the effect of input parameters on surface micro-hardness and adhesions strength. Figure 5.6 shows the mean effects and S/N ration plot for the surface micro-hardness of the developed coating versus reinforcement concentration of TiO_2.

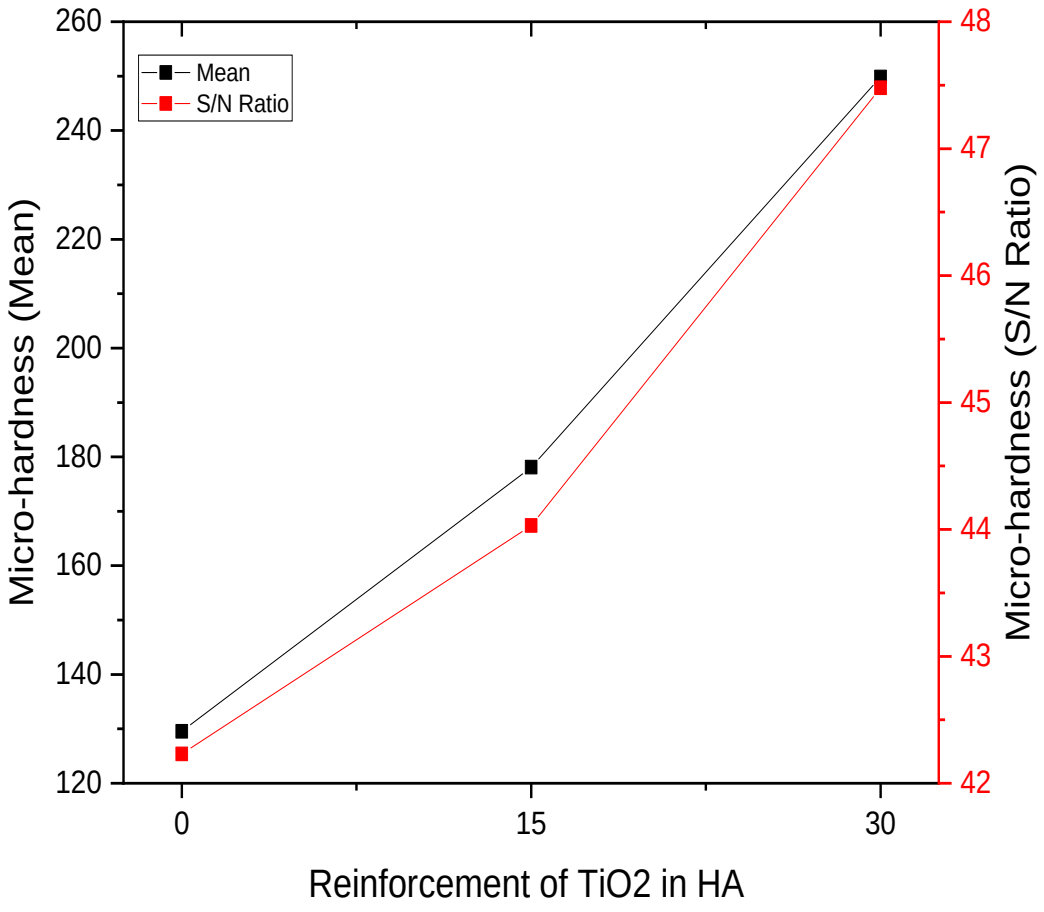

Figure 5.6. Main effect and S/N ratio plot of surface hardness with respect of percentage composition of TiO_2 in HA

As regards the first parameter, reinforcement of TiO_2 concentration, it has been found that when the %wt. of TiO_2 has increased in the HA the resulting surface micro-hardness of the coated implants was also increased. The coated substrates, having 30%wt. of TiO_2, possessed higher surface hardness, nearly about twice, when compared with the uncoated substrate. This is mainly because TiO_2, in comparison with HA and substrate material, exhibits higher mechanical hardness. Further, with greater %wt. of TiO_2, as reinforcement of HA, the coated substrate obtained greater density as well as a reduction in porosity in the coating [44]. The mean effect plot was similar pattern with S/N ration plot. Figure 5.7 shows the mean effects and S/N ration plot for the surface micro-hardness of the developed coating versus gas flow rate.

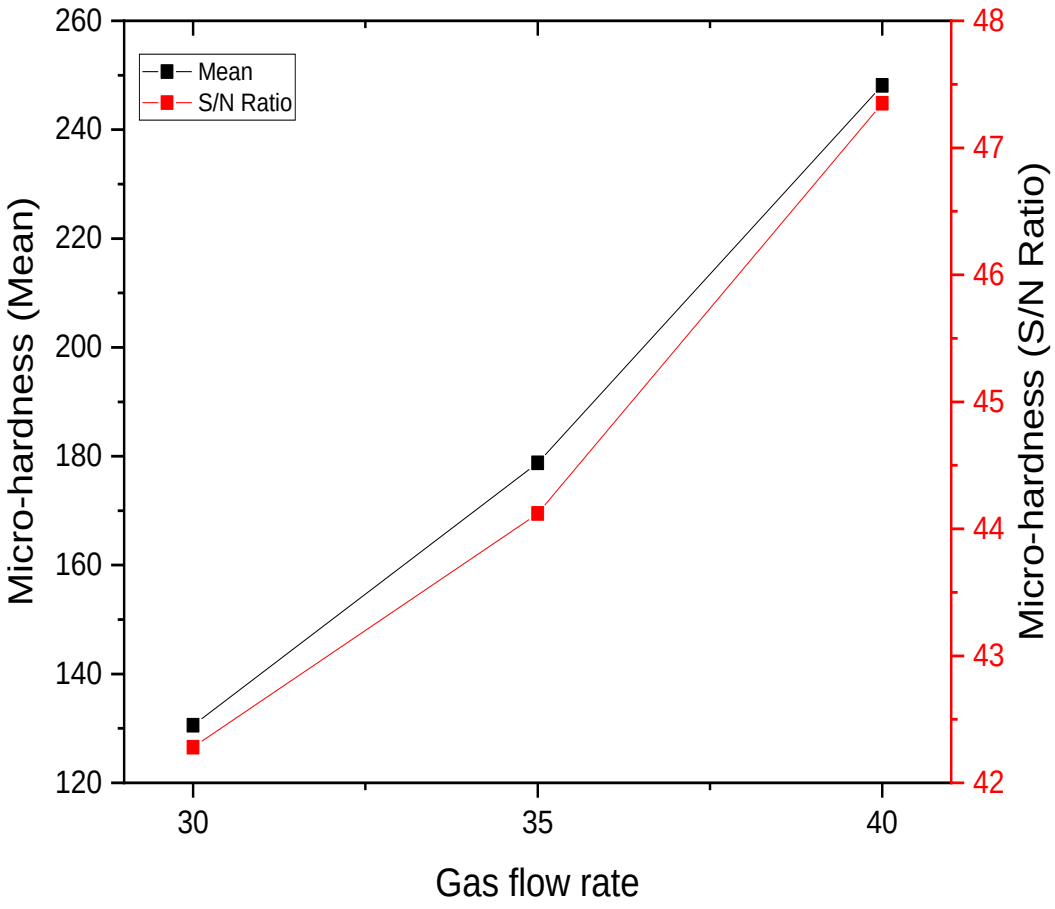

Figure 5.7. Main effect and S/N ratio plot of surface hardness with respect of gas flow rate

In the case of gas flow rate, it has been found that the surface micro-hardness of the coated substrate increased with an increase in the gas flow rate from 30 to 40 l/min. This is because, for surface micro-hardness, the partially melted regions play an important role in determining the final average surface hardness of the coatings. Further, the overall surface hardness of the coatings increases as the volume fraction of partially melted regions decreases with an increase in the gas flow rate. Figure 5.8 shows the mean effects and S/N ratio plot for the surface micro-hardness of the developed coating versus powder feed rate.

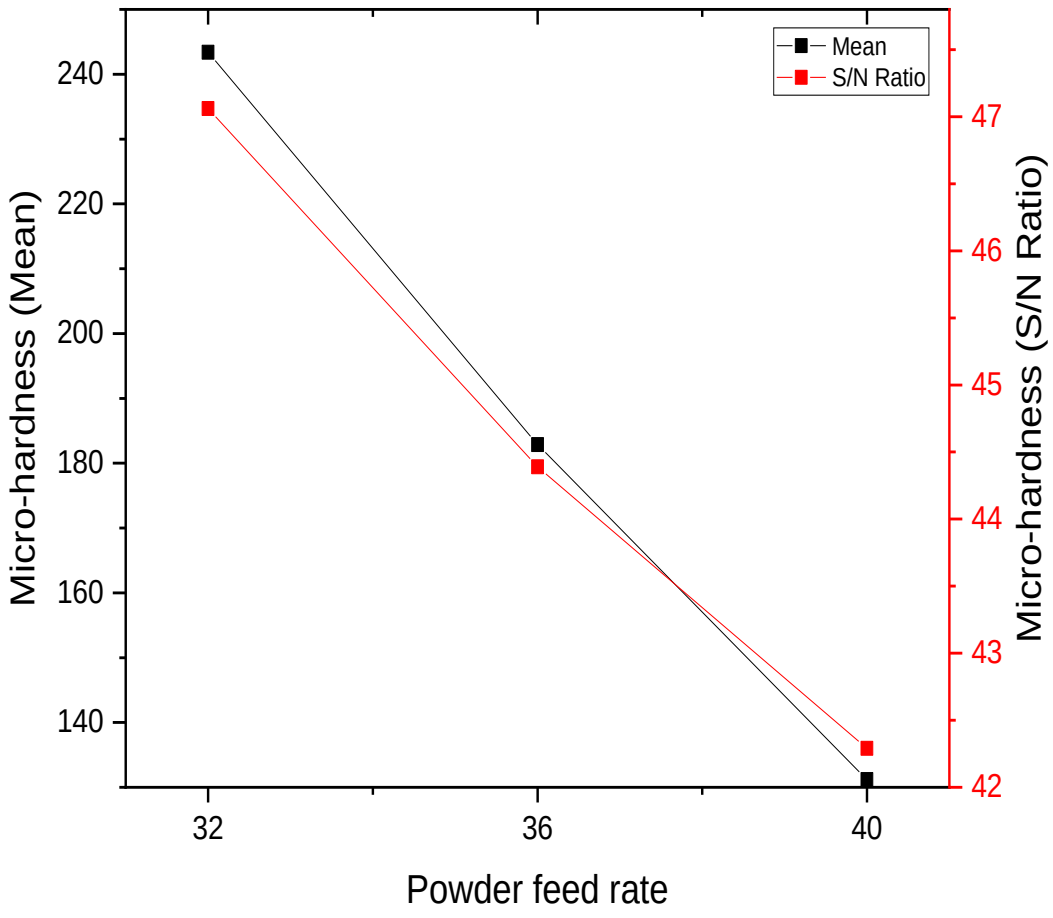

Figure 5.8. Main effect and S/N ratio plot of surface hardness with respect of powder feed rate

In the case of powder feed rate, it has been found that the surface hardness of the coatings increased with a decrease in the feed rate of the powder. It has been found that when the feed rate of the powder is higher, more dwelling time was needed for the melting of the powder particles, therefore, to make the coating denser. Moreover, at a low carrier gas pressure, with a low powder feed rate, the difficulties of heat transfer from the surface into the interior of particles can cause high porosity of the powders [153].

From the Figure 5.6 to 5.8, it can be seen that the optimized process parametric levels for obtaining maximum surface micro-hardness are: powder ratio – 30% wt. of TiO_2, gas flow rate – 40 l/min, and powder feed rate – 32 g/min. The average value of mean (raw data) and S/N ratio for surface micro-hardness at different levels of input parameters are depicted in Table 5.4 and 5.5 respectively. From the observations, it can be seen that reinforcement of TiO_2 in HA has rank 1, gas flow rate rank 2, and powder feed rate has rank 3.

Table 5.4. Response table for means of surface micro-hardness of coating

Level	**Reinforcement of TiO_2 in HA**	**Gas flow rate**	**Powder feed rate**
1	129.5	130.6	243.4
2	178.1	178.8	182.9
3	249.8	248.1	131.2
Delta	120.3	117.6	112.2
Rank	1	2	3

Table 5.5. Response table for S/N ratio of surface micro-hardness of coating

Level	**Reinforcement of TiO_2 in HA**	**Gas flow rate**	**Powder feed rate**
1	42.24	42.29	47.07
2	44.03	44.12	44.4
3	47.49	47.35	42.3
Delta	5.25	5.06	4.77
Rank	1	2	3

To find out the significance of the input process parameters, analysis of variance (ANOVA) has been conducted, refer to Table 5.6. It can be seen from ANOVA Table that all the three selected input parameters have statically significantly, at a 95% confidence level, contributed in the resulted surface micro-hardness of the coated specimens, as their respective P-value < 0.05. Despite this, the process parameter,

reinforcement of TiO_2 in HA has a maximum contribution (about 35.39%), while the gas flow rate has contribution about 33.76%, powder feed rate has contribution about 30.49%, and error has only 0.36% contribution in affecting the surface hardness of the coatings.

Table 5.6. Analysis of variance (ANOVA) for surface micro-hardness

Source	DF	Seq-SS	Adj-SS	Adj-MS	F	P	% Contribution
A	2	21968.7	21968.7	10984.3	98.13	0.01	35.39
B	2	20953.5	20953.5	10476.7	93.6	0.011	33.76
C	2	18925.4	18925.4	9462.7	84.54	0.012	30.49
Residual	2	223.9	223.9	111.9			0.36
Total	8	62071.4					

5.2.2. Effect of coating parameters on adhesion strength

Figure 5.9 shows the mean effects and S/N ratio plot for the adhesion strength of the developed coating versus reinforcement concentration of TiO_2. It can be seen for the powder ratio that the adhesion strength of the coating increased, as the powder ratio increased from 0 to 30% wt. of TiO_2. From this, it can be estimated that the adhesion strength for the coating was considerably increased by adding TiO_2 particles in HA. The higher bonding strength (about 26.57 MPa) was achieved at 30% wt. of TiO_2 in HA. The reinforcement of TiO_2 reduced the brittleness of the HA and improved the adhesion properties during the coating.

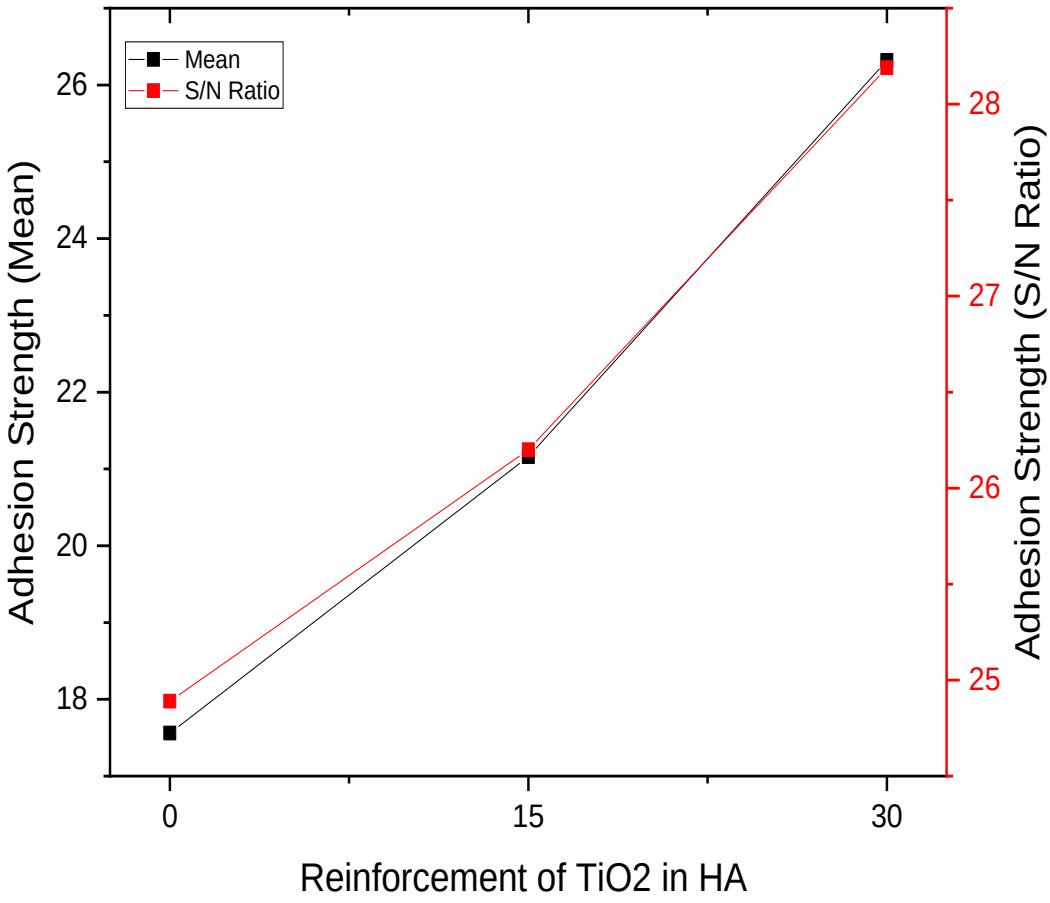

Figure 5.9. Main effect and S/N ratio plot of adhesion strength of coating with respect of percentage composition of TiO_2 in HA

Figure 5.10 shows the mean effects and S/N ration plot for the adhesion strength of the developed coating versus gas flow rate. In the case of gas flow rate, it has been found that the adhesion strength of the coating increased with an increase in the gas flow rate during plasma spraying. An increase in gas flow rate tends to increase the velocity of the spray, however, it increases the plasma jet temperature that led to an increase in the particle melting [153-154]. Therefore, particles were succeeded in the plasma gas flow rate, an increases in the plasma/particle interaction duration, resulting in high adhesion strength.

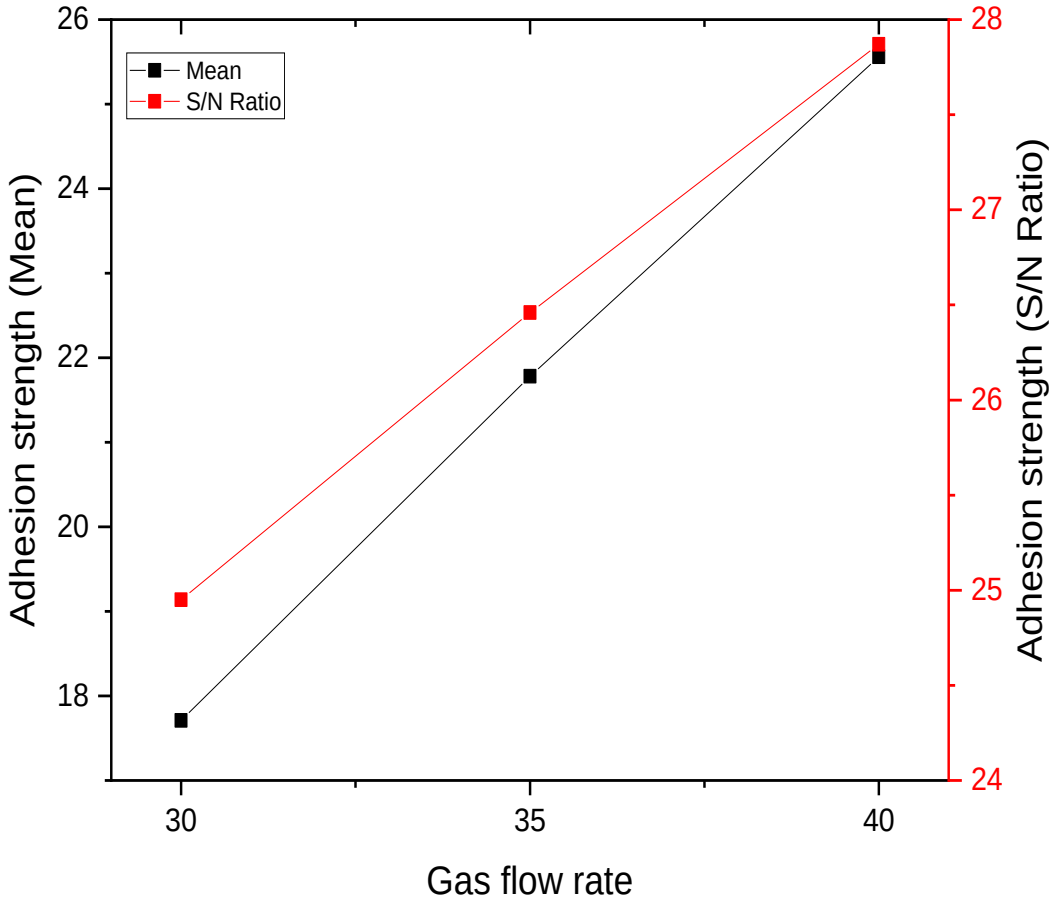

Figure 5.10. Main effect and S/N ratio plot of adhesion strength of coating with respect of gas flow rate

Figure 5.11 shows the mean effects and S/N ration plot for the adhesion strength of the developed coating versus powder feed rate. Lastly, in the case of powder feed rate, it has been noticed that the adhesion strength of the coating suffered, significant when the powder feed rate was incremented. Any change in the powder feed rate affects the count of particles, sharing the kinetic/thermal energies of the flame [160]. This, indeed, as a result, affects the particle velocity and the temperature. Higher feed rate intends to release and deposit un-melted powder particles that cause a reduction in the splat flattening ratio and an increase in the porosity. Since the sprayed particles are unable to attain required velocity and temperature, therefore, adhesion strength has to compromise. Along with this, higher feed rate tends to enforce mutual interaction amongst the particles and the momentum, as well as temperature, of the plasma jet decrease.

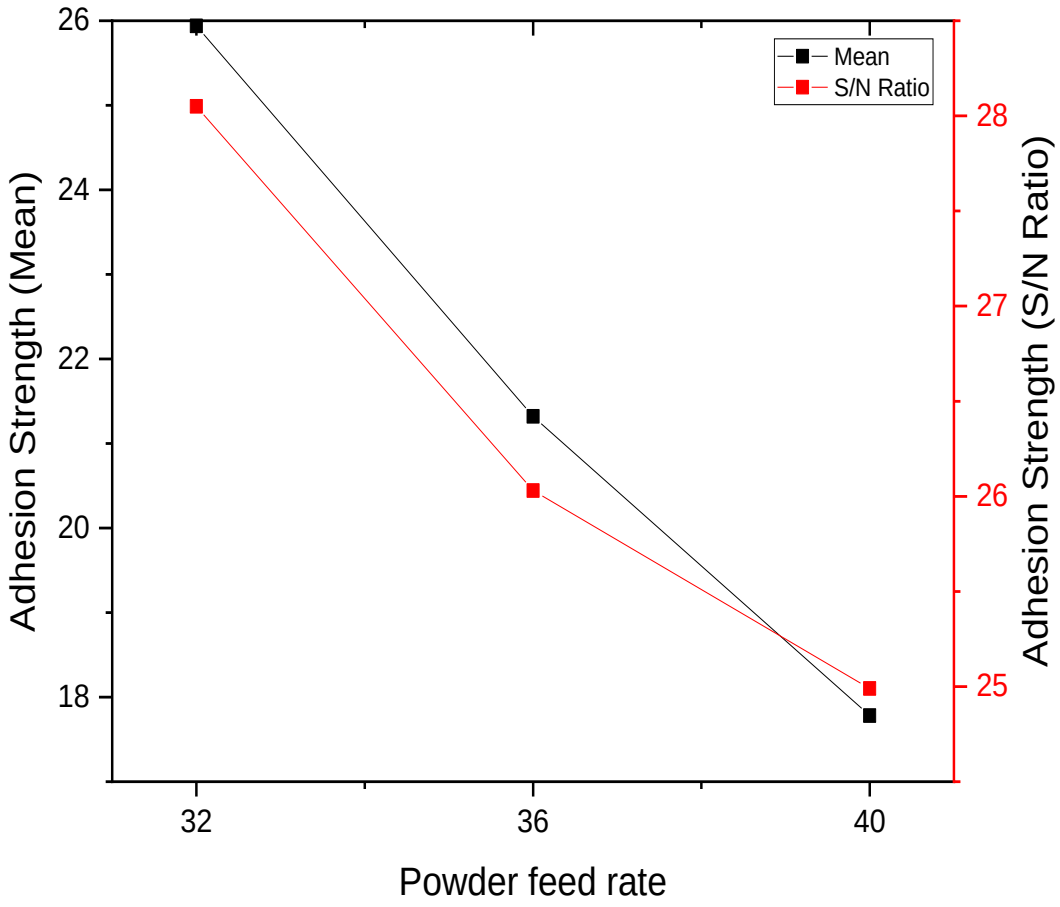

Figure 5.11. Main effect and S/N ratio plot of adhesion strength of coating with respect of powder feed rate

From the Figure 5.9 to 5.11, it can be seen that the optimized process parametric levels for obtaining maximum adhesion strength of coatings are: powder ratio – 30% wt. of TiO_2, gas flow rate – 40 l/min, and powder feed rate – 32 g/min. The average value of mean (raw data) and S/N ratio for adhesion strength at different levels of input parameters are depicted in Table 5.7 and 5.8 respectively. From the observations, it can be seen that reinforcement of TiO_2 in HA has rank 1, gas flow rate rank 3, and powder feed rate has rank 2.

Table 5.7. Response table for means of adhesion strength of coating

Level	Reinforcement of TiO_2 in HA	Gas flow rate	Powder feed rate
1	24.89	24.95	28.06
2	26.2	26.46	26.24

3	28.2	27.87	24.99
Delta	3.31	2.92	3.06
Rank	1	3	2

Table 5.8. Response table for S/N ratio of adhesion strength of coating

Level	Reinforcement of TiO_2 in HA	Gas flow rate	Powder feed rate
1	17.57	17.72	25.95
2	21.17	21.78	21.33
3	26.32	25.56	17.78
Delta	8.76	7.84	8.16
Rank	1	3	2

Analysis of variance (ANOVA) for adhesion strength of coatings has been presented in Table 5.9. It can be seen from ANOVA table that selected input parameters, except gas flow rate, have significantly, at a 95% confidence level, contributed in the resulted adhesion strength of the coated specimens, as their respective P-value < 0.05. The parameter, reinforcement of TiO_2 in HA has a maximum contribution (about 37.47%), while the gas flow rate has about 29.76% contribution, powder feed rate has contribution about 32.41%, and error have 0.35% contribution in affecting the adhesion strength. For the confirmation of the predicted optimized settings, by Taguchi L9 orthogonal array, a set of three confirmatory experiments have been performed. It has been found that the experimental values obtained at optimized settings are: surface micro-hardness – 369 HV GPa and adhesion strength – 34.45 MPa. The average experimental values of the confirmatory experiments are greater than the values obtained during the design of experiments, indicating the reliability of the optimized setting in improving the performance characteristics of the coated implants. Table 5.10 shows the conformation of experiments.

Table 5.9. Analysis of variance (ANOVA) for surface adhesion strength

Source	DF	Seq-SS	Adj-SS	Adj-MS	F	P	% Contribution
A	2	116.23	116.23	58.1152	106.77	0.009	37.47
B	2	92.317	92.317	46.1585	84.8	0.012	29.76
C	2	100.54	100.54	50.2698	92.35	0.011	32.41
Residual	2	1.089	1.089	0.5443	0.5443		0.35
Total	8	310.176					

Table 5.10. Confirmation of experiments

Response (Units)	Optimal Levels of process parameters	Predicted Value	Experimental Value	Percentage Error (%)
Micro-hardness (HV)	A_3 B_3 C_1	369.70	365	5.08
Adhesion Strength (MPa)	A_3 B_3 C_1	34.45	33.57	3.22

5.3. Coating Morphology and Performance

5.3.1. Study-I

Surface morphology of HA and HA-TiO_2 coatings obtained at process parameters as per Table 5.11 has been analyzed. Where the effect of reinforcement of TiO_2 in HA, gas flow rate, and powder feed stock has been considered.

Table 5.11. Plasma Spray Parameters

Spraying Parameters	Value
Primary Gas Flow (Argon)	40 NLPM
Secondary Gas Flow (Hydrogen)	2.0 NLPM
Voltage	65 volt
Current	500Amp
Feed rate	32 g/min
Spray Distance	120 mm

5.3.1.1. Surface morphology of coating

Figure 5.12 and 5.13, and 5.14 shows the coating morphologies of two HA, HA-15TiO_2, and HA-30TiO_2 coated surface at different views (top and cross-sectional). Both coating specimens display a heterogeneous partly and completely melted surface fusion of particles consisting of high ribs of embedded, dispersed molten metal (presented via yellow arrow), micro-cracks (presented via white arrow), micro-globules (presented via red arrow) and surface porosity (shown in the yellow circles), all of which are the expected surface characteristics obtained from the plasma scraper [142]. From the cross-section micrographs, it can be seen that the thickness of HA, HA-15TiO_2, and HA-30TiO_2 coatings were measured approximately ~185-200 μm.

Figure 5.12 (a) and (b) show the top surface and cross-section morphology of HA-coated substrates. The HA-coating comprised bigger and high degree of globules of un-melted particles and interconnected surface porosities as compared to HA-15TiO_2, and HA-30TiO_2 coatings, as can be seen in Figure 5.12(a).

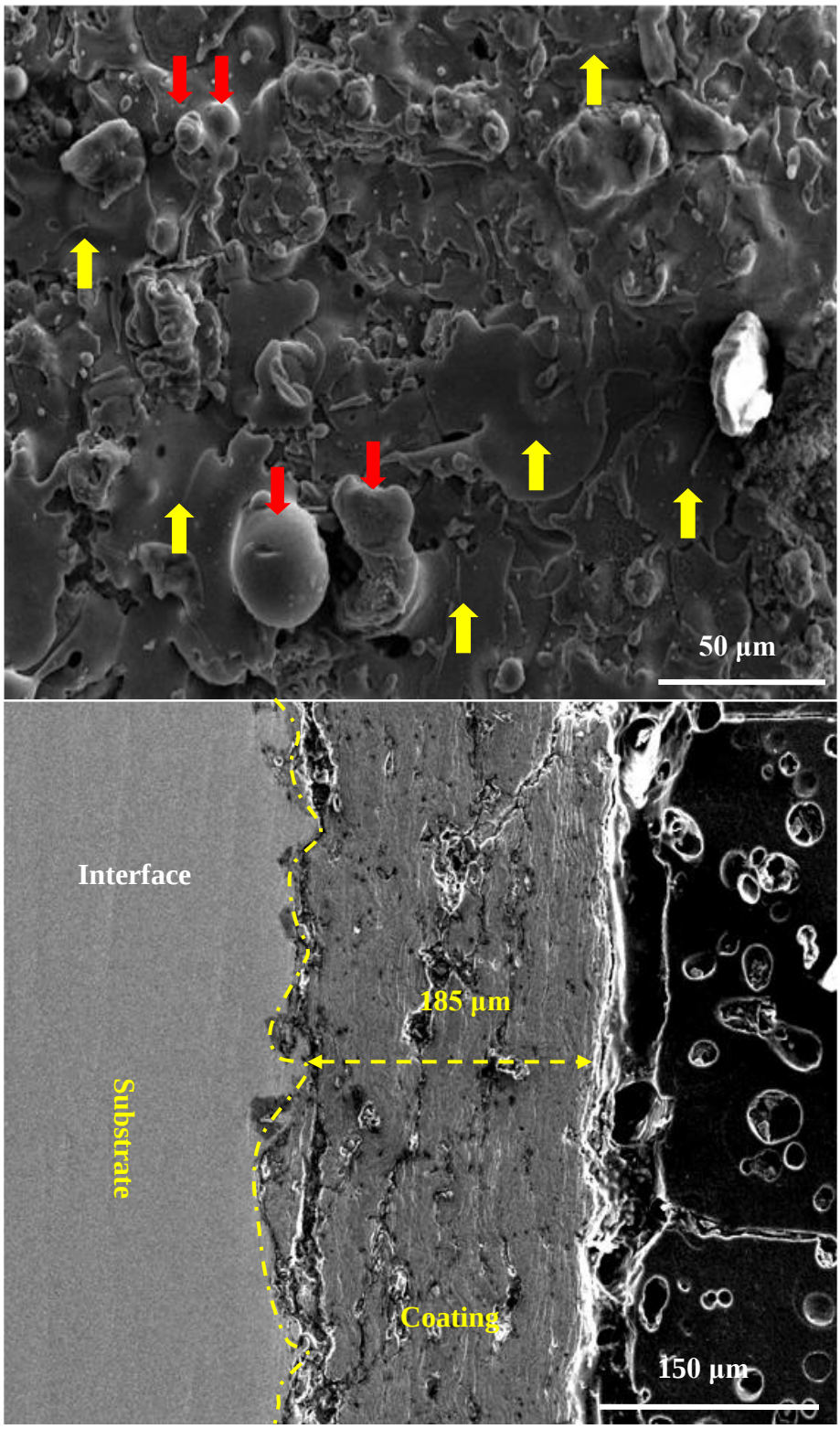

Figure 5.12. Top surface and cross-section morphology of HA coating

It is evident from the cross-section that HA coating's surface comprises micro-cracks and micro-holes of different sizes which are unevenly distributed. From the interface

of HA coating and substrate, it can be seen that the coating has poor bonding with the substrate owing to the high brittle nature of HA, which degraded the mechanical properties of the coating. This is attributed because of high-temperature HA disintegrated into 'Ca' and 'P' and during deposition, these phases form porous structure and amorphous hump as a result poor interface-bonding was obtained. On the other hand, when TiO_2 was reinforced in HA, a positive effect on surface morphology, microstructure, and adhesion strength of coating material with the substrate was observed. Figure 5.13 (a) and (b) shows the top surface and cross-section morphology of HA-15TiO_2 coated surface. The surface morphology of top-surface is competitive flat, smooth, and less defective. It has been found that the surface was comparatively denser than the *HA* coated surface and agglomeration of *HA/TiO₂* nano-particles was observed. The reinforcement of *TiO₂* in *HA* has prevented the formation of larger pores, as can be seen in Figure 5.13(a). From the cross-section micrograph, it can be seen that coating layer exhibit small micro-cracks, porosity, un-melted particles and smaller quantities of micro-holes. The laminar structure in the HA matrix was formed by the TiO_2 due to that extremely dense coating was obtained, which improve the mechanical properties. Figure 5.14 (a) and (b) show the top surface and cross-section morphology of HA-30TiO_2 coated surface. The surface morphology of top-surface is competitive flat, smooth, and less defective. It has been found that the surface was comparatively denser than the HA coated surface and HA-15TiO_2 coated surface. The agglomeration of HA/TiO_2 nano-particles can be clearly seen in the coating. The reinforcement of TiO_2 in HA formed lamellar structure and rich layer of TiO_2 acted as a reservoir to hold the protein in the host body and improved the osseointegration and corrosion resistance.

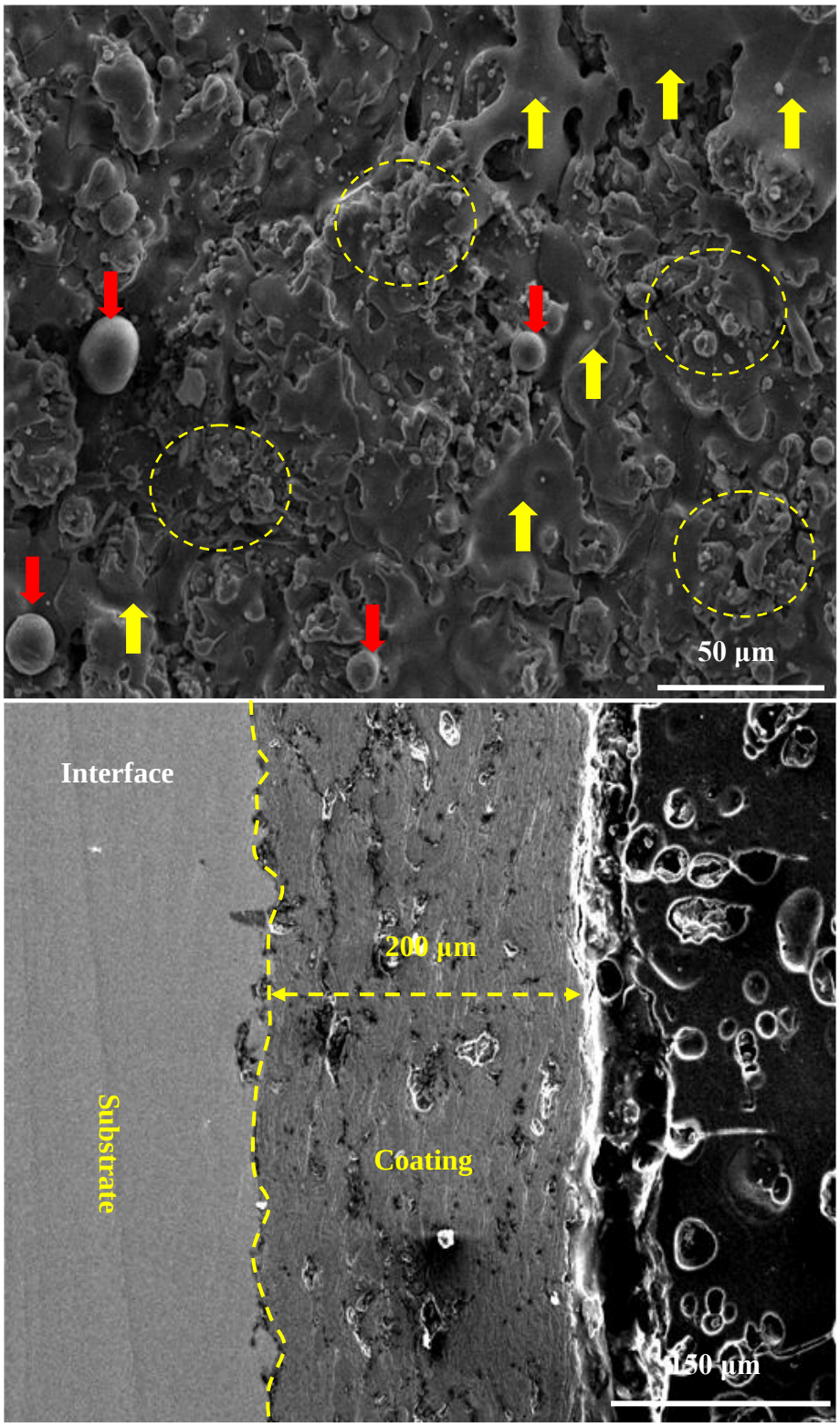

Figure 5.13. Top surface and cross-section morphology of HA-15TiO_2 coating

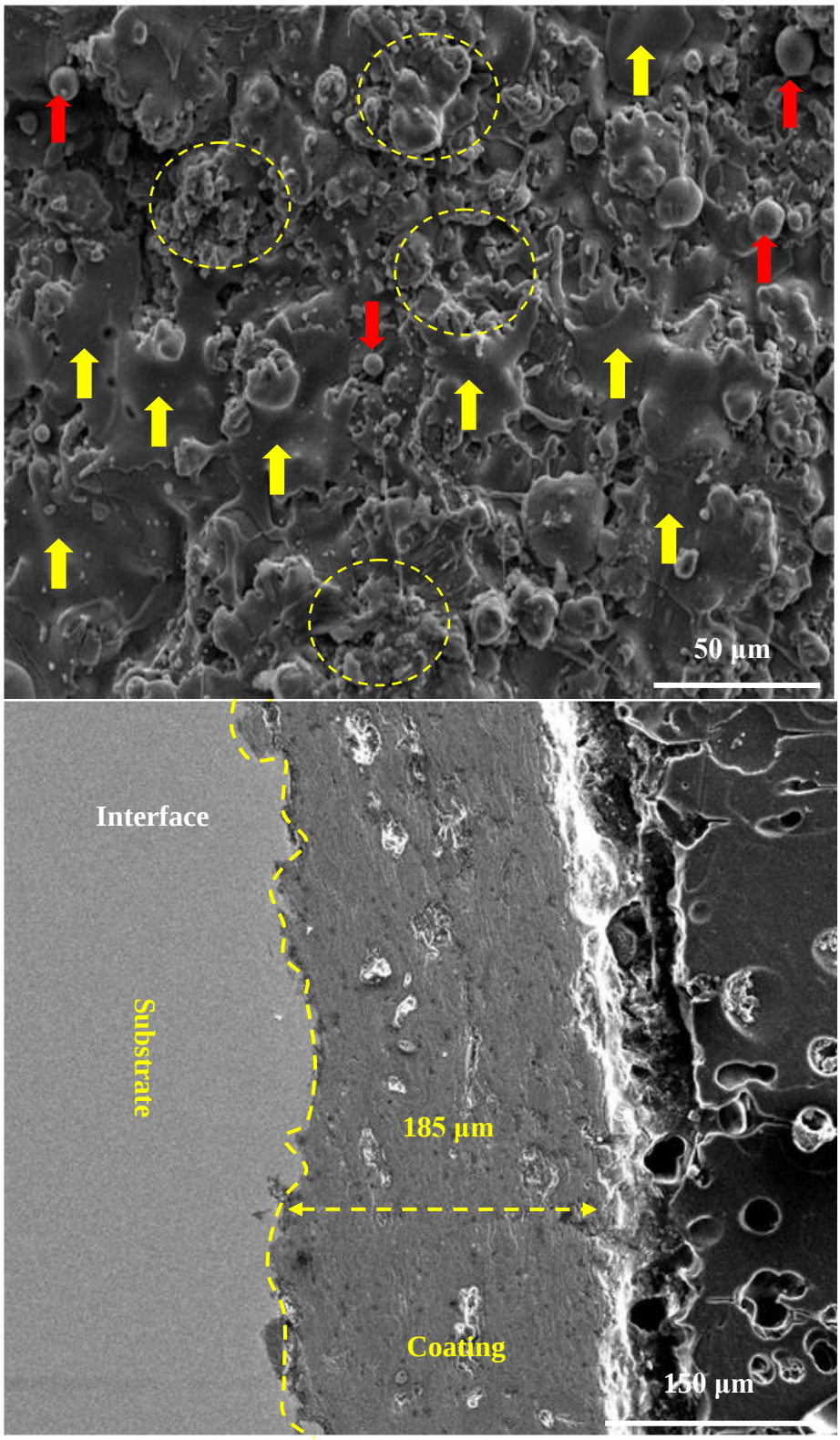

Figure 5.14. Top surface and cross-section morphology of HA-30TiO_2 coating

Figure 5.15 shows the EDS spectrum and XRD pattern of HA-coated and HA-30TiO_2 coated surface. Figure 5.15 (a) shows the EDS spectrum of *HA* coating and it can be seen that high-intensity peak of 'Ca', 'P', and 'O', beside base elements, confirming the deposition of *HA*. On the other hand, the EDS spectrum of *HA-T_y* coating shows the high-intensity peaks of 'Ti', 'Ca', and 'P' confirmed the deposition of *HA/TiO_2*, as can be seen in Figure 5.15(b). The ratio of 'Ca' and 'P' in the elemental composition was found 1.67 and the finding is in line with the previously published research [153]. From the EDS observations, it can be concluded that *HA* was disintegrated into non-apatite and expected to form α/β TCP phases, CaO, TTCP along with *TiO_2* phases and during PSD. The elements formed various bio-ceramic based oxides and improved the corrosion resistance and bio-performance of the alloy [24, 25]. From the XRD pattern of un-coated *β-TNTZ* alloy and the pattern metastable β-type phases, such as 'Nb', 'Ta', and 'Zr', can be seen in Figure 5.15(c). From the XRD pattern of *HA* coated samples, the amorphous phases, for instance, β-TCP, TTCP phases, $Ca_3(PO_4)_2$, and CaO, can be observed between diffraction angles 30.5º and 31.7º, which were owing to the disintegration of *HA* as a consequence of thermal sequence and speedy cooling involved in PSD [155-156]. From the XRD pattern of HA-15TiO_2, and HA-30TiO_2 coated samples, non-apatite and α/β TCP phases co-exist, along with TiO_2. The bone ingrowth and osseointegration depend on the surface roughness, porosity, and chemical composition. HA-coating contains higher surface porosities (6.75%) as compared HA-15TiO_2 (4.15%) and HA-30TiO_2 (2.55%) coatings. This is because HA form amorphous structure in coating. The structural porosities decreased with the reinforcement of *TiO_2* in *HA*. This was attributed because *TiO_2* reinforcement is smaller is size than HA, and occupies the space/void in between *HA*-particles that prevented the formation of the porosities.

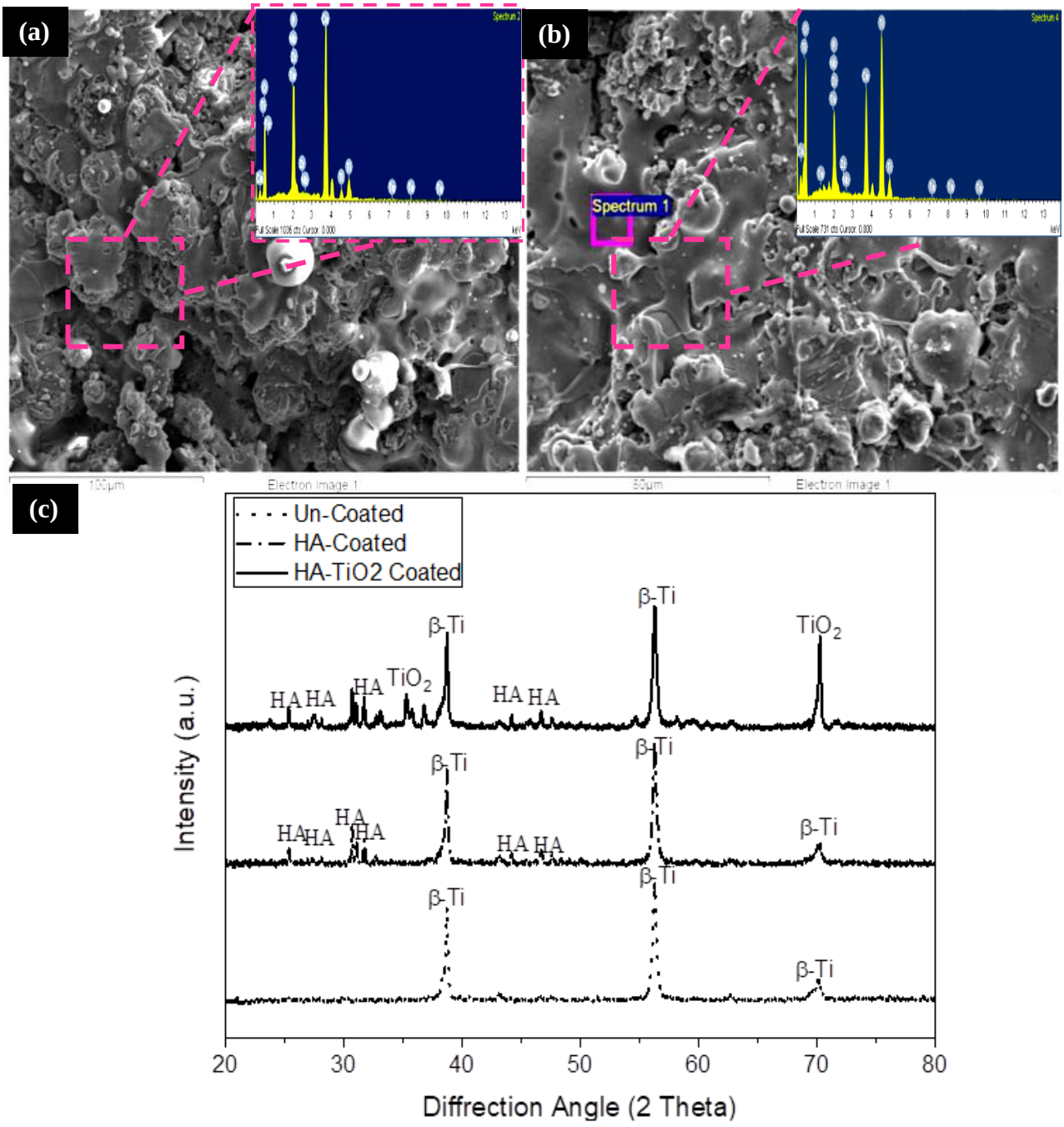

Figure 5.15 SEM morphology, EDS spectrum, and XRD pattern of (a) HA-coated (b) HA-30TiO_2 coatings (c) XRD pattern of un-coated, HA coated, and HA-30TiO_2 coated β-TNTZ alloy

The surface roughness also an important parameter that affects the corrosion resistance and bioactivity and it was reported that the size of the particles has affected the surface roughness [195-197]. Gross and Muller reported that the surface roughness of *HA* coating was measured 4.8, 7.4, and 9.5 μm for feedstock powder

particles size of 20-40, 40-60, and 60-80 μm. A total of five readings were taken to find out the average surface roughness. The surface roughness of *HA*, HA-15TiO_2, and HA-30TiO_2 coatings were measured 7.65, 5.45, and 4.85 μm, respectively. The obtained surface roughness was in good agreement with the values reported in literature and also sufficient to promote bone-ingrowth around the implant.

5.3.1.2. Mechanical properties analysis

Figure 5.16 shows the mechanical properties of coatings in terms of hardness, elastic modulus, and adhesion strength. The mechanical properties of coating depend upon its microstructure and purity of coating.

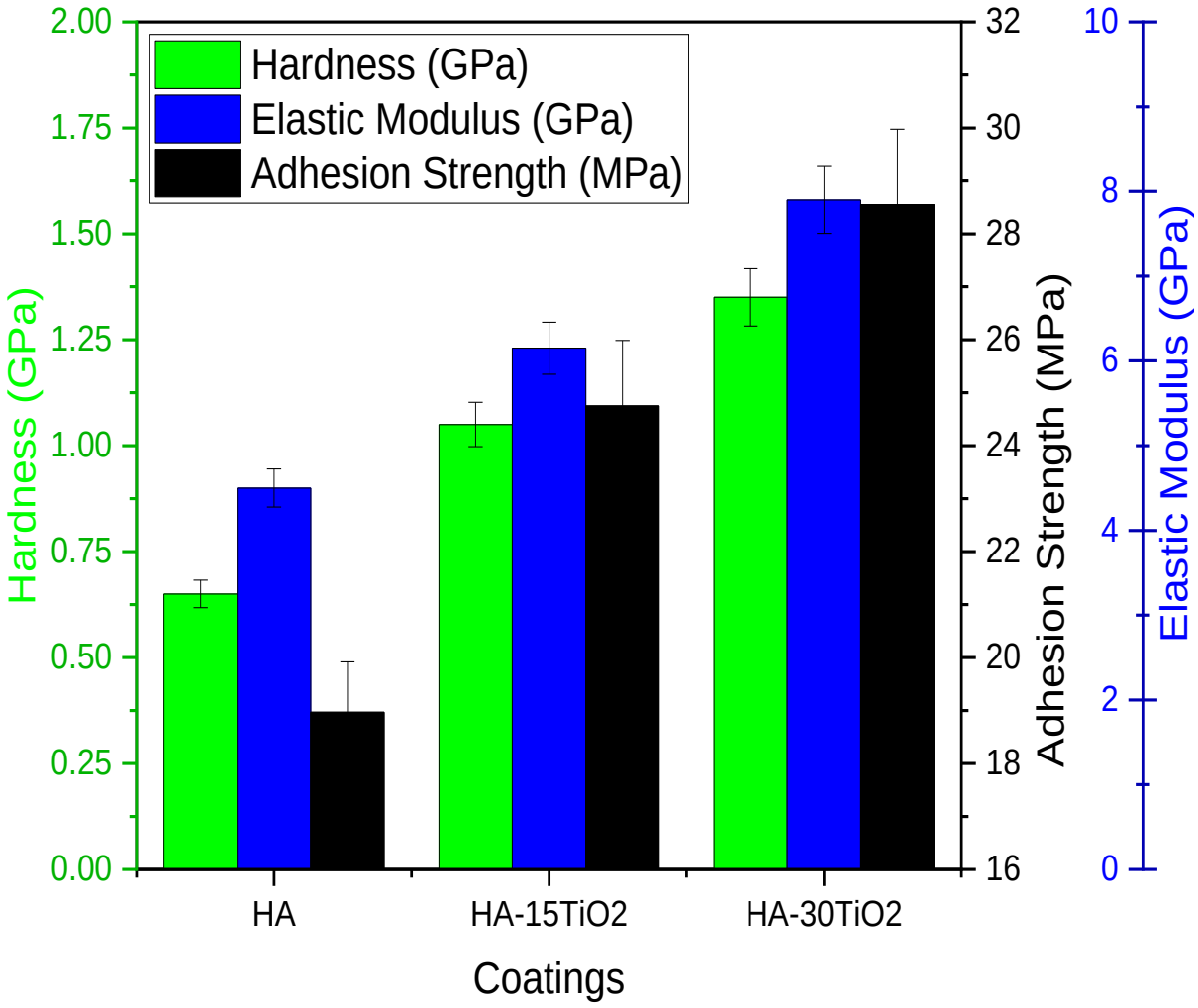

Figure 5.16. Mechanical properties: hardness and adhesion strength of HA, HA-15TiO_2, and HA-30TiO_2 coatings

The hardness increased with the increase in the reinforcement of TiO_2 in *HA*. The hardness of *HA*, HA-15TiO_2, and HA-30TiO_2 coatings was measured 0.65, 1.05, and 1.35 GPa, respectively. The *HA* transformed during the coating and deposited coating contains cracks, micro-size voids, the porous and amorphous structure which leads to decrease in mechanical properties. With the alloying of TiO_2 in *HA*, the brittleness reduced and the deposited coating possessed dense and lamellar nanostructure which leads to increase the mechanical properties. The elastic modulus was dependent on the hardness of the coating. With the addition of TiO_2, brittleness reduced and ductility improved as a result of strength of coating improved and results in the increase in elastic modulus.

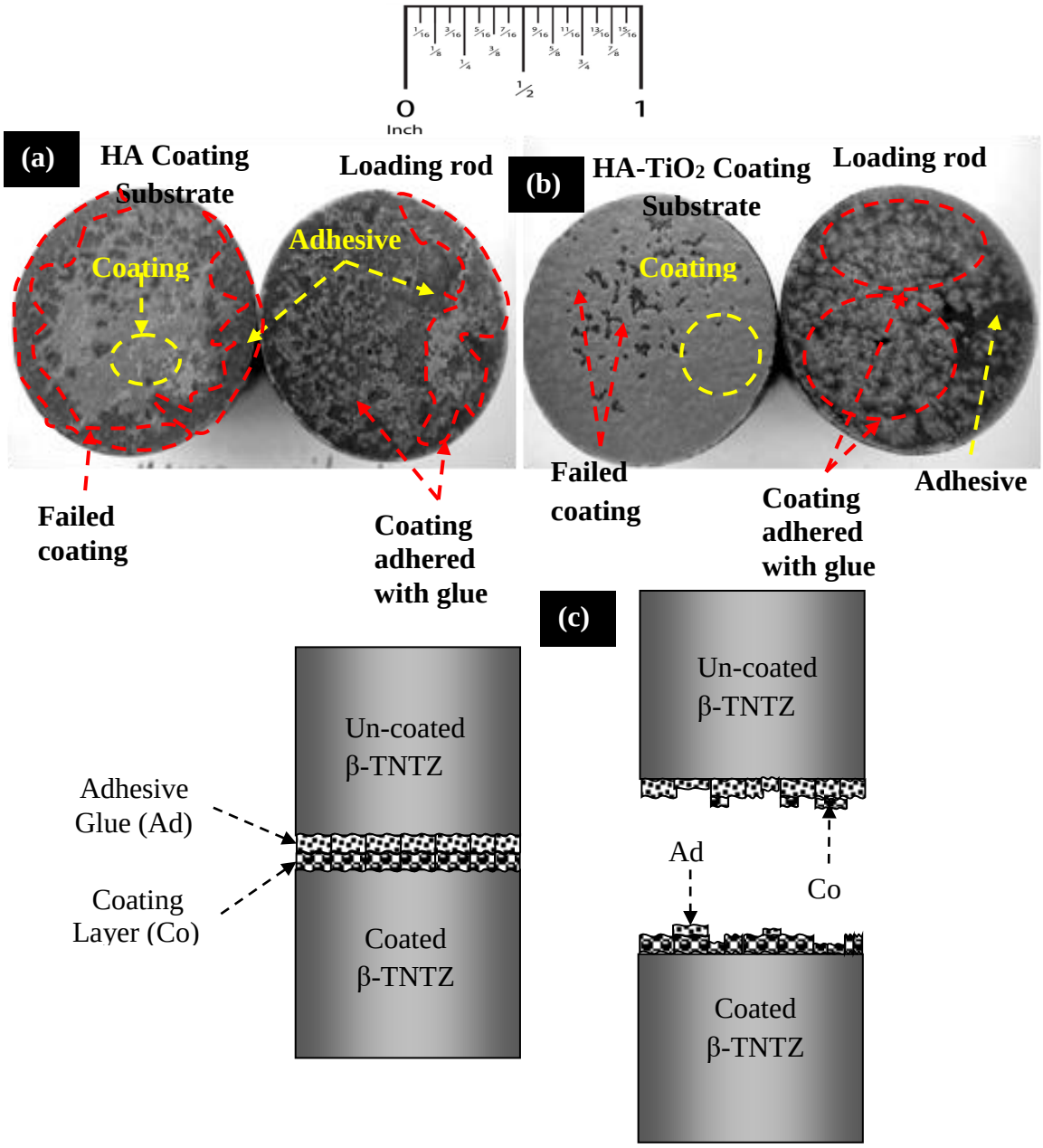

Figure 5.17. Optical macrograph of tensile bond strength specimens (a) HA coating (b) HA-TiO_2 coatings, and (c) mechanism of failure of coating

The adhesion strength of coating depends upon the interface of coating and substrate and type of bonding. The adhesion strength of *HA*, HA-15TiO_2, and HA-30TiO_2 coating were measured 20.07, 24.75, and 28.55 MPa, respectively. Figure 5.17 (a-b) shows the fractured morphology of coatings after adhesion tensile test. From the micrograph, it can be seen that the *HA* coating was delaminated or remove from the surface along with glue. This is because the *HA* coating was poorly mechanically-

bonded with the substrate and exhibit cracks in the interface which was removed from the substrate; thus results in low adhesion strength, refer Figure 5.17(a). On the other hand, with the alloying of TiO_2, mechanically-bonding of the coating increased with the substrate, which increases in adhesion strength of coating, refer Figure 5.17(b). Similar results were observed in the previous research work [198-200]. Figure 5.17(c) presented the mechanism of delamination/de-bonding or removal of coating from the substrate.

5.3.1.3. In-vitro corrosion behavior

Figure 5.18 shows the Tafel extrapolation plot of un-coated, HA, HA-15TiO_2, and HA-30TiO_2 coated *β-TNTZ* alloy samples. The obtained electrochemical corrosion parameters are shown in Table 5.9. From the Tafel extrapolation curve, it can be seen that all surfaces exhibit similar corrosion mechanism 'anodic' slope is far higher than the 'cathodic' slope which indicates strong passivity. The I_{corr} and E_{corr} of un-coated samples were measured 6.5 µA/cm^2 and - 290 mV, respectively. The Tafel extrapolation curve of *HA* coating shifted toward the left side that holds low current density as compared to uncoated samples. The I_{corr} and E_{corr} values of *HA*-coated samples were measured as 7.35 µA/cm^2 and - 330 mV, respectively. The *HA*-coated samples have better corrosion resistance as compared to uncoated samples. When TiO_2 was alloyed, the Tafel extrapolation curve again more shifted toward the left side that indicates samples hold low current density as compared to *HA* and uncoated samples. The I_{corr} and E_{corr} values of HA-15TiO_2 coating were measured as 8.15 µA/cm^2 and -370mV, respectively. Similarly, for HA-30TiO_2 coating, the values were 9.17 µA/cm^2 and -420 mV, respectively. The material holds low current density and high potential that possessed high corrosion resistance [201]. It can be outlined that HA/TiO_2 coatings exhibit higher corrosion resistance as compared to *HA*-coatings and un-coated samples. The un-coated samples have an inert TiO_2 layer that had low adhesion strength and braked in the corrosive medium and allows current to flow in the medium. The *HA*-coating contains the porosities, cracks, and brittle amorphous structure, which degraded easily in the SBF medium. These cracks form the active sites for this dissolution which resulted in pitting corrosion. Morks also observed similar results [202]. On the other hand, HA/TiO_2 coatings contain the defect-free

dense lamellar structure of TiO_2 in nano-form, which acted as a barrier to corrosive medium and acted as an anti-corrosive layer. Moreover, the *HA/TiO_2* coatings comprised bioceramic oxides also improved the corrosion resistance.

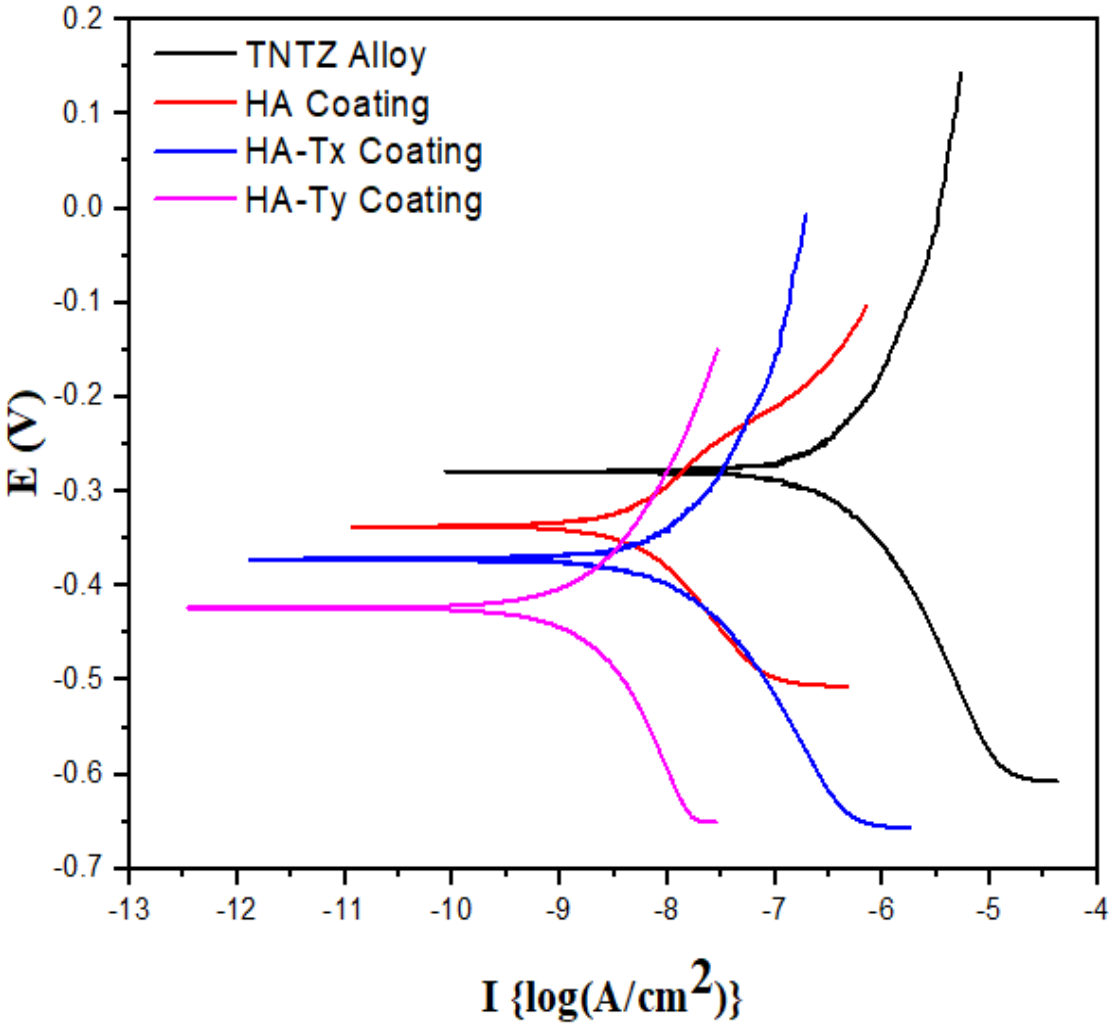

Figure 5.18. Tafel extrapolation plot of un-coated, HA-coated, HA-15TiO_2 and HA-30TiO_2 coated β-TNTZ alloy samples in SBF

Figure 5.19 shows the SEM micrograph and EDS analysis of un-coated, *HA*, HA-15TiO_2 and HA-30TiO_2 coated samples before and after the corrosion test. Apatite growth can be seen on the surface of samples and can be detected by bright white color dots and agglomerations. The sample before the corrosion test showed plane surface and base elements, refer to Figure 5.19(a). On the other hand, after the corrosion test, sub-micron scale pits can be observed which are formed due to the

failure of the inert layer in corrosive medium, refer Figure 5.19(b). Moreover, the development of the apatite layer was also observed in the sample in the form of a white pattern. The EDS analysis showed the presence of 'Ca', 'P', and 'O' elements along with base elements and confirmed the growth of apatite. The ratio of 'Ca' and 'P' was 1.67.

Figure 5.20 shows the HA-coating morphology before and after corrosion test. Before the corrosion test, HA-coatings comprised micro-cracks, porosities, and amorphous structures, refer Figure 5.20(a). After corrosion, the development of micro-scale pits was observed; refer Figure 5.20 (b). This is attributed owing to the dissolution and premature failure of porous amorphous *HA-layer* and pitting corrosion takes place that leads to the formation of pits. The HA promotes the formation of apatite-like structure and EDS analysis confirmed the growth of apatite-like structure on the coating, as the 'Ca' and 'P' percentage increased on the coating.

Figure 5.21 and 5.22 shows the HA-15TiO_2 and HA-30TiO_2 coating morphology before and after corrosion test. Before the corrosion test, the HA-15TiO_2 and HA-30TiO_2 coating have a better microstructure and comparatively denser as compared to the HA-coating surface, refer Figure 5.21(a) and 5.22(a), respectively. On the other hand, the morphology of HA-15TiO_2 and HA-30TiO_2 coated samples after the corrosion test showed that the surface was comparatively very less corroded as compared to HA-coatings. Moreover, the thick growth of apatite was also observed and spread over the whole surface; refer Figure 5.21(b) and 5.22(b), respectively. EDS analysis confirmed the significant increase in the wt.% percentage of 'Ca' and 'P' on both coating's surface. This because the HA-15TiO_2 and HA-30TiO_2 coated substrates is a denser and free-formed amorphous and porous structure. The formation of the *TiO_2* lamellar structure in the *HA* matrix acted as a barrier to corrosion and improve the corrosion resistance. The above findings indicate that HA-30TiO_2 coating increased the corrosion resistance in a simulated environment and promoted chemical integration with the bone–tissues.

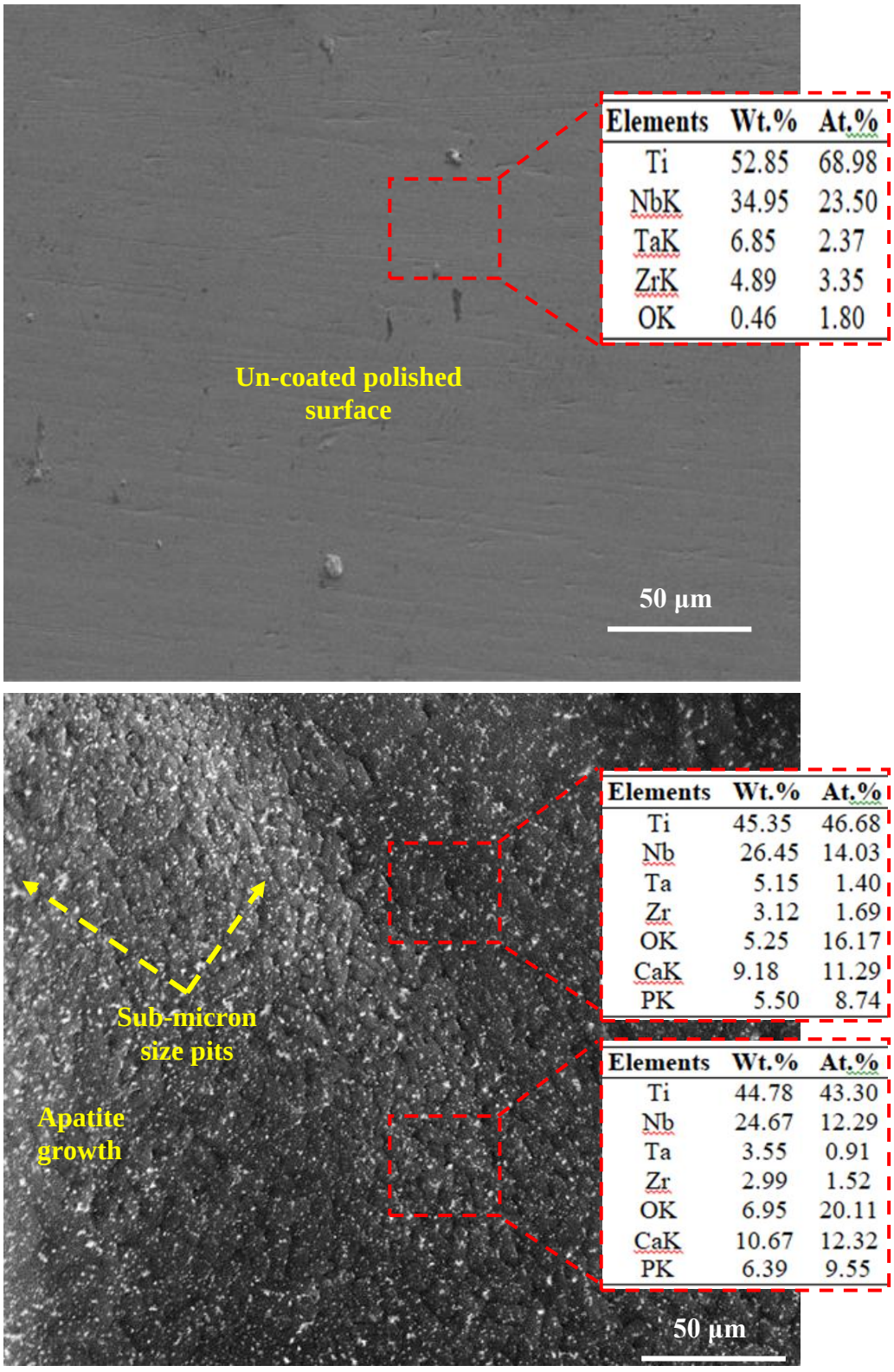

Figure 5.19. Morphology and EDS analysis of un-coated surface (a) before and (b) after corrosion test

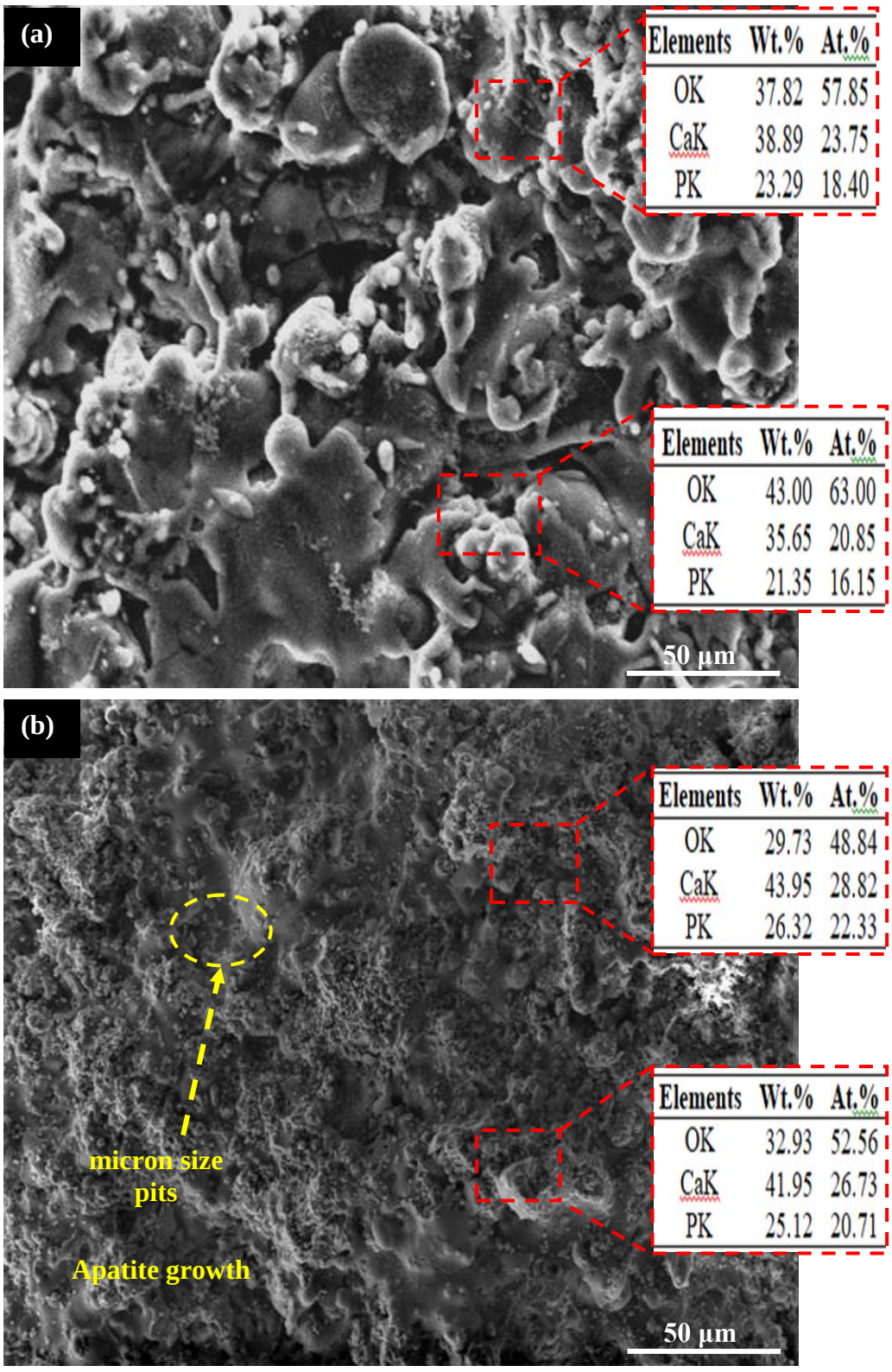

Figure 5.20. Morphology and EDS analysis of HA-coated surface (a) before and (b) after corrosion test

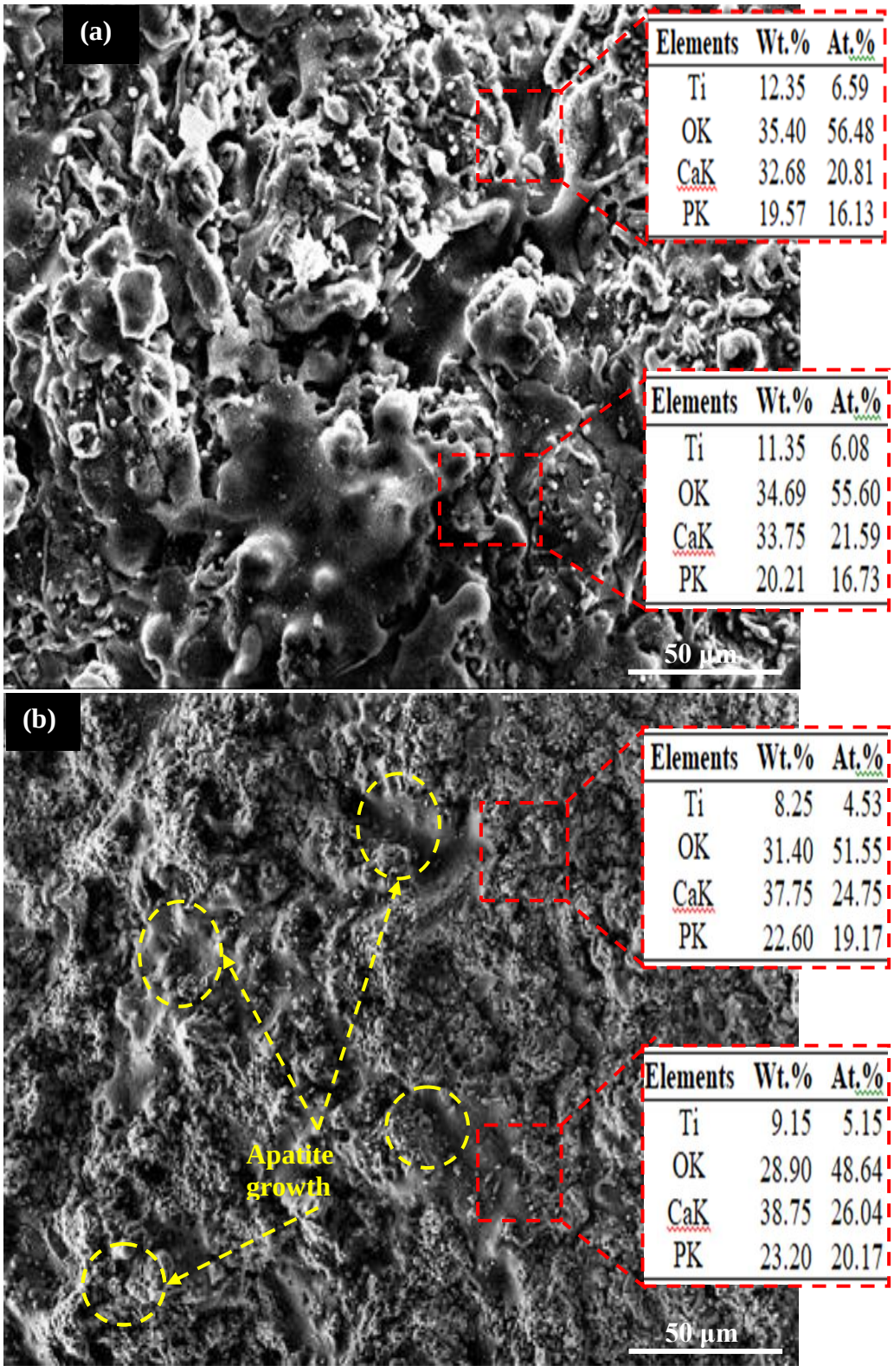

Figure 5.21. Morphology and EDS analysis of HA-15TiO_2 coated surface (a) before and (b) after corrosion test

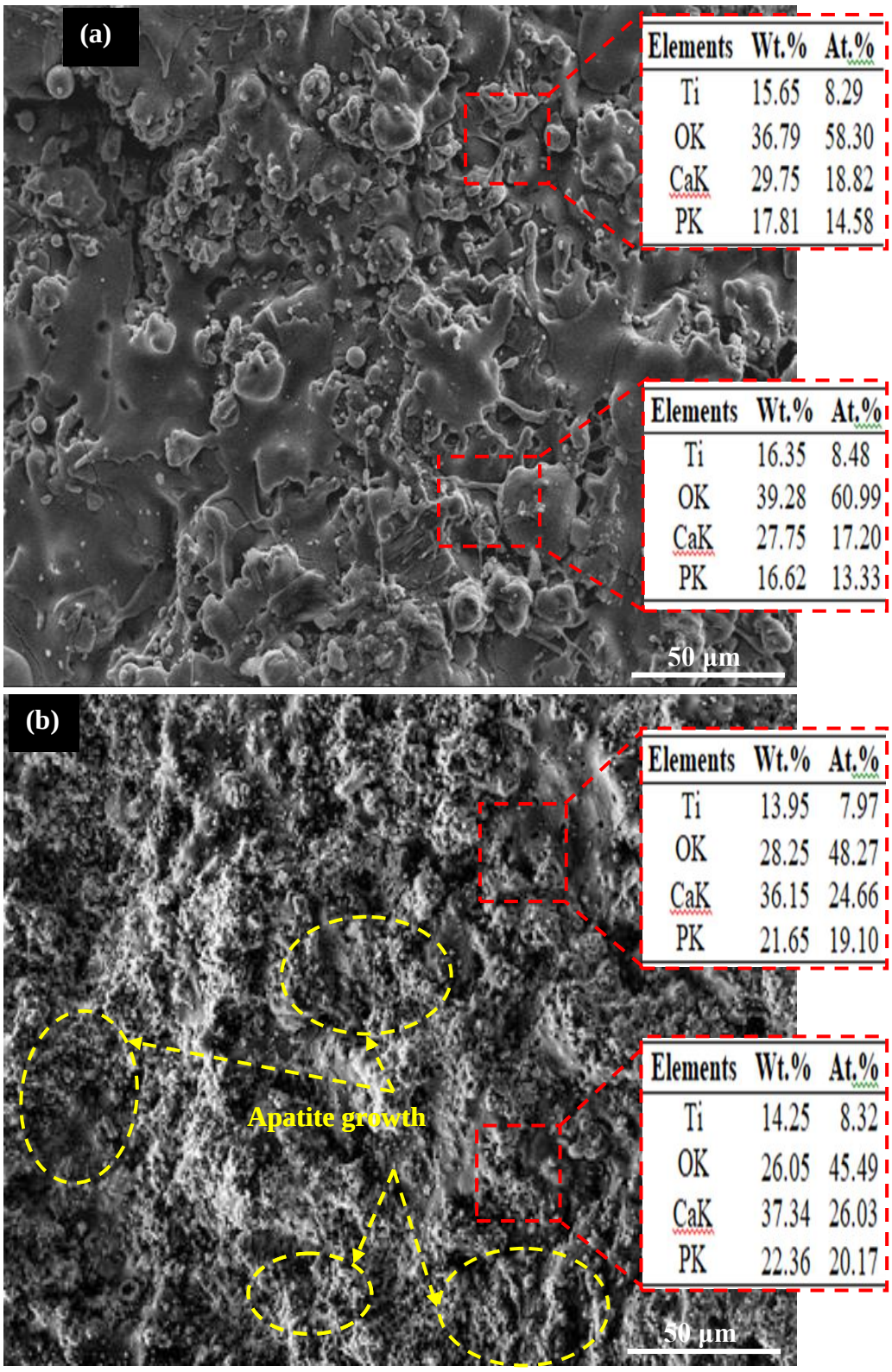

Figure 5.22. Morphology and EDS analysis of HA-30TiO_2 coated surface (a) before and (b) after corrosion test

5.3.1.4. In-vitro bioactivity behavior

Figure 5.23, 5.24, 5.25, and 5.26 shows the cell viability and activity such as cell count, optical density of MTT assay, DNA content, ALP-like differentiation activity on un-coated, *HA*, HA-15TiO_2 and HA-30TiO_2 coatings on 1st day, 3rd day, and 7th day. Analysis of variance (ANOVA) has been carried out to test the significance of obtained data and it has been found that all data is statically significant ($p < 0.001$) at a 95% confidence interval. The cell growth and proliferation depend upon the surface energy, which further depends on surface chemistry. Figure 5.23 shows the cell growth number on the on un-coated, *HA*, HA-15TiO_2, and HA-30TiO_2 coated samples.

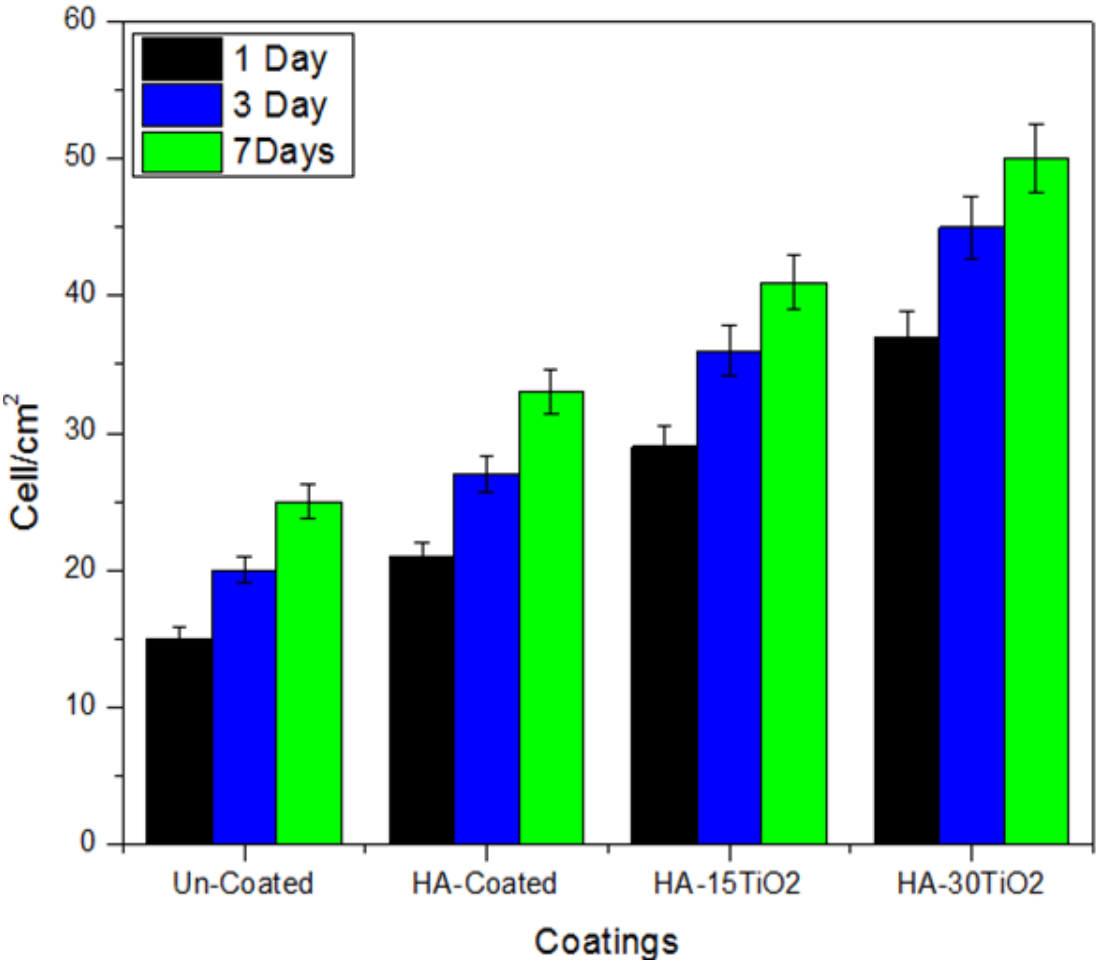

Figure 5.23. Cell viability and activity: Cell count activity on un-coated, *HA*-coated, HA-15TiO_2 and (g-h) HA-30TiO_2 β-TNTZ alloy samples

The cell growth was more on the coated samples and a higher number of cell growth was found on the *HA/TiO_2* coated surfaces. This is attributed because *HA*

facilitates the development of apatite, and apatite promotes other biological activities such as cytoplasmic extensions, filopodia charges, and extracellular matrix (ECM) retraction and makes chemical integration with coating surface. Moreover, the presence of the TiO_2 lamellar structure in the matrix, acted as a reservoir to absorb protein that escalated the osseointegration process. Figure 5.24 shows the cell proliferation in terms of optical density obtained after MTT assay for un-coated, *HA*, HA-15TiO_2, and HA-30TiO_2 coated samples.

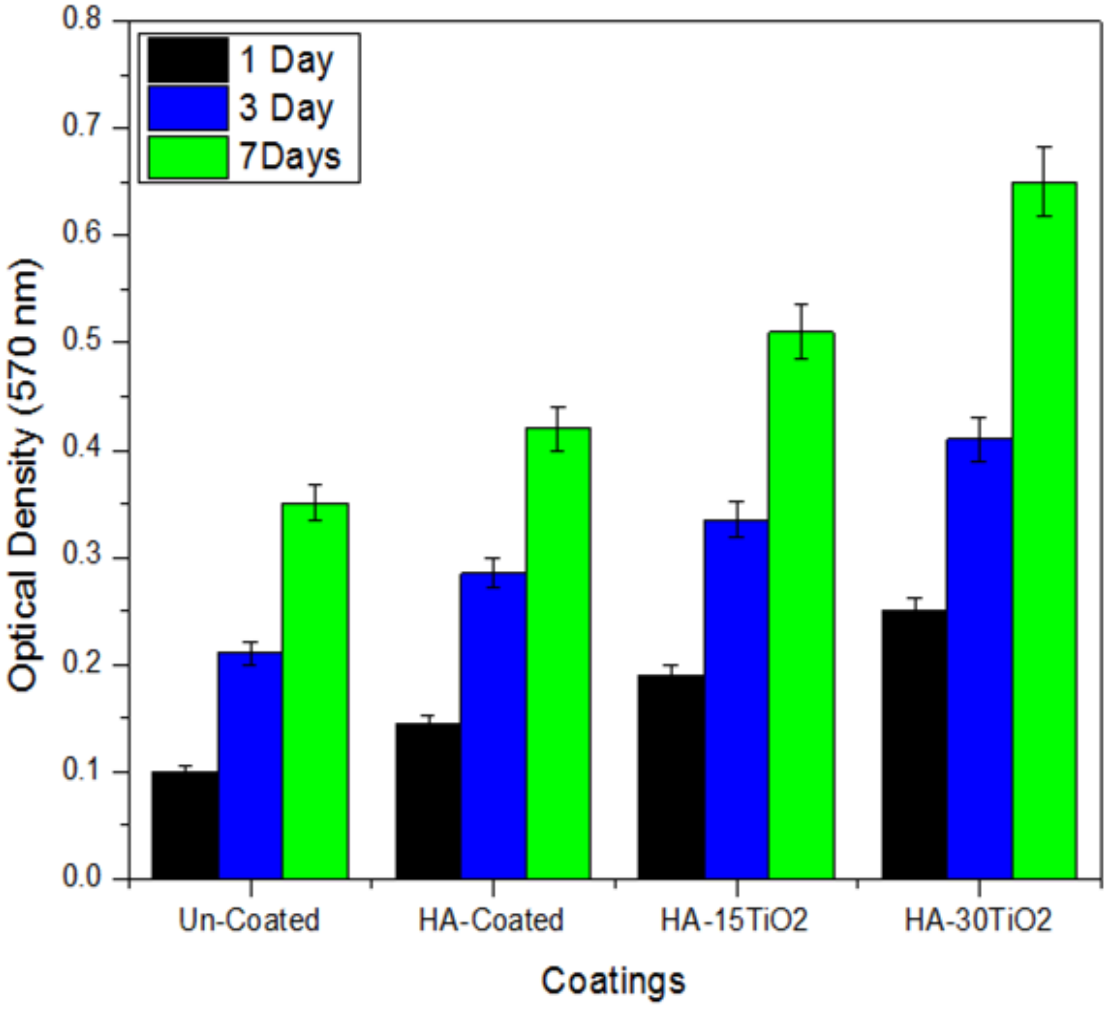

Figure 5.24. Cell viability and activity: MTT assay activity on un-coated, HA, HA-15TiO_2, and HA-30TiO_2 coated β-TNTZ alloy samples

MTT assay suggested that no cytotoxic effect has been observed on Mg-63 cells of the different coating compositions. The optical density was found on the coated samples and higher optical density was found on the *HA/TiO_2* coated surfaces. Cell

proliferation increased with the growth of cells. The DNA content growth dependent on the protein absorption. From Figure 5.25 it can be seen that *HA/TiO₂* coating samples had higher DNA content. The TiO_2-reinforced HA absorbs more protein as compared to the untreated and HA-treated surface. Figure 5.26 shows the ALP-like differentiation activities of MG-63 cells on the un-coated, HA, HA-15TIO_2, and HA-30TIO_2 coated samples. Greater ALP-like differentiation-activities were observed on the HA-30TIO_2 coated samples because of the high serum level.

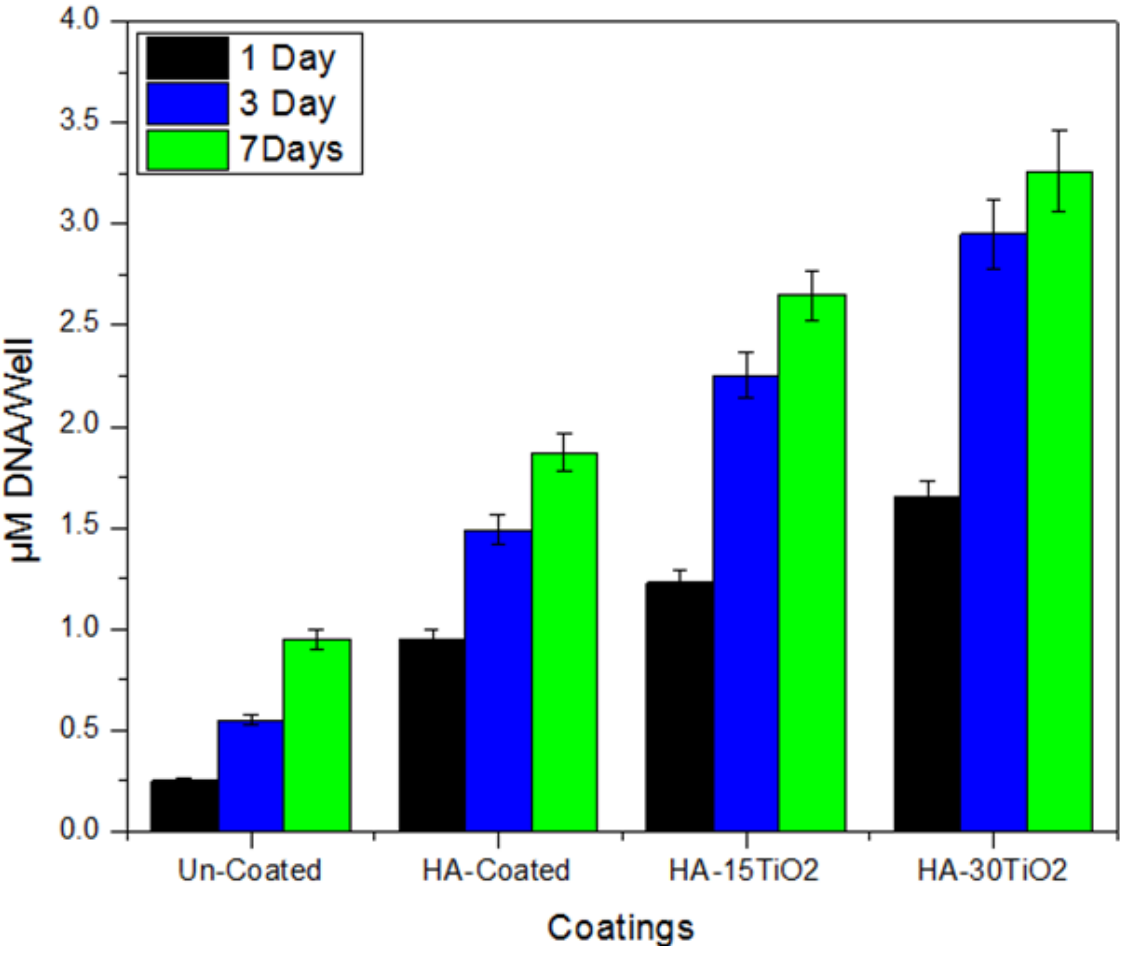

Figure 5.25. Cell viability and activity: DNA activity on un-coated, *HA*, *HA-T_x* and *HA-T_y* -coated β-TNTZ alloy samples

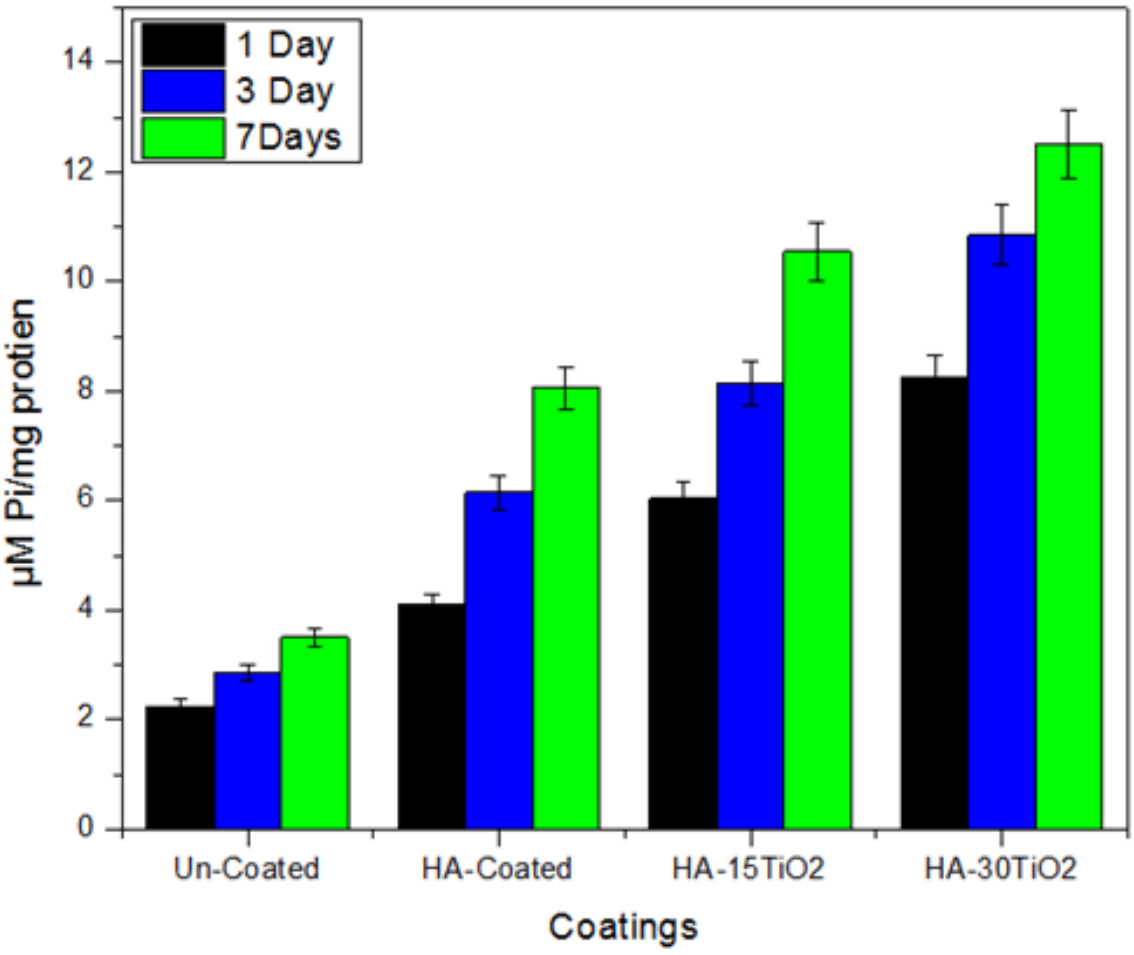

Figure 5.26. Cell viability and activity: ALP activity on un-coated, HA, HA-15TiO_2, and HA-30TiO_2 coated β-TNTZ alloy samples

Figure 5.27, 5.28, 5.29, and 5.30 shows the attached cell morphology on un-coated, *HA*, HA-15TiO_2, and HA-30TiO_2 coated samples after 3rd day, respectively. Various biological activities like cytoplasmic extensions, redirection of extracellular matrix (ECM), and filopodia/lamellipodia augmentation were observed in all specimens surface that confirmed that cells were attached and grown on samples. Figure 5.27 (a-c) shows the optical image, florescent, and FE-SEM image of cells attached on un-coated samples and it can be seen that un-coated surface exhibit less degree of attached cells. This is because the surface of un-treated alloy is non-active and promotes less growth and proliferation of Mg-63 cells.

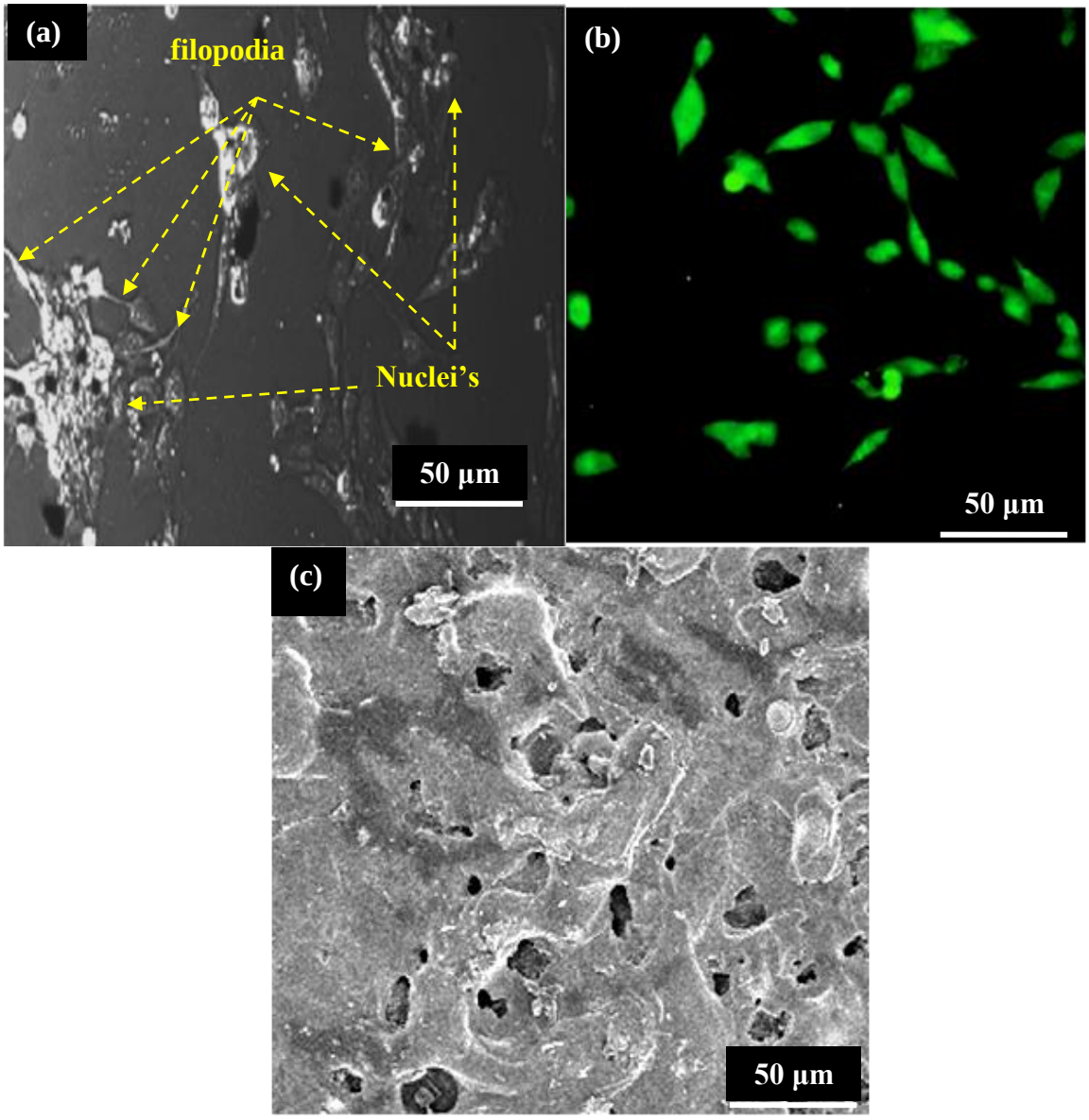

Figure 5.27. Cell adhesion & Florescent image after 3rd day of culturing on un-coated surface (a) Optical image (b) Fluorescent image, and (c) FE-SEM image

Figure 5.28 (a-c) shows the optical image, florescent, and FE-SEM image of cells attached on HA-coated samples and it can be seen that HA-coated surface exhibit high degree of attached cells as compared to un-treated cell. The formation of large nuclei can be seen. This is because HA is a bone mineral element which promotes bone in-growth, as a result HA-coated surface comprised more cell attachment and growth compared to un-treated surface.

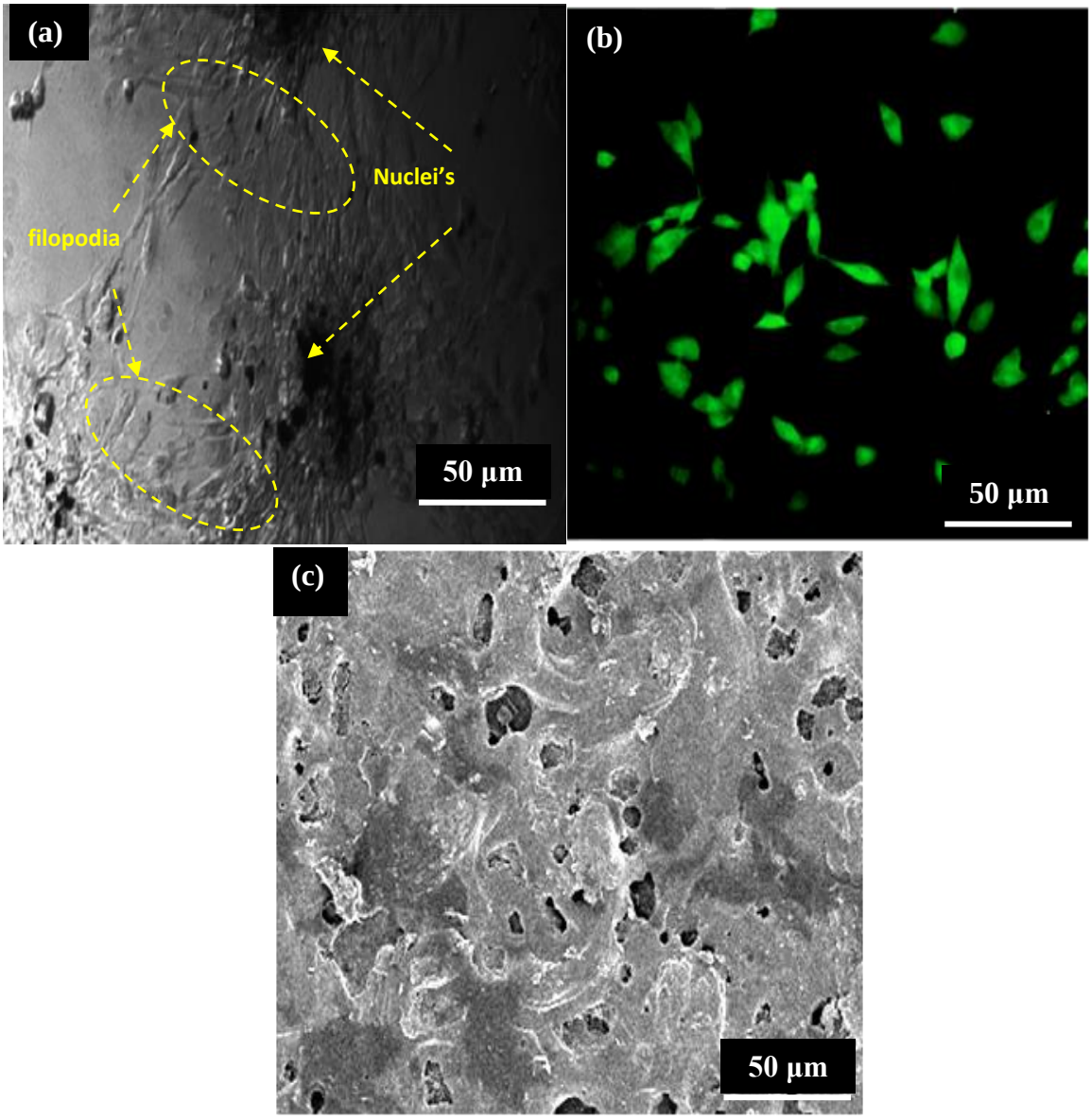

Figure 5.28. Cell adhesion & Florescent image after 3rd day of culturing on un-coated surface (a) Optical image (b) Fluorescent image, and (c) FE-SEM image

Figure 5.29 (a-c) shows the optical image, florescent, and FE-SEM image of cells attached on HA-15%TiO_2 coated samples and it can be seen that HA-15%TiO_2 coated surface exhibit high degree of attached cells as compared to un-treated and HA-coated surface. The formation of large nuclei can be seen. The HA-15%TiO_2 coated samples exhibited a high degree of attached and spread cells. The formation of large nuclei can be seen. The Mg-63 cells were completely attached, proliferated on the whole surface of the HA-15%TiO_2 coated substrate, and made maximum contact with coatings. The

green florescent represents the live, viable, and healthy cells on the coatings. This is because TiO_2 in HA-matrix acted as reservoir for protein absorption and promotes cell growth.

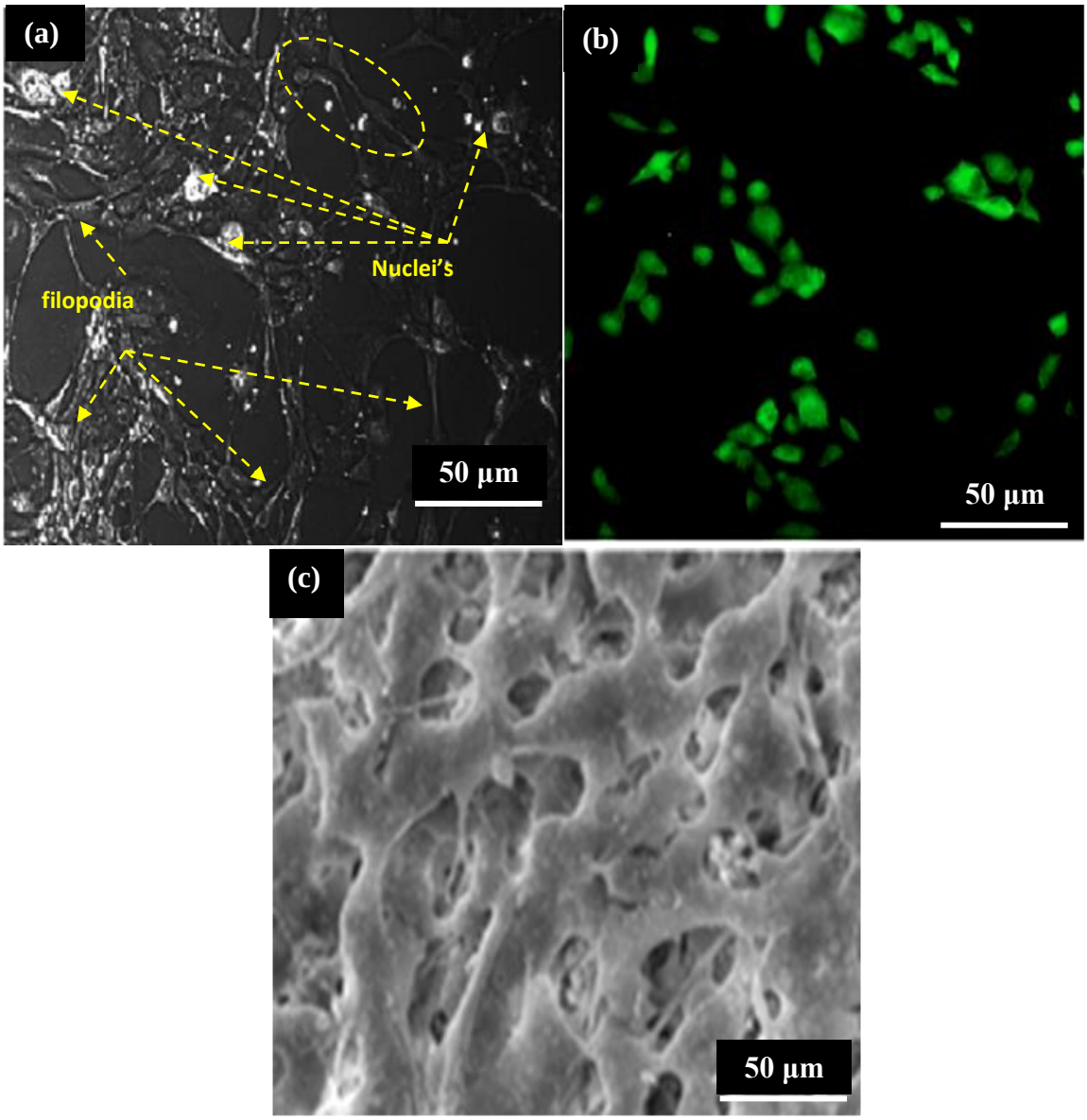

Figure 5.29. Cell adhesion & Florescent image after 3rd day of culturing on HA-15TiO_2 coated surface (a) Optical image (b) Fluorescent image, and (c) FE-SEM image

Figure 5.30 (a-c) shows the optical image, florescent, and FE-SEM image of cells attached on HA-30%TiO_2 coated samples and it can be seen that HA-30%TiO_2 coated

surface exhibit highest degree of attached cells as compared to un-treated, HA-coated, and HA-15%TiO_2 surface.

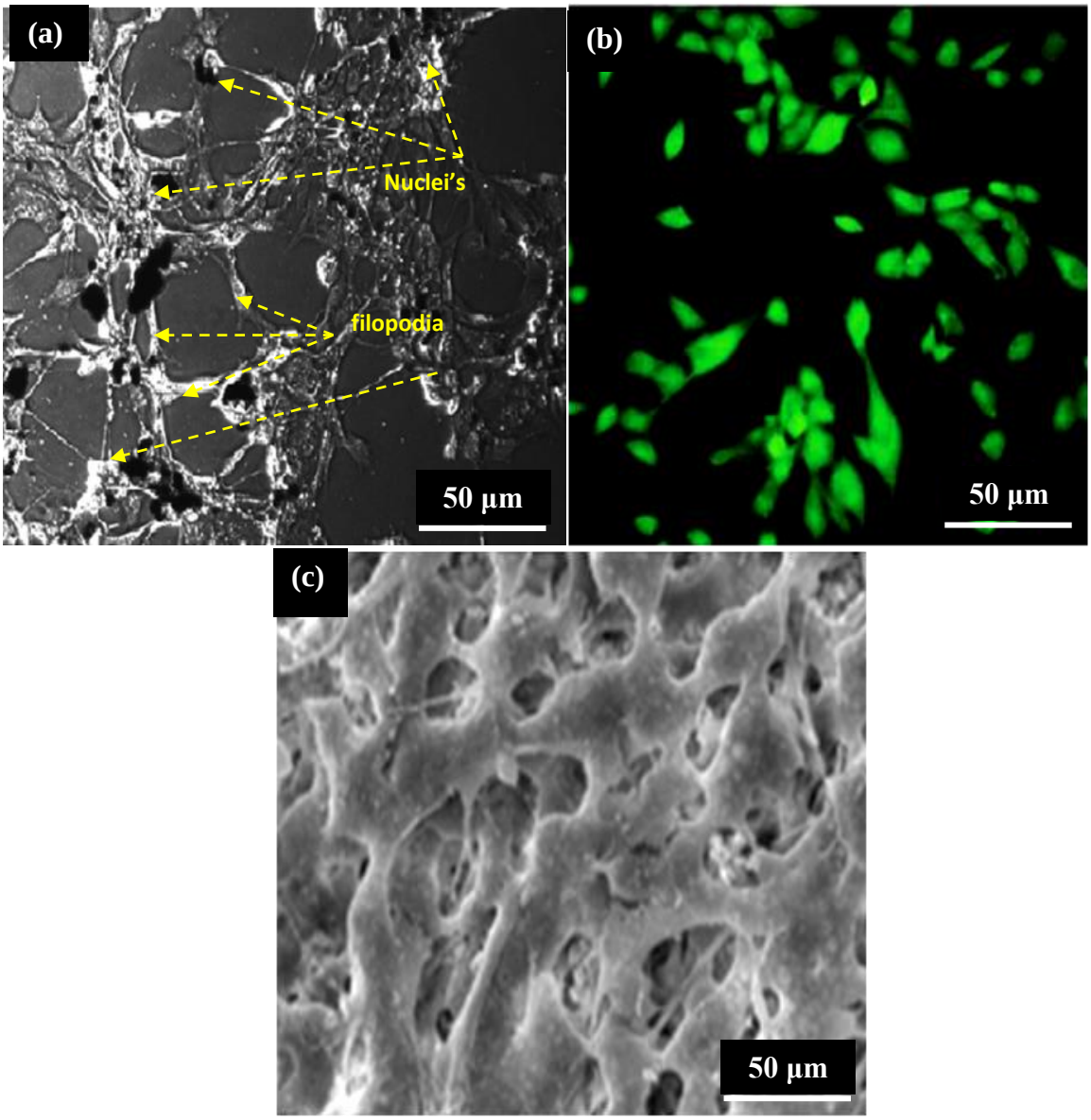

Figure 5.30. Cell adhesion & Florescent image after 3rd day of culturing on HA-30TiO_2 coated surface (a) Optical image (b) Fluorescent image, and (c) FE-SEM image

Furthermore, green florescent represents the live, viable, and healthy cells on the coatings. The SEM-micrograph of attached cell morphology on the surface of the sample on 3rd day and excellent cell growth and proliferation can be confirmed. The higher proliferation and spreading of Mg-63 cells over a wider surface area on the

HA-30%TiO_2 coated substrate was seen as compared to *HA* and uncoated surfaces. From the observation, it can be seen that both HA-15%TiO_2 and HA-30%TiO_2 coatings possessed a higher cellular proliferation rate as compared to *HA*-coated and un-coated specimens. The findings thus indicate that the surface chemistry of the *HA/TiO_2* coating helped to increase the bone ingrowth and osseointegration process. Similarly, Zheng *et al.* reported that *HA/TiO_2* coating possessed good bioactivity and promotes cell growth [203].

5.3.2. Study-II

Surface morphology of HA and HA-TiO_2 coatings obtained at process parameters as presented in Table 5.12 has been analyzed. Where the effect of feed stock concentration, gas flow rate, and powder feed stock has been considered. In this case coating thickness was controlled to 100-125 μm thick.

Table 5.12. Plasma Spray Parameters

Spraying Parameters	Value
Primary Gas Flow (Argon)	35 NLPM
Secondary Gas Flow (Hydrogen)	2.0 NLPM
Voltage	65 volt
Current	500Amp
Feed rate	40 gm/min
Spray Distance	120 mm

5.3.2.1. Surface morphology of coating

Figure 5.31 shows the coating morphologies of HA, HA-30%TiO_2 coated surface at different views (top and cross-sectional). The typical micro-structural features associated with plasma sprayed coatings, for instance, spherical particles, partially melted particles, micro-cracks, and agglomerates can be seen in the deposited coatings. From the SEM micrographs, both coated specimens showed heterogeneous surface fusions of partially and fully melted particles consists of high ridges of deposited molten metal (shown by the yellow arrow), splattered fully melted molten pool (shown by white arrow), globules (shown by the red arrow), and surface porosities (shown by yellow circles) [154]. Further, the globular distribution of the

particles is mainly due to the deposition of micron and sub-micron scaled un-melted particles. The HA-coated surface shows numerous craters, the high degree of globules of unmelted particles, and interconnected surface porosities, as can be seen in Figure 5.31. Further, the amalgamation of fully melted amorphous HA with solid precipitates and pure liquid precipitations is possible because of the reaction that takes place in the plasma jet [162]. The build-up of characteristic fragmented structures has also been seen owing to the internal rupture of liquid precipitates afterward the solid shell formation. The repetition of this process has produced fine globular particles [204]. Submicron scale surface porosities were observed on the coated surface as can be seen on point A in Figure 5.31(a). The formation of surface porosities is because of the high temperature that helped in the disintegration of the HA into Ca $3(PO_4)_2$, and CaO phases and during deposition, and these phases formed porous structure and amorphous hump. At higher magnification (×5000), a clear picture of submicron–scale porosities with pore ranging 0.3-0.850 μm can be seen, presented by yellow circles in Figure 5.31(b). Similarly, HA-30TiO_2 coated surface has been found of less defective when compared to the HA-coated surface, see Figure 5.32(a). The reinforcement of TiO_2 was seen and presented by the yellow arrow in Figure 5.32(b). It has been found that the surface was comparatively denser than the HA-coated surface. The agglomeration of HA-TiO_2 nano-particles was also more and the reinforcement of TiO_2 in HA has prevented the formation of larger pores.

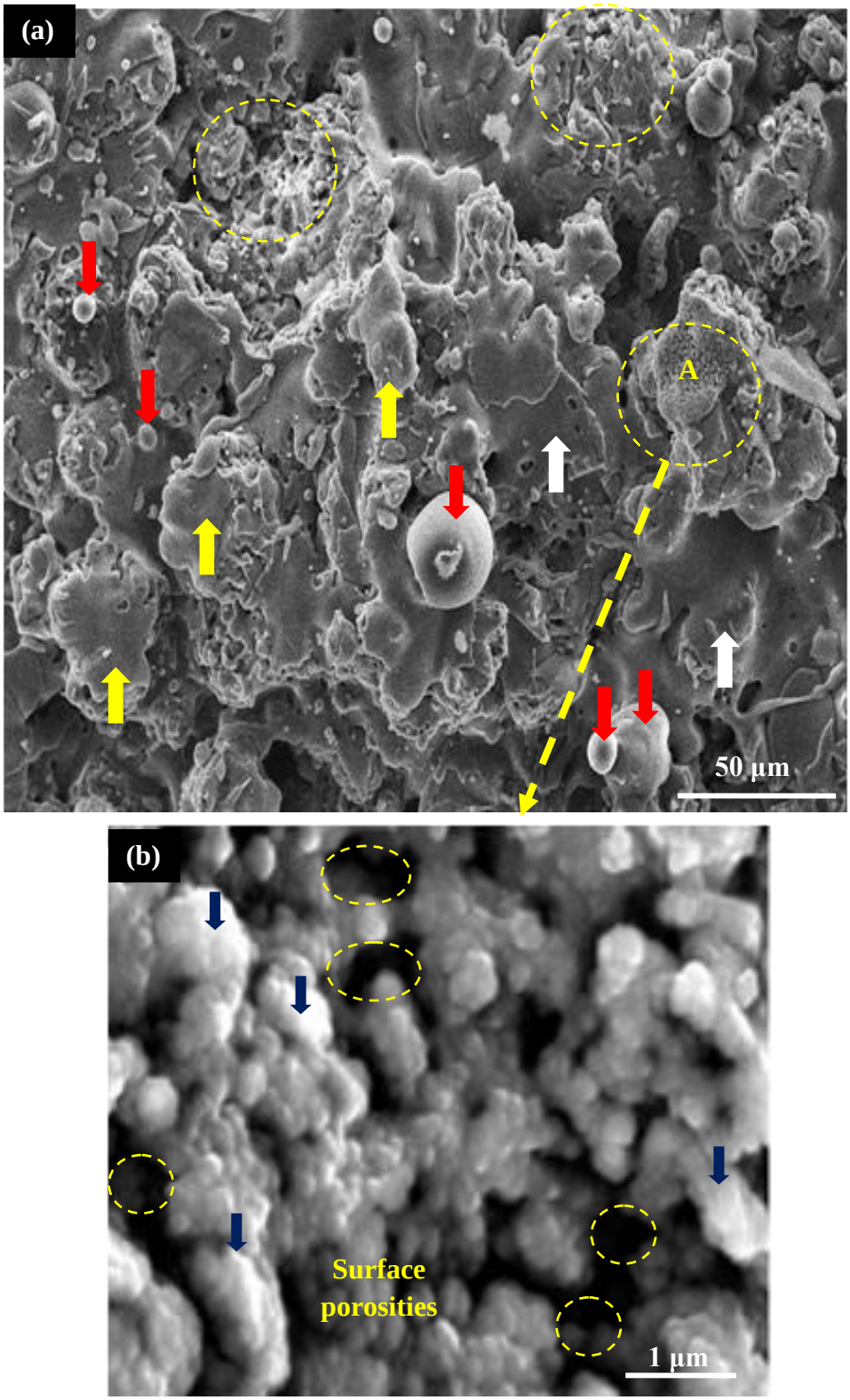

Figure 5.31. SEM morphology and EDS spectrum of HA-coated Ti-Nb-Ta-Zr alloy surface [(a-b) ×500 and (c-d) ×5000]

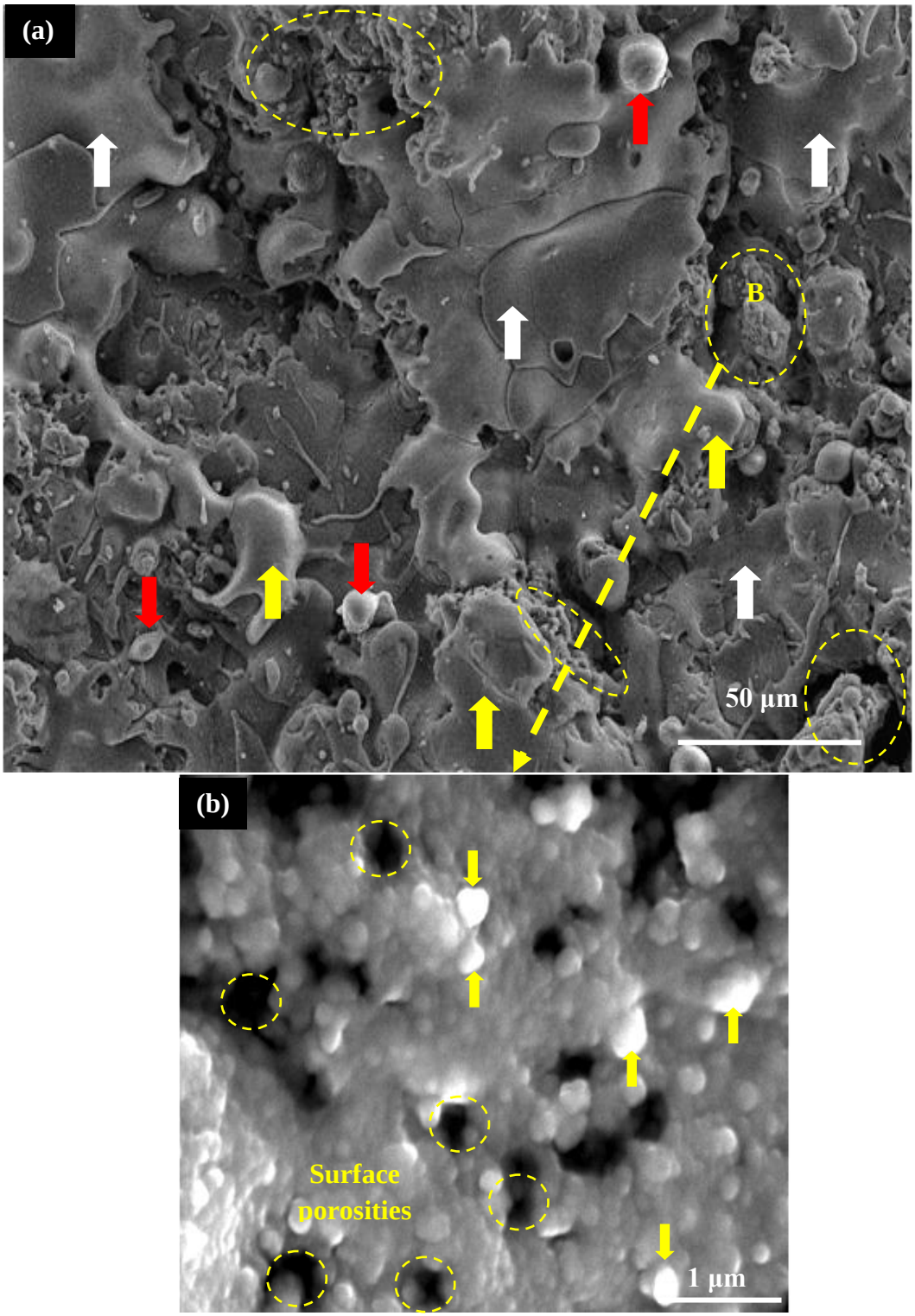

Figure 5.32 SEM morphology and EDS spectrum of HA-30TiO_2 coated Ti-Nb-Ta-Zr alloy surface [(a-b) ×500 and (c-d) ×5000]

From the higher magnification (×5000) micrograph, nano-scale surface porosities were generated in HA-TiO_2 coating but with less intensity. The as visible pores, in this case, are limited to a range of 200-600 nm. The agglomeration of HA-TiO_2 and generation of un-melted nano-particles has been attributed to the difference in the melting point of HA (1500 ºC) and TiO_2 (1800 ºC). A similar observation was reported by researchers [154].

Figure 5.33 shows the EDS spectrum and elemental analysis of HA and HA- TiO_2 coatings. The associated EDS spectrum of HA coating shows the high-intensity peaks of calcium (Ca), phosphorous (P), and oxygen (O) beside base elements (Ti, Nb, Ta, Zr), that confirms the deposition of HA, refer Fig. 5.33. The ratio of Ca and P in the elemental composition was found 1.67 and the finding is in line with the previously published research [163]. The elements formed various bio-ceramic based oxides and improved the corrosion resistance and biomechanical performance of the alloy [204-205]. The associated EDS spectrum of HA-TiO_2 coating showed the high-intensity peaks of Ti, Ca, P, and O elements to confirm the presence of TiO_2 and HA, refer Fig. 5.34. Similarly in this, the ratio of Ca and P was found 1.67, which confirmed that HA was disintegrated into non-apatite and α/β TCP, CaO, TTCP along with TiO_2 phases. This resulting bio-ceramic coating has increased the surface energy and this high surface energy enhanced bioactivity which will helpful in bone-ingrowth, osseointegration, and improved implant stability [206-207].

Figure 5.35 shows the XRD pattern of un-treated, HA-coated, and HA-TiO_2 coated β-phase Ti-Nb-Ta-Zr alloy specimens. From the XRD pattern of un-treated β-phase Ti-Nb-Ta-Zr alloy, pattern metastable β-type phase Nb, Ta, and Zr can be seen. From the XRD pattern of as-sprayed HA-coated samples, bioceramic phases, for instance, α/β TCP phases, Ca3(PO4)2, CaO can be observed between diffraction angles 30.5º and 31.7º, which were owing to the disintegration of HA as a consequence of thermal sequence and speedy cooling involved in plasma spray process [208-211].

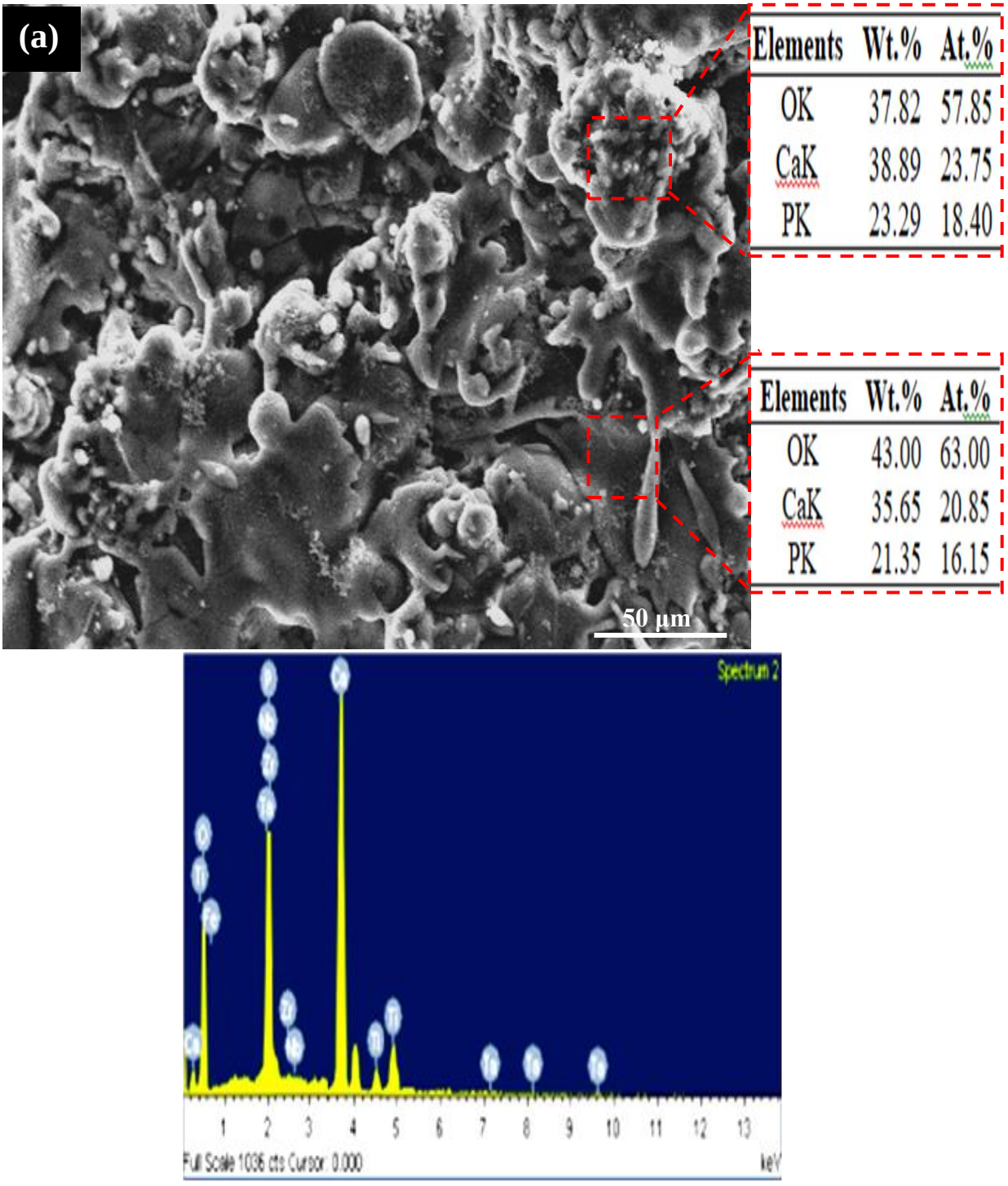

Figure 5.33. Morphology and EDS elemental analysis of HA coatings

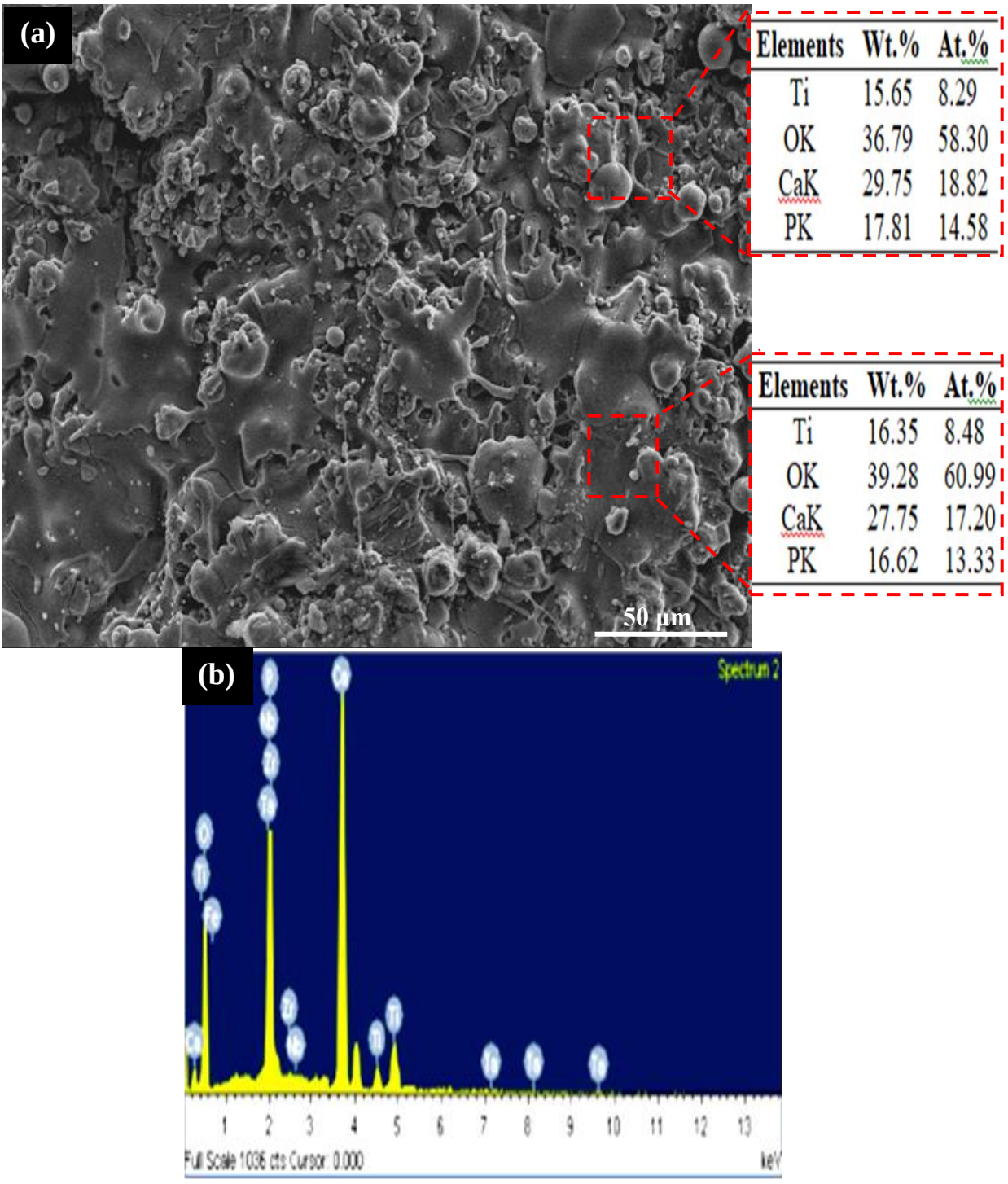

Figure 5.34. Morphology and EDS elemental analysis of HA-30TiO_2 coatings

From the XRD pattern of as-sprayed HA-TiO_2 coated samples, bioceramic phases, for instance, non-apatite and α/β TCP phases, Ca3(PO4)2, CaO, TTCP along with TiO_2 can be observed, which were resulted by the disintegration and reaction of HA and TiO_2. It has been observed that the XRD peaks of pure HA are not sharper and this is

attributed to the conversion of crystalline content of HA into the amorphous phase during the plasma spray process.

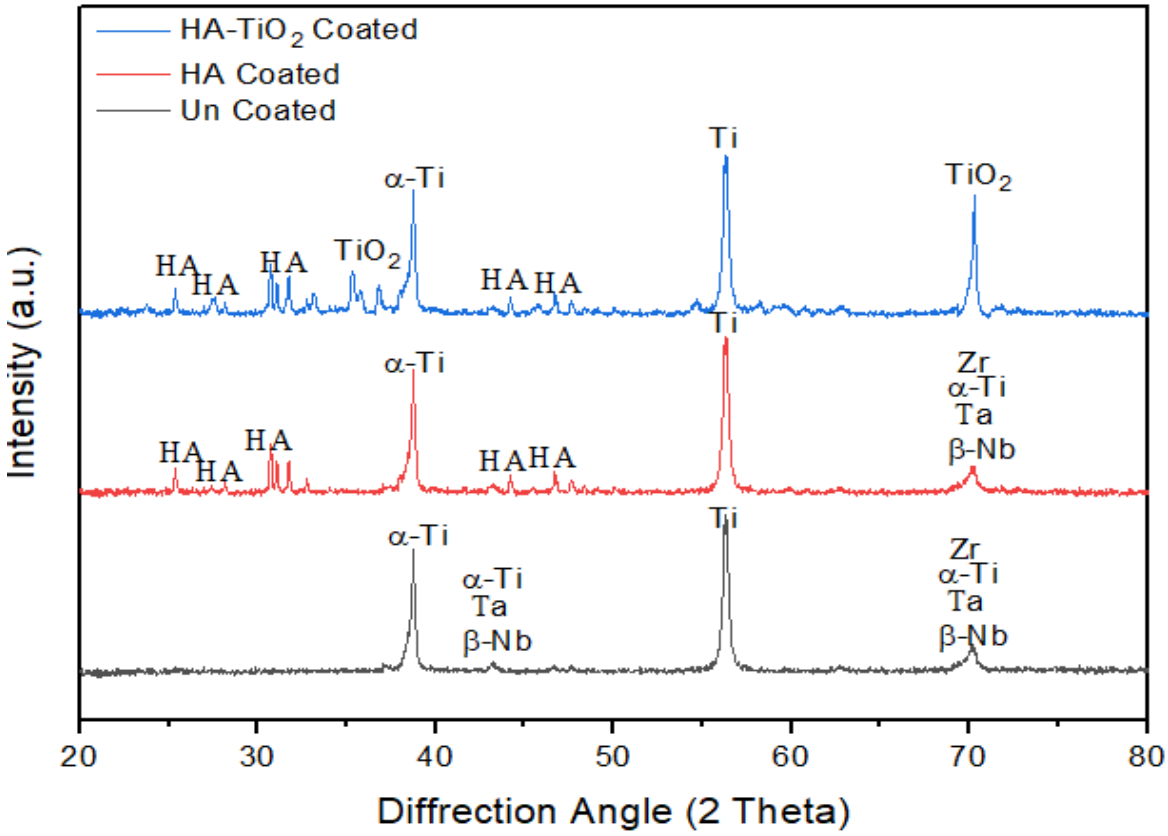

Figure 5.35. XRD pattern of un-coated, HA-coated, and HA-TiO_2 coated β-phase Ti (Ti-Nb-Ta-Zr) alloy

Figure 5.36 and 5.37 shows the cross-section morphology of HA and HA-TiO_2 coated β-phase Ti alloy, respectively. Coating thickness and the resulting interface can also be seen. From the micrographs, it can be seen that the coating thickness ranged between 100–125 μm. The specific thickness of the coating, in the case of HA and HA-TiO_2, has been found as 125 μm and 120 μm, respectively. Further, the interface between coating and substrate has been identified as a strong mechanical bonding and interlocking to offer high adhesion strength that enhances implant stability. It is evident from Figure 5.36(a) that the as-sprayed HA coating surface comprised of unevenly distributed micro-cracks and micro-holes of different sizes. This may be due to the disintegration of HA into Ca, P, and O phases, which has generated a porous structure in the coating. Figure 5.36(b) shows the EDS mapping of the HA-coated layer.

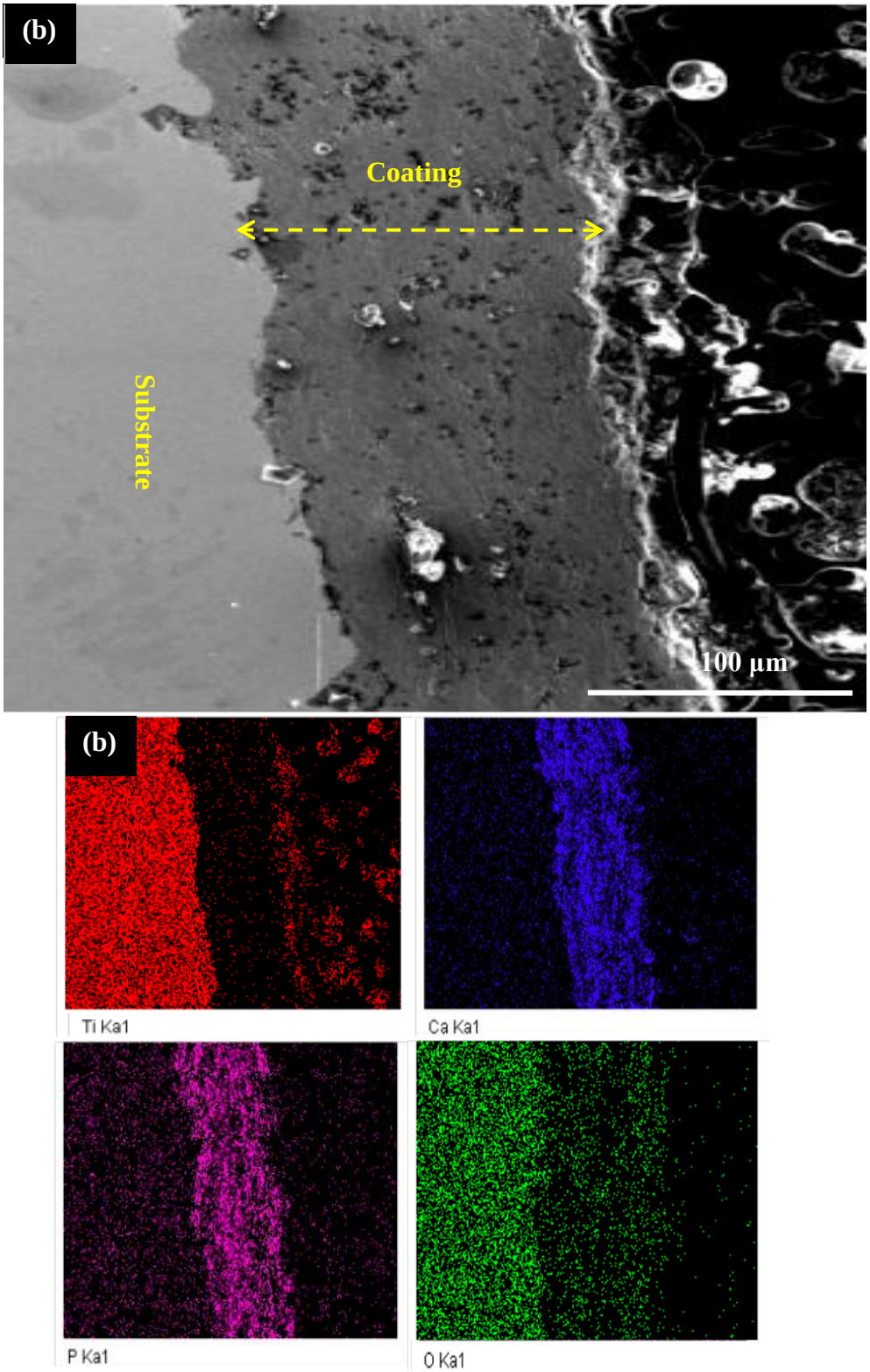

Figure 5.36. Cross-section micrograph of HA-coated Ti-Nb-Ta-Zr alloy surface

Further, from the elemental mapping of HA-coated implant, it can be seen that only elements such as Ca, P, and O has been identified, no other elements were observed. The observation was confirmed and conferred that only pure HA was successfully deposited without any contamination.

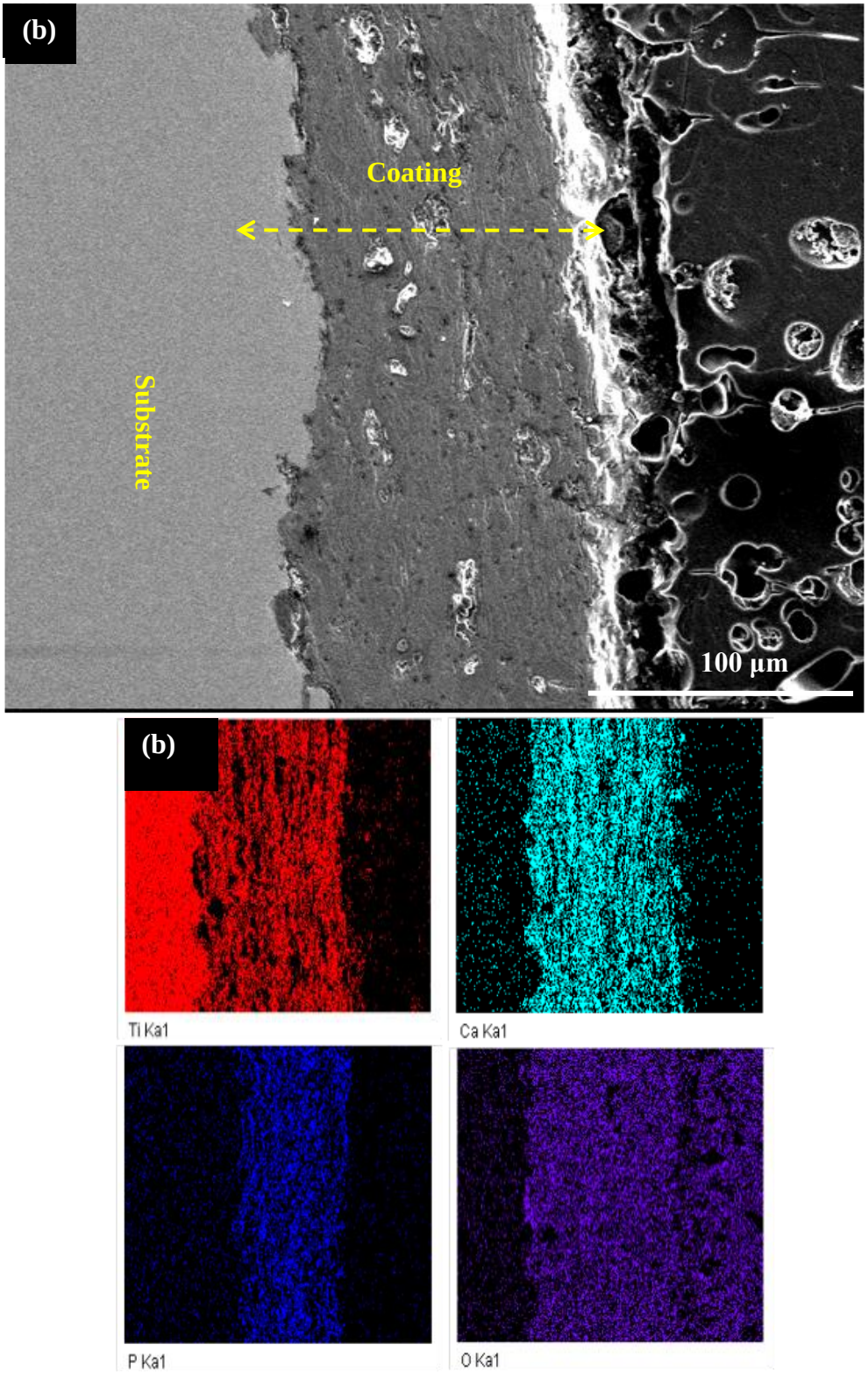

Figure 5.37. Cross-section micrograph of HA-TiO_2 coated Ti-Nb-Ta-Zr alloy surface

Similarly, Figure 5.37(a) shows the cross-section of the HA-TiO_2 coated specimen's surface. Conversely, the microstructure and morphology of the HA-TiO_2 coated sample are quite different as compared to as-coated specimens of HA samples. Negligible micro-cracks, porosities, un-melted particles, and fewer amounts of micro-holes were witnessed in the HA-TiO_2 coated sample. The TiO_2 formed lamellar structure in the HA matrix, acted as a reservoir to hold the protein in the host body, and improved the osseointegration and corrosion resistance [157]. Figure 5.37(b) shows the EDS mapping of the HA-TiO_2 coated layer and it can be seen that the coated elements (Ti, Ca, P, and O) were evenly dispersed in the layer, without any type of impurities. The observation was confirmed and conferred that only pure HA-TiO_2 was successfully deposited without any contamination.

Further, the interface between coating and substrate has been identified as a strong mechanical bonding and interlocking to offer high adhesion strength that enhances implant stability. It is evident from Figure 5.36(a) that the as-sprayed HA coating surface comprised of unevenly distributed micro-cracks and micro-holes of different sizes. This may be due to the disintegration of HA into Ca, P, and O phases, which has generated a porous structure in the coating. Figure 5.36(b) shows the EDS mapping of the HA-coated layer. Further, from the elemental mapping of HA-coated implant, it can be seen that only elements such as Ca, P, and O has been identified, no other elements were observed. The observation was confirmed and conferred that only pure HA was successfully deposited without any contamination. Similarly, Figure 5.37(a) shows the cross-section of the HA-TiO_2 coated specimen's surface. Conversely, the microstructure and morphology of the HA-TiO_2 coated sample are quite different as compared to as-coated specimens of HA samples. Negligible micro-cracks, porosities, un-melted particles, and fewer amounts of micro-holes were witnessed in the HA-TiO_2 coated sample. The TiO_2 formed lamellar structure in the HA matrix, acted as a reservoir to hold the protein in the host body, and improved the osseointegration and corrosion resistance [157]. Figure 5.37(b) shows the EDS mapping of the HA-TiO_2 coated layer and it can be seen that the coated elements (Ti, Ca, P, and O) were evenly dispersed in the layer, without any type of impurities. The

observation was confirmed and conferred that only pure HA-TiO_2 was successfully deposited without any contamination.

The bone-ingrowth and osseointegration were also dependent on the surface roughness, porosity, and crystallinity. High surface energy enhanced bone in-growth and osseointegration. Crystallinity (%), porosity (%), and surface roughness of HA and HA-TiO_2 coating are shown in Table 5.13. The XRD data of HA and HA-TiO_2 coating between 20º to 60º angle range was used to estimate the crystalline content. The observed results revealed that the HA-TiO2 coating exhibited more crystalline content (89.6%) as compared to HA coatings (74.8%). The disintegration of HA at high temperature has been confirmed after observing a small hump α-TCP, β-TCP, and TTCP phases on the XRD pattern between 30º and 32º. On the other hand, the amorphous hump was not identified, however, a small amount of CaO has been observed at 37.7º [208-211].

Table 5.13 Crystallinity (%), porosity (%) and surface roughness of as-sprayed coatings

	Grit Blasted Ti-Nb-Ta-Zr Substrate	**HA coating**	**HA- TiO_2 Coating**
Crystallinity (%)	-	74.8	89.6
Porosity (%)	-	3.28	1.27
Surface Roughness (R_a)	4.04 μm	4.65 μm	3.5 μm

The porosity in the as-coated HA and HA-TiO_2 coatings was found as 3.28 and 1.27%, respectively. This is mainly due to the presence of TiO_2 reinforcement in HA, which formatted porous structure and helped in the formation of biomimetic phases on the coating. The average of five readings was recorded for surface roughness. It has been reported that the size of the particles can affect the surface roughness. Gross and Muller reported that the surface roughness of HA coating was measured 4.8, 7.4, and 9.5 μm for feedstock powder particles size of 20-40, 40-60, and 60-80 μm [209].

Figure 5.38 shows the 3D surface plot of surface roughness. The surface roughness for the as-coated HA and HA-TiO_2 coatings was found to be 4.65 μm and 3.5 μm, respectively. The skewness and kurtosis are the important parameters of surface roughness that affect the corrosion and wear performance of biomedical implants. The skewness in the surface roughness of both surfaces was negative. The HA-coated surface has very deep valleys in the layer as a result roughness is a high Kurtosis of more than 9.5, this may affect the corrosion and wear performance. On the other hand, HA-TiO_2 coated surfaces have valleys in the layer but less deep as compared to HA-coatings. The kurtosis in the case of the HA-TiO_2 coated surface is less near 4.5, which results in better surface finish as compared to HA-coatings. Thus, the surface is better for tribological performance and wear-resistant. The obtained surface roughness was the lowest of the available knowledge of the scientific literature and also sufficient to promote bone-ingrowth around the implant [211].

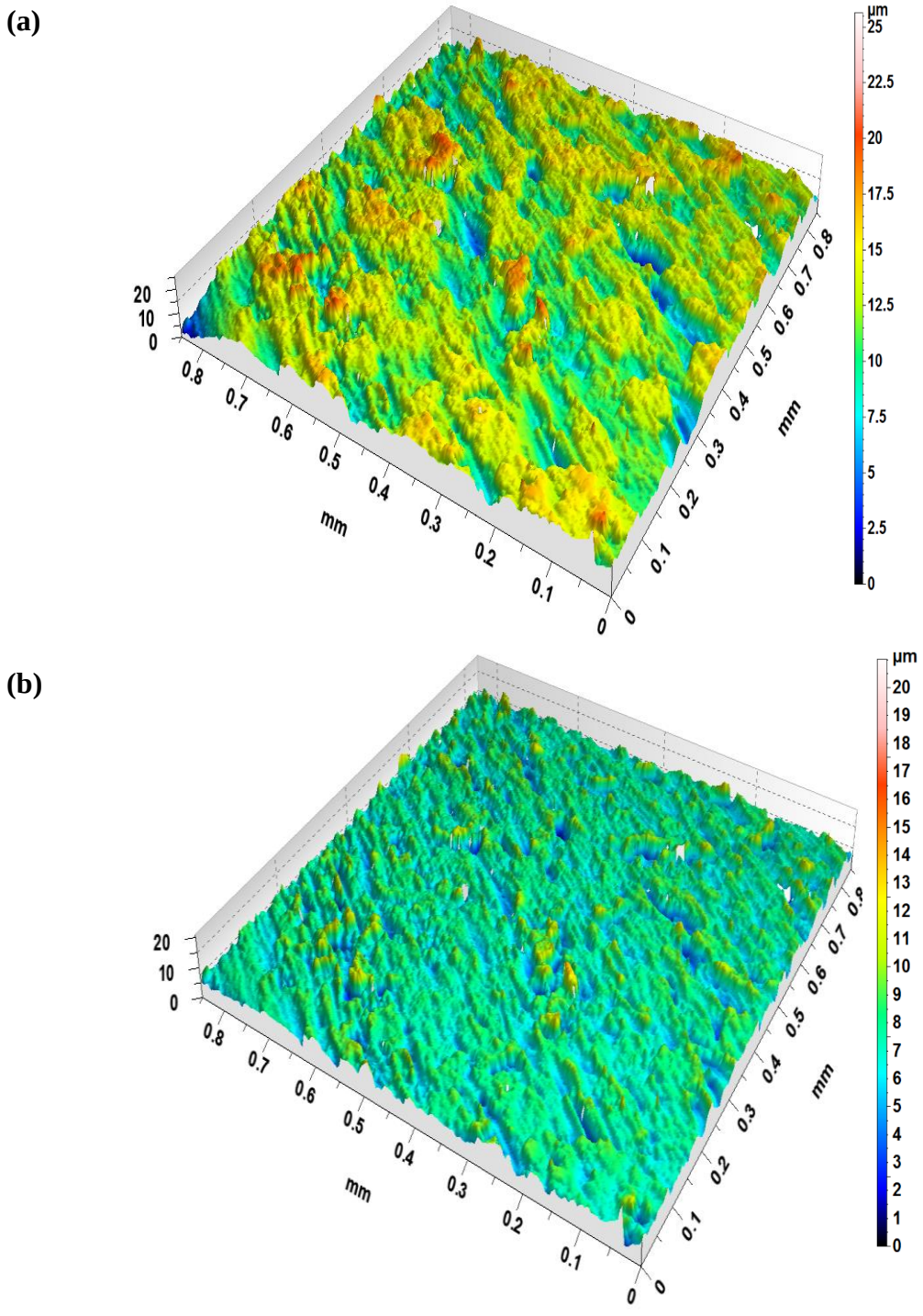

Figure 5.38. 3D surface plot of surface roughness of HA and HA-TiO_2 coatings

5.3.2.2. Biomechanical properties

Figure 5.39 and 5.40 shows the mechanical properties such as surface hardness and adhesion strength of HA and HA-TiO_2 coatings. Figure 5.39(a) showed the nano-indentation plot of HA and HA-TiO_2 coatings. The surface hardness and elastic modulus of the coatings measured observed by the nano-indentation technique. The mechanical properties of coating depend upon the microstructure and purity of coating. The hardness increased with the increase in the alloying of TiO_2 in HA. The hardness of as-sprayed HA and HA-30wt.% coatings were measured 1.65 GPa and 2.95 GPa, respectively. The HA transformed into Ca/P based amorphous structure during the deposition that results in coating contains cracks, micro-size voids, and porosities which leads to decrease in the mechanical properties. With the alloying of TiO_2 in HA, the brittleness reduced and the deposited coating possessed dense and lamellar nanostructure which leads to increase in the mechanical properties. The elastic modulus was dependent on the hardness of the coating. With the addition of TiO_2 in HA, brittleness reduced and ductility improved, as a result, the strength of coating improved and results in the increase in the elastic modulus [153-154]. The elastic modulus of as-sprayed HA and HA-30wt.% coatings were measured 15.7 GPa, and 41.75 GPa, respectively. The adhesion strength of the coating is increased with the addition of TiO_2 in HA, refer Figure 5.39(b). The reinforcement of TiO_2 in HA prevents the formation of pinholes at the interface. The adhesion strength of HA and HA-TiO_2 coating was measured around 25.79 MPa and 32.95 MPa, respectively. Figure 5.40 shows the optical micrograph of tensile bond strength and failure mechanism of coatings. Figure 5.40 (a-b) shows the optical micrograph of tensile bond strength specimens of HA and HA-TiO_2 coatings. From the micro-graph, it can be seen that the *HA* coating was delaminated or remove from the surface along with glue as compared with HA-TiO_2. This is because the *HA* coating was poorly mechanically-bonded with the substrate and exhibit cracks in the interface which was removed from the substrate; thus results in low adhesion strength. The HA-TiO_2 coating possessed higher adhesion strength as compared to HA-coatings because of two reasons (i) reinforcement of TiO_2 particles and (ii) phase purity and content. The nano-sized powder particles in feedstock suspension significantly reduced the tensile

strength in the deposited coating and, therefore, increased the adhesion strength [208]. The microstructure, phase content, and purity also affect the adhesion strength. The HA-coating has a porous microstructure with unevenly distributed micro-cracks. Moreover, during deposition HA transformed into Ca and P contents, and the crystallinity of HA was decreased and this results in low adhesion strength. On the other hand, owing to the presence of TiO_2, a laminar structure was obtained that reduced the formation of micro-cracks and porosities. Figure 5.40(c) presented the mechanism of delamination/de-bonding or removal of coating from the substrate.

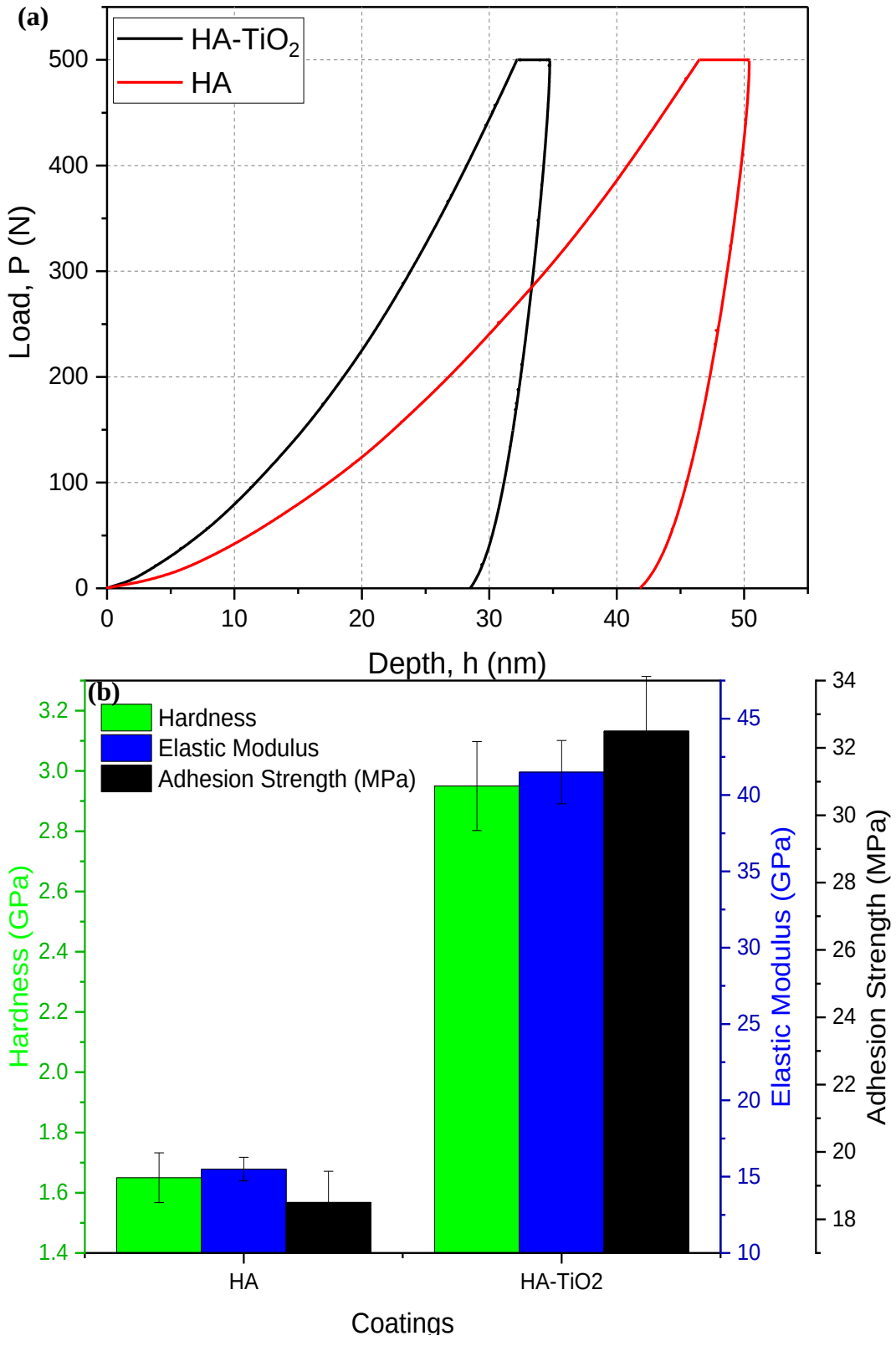

Figure 5.39. (a) nano-indentation plot and (b) Surface-hardness, elastic modulus, and adhesion strength of HA and HA-TiO_2 coatings

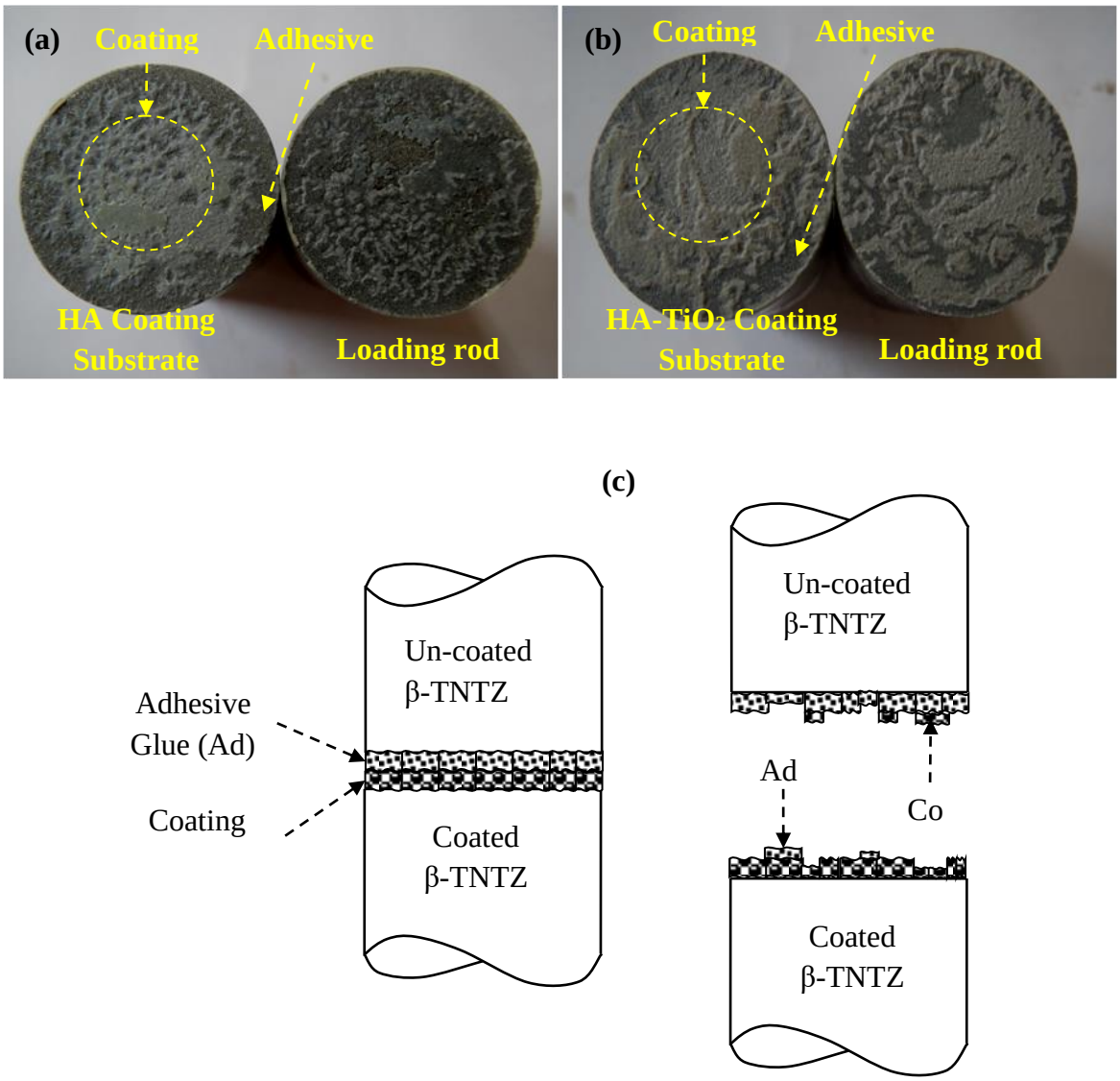

Figure 5.40. (a-b) Optical micrograph of tensile bond strength specimens of HA coating and HA-TiO_2 coatings and (c) Mechanism of delamination of coatings

5.3.2.3. Wettability Analysis

The wettability of implant surfaces have been determined for verifying the bioactivity and wettability depends upon the hydrophilic/hydrophobic nature of the surface of implants, which affects the performance of implants. The bioactivity of HA and HA-TiO_2 coating was accessed through the wettability test. For this, the effect of the different coating composition on the water contact angle was investigated. Figure 5.41 shows the water contact angle for un-coated, HA-coated, and HA-TiO_2 coated

samples after 1 and 3 min of interval. For 1 min of the interval, the contact angle in case of un-coated, HA-coated, and HA-TiO_2 coated samples were measured as 115.5º, 58.5º, and 41.25º, respectively.

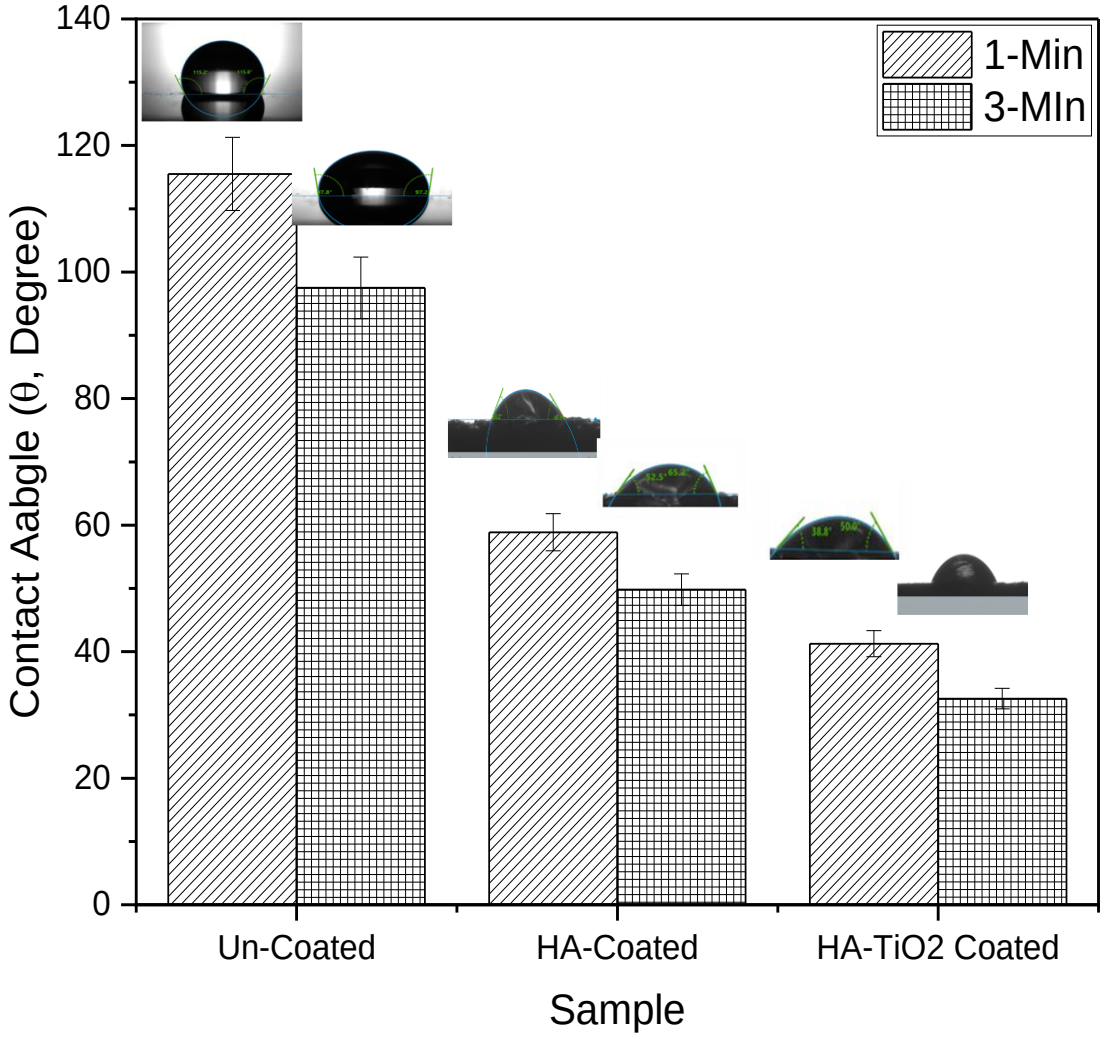

Figure 5.41. Contact angle measurement. Measurement of the degree of contact angle with water drop on Un-coated, HA-coated, and HA-TiO_2 coated surface samples after 1 and 3 min of interval

It has been found that the HA and HA-TiO_2 coated surfaces being hydrophilic, by nature, have sufficient surface energy for water absorption and a greater capillary action was noticed. The water droplet distribution on the surface of the coated samples was higher when compared to the plane or un-coated samples. It has been found that in literature, TiO_2 acted as a reservoir to increase the protein absorption,

which further improves the biological activities in the coating [53]. Both HA and TiO_2 absorbed the water droplets and improved the wettability of coating; thus improved the bioactivity of the coating. It was noticed that the contact angle was decreased with an increase in contact time in all samples. The water contact angle after 3 minutes on un-coated, HA-coated, and HA-TiO_2 coated samples was measured 97.8º, 49.5º, and 32.5º, respectively. From the observation, it has been found that HA-TiO_2 has the lowest water contact angle, which revealed that the coating has the highest wettability and excellent bioactivity.

5.3.2.4. Wear resistance

Figure 5.42 shows the wear resistance and behavior of HA and HA-TiO_2 coatings. The wear rate of coating decreased with the reinforcement of TiO_2 in the HA matrix. This is because TiO_2 improved microstructure and mechanical properties. The adhesion and cohesion strength of the layer in the case of HA-TiO_2 coating is high as compared to HA-coating, which prevents the delamination of coated- material [45]. Wear rate decreased from 0.6 mg/N.m to 0.38 mg/N.m with the addition of 30wt%TiO_2 in the HA matrix. For orthopedic applications, the wear-resistant coating is required to maintain the functionality of the artificial organ. The HA-TiO_2 coating possessed less wear resistance as compared to HA-coating because of high hardness than HA-coating. The coefficient of friction in the case of HA-TiO_2 is less because TiO_2 implies the ductility in the coating and prevents the abrasion of the layer. Figure 5.42 (b) and (c) shows the worn surface morphology of HA and HA-TiO_2 coatings. From the SEM-micrograph the failure of the surface due to the delamination of coatings can be seen. The red arrow shows the delamination; the white arrow shows the debris, and the yellow arrow shows the ploughing/grooving.

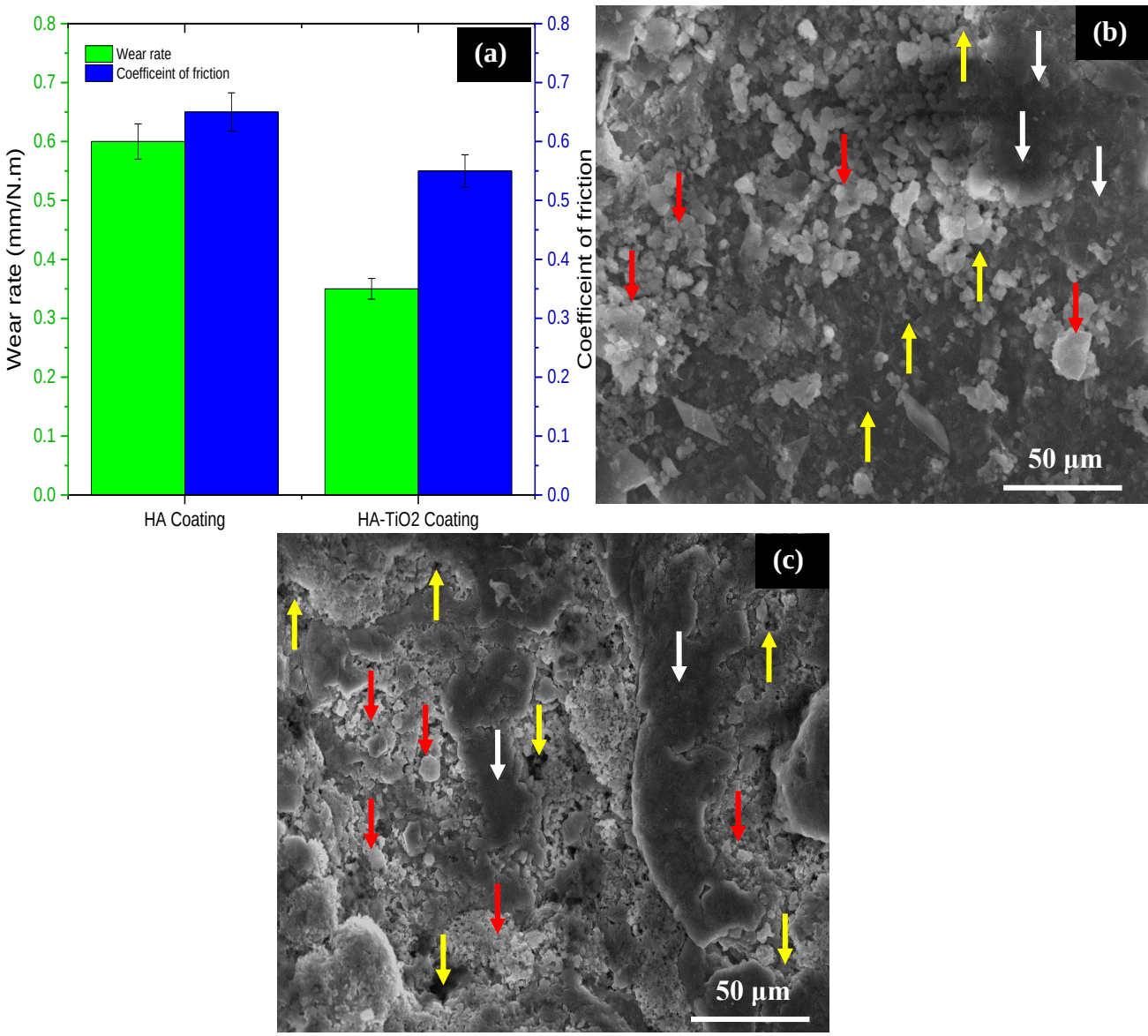

Figure 5.42. (a) Wear rate and coefficient of friction and (b-c) worn morphology of HA and HA-TiO_2 coatings

From the SEM-micrograph, it can be seen that the HA-coated surface was high worn out. Loose debris and delamination of HA particles can be seen, refer Fig. 5.42(b). This is attributed because, HA-coating had brittle, amorphous, porous structure, and low hardness. As a result, coating delaminated from the top surface and worn out. The main wear is attributed due to the abrasion of the coating layer; refer Fig. 5.42(c). On the other hand, the delamination of HA-TiO_2 coating can be seen, but very less as compared to HA-coating. The TiO_2 prevents the delamination of HA

particles from the coating. Moreover, with the reinforcement of TiO_2, the brittleness of the coating is reduced, as a result, less friction developed. Moreover, TiO_2 is a ceramic element that helped in reducing the friction of the coating layer and as a result, less wear occurred. At optimized setting, a biomimetic layer of HA-TiO_2 was deposited on the β-TNTZ alloy, which can be further used as HiP-stem for the Indian population, refer Figure 5.43.

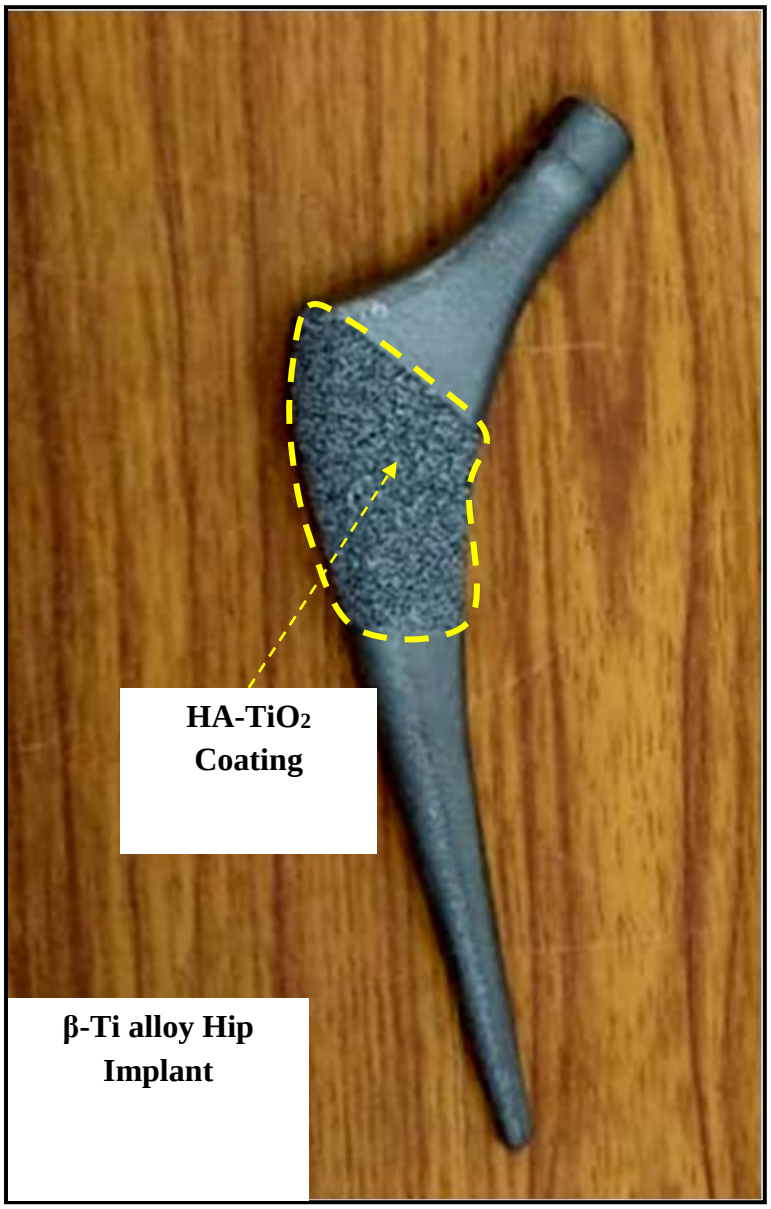

Figure 5.43. HA-TiO_2 Coated β-Ti alloy Hip Stem for Indian Popolation

5.3.2.5. Fatigue Performance

The fatigue performance of HA and HA-TiO_2 coatings was measured in terms of stress versus number of cycle. The S-N curve has been presented in Fig. 5.44. The fatigue performance of HA and HA-TiO_2 coatings were compared with the bench mark sample (polished) with nano-scale surface roughness.

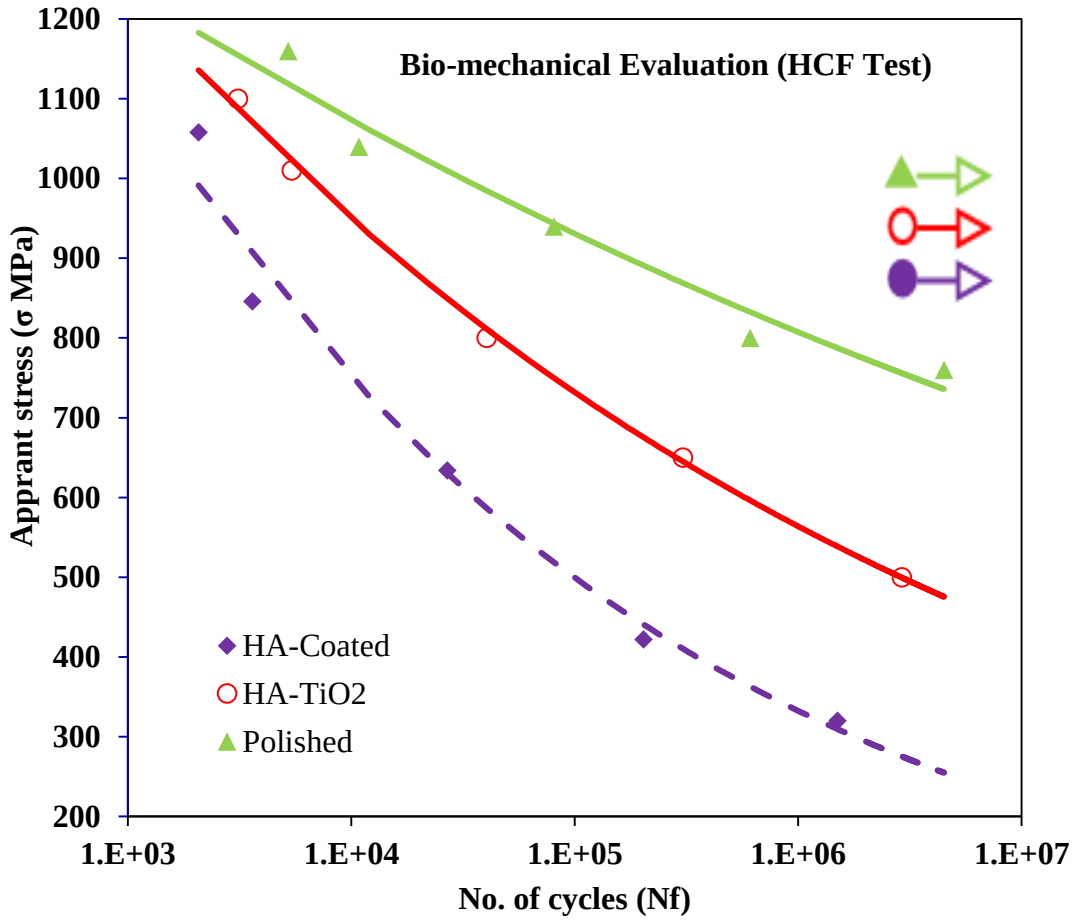

Fig. 5.44. High cycle fatigue S-N Curve for un-coated, HA-coated, and HA-TiO_2 coated

From the figure it can be seen that un-coated specimens has high fatigue endurance as compared to HA-coated, and HA-TiO_2 coated specimens. This is because; the un-coated specimens are high polished and free from surface defects. As results, it showed high fatigue endurance strength. On the other hand, HA-coating has lower fatigue strength as compared to un-coated and HA-TiO_2 coated specimens. This is

attributed because, HA-coating comprised various surface defects such as porosity and micro-cracks, which causes stress concentration and initiate the crack-propagation; thus failed very soon at cyclic load condition. However, HA-TiO_2 coated specimens exhibit higher fatigue performance in comparison with HA-coated and lower as compared to un-coated polished specimens. The reinforcement of TiO_2 in HA-matrix improved the mechanical properties and reduced the brittleness of HA. As a result, crack free dense surface obtained in coating layer. The dense structure resists the coating against high cycle load condition and material offered better life.

CHAPTER-VI

CONCLUSIONS AND SCOPE FOR FUTURE RESEARCH WORK

In the present research work, the application of plasma spray technique has been explored for the deposition of bioactive HA-TiO_2 coating on β-phase Ti-Nb-Ta-Zr alloy based HIP stem for orthopaedic application.

6.1. Research Conclusions

After inclusive analysis of presented work, the major conclusions can be drawn as below:

1. A low elastic (55 GPa) β-phase type Ti-Nb-Ta-Zr alloy has been developed using vacuum arc melting process.
2. To make the mechanical suitability for HIP implant, the β-phase type Ti-Nb-Ta-Zr alloy has been subjected to heat treatment. The tensile strength and micro-hardness of the β-TNTZ sample after heat treatment have been increased from 590 to 1195MPa and 245 to 515HV, respectively. The elastic modulus of the β-$TNTZ_{th}$ alloy is 89 GPa, which is lower than the Ti-4Al-4V alloy (110 GPa) and Co-Cr alloy (220 GPa).
3. The β-phase type Ti-Nb-Ta-Zr alloy surface was modified by plasma spray technique to enhance its corrosion resistance, wear resistance, and bioactivity.
4. Effect of plasma spray process parameters such as reinforcement of TiO_2 in HA, gas flow rate, and powder feed rate on the coating out characteristics such as micro-hardness and adhesion strength has been studied. The optimized process parametric levels for obtaining maximum surface micro-hardness and adhesion strength are: powder ratio – 30% wt. of TiO_2, gas flow rate – 40 l/min, and powder feed rate – 32 g/min.
5. At, gas flow rate 40 l/min and feed rate 32 gm/min, the *HA/TiO_2* coating exhibited cracks free and dense surface in comparison with *HA*-coating. The reinforcement

of *TiO_2* improved the microstructure and mechanical bonding of coating with substrate.

6. From the cross-section micrographs, it can be seen that the thickness of HA, HA-15TiO_2, and HA-30TiO_2 coatings were measured approximately ~185-200 μm. The *HA-30TiO_2* (*HA-T_y*) coating exhibit high surface hardness (1.35 GPa) and adhesion strength (28.75MPa).
7. The surface roughness of *HA*, HA-15TiO_2, and HA-30TiO_2 coatings were measured 7.65, 5.45, and 4.85 μm, respectively. The obtained surface roughness was in good agreement with the values reported in literature and also sufficient to promote bone-ingrowth around the implant.
8. The reinforcement of TiO_2 in HA formed lamellar structure and rich layer of TiO_2 acted as a reservoir to hold the protein in the host body and improved the osseointegration and corrosion resistance.
9. The *HA*-coated samples have better corrosion resistance as compared to uncoated samples. When *TiO_2* was alloyed, the Tafel extrapolation curve again more shifted toward the left side that indicates samples hold low current density as compared to *HA* and uncoated samples. The I_{corr} and E_{corr} values of HA-15TiO_2 coating were measured as 8.15 μA/cm^2 and -370mV, respectively. Similarly, for HA-30TiO_2 coating, the values were 9.17 μA/cm^2 and -420 mV, respectively. The HA-30TiO_2 coating exhibit best and highest corrosion resistance.
10. The HA-15%TiO_2 and HA-30%TiO_2 coatings possessed a higher cellular proliferation rate as compared to *HA*-coated and un-coated specimens. The findings thus indicate that the surface chemistry of the *HA/TiO_2* coating helped to increase the bone ingrowth and osseointegration process
11. At gas flow rate 32 l/min and feed rate 40 gm/min. The reinforcement of TiO_2 improved the microstructure of coating by prevented the formation of micro-cracks in the layer and improved the mechanical bonding of coating with the substrate. The HA/TiO_2 coating exhibited a dense surface in comparison with HA-coating.
12. The coating thickness was measured for HA and HA-TiO_2 coated surface was 125 μm and 120 μm, respectively. Moreover, the reinforcement of TiO_2 formed lamellar structure in the HA-matrix and formed various non-apatite phases like

α/β-TCP phases, Ca3(PO4)2, CaO, TTCP along with TiO_2, which enhanced the mechanical properties and bioactivity of the coating. The adhesion strength of HA-TiO2 coating (32.95 MPa) was higher than the HA-coating (25.79 MPa). The hardness and elastic modulus of HA-TiO_2 coating were measured around 2.95 GPa and 41.5 MPa, which was beneficial to enhance the wear resistance properties.

13. The HA-TiO2 coating exhibited more crystalline content (89.6%) as compared to HA coatings (74.8%). The surface roughness for the as-coated HA and HA-TiO_2 coatings was found to be 4.65 μm and 3.5 μm, respectively. The skewness and kurtosis are the important parameters of surface roughness that affect the corrosion and wear performance of biomedical implants. The skewness in the surface roughness of both surfaces was negative. The HA-coated surface has very deep valleys in the layer as a result roughness is a high Kurtosis of more than 9.5, this may affect the corrosion and wear performance.
14. The hardness of as-sprayed HA and HA-30wt.% coatings were measured 1.65 GPa and 2.95 GPa, respectively. The elastic modulus of as-sprayed HA and HA-30wt.% coatings were measured 15.7 GPa, and 41.75 GPa, respectively. The adhesion strength of the coating is increased with the addition of TiO_2 in HA. The adhesion strength of HA and HA-TiO_2 coating was measured around 25.79 MPa and 32.95 MPa, respectively.
15. The water contact angle after 3 minutes on un-coated, HA-coated, and HA-TiO_2 coated samples was measured 97.8º, 49.5 º, and 32.5º, respectively. It has been found that HA-TiO_2 has the lowest water contact angle, which revealed that the coating has the highest wettability and excellent bioactivity.
16. The delamination of HA-TiO_2 coating can be seen, but very less as compared to HA-coating. The TiO_2 prevents the delamination of HA particles from the coating. Moreover, with the reinforcement of TiO_2, the brittleness of the coating is reduced, as a result, less friction developed. Moreover, TiO_2 is a ceramic element that helped in reducing the friction of the coating layer and as a result, less wear occurred. At optimized setting, a biomimetic layer of HA-TiO_2 was deposited on the β-TNTZ alloy, which can be further used as HIP-stem for the Indian population.

17. The HA-TiO_2 coating exhibit better fatigue endurance as compared to HA-coatings.

6.2. Scope for Future Research Work

Analysis of the results acquired from the current work advocates quite a few possible extensions to the research. A few of them are listed:

1. Apart from the use of micro sized powder particle, there is ample scope for the use of nano-sized powder particles using suspension plasma spray technique.

2. In this research, experimental investigation on the effects of TiO_2 powder as reinforcement on the surface characteristics has been studied. However, there is a scope for the use of powder particles of other materials such as Al_2O_3, ZrO_2, and other biocompatible materials.

3. There is a scope on the finite element modeling and analysis to simulate the coating process for better understanding of phenomena and predict the thermal stresses.

4. The coatings of HA and HA-TiO_2 using PVD and other advanced coating techniques can be compared.

5. The bioactivity and biocompatibility of plasma spray coated β-Ti alloy based implant have been investigated by In-Vitro study (Cell culture). The effect of bone ingrowth needs to be investigated in more detail by In-Vivo (animal study).

REFERENCES

[1]. Natarajan, S. Biomimetic, Bioresponsive, and Bioactive Materials edited by Matteo Santin and Gary J. Phillips. Materials and Manufacturing Processes, 2016, 31(7), 976–977.

[2]. Geetha, M., Singh, A.K., Asokamani, R. and Gogia, A.K. Ti-based biomaterials, the ultimate choice for orthopaedic implants–a review. Progress in materials science, 2009, 54(3), pp.397-425.

[3]. Gao, C.; Peng, S.; Feng, P.; Shuai, C., Bone biomaterials and interactions with stem cells, Bone Research, 2017, 5, 1-33. Doi:10.1038/boneres.2017.59

[4]. Prakash, C., Kansal, H.K., Pabla, B.S., Puri, S. and Aggarwal, A. Electric discharge machining–A potential choice for surface modification of metallic implants for orthopedic applications: A review. Proceedings of the Institution of Mechanical Engineers, Part B: Journal of Engineering Manufacture, 2016, 230(2), pp.331-353.

[5]. Liu, X., Chu, P.K. and Ding, C. Surface modification of titanium, titanium alloys, and related materials for biomedical applications. Materials Science and Engineering: R: Reports, 2004, 47(3-4), pp.49-121.

[6]. Bartolo, P., Kruth, J.P., Silva, J., Levy, G., Malshe, A., Rajurkar, K., Mitsuishi, M., Ciurana, J. and Leu, M. Biomedical production of implants by additive electro-chemical and physical processes. CIRP Annals-Manufacturing Technology, 2012, 61(2), pp.635-655.

[7]. Kang, C.W. and Fang, F.Z. State of the art of bioimplants manufacturing: part I. Advances in Manufacturing, 2018, 6(1), pp.20-40.

[8]. Kang, C.W. and Fang, F.Z. State of the art of bioimplants manufacturing: part II. Advances in Manufacturing, 2018, 6(1), pp.137-154.

[9]. Prakash, C., Kansal, H.K., Pabla, B.S. and Puri, S. On the influence of nanoporous layer fabricated by PMEDM on β-Ti implant: Biological and computational evaluation of bone-implant interface. Materials Today: Proceedings, 2017, 4(2), pp.2298-2307.

[10]. Zhao, B., Gain, A.K., Ding, W., Zhang, L., Li, X. and Fu, Y. A review on metallic porous materials: pore formation, mechanical properties, and their applications. The International Journal of Advanced Manufacturing Technology, 2018, 95(5-8), pp.2641-2659.

[11]. Raza, M. R., Sulong, A. B., Muhamad, N., Akhtar, M. N., & Rajabi, J. Effects of binder system and processing parameters on formability of porous Ti/HA composite through powder injection molding. Materials & Design, 2015, 87, 386-392.

[12]. Ryan, G., Pandit, A., & Apatsidis, D. P. Fabrication methods of porous metals for use in orthopaedic applications. Biomaterials, 2006, 27(13), 2651-2670.

[13]. Zhang, L., He, Z. Y., Zhang, Y. Q., Jiang, Y. H., & Zhou, R. Rapidly sintering of interconnected porous Ti-HA biocomposite with high strength and enhanced bioactivity. Materials Science and Engineering: C, 2016, 67, 104-114

[14]. Torres-Sanchez, C., McLaughlin, J. and Fotticchia, A. Porosity and pore size effect on the properties of sintered Ti35Nb4Sn alloy scaffolds and their suitability for tissue engineering applications. Journal of Alloys and Compounds, 2018, 731, pp.189-199.

[15]. Cook, S.D., Walsh, K.A. and Haddad, J.R., 1985. Interface mechanics and bone growth into porous Co-Cr-Mo alloy implants. Clinical orthopaedics and related research, 1985, (193), pp.271-280.

[16]. Camron, H.U., Pilliar, R.M. and Macnab, I. The rate of bone ingrowth into porous metal. Journal of biomedical materials research, 1976, 10(2), pp.295-302.

[17]. Hofmann, A.A., Bloebaum, R.D. and Bachus, K.N. Progression of human bone ingrowth into porous-coated implants: Rate of bone ingrowth in humans. Acta Orthopaedica Scandinavica, 1997, 68(2), pp.161-166.

[18]. Bobyn, J.D., Pilliar, R.M., Cameron, H.U. and Weatherly, G.C. The optimum pore size for the fixation of porous-surfaced metal implants by the ingrowth of bone. Clinical orthopaedics and related research, 1980, (150), pp.263-270.

[19]. Hulbert, S.F., Young, F.A., Mathews, R.S., Klawitter, J.J., Talbert, C.D. and Stelling, F.H. Potential of ceramic materials as permanently implantable skeletal prostheses. Journal of biomedical materials research, 1970, 4(3), pp.433-456.

[20]. Barth, E., Ronningen, H., Solheim, L.F. and Saethren, B. Bone ingrowth into weight-bearing porous fiber titanium implants. Mechanical and biochemical correlations. Journal of orthopaedic research, 1986, 4(3), pp.356-361.

[21]. Tsuruga, E., Takita, H., Itoh, H., Wakisaka, Y. and Kuboki, Y. Pore size of porous hydroxyapatite as the cell-substratum controls BMP-induced osteogenesis. The journal of biochemistry, 1997, 121(2), pp.317-324.

[22]. Clemow, A.J.T., A.M. Weinstein, J.J. Klawitter, J. Koeneman, and J. Anderson, Interface mechanics of porous titanium implants. Journal of Biomedical Materials Research, 1981. **15**(1): p. 73-82.

[23]. Bobyn, J.D., G.J. Stackpool, S.A. Hacking, M. Tanzer, and J.J. Krygier, Characteristics of bone ingrowth and interface mechanics of a new porous tantalum biomaterial. Journal of Bone & Joint Surgery, British Volume, 1999. **81**-**B**(5): p. 907.

[24]. Vasconcellos, L.M.R.d., D.O. Leite, F.N.d. Oliveira, Y.R. Carvalho, and C.A.A. Cairo, Evaluation of bone ingrowth into porous titanium implant: histomorphometric analysis in rabbits. Brazilian Oral Research, 2010. **24**: p. 399-405.

[25]. Taniguchi, N., S. Fujibayashi, M. Takemoto, K. Sasaki, B. Otsuki, T. Nakamura, T. Matsushita, T. Kokubo, and S. Matsuda, Effect of pore size on bone ingrowth into porous titanium implants fabricated by additive manufacturing: An in vivo experiment. Materials Science and Engineering: C, 2016. **59**: p. 690-701.

[26]. Wen, C.E., Y. Yamada, K. Shimojima, Y. Chino, T. Asahina, and M. Mabuchi, Processing and mechanical properties of autogenous titanium implant materials. Journal of Materials Science: Materials in Medicine, 2002. **13**(4): p. 397-401.

[27]. Singh, R., Singh, B. P., Gupta, A., & Prakash, C. Fabrication and characterization of Ti-Nb-HA alloy by mechanical alloying and spark plasma sintering for hard tissue replacements. In IOP Conference Series: Materials Science and Engineering 2017, August, (Vol. 225, No. 1, p. 012051). IOP Publishing.

[28]. Sharma, N., & Kumar, K. Mechanical characteristics and bioactivity of porous Ni50− x Ti50Cu x (x= 0, 5 and 10) prepared by P/M. Materials Science and Technology, 2018, 34(8), 934-944.

[29]. Sharma, B., Vajpai, S. K., & Ameyama, K. Microstructure and properties of beta Ti–Nb alloy prepared by powder metallurgy route using titanium hydride powder. Journal of Alloys and Compounds, 2016, 656, 978-986.

[30]. Roseti, L., Parisi, V., Petretta, M., Cavallo, C., Desando, G., Bartolotti, I. and Grigolo, B. Scaffolds for bone tissue engineering: state of the art and new perspectives. Materials Science and Engineering: 2017, C, 78, pp.1246-1262.

[31]. Zhu, S. L., Yang, X. J., Hu, F., Deng, S. H., & Cui, Z. D. Processing of porous TiNi shape memory alloy from elemental powders by Ar-sintering. Materials Letters, 2004, 58(19), 2369-2373.

[32]. Zhang, L., He, Z.Y., Zhang, Y.Q., Jiang, Y.H. and Zhou, R. Rapidly sintering of interconnected porous Ti-HA biocomposite with high strength and enhanced bioactivity. Materials Science and Engineering: 2016, C, 67, pp.104-114.

[33]. Prakash, C., Singh, S., Gupta, M., Mia, M., Królczyk, G. and Khanna, N. Synthesis, Characterization, Corrosion Resistance and In-Vitro Bioactivity Behavior of Biodegradable Mg–Zn–Mn–(Si–HA) Composite for Orthopaedic Applications. Materials, 2018, 11(9), p.1602.

[34]. Prakash, C., Singh, S., Pabla, B.S., Sidhu, S.S. and Uddin, M.S. Bio-inspired low elastic biodegradable Mg-Zn-Mn-Si-HA alloy fabricated by spark plasma sintering. Materials and Manufacturing Processes, 2018, pp.1-12.

[35]. Prakash, C., Singh, S., Abdul-Rani, A.M., Uddin, M.S., Pabla, B.S. and Puri, S. Spark Plasma Sintering of Mg-Zn-Mn-Si-HA Alloy for Bone Fixation Devices: Fabrication of Biodegradable Low Elastic Porous Mg-Zn-Mn-Si-HA Alloy. In Handbook of Research on Green Engineering Techniques for Modern Manufacturing.2019, (pp. 282-295). IGI Global.

[36]. Yazdimamaghani, M., Razavi, M., Vashaee, D., Moharamzadeh, K., Boccaccini, A.R. and Tayebi, L. Porous magnesium-based scaffolds for tissue engineering. Materials Science and Engineering: 2017, C, 71, pp.1253-1266.

[37]. Kirkland, N.T., Kolbeinsson, I., Woodfield, T., Dias, G.J. and Staiger, M.P. Synthesis and properties of topologically ordered porous magnesium. Materials Science and Engineering:2011, B, 176(20), pp.1666-1672.

[38]. Witte, F., Ulrich, H., Rudert, M., Willbold, E. Biodegradable magnesium scaffolds: part 1: appropriate inflammatory response, J. Biomed. Mater. Res. A 81 (2007) 748–756.

[39]. Uddin, M.S.; Hall, C.; Murphy, P., Surface treatments for controlling corrosion rate of biodegradable Mg and Mg-based alloy implants. Science and Technology of Advanced Materials 2015, 16, 053501.

[40]. Uddin, M.S.; Rosman, H.; Hall, C.; Murphy, P., Enhancing the corrosion resistance of biodegradable Mg-based alloy by machining-induced surface integrity: influence of machining parameters on surface roughness and hardness. The International Journal of Advanced Manufacturing Technology 2017, 90, 2095-2108. doi.org/10.1007/s00170-016-9536-x

[41]. Hedayati, R., Ahmadi, S.M., Lietaert, K., Tümer, N., Li, Y., Amin Yavari, S. and Zadpoor, A.A. Fatigue and quasi-static mechanical behavior of bio-degradable porous biomaterials based on magnesium alloys. Journal of Biomedical Materials Research Part A.2018

[42]. Bakhsheshi-Rad, H.R., Hamzah, E., Staiger, M.P., Dias, G.J., Hadisi, Z., Saheban, M. and Kashefian, M. Drug release, cytocompatibility, bioactivity, and antibacterial activity of doxycycline loaded Mg-Ca-TiO2 composite scaffold. Materials & Design, 2018, 139, pp.212-221.

[43]. Ghomi, H. and Emadi, R. Fabrication of bioactive porous bredigite (Ca7MgSi4O16) scaffold via space holder method. International Journal of Materials Research, 2018, 109(3), pp.257-264.

[44]. Singh, S. and Bhatnagar, N. A survey of fabrication and application of metallic foams (1925–2017). Journal of Porous Materials, 2018, 25(2), pp.537-554.

[45]. Singh, S. and Bhatnagar, N. A novel approach to fabricate 3D open cellular structure of Mg10Zn alloy with controlled morphology. Materials Letters, 2018, 212, pp.62-64.

[46]. Dutta, S., Devi, K.B. and Roy, M. Processing and degradation behavior of porous magnesium scaffold for biomedical applications. Advanced Powder Technology, 2017, 28(12), pp.3204-3212

[47]. Bose, S., Ke, D., Sahasrabudhe, H. and Bandyopadhyay, A. Additive manufacturing of biomaterials. Progress in Materials Science, 2018, 93, pp.45-111.

[48]. DebRoy, T., Wei, H.L., Zuback, J.S., Mukherjee, T., Elmer, J.W., Milewski, J.O., Beese, A.M., Wilson-Heid, A., De, A. and Zhang, W. Additive manufacturing of metallic components–process, structure and properties. Progress in Materials Science, 2018, 92, pp.112-224.

[49]. Wang Y, Shen Y, Wang Z. Development of highly porous titanium scaffolds by selective laser melting. Mater Lett, 2010, 64(6):674–676

[50]. Pattanayak DK, Fukuda A, Matsushita T. Bioactive Ti metal analogous to human cancellous bone: fabrication by selective laser melting and chemical treatments. Acta Biomater, 2011, 7(3):1398–1406

[51]. Weißmann V, Bader R, Hansmann H. Influence of the structural orientation on the mechanical properties of selective laser melted Ti6Al4V open-porous scaffolds. Mater Des, 2016, 95:188–197

[52]. Mueller B. Additive manufacturing technologies: rapid prototyping to direct digital manufacturing. Assem Autom, 2012, 32(2):151–154.

[53]. Shipley, H., McDonnell, D., Culleton, M., Lupoi, R., O'Donnell, G. and Trimble, D. Optimisation of process parameters to address fundamental challenges during selective laser melting of Ti-6Al-4V: A review. International Journal of Machine Tools and Manufacture.2018.

[54]. Khorasani, A., Gibson, I., Awan, U.S. and Ghaderi, A. The effect of SLM process parameters on density, hardness, tensile strength and surface quality of Ti-6Al-4V. Additive Manufacturing, 2019, 25, pp.176-186.

[55]. Zhao, B., Wang, H., Qiao, N., Wang, C. and Hu, M. Corrosion resistance characteristics of a Ti-6Al-4V alloy scaffold that is fabricated by electron beam melting and selective laser melting for implantation in vivo. Materials Science and Engineering: 2017, C, 70, pp.832-841.

[56]. Ran, Q., Yang, W., Hu, Y., Shen, X., Yu, Y., Xiang, Y. and Cai, K. Osteogenesis of 3D printed porous Ti6Al4V implants with different pore sizes. Journal of the mechanical behavior of biomedical materials, 2018, 84, pp.1-11.

[57]. Yan, C., Hao, L., Hussein, A., Wei, Q. and Shi, Y. Microstructural and surface modifications and hydroxyapatite coating of Ti-6Al-4V triply periodic minimal surface lattices fabricated by selective laser melting. Materials Science and Engineering: 2017, C, 75, pp.1515-1524.

[58]. Subbiah, T., Bhat, G.S., Tock, R.W., Parameswaran, S. and Ramkumar, S.S. Electrospinning of nanofibers. Journal of applied polymer science, 2005, 96(2), pp.557-569.

[59]. Reneker DH, Yarin AL. Electrospinning jets and polymer nanofibers. Polymer 2008;49: 2387–425.

[60]. He J, Wan YQ, Yu JY. Scaling law in electrospinning: relationship between electric current and solution flow rate. Polymer 2005;46:2799–801.

[61]. He W, Horn SW, Hussain MD. Improved bioavailability of orally administered mifepristone from PLGA nanoparticles. Int J Pharm 2007;334:173–8.

[62]. Chew SY, Wen Y, Dzenis Y, Leong KW. The role of electrospinning in the emerging field of nanomedicine. Curr Pharm Des 2006a;12:4751–70.

[63]. Chew SY, Hufnagel TC, Lim CT, Leong KW. Mechanical properties of single electrospun drug-encapsulated nanofibres. Nanotechnology 2006b;17:3880–91.

[64]. Liang D, Hsiao BS, Chu B. Functional electrospun nanofibrous scaffolds for biomedical applications. Adv Drug Deliv Rev 2007;59:1392–412.

[65]. Bhardwaj, N. and Kundu, S.C. Electrospinning: a fascinating fiber fabrication technique. Biotechnology advances, 2010, 28(3), pp.325-347.

[66]. Doustgani, A., E. Vasheghani-Farahani, and M. Soleimani, Aligned and random nanofibrous nanocomposite scaffolds for bone tissue engineering. Nanomedicine Journal, 2013. 1(1): p. 20-27.

[67]. Raeisdasteh Hokmabad, V., Davaran, S., Ramazani, A. and Salehi, R. Design and fabrication of porous biodegradable scaffolds: a strategy for tissue engineering. Journal of Biomaterials science, Polymer edition, 2017, 28(16), pp.1797-1825.

[68]. Yao, J., C.W. Bastiaansen, and T. Peijs, High strength and high modulus electrospun nanofibers. Fibers, 2014. **2**(2): p. 158-186.

[69]. Petrík, S., Industrial production technology for nanofibers. Nanofibers–Production, Properties and Functional Applications, 2011: p. 1.

[70]. Esmaeilzadeh, I., et al., A feasibility study on semi industrial nozzleless electrospinning of cellulose nanofiber. International Journal of Industrial Chemistry, 2015. **6**(3): p. 193-211.

[71]. Dubský, M., et al., Nanofibers prepared by needleless electrospinning technology as scaffolds for wound healing. Journal of Materials Science: Materials in Medicine, 2012. **23**(4): p. 931-941.

[72]. Brown, T.D., et al., Design and fabrication of tubular scaffolds via direct writing in a melt electrospinning mode. Biointerphases, 2012. **7**(1): p. 13.

[73]. Muerza-Cascante, M.L., et al., Melt electrospinning and its technologization in tissue engineering. Tissue Engineering Part B: Reviews, 2014. **21**(2): p. 187-202.

[74]. Mota, C., et al., Melt electrospinning writing of three-dimensional star poly (ϵ-caprolactone) scaffolds. Polymer International, 2013. **62**(6): p. 893-900.

[75]. Gazzarri, M., et al., Fibrous star poly (ε-caprolactone) melt-electrospun scaffolds for wound healing applications. Journal of Bioactive and Compatible Polymers, 2013. **28**(5): p. 492-507.

[76]. Li, X., et al., Preparation and characterization of PLLA/nHA nonwoven mats via laser melt electrospinning. Materials Letters, 2012. **73**: p. 103-106.

[77]. Kim, S.J., et al., Fabrication and characterization of 3-dimensional PLGA nanofiber/microfiber composite scaffolds. Polymer, 2010. **51**(6): p. 1320-1327.

[78]. Asri, R.I.M., Harun, W.S.W., Hassan, M.A., Ghani, S.A.C. and Buyong, Z. A review of hydroxyapatite-based coating techniques: Sol–gel and electrochemical depositions on biocompatible metals. Journal of the mechanical behavior of biomedical materials, 2016, 57, pp.95-108.

[79]. Gurrappa, I. and Binder, L. Electrodeposition of nanostructured coatings and their characterization—a review. Science and Technology of Advanced Materials, 2008, 29(4), p.043001.

[80]. Bicelli, L.P., Bozzini, B., Mele, C. and D'Urzo, L. A review of nanostructural aspects of metal electrodeposition. Int. J. Electrochem. Sci, 2008, 3(4), pp.356-408.

[81]. Qiu, D., Yang, L., Yin, Y. and Wang, A. Preparation and characterization of hydroxyapatite/titania composite coating on NiTi alloy by electrochemical deposition. Surface and Coatings Technology, 2011, 205(10), pp.3280-3284.

[82]. Qiu, D., Wang, A. and Yin, Y. Characterization and corrosion behavior of hydroxyapatite/zirconia composite coating on NiTi fabricated by electrochemical deposition. Applied Surface Science, 2010, 257(5), pp.1774-1778.

[83]. Peng, Ping, Sunil Kumar, Nicolas H. Voelcker, Endre Szili, Roger St C. Smart, and Hans J. Griesser. "Thin calcium phosphate coatings on titanium by electrochemical deposition in modified simulated body fluid." Journal of Biomedical Materials Research Part A: An Official Journal of The Society for Biomaterials, The Japanese Society for Biomaterials, and The Australian Society for Biomaterials and the Korean Society for Biomaterials 76, no. 2 (2006): 347-355.

[84]. Kar, A., Raja, K.S. and Misra, M. Electrodeposition of hydroxyapatite onto nanotubular TiO2 for implant applications. Surface and Coatings Technology, 2006, 201(6), pp.3723-3731.

[85]. Saremi, M. and Golshan, B.M. Microstructural study of nano hydroxyapatite coating obtained by pulse electrodeposition process on Ti–6Al–4V. Transactions of the IMF, 2007, 85(2), pp.99-102.

[86]. Dos Santos, E.A., Moldovan, M.S., Jacomine, L., Mateescu, M., Werckmann, J., Anselme, K., Mille, P. and Pelletier, H. Oriented hydroxyapatite single crystals produced by the electrodeposition method. Materials Science and Engineering: B, 2010, 169(1-3), pp.138-144.

[87]. Park, K.H., Kim, S.J., Hwang, M.J., Song, H.J. and Park, Y.J. Pulse electrodeposition of hydroxyapatite/chitosan coatings on titanium substrate for dental implant. Colloid and Polymer Science, 2017, 295(10), pp.1843-1849.

[88]. Gopi, D., Shinyjoy, E., Sekar, M., Surendiran, M., Kavitha, L. and Kumar, T.S. Development of carbon nanotubes reinforced hydroxyapatite composite coatings on titanium by electrodeposition method. Corrosion Science, 2013, 73, pp.321-330.

[89]. Yan, L., Xiang, Y., Yu, J., Wang, Y. and Cui, W. Fabrication of antibacterial and antiwear hydroxyapatite coatings via in situ chitosan-mediated pulse electrochemical deposition. ACS applied materials & interfaces, 2017, 9(5), pp.5023-5030.

[90]. Lee, C.K. Fabrication, characterization and wear corrosion testing of bioactive hydroxyapatite/nano-TiO2 composite coatings on anodic Ti–6Al–4V substrate for biomedical applications. Materials Science and Engineering: 2012, B, 177(11), pp.810-818.

[91]. Huang, Y., Zhang, X., Mao, H., Li, T., Zhao, R., Yan, Y. and Pang, X., 2015. Osteoblastic cell responses and antibacterial efficacy of Cu/Zn co-substituted hydroxyapatite coatings on pure titanium using electrodeposition method. RSC Advances, 2015, 5(22), pp.17076-17086.

[92]. Saremi, M. and Golshan, B.M. Microstructural study of nano hydroxyapatite coating obtained by pulse electrodeposition process on Ti–6Al–4V. Transactions of the IMF, 2007, 85(2), pp.99-102.

[93]. N.M. Abbas, D.G. Solomon, and M.F. Bahari, A Review on Current Research Trends in Electrical Discharge Machining (EDM), Int. J. Mach. Tools Manuf., 2007, 47, p 1214–1228.

[94]. Prakash, C., Kansal, H.K., Pabla, B.S. and Puri, S. Processing and characterization of novel biomimetic nanoporous bioceramic surface on β-Ti implant by powder mixed electric discharge machining. Journal of Materials Engineering and Performance, 2015, 24(9), pp.3622-3633.

[95]. Peng, P.W.; Ou, K.L.; Lin, H.C.; Pan, Y.N.; Wang, C.H. Effect of electrical-discharging on formation of nanoporous biocompatible layer on titanium. Journal of Alloys and Compounds 2010, 492 (1-2), 625–630.

[96]. Bin, T.C.; Xin, L.D.; Zhan, W.; Yang, G. Electro-spark alloying using graphite electrode on titanium alloy surface for biomedical applications. Applied Surface Science 2011, 257(15), 6364–6371.

[97]. C. Prakash, H.K. Kansal, B.S. Pabla, S. Puri, Potential of Powder Mixed Electric Discharge Machining to Enhance the Wear and Tribological performance of β-Ti Implant for Orthopedic Applications. Journal of Nanoengineering and Nanomanufacturing 2015, 5(4), 261-269

[98]. Prakash, C., Kansal, H.K., Pabla, B.S. and Puri, S. Experimental investigations in powder mixed electric discharge machining of Ti–35Nb–7Ta–5Zrβ-titanium alloy. Materials and Manufacturing Processes, 2017, 32(3), pp.274-285.

[99]. Prakash, C., Kansal, H.K., Pabla, B.S. and Puri, S. Multi-objective optimization of powder mixed electric discharge machining parameters for fabrication of biocompatible layer on β-Ti alloy using NSGA-II coupled with Taguchi based response surface methodology. Journal of Mechanical Science and Technology, 2016, 30(9), pp.4195-4204.

[100]. Prakash, C., Kansal, H.K., Pabla, B.S. and Puri, S. Powder mixed electric discharge machining: An innovative surface modification technique to enhance fatigue performance and bioactivity of β-Ti implant for orthopedics application. Journal of Computing and Information Science in Engineering, 2016, 16(4), p.041006.

[101]. Prakash, C. and Uddin, M.S. Surface modification of β-phase Ti implant by hydroaxyapatite mixed electric discharge machining to enhance the corrosion resistance and in-vitro bioactivity. Surface and Coatings Technology, 2017, 326, pp.134-145.

[102]. Z.J. Xie, Y.J. Mai, W.Q. Lian, S.L. He, X.H. Jie, Titanium carbide coating with enhanced tribological properties obtained by EDC using partially sintered titanium electrodes and graphite powder mixed dielectric. Surface & Coatings Technology 2016, 300, 50-57.

[103]. M. Arun, V. Duraiselvam, and R. Senthilkumar, Synthesis of Electric Discharge Alloyed Nickel–Tungsten Coating on Tool Steel and its Tribological Studies. Mater. Des., 2014, 63, p 257–262.

[104]. Ekmekci, N.; Ekmekci, B. Electrical Discharge Machining of Ti6Al4V in Hydroxyapatite Powder Mixed Dielectric Liquid. Materials and Manufacturing Processes 2015, DOI: 10.1080/10426914.2015.1090591.

[105]. S.F. Ou and C.Y. Wang, Fabrication of a hydroxyapatite-containing coating on Ti–Ta alloy by electrical discharge coating and hydrothermal treatment. Surface & Coatings Technology 2016, 302, 238-243.

[106]. Prakash, C., Singh, S., Pabla, B.S. and Uddin, M.S., 2018. Synthesis, characterization, corrosion and bioactivity investigation of nano-HA coating deposited on biodegradable Mg-Zn-Mn alloy. Surface and Coatings Technology 2018, 346, 9-18 Doi.org/10.1016/j.surfcoat.2018.04.035

[107]. Y. Wang, K. Khor, and P. Chang, Thermal Spraying of Functionally Graded Calcium Phosphate Coatings for Biomedical Implants, Journal of Thermal Spray Technology, 7(1), (1998), 50-57.

[108]. K. Khor, C. Yip, and P. Cheang, Ti-6Al-4V/Hydroxyapatite Composite Coatings Prepared by Thermal Spray Techniques, Journal of Thermal Spray Technology, 6(1), (1997), 109-115.

[109]. J. Mostaghimi, and S. Chandra, Splat Formation in Plasma-Spray Coating, Pure and Applied Chemistry, 74(3), (2002), 441-445.

[110]. S. Fantassi, M. Vardelle, P. Fauchais, and C. Moreau, Investigation of the Splat Formation Versus Different Particulate Temperatures and Velocities Prior to Impact, In Proceeding of 13th International Thermal Spray Conference, C.C. Berndt (Editor), ASM International, Materials Park, OH, USA, Florida, (1992), 755-760.

[111]. Lu, Y.P., Li, M.S., Li, S.T., Wang, Z.G. and Zhu, R.F. Plasma-sprayed hydroxyapatite+ titania composite bond coat for hydroxyapatite coating on titanium substrate. Biomaterials, 2004, 25(18), pp.4393-4403.

[112]. Sarao, T.P.S., Sidhu, H.S. and Singh, H. Characterization and in vitro corrosion investigations of thermal sprayed hydroxyapatite and hydroxyapatite-titania coatings on Ti alloy. Metallurgical and Materials Transactions A, 2012, 43(11), pp.4365-4376.

[113]. Rattan, V., Sidhu, T.S. and Mittal, M.Study and Characterization of Mechanical and Electrochemical Corrosion Properties of Plasma Sprayed Hydroxyapatite Coatings on AISI 304L Stainless Steel. In Journal of Biomimetics, Biomaterials and Biomedical Engineering, 2018, (Vol. 35, pp. 20-34). Trans Tech Publications.

[114]. Rocha, R.C., Galdino, A.G.D.S., Silva, S.N.D. and Machado, M.L.P. Surface, microstructural, and adhesion strength investigations of a bioactive hydroxyapatite-titanium oxide ceramic coating applied to Ti-6Al-4V alloys by plasma thermal spraying. Materials Research, 2018, 21(4).

[115]. Yao, Hai-Long, Xiao-Zhen Hu, Xiao-Bo Bai, Hong-Tao Wang, Qing-Yu Chen, and Gang-Chang Ji. "Comparative study of HA/TiO2 and HA/ZrO2 composite coatings deposited by high-velocity suspension flame spray (HVSFS)." Surface and Coatings Technology 351 (2018): 177-187.

[116]. Hameed, P., Gopal, V., Bjorklund, S., Ganvir, A., Sen, D., Markocsan, N. and Manivasagam, G. Axial Suspension Plasma Spraying: An ultimate technique to tailor Ti6Al4V surface with HAp for orthopaedic applications. Colloids and Surfaces B: Biointerfaces, 2019, 173, pp.806-815.

[117]. Sarao, T.P.S., Singh, H. and Singh, H. Enhancing Biocompatibility and Corrosion Resistance of Ti-6Al-4V Alloy by Surface Modification Route. Journal of Thermal Spray Technology, 2018, pp.1-13.

[118]. Sarkar, M. and Jain, V.K. Nanofinishing of freeform surfaces using abrasive flow finishing process. Proceedings of the Institution of Mechanical Engineers, Part B: Journal of Engineering Manufacture, 2017, 231(9), pp.1501-1515.

[119]. Ghosh, G., Sidpara, A. and Bandyopadhyay, P.P. Review of several precision finishing processes for optics manufacturing. Journal of Micromanufacturing, 2018, p.2516598418777315.

[120]. Jain, V.K.. Nanofinishing: An Introduction. In Nanofinishing Science and Technology, 2016, pp. 23-46. CRC Press.

[121]. Jain, V.K. Nanofinishing science and technology: basic and advanced finishing and polishing processes. 2016, CRC Press.

[122]. Li, S., Wang, Z. and Wu, Y. Relationship between subsurface damage and surface roughness of optical materials in grinding and lapping processes. Journal of Materials Processing Technology, 2008, 205(1-3), pp.34-41.

[123]. Kuhar, M. and Funduk, N. Effects of polishing techniques on the surface roughness of acrylic denture base resins. The Journal of prosthetic dentistry, 2005, 93(1), pp.76-85.

[124]. Zaborski S, Sudzik A, Wołyniec A .Electrochemical polishing of total hip prostheses. Arch Civ Mech Eng 2011, 11(4):1053–1062

[125]. Cheung C, Ho L, Charlton P. Analysis of surface generation in the ultraprecision polishing of freeform surfaces. Pro Inst Mech Eng Part B J Eng Manuf, 2010, 224(1):59–73

[126]. Shiou, F.J. and Chen, C.H. Freeform surface finish of plastic injection mold by using ball-burnishing process. Journal of Materials Processing Technology, 2003, 140(1-3), pp.248-254.

[127]. Jain, V.K.Abrasive-based nano-finishing techniques: an overview. Machining Science and Technology, 2008, 12(3), pp.257-294.

[128]. Ohmori, H., Li, W., Makinouchi, A. and Bandyopadhyay, B.P. Efficient and precision grinding of small hard and brittle cylindrical parts by the centerless grinding process

combined with electro-discharge truing and electrolytic in-process dressing. Journal of Materials Processing Technology, 2000, 98(3), pp.322-327.

[129]. Zhang D, Li C, Jia D. Grinding model and material removal mechanism of medical nanometer zirconia ceramics. Recent Pat Nanotechnol, 2014, 8(1):2–17.

[130]. Ohmori H, Nakagawa T. Analysis of mirror surface generation of hard and brittle materials by ELID (electronic inprocess dressing) grinding with superfine grain metallic bond wheels. CIRP Ann Manuf Technol, 1995, 44(1):287–290.

[131]. Kotani H, Komotori J, Mizutani M. Surface finishing and modification for cobalt-chromium-molybdenum alloy by electrolytic in-process dressing (ELID) grinding. In: 5th international conference on leading edge manufacturing in 21st century, 2009, LEM 2009

[132]. Kotani H, Komotori J, Naruse T. Development of a new grinding system for finishing of hemispherical inside surface. Int J Nanomanuf, 2013, 9(1):77–86

[133]. Baghel, P., Singh, S., Nagdeve, L., Jain, V.K. and Sharma, N.D. Preliminary investigations into finishing of artificial dental crown. International Journal of Precision Technology, 2015, 5(3-4), pp.229-245.

[134]. Nagdeve, L., Jain, V.K. and Ramkumar, J. Experimental investigations into nano-finishing of freeform surfaces using negative replica of the knee joint. Procedia CIRP, 2016, 42, pp.793-798.

[135]. Sarkar, M. and Jain, V.K. Nanofinishing of freeform surfaces using abrasive flow finishing process. Proceedings of the Institution of Mechanical Engineers, Part B: Journal of Engineering Manufacture, 2017, 231(9), pp.1501-1515.

[136]. Sidpara, A.M. and Jain, V.K. Nanofinishing of freeform surfaces of prosthetic knee joint implant. Proceedings of the Institution of Mechanical Engineers, Part B: Journal of Engineering Manufacture, 2012, 226(11), pp.1833-1846.

[137]. Nagdeve, L.; Jain, V.K.; Ramkumar, J. Experimental investigations into nano-finishing of freeform surfaces using negative replica of the knee joint. *Procedia CIRP*, 2016, *42*: 793–798.

[138]. Nagdeve, L., Jain, V.K. and Ramkumar, J. Differential finishing of freeform surfaces (knee joint) using R-MRAFF process and negative replica of workpiece as a fixture. Machining Science and Technology, 2018, 22(4), pp.671-695.

[139]. Kumar, S., Jain, V.K. and Sidpara, A. Nanofinishing of freeform surfaces (knee joint implant) by rotational-magnetorheological abrasive flow finishing (R-MRAFF) process. *Precision engineering*, 2015, *42*, pp.165-178.

[140]. Barman, A. and Das, M. Nano-finishing of bio-titanium alloy to generate different surface morphologies by changing magnetorheological polishing fluid compositions. *Precision Engineering*, 2018, *51*, pp.145-152.

[141]. He Z, Sun S, Deng C. Effect of Hydroxyapatite Coating Surface Morphology on Adsorption Behavior of Differently Charged Proteins. Journal of Bionic Engineering, 2020, 17, 345–356. Harun WS, Asri RI, Alias J, Zulkifli FH, Kadirgama K, Ghani SA, Shariffuddin JH. A comprehensive review of hydroxyapatite-based coatings adhesion on metallic biomaterials. Ceramics International, 2018, 44, 1250-68.

[142]. Ntsoane T P, Topic M, Härting M, Heimann R B, Theron C. Spatial and depth-resolved studies of air plasma-sprayed hydroxyapatite coatings by means of diffraction techniques: Part I. Surface and Coatings Technology, 2016, 294, 153-63.

[143]. Bi Q, Song X, Chen Y, Zheng Y, Yin P, Lei T. Zn-HA/Bi-HA biphasic coatings on Titanium: Fabrication, characterization, antibacterial and biological activity. Colloids and Surfaces B: Biointerfaces, 2020, 189, 110813.

[144]. Wang X, Li B, Zhou L, Ma J, Zhang X, Li H, Liang C, Liu S, Wang H. Influence of surface structures on biocompatibility of TiO2/HA coatings prepared by MAO. Materials Chemistry and Physics, 2018, 215, 339-45.

[145]. Domínguez-Trujillo C, Peón E, Chicardi E, Pérez H, Rodríguez-Ortiz J A, Pavón J J, García-Couce J, Galván J C, García-Moreno F, Torres Y. Sol-gel deposition of hydroxyapatite coatings on porous titanium for biomedical applications. Surface and Coatings Technology, 2018, 333, 158-62.

[146]. He D H, Wang P, Liu P, Liu X K, Ma F C, Zhao J. HA coating fabricated by electrochemical deposition on modified Ti6Al4V alloy. Surface and Coatings Technology, 2016, 301, 6-12.

[147]. Li T T, Ling L, Lin M C, Peng H K, Ren H T, Lou C W, Lin J H. Recent advances in multifunctional hydroxyapatite coating by electrochemical deposition. Journal of Materials Science, 2020, 24, 1-23.

[148]. Suchanek K, Hajdyła M, Maximenko A, Zarzycki A, Marszałek M, Jany BR, Krok F. The influence of nanoporous anodic titanium oxide substrates on the growth of the crystalline hydroxyapatite coatings. Materials Chemistry and Physics, 2017, 186, 167-78.

[149]. Qi J, Yang Y, Zhou M, Chen Z, Chen K. Effect of transition layer on the performance of hydroxyapatite/titanium nitride coating developed on Ti-6Al-4V alloy by magnetron sputtering. Ceramics International, 2019, 45, 4863-9.

[150]. Qadir M, Li Y, Wen C. Ion-substituted calcium phosphate coatings by physical vapor deposition magnetron sputtering for biomedical applications: A review. Acta Biomaterialia, 2019, 89, 14-32.

[151]. Prakash C, Singh S, Pabla B S, Uddin M S. Synthesis, characterization, corrosion and bioactivity investigation of nano-HA coating deposited on biodegradable Mg-Zn-Mn alloy. Surface and Coatings Technology, 2018, 346, 9-18.

[152]. Bao-Chyi W, Edward C, Chyun-Yu Y. Characterization of plasma-sprayed bioactive hydroxyapatite coatings in vitro and in vivo. Materials Chemistry and Physics, 1994, 37, 55-63.

[153]. Singh A, Singh G, Chawla V. Influence of post coating heat treatment on microstructural, mechanical and electrochemical corrosion behaviour of vacuum plasma sprayed reinforced hydroxyapatite coatings. Journal of the Mechanical Behavior of Biomedical Materials, 2018, 85, 20-36.

[154]. Balani K, Anderson R, Laha T, Andara M, Tercero J, Crumpler E, Agarwal A. Plasma-sprayed carbon nanotube reinforced hydroxyapatite coatings and their interaction with human osteoblasts in vitro. Biomaterials, 2007, 28, 618-24.

[155]. Porter A E, Hobbs L W, Rosen V B, Spector M. The ultrastructure of the plasma-sprayed hydroxyapatite–bone interface predisposing to bone bonding. Biomaterials, 2002, 23, 725-33.

[156]. Singh A, Singh G, Chawla V. Mechanical properties of vacuum plasma sprayed reinforced hydroxyapatite coatings on Ti-6Al-4V alloy. Journal of the Australian Ceramic Society, 2017, 53, 795-810.

[157]. Singh A, Singh G, Chawla V. Characterization of vacuum plasma sprayed reinforced hydroxyapatite coatings on Ti–6Al–4V alloy. Transactions of the Indian Institute of Metals, 2017, 70, 2609-28.

[158]. Fazel M, Salimijazi H R, Shamanian M, Apachitei I, Zadpoor A A. Influence of hydrothermal treatment on the surface characteristics and electrochemical behavior of Ti-6Al-4V bio-functionalized through plasma electrolytic oxidation. Surface and Coatings Technology, 2019, 374, 222-31.

[159]. Lu R J, Wang X, He H X, Ling-Ling E, Li Y, Zhang G L, Li C J, Ning C Y, Liu H C. Tantalum-incorporated hydroxyapatite coating on titanium implants: its mechanical and in vitro osteogenic properties. Journal of Materials Science: Materials in Medicine, 2019, 30, 111.

[160]. Singh A, Singh G, Chawla V. Characterization and mechanical behaviour of reinforced hydroxyapatite coatings deposited by vacuum plasma spray on SS-316L alloy. Journal of the mechanical Behavior of Biomedical Materials, 2018, 79, 273-82.

[161]. Misra VC, Chakravarthy Y, Khare N, Singh K, Ghorui S. Strongly adherent Al2O3 coating on SS 316L: Optimization of plasma spray parameters and investigation of unique wear resistance behaviour under air and nitrogen environment. Ceramics International. 2020 May 1;46(7):8658-68.

[162]. Sarao T P, Singh H, Singh H. Enhancing biocompatibility and corrosion resistance of Ti-6Al-4V alloy by surface modification route. Journal of Thermal Spray Technology, 2018, 27, 1388-400.

[163]. Kaur S, Bala N, Khosla C. Investigations of thermal sprayed HAP and HAP-TiO2 composite coatings for biomedical applications. Anti-Corrosion Methods and Materials, 2019, 66, 74-87.

[164]. Yao H L, Hu X Z, Bai X B, Wang H T, Chen Q Y, Ji G C. Comparative study of HA/TiO2 and HA/ZrO2 composite coatings deposited by high-velocity suspension flame spray (HVSFS). Surface and Coatings Technology, 2018, 351, 177-87.

[165]. Balani K, Chen Y, Harimkar S P, Dahotre N B, Agarwal A. Tribological behavior of plasma-sprayed carbon nanotube-reinforced hydroxyapatite coating in physiological solution. Acta Biomaterialia, 2007, 3, 944-51.

[166]. Balani K, Anderson R, Laha T, Andara M, Tercero J, Crumpler E, Agarwal A. Plasma-sprayed carbon nanotube reinforced hydroxyapatite coatings and their interaction with human osteoblasts in vitro. Biomaterials, 2007, 28, 618-24.

[167]. Singh S, Pandey K K, Islam A, Keshri A K. Corrosion behaviour of plasma sprayed graphene nanoplatelets reinforced hydroxyapatite composite coatings in simulated body fluid. Ceramics International, 2020, 46, 13536-13548.

[168]. Ren J, Zhao D, Qi F, Liu W, Chen Y. Heat and hydrothermal treatments on the microstructure evolution and mechanical properties of plasma sprayed hydroxyapatite coatings reinforced with graphene nanoplatelets. Journal of the Mechanical Behavior of Biomedical Materials, 2020, 101, 103418.

[169]. Fu L, Khor K A, Lim J P. Yttria stabilized zirconia reinforced hydroxyapatite coatings. Surface and Coatings Technology, 2000, 127, 66-75.

[170]. Morks M F. Fabrication and characterization of plasma-sprayed HA/SiO2 coatings for biomedical application. Journal of the Mechanical Behavior of Biomedical Materials, 2008, 1, 105-11.

[171]. Singh B, Singh G, Sidhu BS, Bhatia N. In-vitro assessment of HA-Nb coating on Mg alloy ZK60 for biomedical applications. Materials Chemistry and Physics. 2019 Jun 1;231:138-49.

[172]. Pillai RS, Frasnelli M, Sglavo VM. HA/β-TCP plasma sprayed coatings on Ti substrate for biomedical applications. Ceramics International. 2018 Feb 1;44(2):1328-33.

[173]. Ebrahimi N, Zadeh AS, Vaezi MR, Mozafari M. A new double-layer hydroxyapatite/alumina-silica coated titanium implants using plasma spray technique. Surface and Coatings Technology. 2018 Oct 25;352:474-82.

[174]. Unabia RB, Bonebeau S, Candidato Jr RT, Pawłowski L. Preliminary study on copper-doped hydroxyapatite coatings obtained using solution precursor plasma spray process. Surface and Coatings Technology. 2018 Nov 15;353:370-7.

[175]. Zhang C, Xu H, Geng X, Wang J, Xiao J, Zhu P. Effect of spray distance on microstructure and tribological performance of suspension plasma-sprayed hydroxyapatite–titania composite coatings. Journal of Thermal Spray Technology. 2016 Oct 1;25(7):1255-63.

[176]. Clavijo-Mejía GA, Hermann-Muñoz JA, Rincón-López JA, Ageorges H, Muñoz-Saldaña J. Bovine-derived hydroxyapatite coatings deposited by high-velocity oxygen-fuel and atmospheric plasma spray processes: A comparative study. Surface and Coatings Technology. 2020 Jan 15;381:125193.

[177]. Kuo TY, Chin WH, Chien CS, Hsieh YH. Mechanical and biological properties of graded porous tantalum coatings deposited on titanium alloy implants by vacuum plasma spraying. Surface and Coatings Technology. 2019 Aug 25;372:399-409.

[178]. Hameed P, Gopal V, Bjorklund S, Ganvir A, Sen D, Markocsan N, Manivasagam G. Axial suspension plasma spraying: An ultimate technique to tailor Ti6Al4V surface with HAp for orthopaedic applications. Colloids and Surfaces B: Biointerfaces. 2019 Jan 1;173:806-15.

[179]. Ke D, Vu AA, Bandyopadhyay A, Bose S. Compositionally graded doped hydroxyapatite coating on titanium using laser and plasma spray deposition for bone implants. Acta biomaterialia. 2019 Jan 15;84:414-23.

[180]. Singh A, Singh G, Chawla V. Influence of post coating heat treatment on microstructural, mechanical and electrochemical corrosion behaviour of vacuum plasma sprayed reinforced hydroxyapatite coatings. Journal of the Mechanical Behavior of Biomedical Materials. 2018 Sep 1;85:20-36.

[181]. Kaur S, Bala N, Khosla C. Investigations of thermal sprayed HAP and HAP-TiO2 composite coatings for biomedical applications. Anti-Corrosion Methods and Materials. 2019 Jan 7.

[182]. Prakash, C., Kansal, H. K., Pabla, B. S., & Puri, S. Experimental investigations in powder mixed electric discharge machining of Ti–35Nb–7Ta–5Zrβ-titanium alloy. Materials and Manufacturing Processes, 2017, 32(3), 274-285.

[183]. Prakash, C., Kansal, H. K., Pabla, B. S., & Puri, S. On the influence of nanoporous layer fabricated by PMEDM on β-Ti implant: biological and computational evaluation of bone-implant interface. Materials Today: Proceedings, 2017, 4(2), 2298-2307.

[184]. Prakash, C., Kansal, H. K., Pabla, B. S., & Puri, S. Processing and characterization of novel biomimetic nanoporous bioceramic surface on β-Ti implant by powder mixed electric discharge machining. Journal of Materials Engineering and Performance, 2015, 24(9), 3622-3633.

[185]. Merle B, Maier-Kiener V, Pharr GM. Influence of modulus-to-hardness ratio and harmonic parameters on continuous stiffness measurement during nanoindentation. Acta Materialia. 2017 Aug 1;134:167-76.

[186]. Andriollo T, Thorborg J, Hattel J. Analysis of the equivalent indenter concept used to extract Young's modulus from a nano-indentation test: some new insights into the Oliver–Pharr method. Modelling and Simulation in Materials Science and Engineering. 2017 Apr 12;25(4):045004.

[187]. Chen S.L. et. al., "Effect of electro-discharging on formation of biocompatible layer on implant surface," J. Alloys Compd., 456, 413–418, 2008.

[188]. Peng P.W. eet. Al., "Effect of electrical-discharging on formation of nanoporous biocompatible layer on titanium," J. Alloy Comp., 492, 625–630, 2010.

[189]. Lee W.F. et. al., "Nanoporous Biocompatible Layer on Ti-6Al-4V Alloys Enhanced Osteoblast-like Cell Response," J. Exp. Clin. Med., 5(3), 92-96, 2013.

[190]. Tang X, Ahmed T, Rack HJ. Phase transformations in Ti-Nb-Ta and Ti-Nb-Ta-Zr alloys. Journal of Materials Science. 2000 Apr 1;35(7):1805-11.

[191]. Málek J, Hnilica F, Veselý J, Smola B, Bartáková S, Vaněk J. The influence of chemical composition and thermo-mechanical treatment on Ti–Nb–Ta–Zr alloys. Materials & Design. 2012 Mar 1;35:731-40.

[192]. Majumdar P. Microstructural Evaluation of Boron Free and Boron Containing Heat-Treated Ti-35Nb-7.2 Zr-5.7 Ta Alloy. Microscopy and Microanalysis. 2012 Apr 1;18(2):295.

[193]. Niinomi M, Hattori T, Morikawa K, Kasuga T, Suzuki A, Fukui H, Niwa S. Development of low rigidity β-type titanium alloy for biomedical applications. Materials Transactions. 2002;43(12):2970-7.

[194]. Ross P.J., "Taguchi techniques for quality engineering: loss function, orthogonal experiments, parameter and tolerance design," 2nd, McGraw-Hill, 1998.

[195]. Gross, K. A., & Müller, D. M. Topography Control of Hydroxyapatite Coatings. In Key Engineering Materials, 2006, Vol. 309, pp. 693-696. Trans Tech Publications Ltd.

[196]. Lima, R. S., Kucuk, A., & Berndt, C. C. Evaluation of microhardness and elastic modulus of thermally sprayed nanostructured zirconia coatings. Surface and Coatings Technology, 2001, 135(2-3), 166-172.

[197]. Singh, T. P., Singh, H., & Singh, H. Characterization of thermal sprayed hydroxyapatite coatings on some biomedical implant materials. Journal of applied biomaterials & functional materials, 2014, 12(1), 48-56.

[198]. Yao, H.L., Wang, H.T., Bai, X.B., Ji, G.C. and Chen, Q.Y. Improvement in mechanical properties of nano-structured HA/TiO2 multilayer coatings deposited by high velocity suspension flame spraying (HVSFS). Surface and Coatings Technology, 2018, 342, pp.94-104.

[199]. Yao, H.L., Hu, X.Z., Bai, X.B., Wang, H.T., Chen, Q.Y. and Ji, G.C. Comparative study of HA/TiO2 and HA/ZrO2 composite coatings deposited by high-velocity suspension flame spray (HVSFS). Surface and Coatings Technology, 2018, 351, pp.177-187.

[200]. Zheng, X.B. and Ding, C.X. Characterization of plasma-sprayed hydroxyapatite/TiO_2 composite coatings. Journal of thermal spray technology, 2000, 9(4), pp.520-525.

[201]. Prakash C, Singh S, Pabla B S, Uddin M S. Synthesis, characterization, corrosion and bioactivity investigation of nano-HA coating deposited on biodegradable Mg-Zn-Mn alloy. Surface and Coatings Technology, 2018, 346, 9-18.

[202]. Morks, M. F. Fabrication and characterization of plasma-sprayed HA/SiO_2 coatings for biomedical application. Journal of the mechanical behavior of biomedical materials, 2008, 1(1), 105-111.

[203]. Zheng, X.B. and Ding, C.X. Characterization of plasma-sprayed hydroxyapatite/TiO_2 composite coatings. *Journal of thermal spray technology*, 2000, *9*(4), pp.520-525.

[204]. Chen C C, Ding S J. Effect of heat treatment on characteristics of plasma sprayed hydroxyapatite coatings. Materials Transactions, 2006, 47, 935-40.

[205]. Bao-Chyi W, Edward C, Chyun-Yu Y. Characterization of plasma-sprayed bioactive hydroxyapatite coatings in vitro and in vivo. *Materials Chemistry and Physics*, 1994, **37**, 55-63

[206]. Zheng X B, Ding C X. Characterization of plasma-sprayed hydroxyapatite/TiO_2 composite coatings. Journal of Thermal Spray Technology, 2000, 9, 520-5.

[207]. Hameed P, Gopal V, Bjorklund S, Ganvir A, Sen D, Markocsan N, Manivasagam G. Axial suspension plasma spraying: An ultimate technique to tailor Ti6Al4V surface with HAp for orthopaedic applications. Colloids and Surfaces B: Biointerfaces, 2019, 173, 806-15.

[208]. Chen C C, Ding S J. Effect of heat treatment on characteristics of plasma sprayed hydroxyapatite coatings. Materials Transactions, 2006, 47, 935-40.

[209]. Gross K A, Müller D M. Topography Control of Hydroxyapatite Coatings. Key Engineering Materials, 2006, 309, 693-696.

[210]. Lima R S, Marple B R. Thermal spray coatings engineered from nanostructured ceramic agglomerated powders for structural, thermal barrier and biomedical applications: a review. Journal of Thermal Spray Technology, 2007, 16, 40-63.

[211]. Singh T P, Singh H, Singh H. Characterization of thermal sprayed hydroxyapatite coatings on some biomedical implant materials. Journal of Applied Biomaterials & Functional Materials, 2014, 12, 48-56.